INAUGURAL-DISSERTATION

zur

Erlangung der Doktorwürde

der

Naturwissenschaftlich-Mathematischen Gesamtfakultät

der

Ruprecht-Karls-Universität

Heidelberg

vorgelegt von

Diplom-Mathematiker

Jan Rübel

aus Homburg

Tag der mündlichen Prüfung: 2. Juli 2009

Vibrations in Nonlinear Rotordynamics

Modelling, Simulation, and Analysis

Gutachter: Prof. Dr. Dr. h.c. mult. Willi Jäger

Associate Professor Dr. Jens Starke

Abstract

Mechanical vibrations of rotor-bearing systems are an ubiquitous problem in mechanical engineering and the prediction of response frequencies and amplitudes with the help of mathematical models is of major importance for the design of more efficient and reliable machinery. In the present work a model for the dynamics of fast rotating, elastic beams supported in hydrodynamic bearings is derived and its vibration behavior analyzed. Special focus is put on the influence of the nonlinear bearing reaction forces on the dynamics. The continuous rotor is modeled using Euler-Bernoulli beam theory under the inclusion of rotatory inertia and gyroscopic effects. For a general class of support functions the existence of weak solutions to the equations of motion is proved.

The pressure distribution in the oil-lubricated simple journal bearings is modeled by the well known Reynolds' equation. Its derivation from the Navier-Stokes equations by an asymptotic expansion in the film thickness is reviewed and new correction terms for fluid inertia effects are derived. Additional correction terms for the short bearing approximation to Reynolds' equation are also derived by making additional assumptions on the bearings' width-to-radius ratio. Furthermore, the pressure distribution and the bearing reaction forces are computed numerically in dependence of the position and the velocity of the rotor inside the bearings.

The finite element method is applied to discretize the beam equation and the bearing forces are included into the model as point forces in the bearing nodes. While the classical lubrication theory leads to explicit equations of motion, the inertia corrections lead to implicit equations of motion for the rotor-bearing system. The model is evaluated by comparing numerical simulations with experimental results obtained for a passenger car turbocharger. For this example it is shown that the model equations describe the dynamics well, capturing most experimentally observed phenomena, such as unbalance oscillation and self-excited oil whirl. Some differences between model and experiment can be seen in the response frequency of the subharmonic oil whirl. The inertia corrections yield a small improvement compared to the classical models. A new phenomenological correction of the short bearing approximation based on the adaptation of the average circumferential lubricant velocity is proposed and shown to influence the whirl frequency ratio strongly.

Continuation methods for periodic and quasiperiodic solutions are shown to be more efficient and are hence more appropriate tools for the examination of the vibration response behavior than direct numerical simulation. It is shown numerically, that the static gravity load can be neglected for higher rotational frequencies. Combined with a transformation to a co-rotating frame of coordinates this leads to a significant simplification, since the resulting ODE becomes autonomous, and the vibration response can be computed by the continuation of periodic orbits instead of invariant tori. This is applied successfully to study the parameter range where the inertia correction for the short bearing is valid.

All in all, the presented model and its variations prove to be useful for future industrial application in the design of more efficient turbomachinery. Parts of the presented research are already actively used for turbocharger design by the Toyota Central Research and Development Laboratories.

Zusammenfassung

Mechanische Vibrationen von Rotor-Lager Systemen sind ein weit verbreitetes Problem und ihre Vorhersage mit Hilfe mathematischer Modelle ist von außerordentlicher Bedeutung für das Design effizienterer und zuverlässigerer Maschinen. In der vorliegenden Arbeit wird ein Modell für die Dynamik rotierender, elastischer Balken in hydrodynamischen Lagern hergeleitet und sein Vibrationsverhalten untersucht. Besonderes Augenmerk liegt dabei auf dem Einfluss der nichtlinearen Lagerkräfte. Der kontinuierliche Balken wird mit Hilfe der Balkentheorie von Euler und Bernoulli unter Berücksichtigung der Rotationsträgheit und der Kreiselkräfte modelliert. Die Existenz schwacher Lösungen der Bewegungsgleichungen wird für eine allgemeine Klasse von Lagerfunktionen gezeigt.

Die Druckverteilung in den ölgeschmierten Gleitlagern wird durch die Reynolds-Gleichung beschrieben. Die Herleitung dieser klassischen Gleichung aus den Navier-Stokes-Gleichungen durch asymptotische Entwicklung nach der Filmdicke wird erneut durchgeführt. Dabei werden neue Korrekturterme für Trägheitseffekte in der Schmierflüssigkeit durch Berücksichtigung höherer Ordnungen hergeleitet. Unter einer speziellen Annahme an des Verhältnis von Lagerbreite und -radius werden für die Näherungslösung zur Reynolds-Gleichung, die ein kurzes Lager annimmt, ebenfalls Korrekturterme berechnet. Weiterhin werden die Druckverteilung und die daraus resultierenden Lagerkräfte in Abhängigkeit von Rotorposition und Rotorgeschwindigkeit numerisch berechnet.

Durch Anwendung der Methode der finiten Elemente wird die Rotorgleichung diskretisiert. Dabei werden die Lagerkräfte als Punktkräfte in den Lagerknoten modelliert. Während die klassischen Lubrikationsmodelle zu expliziten Systemen gewöhnlicher Differentialgleichungen führen, führt die Berücksichtigung der Korrekturterme zu impliziten Bewegungsgleichungen für das Rotor-Lager-System. Die numerische Evaluation des Modells erfolgt durch Vergleich mit experimentellen Daten, die an einem handelsüblichen Abgasturbolader gewonnen wurden. Am Beispiel des Turboladers wird gezeigt, dass die Modellgleichungen die Schwingungen des Rotors gut beschreiben und die wesentlichen Effekte, insbesondere die unwuchterregte Schwingung und die fluidinduzierte Instabilität (oil whirl), wiedergegeben werden. Die Verwendung der Trägheitskorrekturen führt zu einer leichten Verbesserung der Qualität der Vor-

hersage der Frequenz der Instabilität, bei der kleine Unterschiede zwischen Experiment und Simulation deutlich wurden. Desweiteren wird ein phänomenologisches Modell basierend auf der Adaption der durchschnittlichen Umlaufgeschwindigkeit der Schmierflüssigkeit eingeführt, durch welches die Frequenz der Instabilität stark beeinflusst werden kann.

Kontinuationsmethoden für periodische und quasiperiodische Lösungen erweisen sich als effizienter und daher geeigneter für die Untersuchung des Frequenzverhaltens als die direkte numerische Simulation. Durch Anwendung dieser Methoden wird gezeigt, dass die statische Gewichtslast für große Rotationsfrequenzen vernachlässigt werden kann. In Verbindung mit einer Transformation in ein mitrotierendes Koordinatensystem führt dies zu einer beträchtlichen Vereinfachung des Systems, welches dadurch autonom wird. Durch diese Vereinfachung kann das Schwingungsverhalten durch die Berechnung periodischer Orbits statt invarianter Tori ermittelt werden. Dies wird bei der Untersuchung des Gültigkeitsbereiches der Trägheitskorrektur für das kurze Lager erfolgreich angewendet.

Zusammenfassend lässt sich sagen, dass sich das beschriebene Modell und seine Varianten als geeignet und nützlich für die zukünftige industrielle Anwendung in der Entwicklung effizienterer Turbomaschinen erweist. Einige Ergebnisse dieser Arbeit werden bereits bei den Toyota Central Research and Development Laboratories erfolgreich in der Turboladerentwicklung eingesetzt.

> Time is what happens when
> nothing else happens.
> _____
> Richard P. Feynman
>
> Time is an illusion. Lunchtime
> doubly so.
> _____
> Douglas Adams

Acknowledgements

First of all I would like to express my gratitude to Professor Willi Jäger for giving me the opportunity to work in his group and for granting me the academic freedom to pursue my research. For his open mindedness, his constant support and also for his patience I am very thankful.

Furthermore, I am also very grateful to Professor Jens Starke for initiating the collaboration with the Toyota Central Research and Development Laboratories (TCRDL) and for organizing the research stays in Japan and at the Technical University of Denmark. For his advice, critical remarks, and positive thinking I thank him a lot.

This PhD project has been financially supported by TCRDL for which I am very thankful. My special thank goes to Dr Nobuyuki Mori, Dr Mizuho Inagaki, and Dr Atsushi Kawamoto, as well as all the other members of the Structural Dynamics Lab and the Design Engineering Lab for the good collaboration research. My two stays as a visiting researcher in Nagakute gave me the opportunity for many good discussions on rotordynamics and allowed me to learn a lot about the engineering background and industrial research in general.

During the project I was given the opportunity to spend several weeks in inspiring work exiles at the Department of Mathematics at the Technical University of Denmark. In particular, I have to thank Professor Wolfhard Kliem for the excellent organization, Professor Martin Bendsøe for fruitful discussions and financial support, Michael Elmegård for proof reading and the helpful remarks during the final stage of the thesis, and all the other faculty members for the warm welcome and the good atmosphere. One of the stays was supported by the European Research Training Network, Homogenization and Multiple Scales (HMS 2000).

I am also indebted to Professor Hannes Uecker for the discussions about asymptotic analysis and for his continuing interest in my thesis. Dr Frank Schilder not only kindly provided the continuation software for quasiperiodic tori, the discussions with him also improved my understanding of nonlinear dynamics.

My colleagues in the Applied Analysis group at the University of Heidelberg created a good working atmosphere which I enjoyed a lot and for which I thank them all.

In particular, I would like to thank Christian Reichert for being such a cooperative office companion, Stefan Knauf for the proof reading and his support on `deal.II`, and Eberhard Michel and Cristian Croitoru for their allways available computer advices. I am also very grateful to Frank Strauß, my colleague on the joint research project with TCRDL, for the good cooperation, for many mathematical and non-mathematical discussions, and also for the proof reading. The research stays in Japan and Denmark became even more enjoyable in his company.

Finally, I would like to thank my parents and Verena for their continuing support and nearly endless patience throughout the last years.

Contents

Chapter 1

Introduction

The rotordynamic problems analyzed in this work have originated from a joint research project of the University of Heidelberg and the Toyota Central Research & Development Laboratories. It was the purpose of the project to set up a model for a passenger car turbocharger, to study its dynamics and parameter dependencies. To look at things from a more general point of view, this work focuses on the modeling aspect as well as on the nonlinear dynamics of turbomachinery in general. We will derive the equations of motion from first principles and subsequently analyze them. We prove existence for the equations of motion for a quite general set of bearing force functions. It shows that especially the nonlinear effects of the bearing reaction forces have a large influence on the dynamics. A large part of the work is therefore contributed to the derivation of laws for the bearing pressure distribution by a thin film approximation to the Navier-Stokes equation and to the analysis of their dynamical effects by the numerical solution of the corresponding equations and by numerical continuation methods. The findings obtained from the numerical bifurcation analysis of the proposed model provide a better understanding of the influence of the physical parameters like damping, bearing clearance and width, or weight on the mechanical vibration of the rotor, and hence on the emitted noise and the material fatigue. Thus allowing the industrial engineers to improve future rotating machinery.

The purpose of this introduction is twofold. First it is to introduce the reader with a background in mathematics into the engineering subject of rotordynamics and vice versa. The second purpose is to give an outline of the structure of this thesis and to summarize the main results. Therefore, additionally to the very short abstract at the beginning of this thesis (page *i*), a more detailed summary of the main results is given in Section 1.3 on page 9.

1.1   Rotordynamics

Rotordynamics is the discipline of mechanics that is concerned with the study of the dynamics of systems containing parts that rotate with a significant angular momentum (Crandall, 1995). Rotating mechanical systems are ubiquitous and examples range from the dynamics of planets, satellites and spinning tops to machines such as turbines, compressors, pumps, helicopters, gyroscopic wheels and computer hard drives. There has been a keen interest in rotordynamics since the first steam engines and there is an extensive literature, especially in engineering; for overviews we refer to (Childs, 1993; Gasch *et al.*, 2002; Vance, 1988; Yamamoto & Ishida, 2001; Ehrich, 1999). Rotating machinery is called turbomachinery, if the rotor is used to handle fluids or gases, and energy is exchanged between the process fluid and the rotor. Typical examples of turbomachinery are pumps and compressors, gas and steam turbines, as well as turbochargers.

1.1.1   The Turbocharger

The turbocharger is a prime example of a nonlinear rotordynamical system. A turbocharger is a supercharging device used in many modern engines – especially diesel engines – to increase engine power and to reduce fuel consumption. The turbocharger
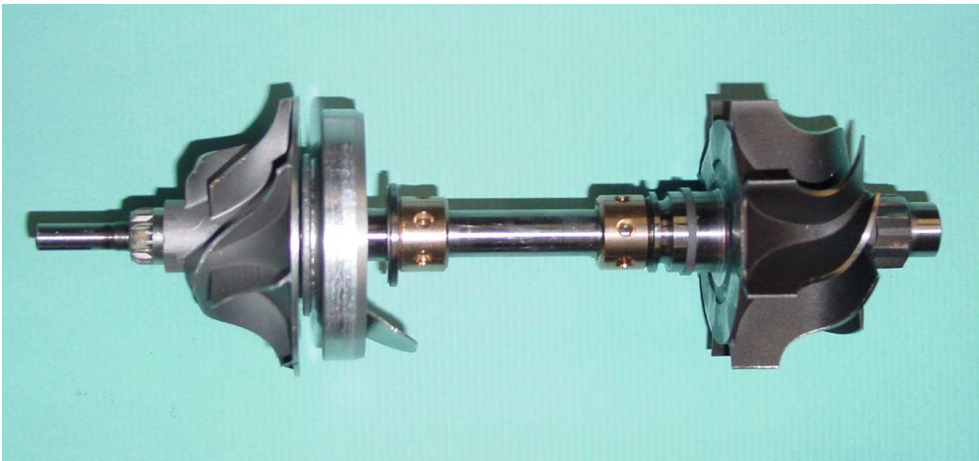
Figure 1.1: The rotor of a turbocharger consists of the shaft, the compressor (left) and the turbine wheel (right). The small brass rings are floating rings and mark the position of the bearings.

for an internal combustion engine consists of a compressor which is powered by a turbine. The turbine is driven by the exhaust gases of the previous combustions. The central part in a typical passenger car turbocharger is the rotor which is depicted in Figure 1.1. It consists of a slender rotor shaft to which the compressor (or impeller) wheel and the turbine wheel are attached. This rotor is supported by oil lubricated bearings
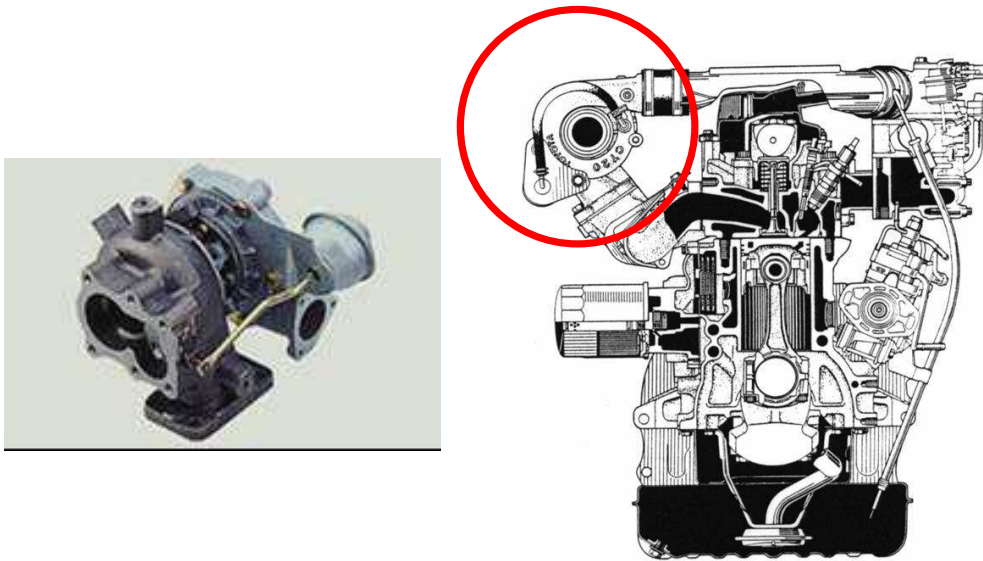
Figure 1.2: The rotor is contained in the casing which is attached to the engine block, here on the upper left of the motor.

and contained in a casing which itself is attached to the engine block (Figure 1.2).

The supercharging of the engine, i.e. higher pressures of the air-fuel mixture inside the cylinders, leads to a higher efficiency of the combustion and thus to reduced fuel consumption and/or more powerful motors. In recent years there has been a renaissance of diesel engines in passenger cars and also in motor sports to which the increasing use of turbochargers has contributed notably. The main working principle of a turbocharger is that the exhaust gases from the cylinders drive the turbine wheel which transmits the rotation to the compressor via the shaft. The pressure of the exhaust gases driving the turbine is regulated by the wastegate. The rotational frequency of the shaft reaches values as high as 120000 RPM, i.e. 2000 Hz.

Higher rotational velocities are desirable for an even better compression. However, it is not possible to increase the frequencies ad infinitum, as the turbocharger and other turbomachinery are subject to major mechanical vibration problems.

1.1.2   Vibration Problems in Rotordynamics

The two most common problems in rotordynamics of turbomachinery are the occurrence of large amplitude steady state synchronous vibrations and the occurrence of subharmonic instabilities (San Andrés, 2006). The former have their source in the unbalance of the rotor due to inevitable production inaccuracies. If e.g. the center of gravity is not aligned with the rotation axis, the centrifugal forces will lead to a periodic forcing of the system. Resonances occur for rotational speeds equal to one of

the rotor's eigenfrequencies. These angular velocities are called critical speeds.

These undesirable oscillations cause noise, wear, material fatigue and failure due to contact, which can have serious consequences since the rotational energy contained in the system is very high. A common countermeasure to unbalance oscillation is the balancing of the rotor to reduce the total unbalance or the introduction of damping. Another possibility is to change the geometry of the rotor-bearing system, such that the resonance frequencies are tuned out of the operation range of the device under consideration. This can be done by shape optimization of the rotor and finding optimal positions of the bearings as has been shown in a related parallel project (Strauß, 2005; Strauß *et al.*, 2007).

The subharmonic vibrations have their source in the nonlinear reaction forces of the fluid bearings, seals and fly wheels interacting with the rotor. These vibrations can also have very high amplitudes and therefore cause noise and wear. Their suppression can be achieved again by changing the geometry of the system to tune the frequencies or by introducing damping. The most desirable option is the elimination of the source of instability. The instability caused by oil lubricated bearings is called oil whirl and can be partially suppressed by using e.g. elliptical bearings instead of circular bearings (San Andrés, 2006).

Several experiments were carried out at Toyota Central R&D Laboratories (TCRDL) for a passenger car turbocharger. The turbocharger was driven by pressurized air and operated at different rotational speeds from 7839 RPM to 101000 RPM ($\sim 130-1700$ Hz). The x- and y-deflection of the shaft was measured by eddy current sensors at both ends and in the middle of the rotor between the two simple journal bearings.

Usually, floating ring bearings are used for the high-speed turbochargers for diesel engines. The use of the simpler plain circular journal bearings leads to more unstable behavior and is not advised in practice. However, in the experiments which were carried out for this project at TCRDL and in the modeling we will examine plain circular journal bearings. The observed dynamics are rich, while the modeling stays simple. The modeling techniques can be easily adapted to more complicated bearing geometries.

Figure 1.3 shows a power spectrum of the observed vibrations and some orbits of the impeller side tip of the rotor, measured at different driving speeds. The orbits show the increasingly complex dynamics of the rotor. In the spectrum in Figure 1.3 we observe two principal vibration modes: a harmonic part with a resonance peak at about 1000 Hz and a subharmonic part setting in at a threshold forcing frequency of about 400 Hz. The frequency of this latter vibration is slightly less than half the forcing frequency. For higher rotational speeds the frequency of the subharmonic increases further, but the shift of the peaks away from the $\frac{\omega}{2}$-line gets larger and the curve on which the peaks are located seems to bend away from the $\frac{\omega}{2}$-line.
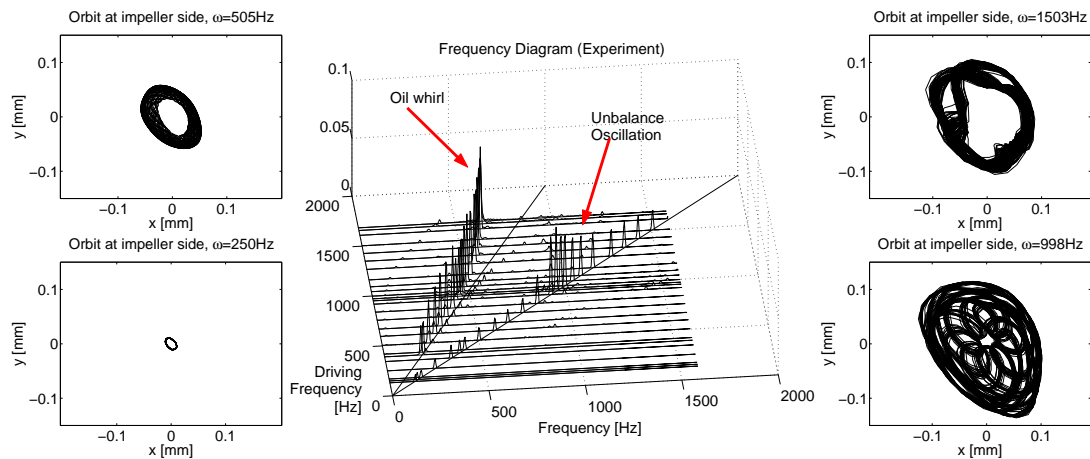
Figure 1.3: Waterfall diagram of the response spectrum for varying driving frequencies and orbits of impeller end of rotor measured in the experiments. Mainly two kinds of vibration occur in the examined frequency range: the subharmonic oil whirl and the synchronous unbalance oscillation of a bending mode.

Analyzing the two kinds of vibration we observe that the harmonic part is mainly due to bending vibration with resonance of the first bending mode at approximately 1000 Hz. In contrast to that the mode shape of the subharmonic vibration is a conical one. The occurrence of the subharmonic vibration has been observed for a long time (Newkirk & Taylor, 1925); see (Yamamoto & Ishida, 2001) for an overview. This self-excited vibration with roughly half the driving frequency is called oil whirl and is caused by the nonlinearity of the supporting oil film. In a series of papers (Muszynska, 1986; Muszynska, 1987; Muszynska, 1988) the occurrence and the stability of this unwanted phenomenon are studied. In the resonance region of the first bending mode of the shaft the amplitude of the self excited oil whirl drops. This phenomenon is called entrainment. It is known (Crandall, 1996) that the ratio of the subharmonic to the driving frequency changes drastically when the angular velocity approaches twice the critical speed and that the so-called oil whip occurs, a large amplitude response with a frequency equal to two times the critical speed of the rotor. In the shown experiment the transition happens slowly. The prediction of the frequency of the subharmonic response and especially setting up a model that reproduces the shift of the subharmonic frequency are two targets of this work.

1.2 Mathematical Modeling

Mathematical modeling has always played an important role in the study of rotordynamic problems. The prediction of the critical speeds of the more and more complicated rotors was the main interest in the early days of rotordynamics at the end of the
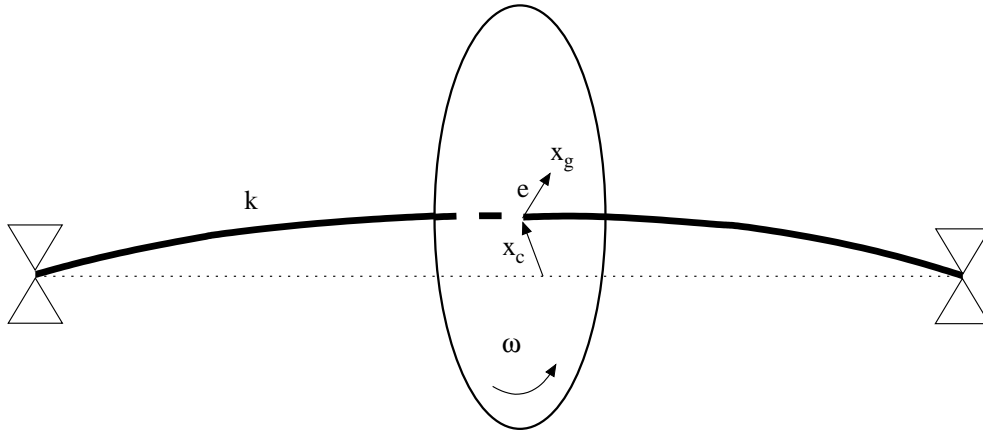
Figure 1.4: The Laval rotor consists of a disk of mass m and a shaft of stiffness k which is fixed at both ends. It rotates with angular velocity ω. The shaft pierces the disk in its center x_c. The center of mass x_g has constant distance e to the center.

nineteenth and the beginning of the 20th century.

A simple and classical example for the usefulness of mathematical modeling in rotor-dynamics is Jeffcott's model for the simple 2-D Laval rotor (Gasch & Pfützner, 1975). The model has been introduced in 1919 and the rotor depicted in Figure 1.4 is therefore also called Jeffcott rotor. It consists of an rotating elastic shaft with stiffness k which is fixed at both ends. A disk of mass m is attached to it in the middle and rotates with the shaft. The center of mass x_g of the disk is supposed to be at distance e from the center x_c of the disk. The balance of the linear elastic force and the inertial force yields

$$m\ddot{x}_g = -kx_c. \tag{1.1}$$

Due to the rotation of the disk the position of the center of gravity can be expressed by

$$x_g = x_c + e\left(\begin{array}{c} \cos\omega t \\ \sin\omega t \end{array}\right). \tag{1.2}$$

Hence the equation of motion for the shaft center is

$$m\ddot{x}_c = -kx_c + m\omega^2 e\left(\begin{array}{c} \cos\omega t \\ \sin\omega t \end{array}\right). \tag{1.3}$$

In this simple example the centrifugal force of the unbalance leads to a periodic forcing term whose amplitude grows quadratically with the angular velocity. The general analytic solution of this differential equation is

$$x(t) = c_1 \cos\omega_c t + c_2 \sin\omega_c t + \frac{\omega^2 e}{\omega_c^2 - \omega^2}\left(\begin{array}{c} \cos\omega t \\ \sin\omega t \end{array}\right), \quad c_1, c_2 \in \mathbb{R}^2. \tag{1.4}$$

Spinning the rotor in the example with the angular velocity $\omega_c = \sqrt{\frac{k}{m}}$ leads to an unbounded solution, i.e. a resonance catastrophe. Therefore ω_c is called critical speed.

In the presence of damping running the system near the critical speed results in a large amplitude response. Despite being very simple, Jeffcott's model exhibits already one of the most important features of rotordynamics, that of unbalance excitation. Using this model Jeffcott proved, that a rotor can be driven at super-critical speeds, i.e. at rotational speeds higher than the critical speed which was doubted before.

The use of more complicated rotor geometries led to a multitude of different models which take into account gyroscopic effects, asymmetries and varying cross sections of the rotor and interactions with the bearings, both with ordinary and partial differential equations. For a detailed overview of the history of rotordynamics we refer to the introduction of (Yamamoto & Ishida, 2001) and to (Nelson, 2003).

In the last decades computer aided engineering (CAE) has become more and more important in the industrial development process. In the automotive industry CAE reduces the cost notably, since the number of prototypes produced for testing purposes can be decreased by using mathematical modeling and applying simulation and optimization algorithms. In rotordynamics CAE is used to predict the vibrations of the rotor. For this the calculation of the critical speeds as well as of the frequencies of eventual self-excited oscillations is necessary. Only if these responses are known, optimization of the vibration level is possible in a second step.

For the investigation of the critical speeds today the finite element method (FEM) is most popular. This method has been developed parallely and rather independently by engineers and mathematicians who have different viewpoints on the method. While mathematicians see it as an approximation method for variational problems in special, low-dimensional function spaces, engineers often see the finite elements as building parts of a mesh that approximates the real object under consideration. Classical works for FEM are (Strang & Fix, 1973) for the mathematical viewpoint, and (Clough, 1960) for the engineering viewpoint. Finite elements for slender rotating beams are introduced in (Nelson & McVaugh, 1976) and are now widely used for the computation of the critical speeds.

Parallely with the increasing computing possibilities, not only the FEM has grown in importance, but also a deeper investigation of the nonlinear dynamics of rotormachinery has been made possible. There is a multitude of nonlinear effects possible in rotordynamics, from nonlinear beam theory for strongly bent rotors to the clearance effects in ball bearings, from hysteretic internal damping to the fluid-structure interaction in the bearings, seals, and fly-wheels (Yamamoto & Ishida, 2001). Though nonlinear effects like oil whirl and whip have been known for a long time (Newkirk & Taylor, 1925), the use of modern simulation methods and numerical analysis has contributed strongly to the theoretical understanding of these effects.

Especially the fluid-structure interaction has drawn major attention, as the development of high-speed turbomachinery beginning in the 1960s and 70s revealed several

rotor instability problems (Childs, 1993). Since the computation of the full 3 dimensional flow of the lubricant and of the pressure distribution in the bearing is a difficult and computationally expensive task, many simplifications and approximations have been proposed. Probably the most famous approximation is Reynolds' equation which reduces the problem to the solution of a scalar, elliptic equation in a two-dimensional domain (Ockendon & Ockendon, 1995). Further simplifications are the so-called short bearing or the long bearing approximation, which allow for an analytic formulation of the pressure distribution (Sommerfeld, 1964; Yamamoto & Ishida, 2001). There is a vast literature dedicated solely to the behavior of hydrodynamic journal bearings bearings, e.g. considering cavitations (Elrod, 1981), turbulent flow (San Andrés *et al.*, 1995), higher order correction terms for Reynolds' equation (Crandall & El-Shafei, 1993; El-Shafei, 1995). For an overview and further references we refer the reader to (Lang & Steinhilper, 1978; Szeri, 1998; Childs, 1993; San Andrés, 2006).

The mathematical models for the bearing pressure distribution allow the computation of the bearing reaction forces acting on the rotor. These models combined with the finite element rotor models allow for the prediction of the instabilities, the frequency response and the amplitudes of the vibrations of the rotor-bearing system. The method of Lund for the computation of bearing coefficients from the bearing forces, which allow to predict the onset of instability has to be mentioned in this context (Lund, 1987). Other examples are (Muszynska, 1987; Muszynska, 1988), where a simple bearing model is used to clarify the onset mechanism of oil whirl and whip, or (Hollis & Taylor, 1986), where the limit cycles of fluid-induced oscillations are calculated by direct numerical simulation. Modern finite element methods for the computation of flow and pressure in the bearings allow an even better prediction of the rotor instabilities and response frequencies (Holt *et al.*, 2005).

The direct numerical simulation of the model equations is a popular approach for the investigation of systems response. By solving multiple initial value problems it allows the validation of the model equations for different parameter sets and also the classification of solutions. However, the direct numerical simulation can be very time consuming, not only because transient behavior has to be accounted for, but also due to long data sets being necessary for the subsequent analysis of the solution with e.g. Fourier analysis.

Numerical continuation and bifurcation methods are therefore an useful and efficient alternative. These techniques provide efficient means of computing branches of solutions of algebraic or differential equations by taking prediction steps along the branch and employing Newton type methods as corrector. Furthermore, they allow the detection and classification of bifurcations, i.e. qualitative changes of the solution. The continuation of locus curves of bifurcations allows the partition of the parameter space into domains of qualitatively equal behavior. Furthermore, continuation methods allow the investigation of unstable solutions, and thus of hysteretic behavior, which

is also not possible by direct numerical simulations, since unstable solutions can not be reached by simulating the underlying system forward in time. They are therefore better suited for extensive parameter studies. The theory of numerical continuation and bifurcation methods is a broad field. We refer to the textbooks (Chow & Hale, 1982; Kuznetsov, 2004; Nayfeh, 2000; Nayfeh & Balachandran, 1995; Wiggins, 1990) and the references there for more information.

1.3 Main Results and Structure of the Thesis

The interest in an accurate model of the turbocharger to predict the vibration response stood at the beginning of this work and the joint research project with TCRDL. The prediction of response amplitude and frequency is of utter importance for the design process. As the existing models did not describe the dynamics of the rotor sufficiently exact and especially the frequency response was not captured correctly, it became necessary to review the modeling process and to introduce some modifications and extensions to the model. Special attention is given here to the modeling of the bearings and to the model validation with techniques for the computation of periodic and quasiperiodic responses.

The thesis is structured into three main parts. The first part consists of the Chapters 2, 3, and 4 where the modeling of rotating beams is reviewed, existence of solutions of the derived partial differential equation is proved, and the finite element method is applied to discretize the equation of motion of the rotor. The second part is identical with Chapter 5 where the lubrication theory for the hydrodynamical journal bearings is derived. Higher order terms from an asymptotic expansion of the Navier-Stokes equations are used to compute correction terms for Reynolds' equation and the short bearing approximation. The third part consists of Chapters 6 and 7. There, we validate the model by direct numerical simulations and use continuation methods for periodic orbits and quasiperiodic tori to compute the frequency response and its parameter dependence. In the conclusions in Chapter 8 we summarize the results again with a special view to future developments and applications.

1.3.1 First Part: The Model for the Rotor

The partial differential equations for the transverse motion of a continuous, isotrope, rotating beam with varying cross-section are the foundation of our model. These equations are derived in Chapter 2 by the Lagrangian formalism using Euler-Bernoulli beam theory and taking into account rotatory inertia and gyroscopic effects following (Yamamoto & Ishida, 2001) and (Nelson & McVaugh, 1976).

The equations obtained for the lateral deflections u and v of the beam as shown in
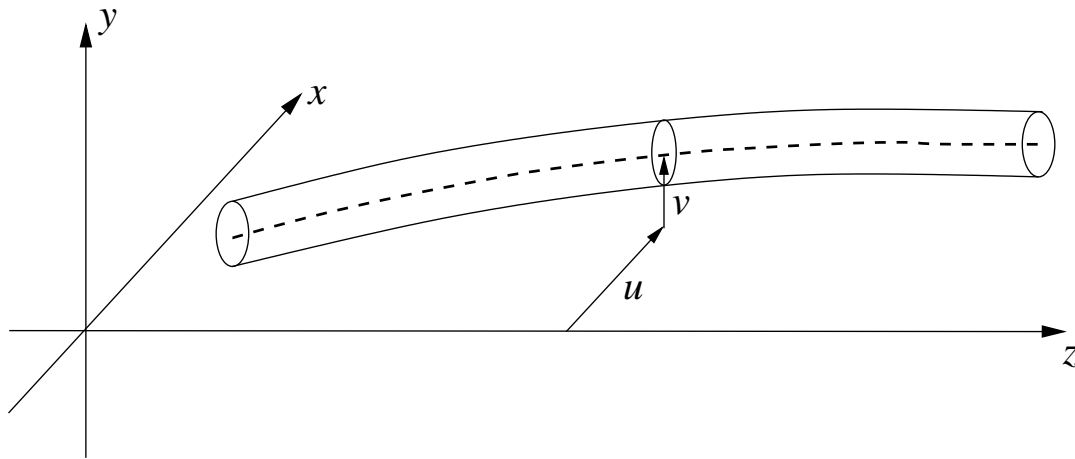
Figure 1.5: The displacement of the rotating beam in x and y direction at the axial position z is described by $u(z)$ and $v(z)$.

Figure 1.5 are

$$(EI_a u'')'' + \mu \ddot{u} - (I_a \ddot{u}')' - \omega(I_p \dot{v}')' + c\dot{u} = \mu\omega^2(r_{G,1} \cos \omega t - r_{G,2} \sin \omega t), \tag{1.5}$$

$$(EI_a v'')'' + \mu \ddot{v} - (I_a \ddot{v}')' + \omega(I_p \dot{u}')' + c\dot{v} = \mu\omega^2(r_{G,1} \sin \omega t + r_{G,2} \cos \omega t) - \mu g, \tag{1.6}$$

where $'$ denotes the derivative with respect to the axial position z, and $\dot{}$ the derivative with respect to time. I_a and I_p are the beams cross-sectional diametral and polar moments of inertia, E is Young's modulus, μ is the mass per length, c the external viscous damping factor, and g the gravitational acceleration. r_G denotes the position of the center of gravity of a cross-section relative to the rotation axis. One sees that analogously to the Jeffcott rotor, the misalignment of center of mass and the rotation axis leads to the appearance of a harmonic forcing term.

The shaft is supported by bearings. The reaction forces of these bearings are modeled as boundary or transmission conditions to the equations of motion. The bending moment and the shear force have jumps of the size of the reaction forces at the location of the bearings ($[f]_z = f(z^+) - f(z^-)$ denotes the jump of f at z)

$$\left[-I_a \ddot{u}' - \omega I_p \dot{v}' + (EI_a u'')'\right]_{z_{b_i}} = f_{b_i,1}, \tag{1.7}$$

$$\left[-I_a \ddot{v}' + \omega I_p \dot{u}' + (EI_a v'')'\right]_{z_{b_i}} = f_{b_i,2}, \tag{1.8}$$

$$\left[-EI_a u''\right]_{z_{b_i}} = t_{b_i,1}, \tag{1.9}$$

$$\left[-EI_a v''\right]_{z_{b_i}} = t_{b_i,2}. \tag{1.10}$$

Together with appropriate initial conditions these 6 equations state the initial/boundary value problem for the motion of the rotor.

In Chapter 3 we prove existence and uniqueness of weak solutions of these equations for a quite general class of bearings. To facilitate notation in that chapter, we use a

complex formulation for the displacement of the form $w = u + iv$, where u and v are the lateral displacements from (1.5) to (1.10). We define general bearing function of the following form

$$f : \mathbb{C}^2 \supset B_{c_r}(0) \times \mathbb{C} \to \mathbb{C}, \tag{1.11}$$
$$(x + iy, v + iw) \mapsto e^{i\gamma}(f^n(r, \dot{r}, \dot{\gamma}) + if^t(r, \dot{r}, \dot{\gamma})),$$

where c_r is the bearing clearance and

$$r = \sqrt{x^2 + y^2}, \ \gamma = arg(x + iy), \ \dot{r} = v \cos \gamma + w \sin \gamma, \ \dot{\gamma} = (w \cos \gamma - v \sin \gamma)/r. \tag{1.12}$$

Note that f is defined only on $B_{c_r}(0) \times \mathbb{C}$ to model the confinement of the shaft inside the bearings. With these bearing functions we prove the following existence theorem.

Theorem. *Let f be a locally Lipschitz, nonlinear support function as in (1.11). Let $a, b \in \Omega = [0, L]$ and let the coefficients μ, E, I_p, $I_a \in L^\infty(\Omega)$ be strictly positive. Furthermore let $g \in H^1(0, T; L^2(\Omega))$ and let $w_0 \in H^3(\Omega)$ with $|w_0(a)|$, $|w_0(b)| < c_r$, and $w_1 \in H^2(\Omega)$.*

There exists a short time weak solution to the initial/boundary value problem (1.5)-(1.10) with support function f, i.e. there is a $T > 0$ and

$$w \in C^0(0, T; H^2(\Omega)), \quad with \quad w' \in C^0(0, T; H^1_m(\Omega)), \tag{1.13}$$

such that for all $\psi \in H^2(\Omega)$ and for almost all $t \in [0, T]$

$$\int_0^L \left[\mu w_{tt} \bar{\psi} + I_a w_{ttx} \bar{\psi}_x - i\omega I_p w_{tx} \bar{\psi}_x + EI_a w_{xx} \bar{\psi}_{xx} \right] dx - \sum_{x_i \in \{a, b\}} f(w(x_i), w_t(x_i)) \bar{\psi}(x_i) = \int g \bar{\psi} dx. \tag{1.14}$$

Furthermore w satisfies the initial conditions:

$$w(0) = w_0 \in H^3(\Omega) \quad and \quad w_t(0) = w_1 \in H^2(\Omega). \tag{1.15}$$

The proof is split in two parts. In the first part we use Galerkin's method to prove existence and uniqueness for the case of linear support functions. In a second step we then use a fixed point argument to prove existence in the nonlinear case.

In Chapter 4 the finite element method is applied to Equations (1.5)-(1.10). We use standard 3rd order Hermite polynomials to compute the well known system stiffness matrix K, gyroscopic matrix G, damping matrix C and mass matrix M for beam elements of constant diameter. A rotor with varying cross-sections can be composed from several such simple beam elements of constant diameter like in Figure 1.6. The individual beam element matrices are then assembled to yield a system of ordinary equations describing the motion of the nodal coordinates of whole beam.
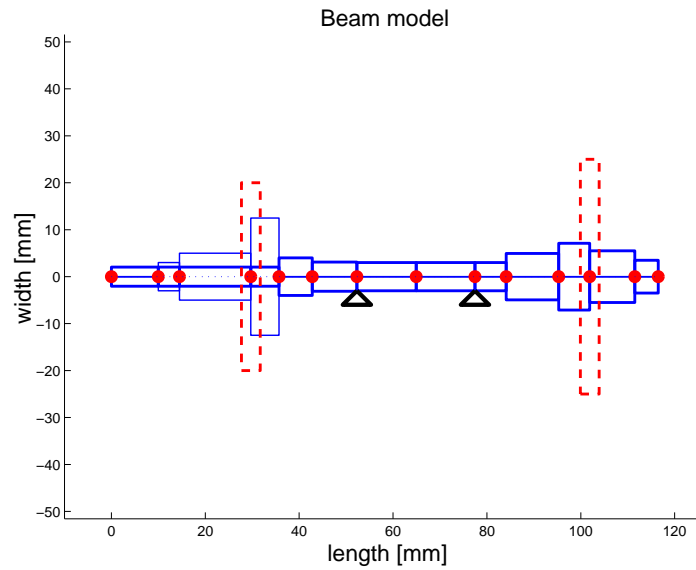
Figure 1.6: Detailed beam model of turbocharger: the rotor shaft is modelled with 13 finite elastic beam elements shown in blue, the turbine and impeller wheels are modelled as rigid disks and are shown with dashed red lines, and the positions of the bearings are indicated by the black triangles.

1.3.2   Second Part: The bearing model

As already mentioned in the previous sections the influence of the bearings is crucial for entire dynamics of the rotor. We assume plain circular journal bearings throughout this work, since bearings of this kind were also used in the experimental setup at TCRDL. The shaft rotates inside this cylindrical bearing and the thin clearance between shaft and bearing is filled with a lubricant fluid as shown in Figure 1.7. The rotation of the shaft creates a circular flow pattern by dragging along the fluid. This flow pattern causes the impedance of the bearing to loads on the shaft by causing higher pressures in narrowing regions of the bearing. This creates reaction forces that oppose the movement. The reaction forces can be calculated from the pressure distribution inside the bearing by integration over the bearing surface. For a thin fluid film of thickness h bounded by two moving surfaces with relative velocities V_φ and V_r the pressure distribution p is given approximately by the well known Reynolds' equation

$$\delta^2 \partial_\varphi(h^3 \partial_\varphi p) + \partial_z(h^3 \partial_z p) = -12(V_r + \frac{1}{2}V_\varphi \partial_\varphi h) \quad \text{for} \quad (\varphi, z) \in [0, 2\pi] \times [0, 1]. \quad (1.16)$$

In Chapter 5 we review the derivation of this elliptic, second order equation from the Navier-Stokes equations by asymptotic analysis with the ratio ε of bearing clearance and bearing radius as small parameter (Ockendon & Ockendon, 1995).

The short bearing approximation to Reynolds' equation is usually derived (Yamamoto & Ishida, 2001) from Reynolds' equation by an additional asymptotic expansion under
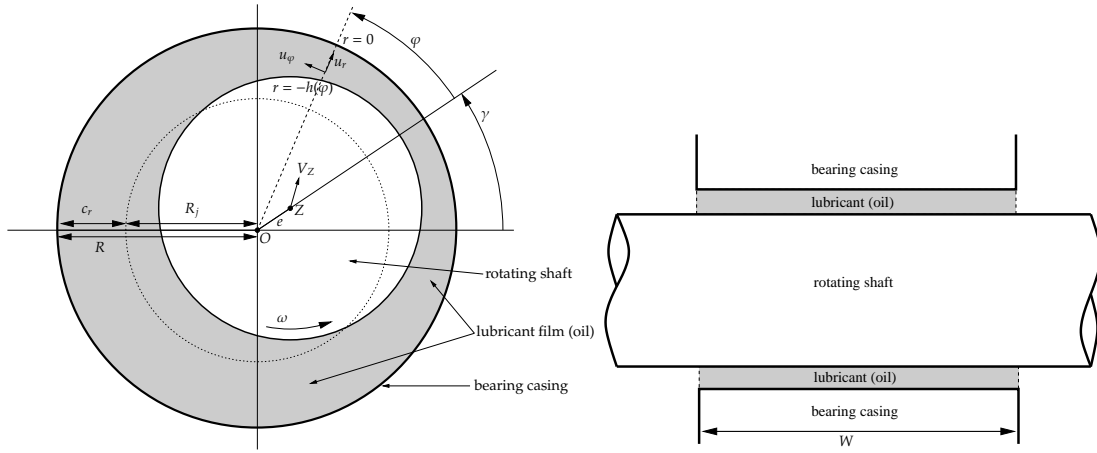
Figure 1.7: Sketch of simple journal bearing; view in axial direction (left) and lateral direction (right); the radial bearing clearance c_r is exaggerated for illustration

the assumption that the ratio δ of the axial length to the radius of the bearing is small. We derive both, Reynolds equation and the short bearing approximation in Chapter 5 in one step from the Navier-Stokes equations by assuming a special relation between the two scaling parameters. With this special scaling we can identify inertia correction terms from higher order terms of the asymptotic expansion. All in all we consider four cases in this work which differ by higher order terms and by the ratio of the bearing width W to the bearing radius R:

1. The classical Reynolds' equation: The ratio $\varepsilon = \frac{c_r}{R}$ is small, while the ratio $\delta = \frac{W}{R}$ is of order 1; no higher order terms are considered.

2. The short bearing approximation: the ratio $\delta = \frac{W}{R}$ is also small in addition to ε. To derive the approximate equations in one step we set $\varepsilon = K\delta^2$. Then the equations simplify even more and an analytical solution for the bearing forces can be obtained.

3. Reynolds' equation with inertia corrections: In the derivation of Reynolds' equation only terms of zeroth order in ε are considered. The inertia correction takes into account also terms of order ε^1.

4. Short bearing with inertia corrections: As above the additional assumption of small δ and $\varepsilon = K\delta^2$ allows for further simplification and analytical solution for the pressure distribution also for the higher order terms.

While the results for points 1 and 2 are well known, the corrected solutions from point 3 and 4 obtained in Chapter 5 are new. We summarize them in two statements.

Statement 1.1. *The pressure solution for the zeroth order short bearing approximation corresponding to point 2 in the list is*

$$p^0 \;=\; -6z(z-1)\frac{\left((\gamma' - \tfrac{1}{2})\kappa \sin\varphi + \kappa' \cos\varphi\right)}{(1 - \kappa \cos\varphi)^3}. \tag{1.17}$$

The inertia correction for the short bearing pressure distribution has the following structure

$$p^1 = F_0 + \mathcal{R}F_1 + \gamma'F_2 + \mathcal{R}\gamma'F_3 + \mathcal{R}(\gamma')^2F_4 + \mathcal{R}\gamma''F_5$$
$$+\mathcal{R}\kappa''F_6 + \kappa'F_7 + \mathcal{R}\kappa'F_8 + \mathcal{R}\kappa'\gamma'F_9 + \mathcal{R}(\kappa')^2F_{10}, \tag{1.18}$$

where the F_j are rational functions of h, $\kappa \cos\varphi$ and $\kappa \sin\varphi$. The detailed formula is given in Equation (5.61). An alternative formulation is given in Appendix E.1. We call $p = p^0 + \varepsilon p^1$ the first order short bearing approximation. This approximation corresponds to point 4 in the list above.

While Statement 1.1 holds for bearings where the ratios $\varepsilon = \frac{c_r}{R}$ and $\delta = \frac{W}{R}$ are both small and approximately fulfill the additional relation $\varepsilon = K\delta^2$, the following statement holds for bearings where only $\varepsilon = \frac{c_r}{R}$ is small and which can have arbitrary width W.

Statement 1.2. *The pressure distribution in a circular hydrodynamic bearing with lubrication film thickness $h_0 = 1 - \kappa \cos\varphi$ is determined by three equations with the same differential operator*

$$L(\cdot) = \delta^2\partial_\varphi^2(\cdot) + \delta^2\frac{3\partial_\varphi h_0}{h_0}\partial_\varphi(\cdot) + \partial_z^2(\cdot) \tag{1.19}$$

and varying right hand sides

$$\varepsilon^0 : \qquad L(p^0) = f_0(\kappa, \dot{\kappa}, \dot{\gamma}), \tag{1.20}$$

$$\varepsilon^1 : \qquad L(p^1) = \Psi(\kappa, \dot{\kappa}, \dot{\gamma}, \ddot{\kappa}, \ddot{\gamma}, p^0, \nabla p^0, \nabla^2 p^0, \nabla^3 p^0, \nabla^2(\partial_t p^0)), \tag{1.21}$$

$$where \qquad L(\partial_t p^0) = \partial_t f_0 - \delta^2\partial_\varphi p^0\left(\frac{3\partial_\varphi\partial_t h_0}{h} + \frac{\partial_t h_0\partial_\varphi h_0}{h_0^2}\right). \tag{1.22}$$

Here the p_i are scalar functions defined on $\Omega = (0,1) \times (0, 2\pi)$. The boundary conditions are

$$p^i(\varphi, 0) = p^i(\varphi, 1) = 0 \qquad\qquad for\ \varphi \in (0, 2\pi), \tag{1.23}$$
$$p^i(0, z) = p^i(2\pi, z) \qquad\qquad for\ z \in (0, 1). \tag{1.24}$$

The parameters κ, γ, $\dot{\kappa}$, $\dot{\gamma}$, etc. are given by the current shaft position and velocity in polar coordinates. The function f_0 is given in Eq. (5.79), while a detailed expression for Ψ can be found in the Appendix E.2. The pressure distribution p^0 is called the zeroth order solution and corresponds to point 1 in the list. The pressure distribution p^1 is called the inertia correction and we call $p = p^0 + \varepsilon p^1$ the first order solution to Reynolds' equation, corresponding to point 3 in the list.

These higher order effects lead to a nonlinear dependence of the pressure distribution, and hence the bearing reaction forces, on the rotational frequency of the shaft. Reynolds' equation as well as the zeroth order short bearing approximation only yield a linear dependence of the pressure on the driving frequency. In Chapter 6 simulations show that this nonlinearity has an influence on the frequency of the subharmonic vibration. In some parameter regions it decreases that frequency, thus reproducing the effect observed in the experiments to a certain degree.

In addition to these analytically justified bearing models, we introduce a phenomenological correction for the zeroth order short bearing approximation

$$\bar{p}^0 = -6\frac{\bar{z}}{W}\left(\frac{\bar{z}}{W} - 1\right)\frac{W^2 \rho \nu}{c_r^2}\frac{\left((\dot{\gamma} - \frac{\omega}{2} + s(\omega))\kappa \sin\varphi + \dot{\kappa}' \cos\varphi\right)}{(1 - \kappa\cos\varphi)^3}. \tag{1.25}$$

The correction term $s(\omega)$ changes the average circumferential lubricant velocity which is equal to $\frac{\omega}{2}$ in the usual short bearing approximation. This average velocity has been identified as an important parameter for the onset and the frequency of the oil whirl (Muszynska, 1986). By introducing this correction, we provide a simple and effective model which can be tuned to show a certain frequency response, as shown by the simulations in Chapter 6.

Finally, in Chapter 5 we also introduce some numerical schemes for the solution of Reynolds equation. In particular, we give variational formulations of (1.20)-(1.22) and use the finite element toolbox `deal.II` (Bangerth *et al.*, 2008) to compute solutions on an adaptive grid. These are used in the numerical simulation for the calculation of the bearing forces. For a more detailed summary of the modeling of the bearings we refer the reader to the conclusions section 5.7 of Chapter 5.

1.3.3 Third Part: Numerical Analysis

Application of the finite element method with standard C^1-elements to the equation of motion yields a system of coupled ordinary differential equations for the nodal coordinates q

$$M\ddot{q} + (C + \omega G)\dot{q} + Kq = F_{\text{unb}}(t) + F_g + F_{\text{bear}} \tag{1.26}$$

with system mass, damping, gyroscopic and stiffness matrices M, C, G, and K, $2\pi/\omega$-periodic unbalance forcing term $F_{\text{unb}}(t)$, static load F_g and bearing reaction forces F_{bear}. For simpler bearing models like the zeroth order short bearing approximation, the forces depend on the deflection q_b and velocity $\dot{q}_b$ of the node inside the bearing

$$F_{\text{bear}} = F_{\text{bear}}(q_b, \dot{q}_b), \tag{1.27}$$

while for bearing models that include inertial terms, they also depend on the acceleration $\ddot{q}_b$

$$F_{\text{bear}} = F_{\text{bear}}(q_b, \dot{q}_b, \ddot{q}_b), \tag{1.28}$$

thus yielding an implicit differential equation.

This model reproduces the experimental results quite well as is shown in Chapter 6 by direct numerical simulation with standard implicit integration methods for stiff problems like backward differentiation formulas (BDF).
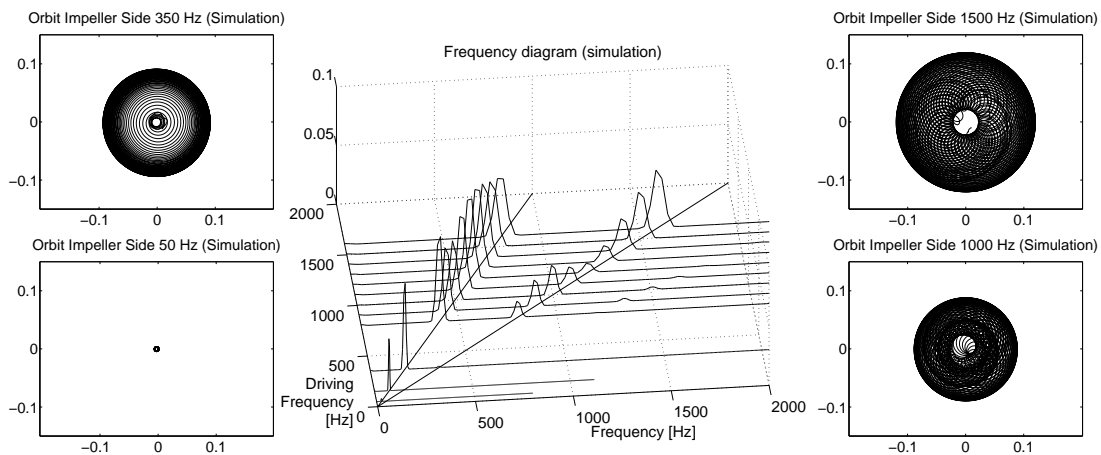
Figure 1.8: Simulated orbits and waterfall diagram showing the response spectrum for 13 element beam model. The parameters are chosen similar to the experimental configuration used for the results in Fig. 1.3. The main experimentally observed vibration effects of subharmonic oil whirl and synchronous unbalance vibration are captured in the model.

Figure 1.8 depicts the simulation results corresponding to the experiment shown in Figure 1.3. It can be seen that the simulated and the experimental results agree to a great deal and that the main dynamical features of the experiment are reproduced. The complexity of the orbits increases with the rotational speed and also the computed amplitudes are only slightly larger than in the experiment. Entrainment can be observed around a rotational speed of 1000 Hz where the first resonance of the harmonic response occurs. There are however two differences between the simulations and the experiments. In the simulations there appears a second peak in the harmonic response, which is caused by the resonance of a second bending mode. This can not be observed in the experiments. Furthermore, the ratio of the oil whirl frequency and the driving frequency remains constant $\frac{1}{2}$ and the shift to lower frequency ratios does not occur.

Further simulations reveal that the inertia corrections of the bearing functions have a small effect on the frequency shift. The right panel in Figure 1.9 shows the response spectra from two simulations of a smaller system. It can be clearly seen, that the use of the inertia correction in the bearing function reduces the subharmonic frequency. The effect of phenomenological correction (1.25) is more pronounced, as can be seen from the left panel in Figure 1.9. By choosing an appropriate correction term, it allows to reproduce a measured frequency behavior of a certain bearing type without detailed modeling of the bearing, and without the computational effort of solving
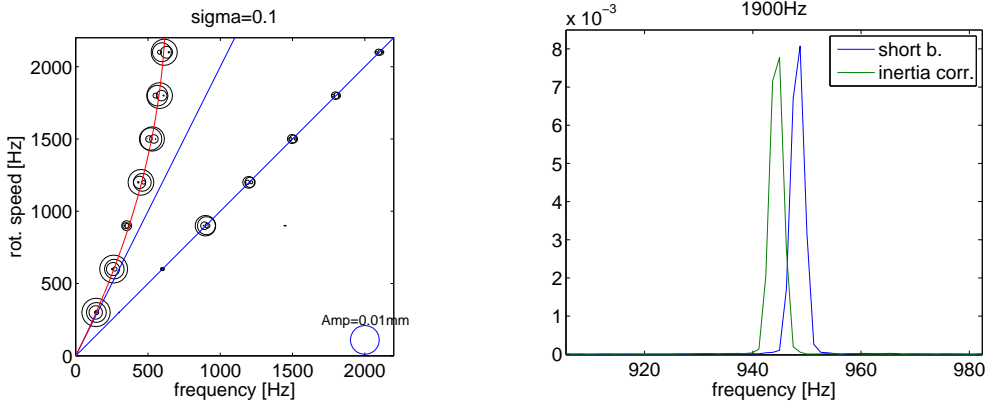
**Figure 1.9:** Left: The phenomenological correction of the short bearing approximation can be used to influence the frequency shift of the subharmonic response frequency. Right: The first order correction of the short bearing approximation has a small effect on the subharmonic response. The blue peak shows the response frequency of the system with an uncorrected, the green peak with inertia corrected bearing function. The system is driven with 1900Hz.

partial differential equations in each time or optimization step. The results of Chapter 6 are summarized in more detail in Section 6.6

Direct simulation is useful to validate the model, for the investigation of the parameter dependence of the solutions, however, continuation methods yield better results, because they allow to investigate also unstable solutions as well as bifurcations. As we have seen before, the rotor-bearing systems examined in this work exhibit responses with more than one frequency. Additionally to the harmonic response to the forcing with frequency ω, there appears also a subharmonic, self-excited oscillation with frequency $\omega_2 \leq \frac{\omega}{2}$. In Chapter 7 we analyze the onset of this self-excited oscillation and show numerically that the instability appears through a torus bifurcation of a stable $\frac{2\pi}{\omega}$-periodic orbit. We compute locus curves of the bifurcations, i.e. stability boundaries, in several parameters such as driving frequency, external damping and bearing clearance. It shows that the self-excited oscillation can be suppressed by increasing external damping, or by decreasing the bearing clearance.

A transformation of the equations of motion to a frame of coordinates co-rotating with angular velocity ω

$$M\ddot{p}+(2\omega MH+G+C)\dot{p}+(K-\omega^2 M+\omega GH+\omega CH)p = \tilde{F}_{\text{bear}}(p,\dot{p})+F_{\text{gr}}\cos(\omega t)+\omega^2 F_{\text{unb}} \quad (1.29)$$

together with the neglection of the static (e.g. gravity) load F_{gr} leads to a significant simplification of the equations of motion, since the system becomes autonomous. This has the effect that quasi-periodic solutions with one of the basic frequencies equal to ω in the fixed frame of coordinates are transformed to periodic solutions in the co-rotating frame. This simplification has been applied for the computation of the periodic orbits shown in Figure 1.10 with the software package for numerical
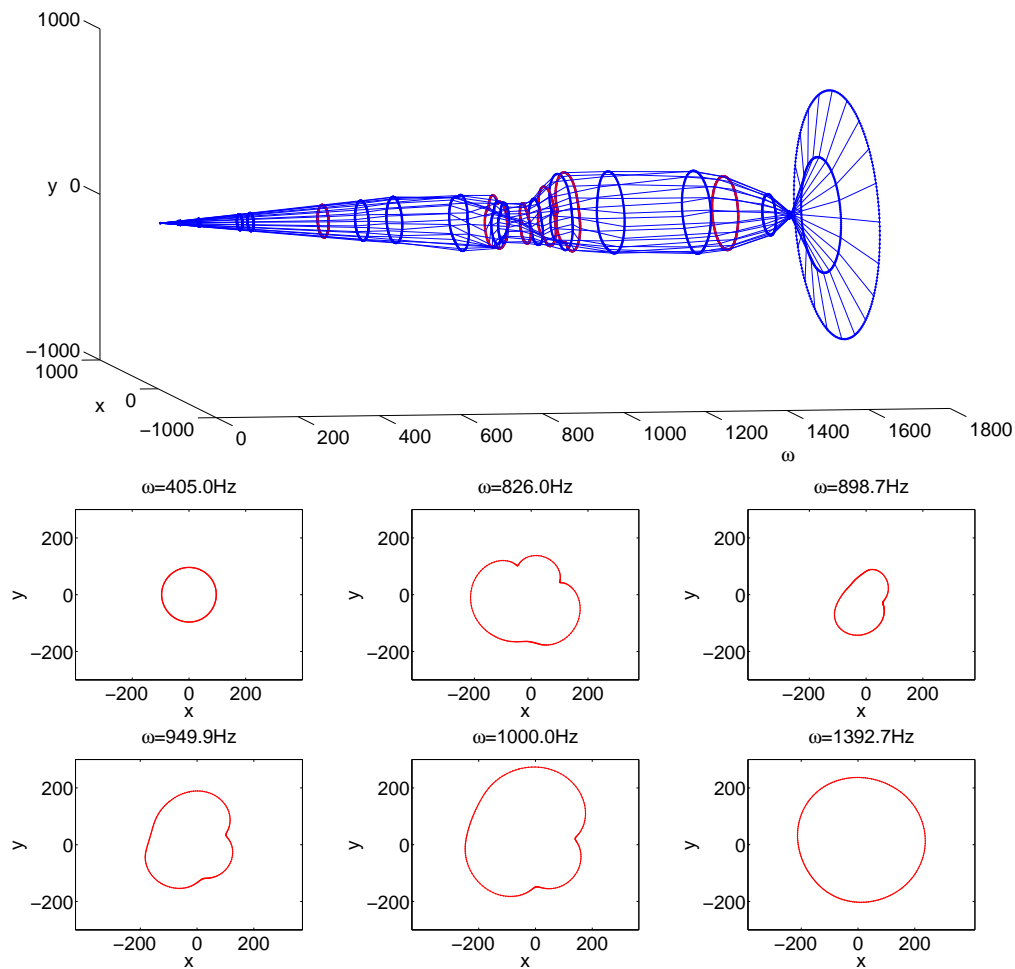
Figure 1.10: Continuation of periodic solutions of Eq. (7.22) in absence of constant load w.r.t. driving frequency; the two lower lines of graphs show the detailed orbits drawn in red in the top figure.

continuation AUTO (Doedel *et al.*, 2000).

A justification for the simplification of neglecting the static load is also given in Chapter 7 through the computation and continuation of the corresponding quasiperiodic tori of the non-simplified system. In Figure 1.11 we show the locus curves of quasiperiodic tori with constant rotation number in the driving frequency- bearing clearance domain. The rotation number given by the color of the respective branch. A comparison with the frequency of the corresponding periodic orbits like those depicted in Figure 1.10 shows significant differences only for small rotational frequencies outside the usual range of operation of the turbocharger. The continuation method for quasiperiodic tori has been applied to a 'real world' problem of this size for the first time in this work and has been published in (Schilder *et al.*, 2007). It is based on a Fourier method proposed in (Schilder & Peckham, 2007).
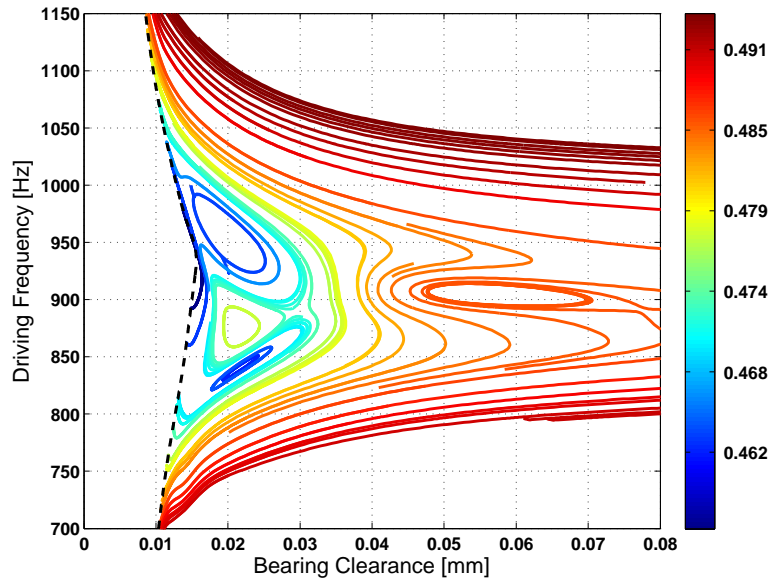
Figure 1.11: Locus curves of quasiperiodic tori with constant rotation number indicated by the color. The dashed line shows the locus of a torus or Neimark-Sacker bifurcation.

The continuation methods combined with the simplification of neglecting gravity and transforming into a co-rotating frame is also used to study the influence of the inertia. The implicity of the equation of motion in that case makes necessary an adaptation of the numerical method since AUTO only can deal with explicit equations. We employ an internal Newton method to solve the implicit equation (1.28) for $\ddot{q}$ in every iteration step of the corrector method of the continuation method. Even though this increases the total number of Newton steps, this is still more efficient than direct numerical simulations. It shows that only very few internal Newton steps are necessary. The results show that the effect of the short bearing inertia correction can be observed over a large parameter range in bearing width ($W = 0.25\,\text{mm} - 2\,\text{mm}$) and driving frequency ($\omega = 0\,\text{Hz} - 2000\,\text{Hz}$). However, the validity of the first order correction for the short bearing approximation is not given for bearings of the length used in the experimental set-up ($W = 5.4$). Instead, the full Reynolds' equation with inertia correction from 1.21 should be used. This is numerically very expensive, which makes a bifurcation analysis of the same detailedness impossible. However, a proof of principle for the method proposed is given in the last section of Chapter 7. Therefore it could be used in the development and validation of future models for rotordynamical systems. The reader is referred to Section 7.9 at the end of Chapter 7 for a more detailed summary of the results of the numerical bifurcation analysis.

The conclusions in Chapter 8 close this thesis with a discussion of the results in the light of further developments and applications.

Chapter 2

Continuous Rotor Model

In this chapter we derive partial differential equations that model the transverse motion a slender rotating beam. The model is based on the theory of linear elasticity and includes gyroscopic effects. In Section 2.1 the geometry of the beam is defined and special attention is paid to the imperfections in the geometry which can be caused during production and which lead to static unbalance excitation. Afterwards we derive the equations of motion for a rotating Rayleigh beam by means of the Lagrangian formalism in Sections 2.2 to 2.4. We obtain two partial differential equations for the transversal displacements which include rotatory inertia and gyroscopic terms. Further modifications for the inclusion of fly wheels into the model are made in Section 2.5. Angular misalignment of the rigid disks modeling the wheels leads to dynamic unbalance excitation. Finally we show how bearings can be added to the model (Sec. 2.6) and introduce a complex valued notation which reduces the number of equations (Sec. 2.7).

2.1 Beam Geometry

A beam is a three-dimensional solid body with a long-stretched geometry, meaning that it has two small dimensions compared to the third. In the following the beam is supposed to be homogeneous and isotropic, i.e. all the material properties like density or Young's modulus do not depend on position. It is supposed to rotate about its center line with constant angular velocity ω. In the undeformed state the rotational axis is identical with the z-axis. In the center of each cross-section we fix a coordinate system spanned by the cross-section's principal axis of inertia $e_1(z)$ and $e_2(z)$, and the normal vector $e_3(z)$). This coordinate system is rotating with the same angular velocity.

In the following we will consider a circular beam of total length L with varying cross-
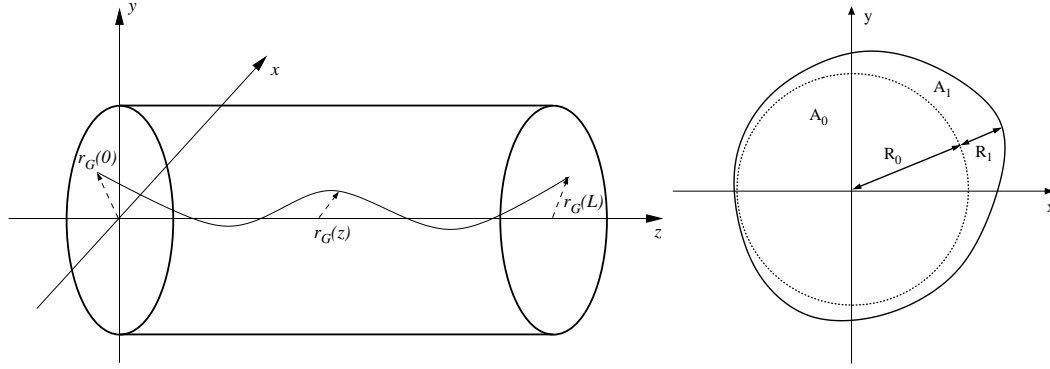
Figure 2.1: Left: Location of the center of mass along the axis of the beam; the eccentricity at axial position z is given by $r_G(z)$. Right: Shape of a cross-section with circular inner part A_0 and perturbed exterior A_1. The size of the perturbation is exaggerated for illustration.

sectional shape. The reference configuration is given by

$$\mathcal{D} = \{(x, y, z) \in \mathbb{R}^3 | z \in [0, L], \sqrt{x^2 + y^2} \leq R(z, \varphi) \ll L\}, \tag{2.1}$$

where $\varphi = \arg(x + iy)$ and the shape function $R : [0, L] \times [0, 2\pi] \to \mathbb{R}$ is a piecewise continuous in z and in φ, bounded, strictly positive function. Where it is more convenient, e.g. in sums, we will also use the notation $r = (x, y, z) = (x_1, x_2, x_3)$ for points in $\mathcal{D}$.

A major source of vibration in real life rotating machine elements is unbalance which is caused by small imperfections in the geometry due to production and by unbalanced loads on the beam. The small imperfections of the rotor can be modelled either by assuming non perfect geometry or by allowing small density variations. We will take the first point of view and assume homogeneous density ρ and the shape function R to be of the form

$$R(z, \varphi) = R_0(z) + R_1(z, \varphi) > 0. \tag{2.2}$$

We take $R_0 > 0$ and $R_1 \geq 0$, and further more we consider the non-circular perturbation R_1 to be small, i.e. for all $(z, \varphi) \in [0, L] \times [0, 2\pi]$ we have

$$\frac{R_1(z)}{R} = \frac{R - R_0}{R} \ll 1. \tag{2.3}$$

Therefore its contribution to the area $A(z)$ of each cross-section is also small,

$$\frac{A_1(z)}{A(x)} = \frac{\int_0^{2\pi} \int_{R_0}^{R_0+R_1} r \, dr \, d\varphi}{\int_0^{2\pi} \int_0^{R_0+R_1} r \, dr \, d\varphi} \ll 1. \tag{2.4}$$

The mass per length μ is given by

$$\mu(z) = \rho A(z). \tag{2.5}$$

We define the center of mass $(r_{G,1}, r_{G,2})(z)$ of a cross-section $A(z)$ orthogonal to the z-axis in the body-fixed coordinate frame of the principal axis of inertia by

$$r_{G,\alpha}(z) \quad = \quad \frac{1}{\mu(z)} \int\limits_{A(z)} \rho x_\alpha \, dx \, dy \tag{2.6}$$

$$= \quad \frac{1}{\mu(z)} \int\limits_{A_0(z)} \rho x_\alpha \, dx \, dy + \frac{1}{\mu(z)} \int\limits_{A_1(z)} \rho x_\alpha \, dx \, dy \tag{2.7}$$

$$= \quad \frac{1}{\mu(z)} \int\limits_{A_1(z)} \rho x_\alpha \, dx \, dy \quad \text{for} \quad \alpha = 1, 2. \tag{2.8}$$

The first integral in (2.7) vanishes due to the circular shape of the unperturbed cross-section with radius R_0. Only the perturbation part of radius R_1 gives a nonzero contribution. However, the smallness of R_1 compared to the entire radius obviously also yields the smallness of $r_{G,\alpha}$ compared to the shaft radius. As shown in Fig. 2.1 r_G describes the eccentricity of the centers of mass of the cross-sections. The coordinate system of the principal axis of inertia is rotating with an angular velocity ω with respect to the coordinate system which is fixed in space. Hence the coordinates r_G of the center of mass in the rotating system and the position of the center of mass r_g in the fixed system are related

$$r_G = A(\omega t) r_g, \tag{2.9}$$

where the matrix A is the rotation matrix

$$A(\omega t) = \begin{pmatrix} \cos \omega t & \sin \omega t \\ -\sin \omega t & \cos \omega t \end{pmatrix}. \tag{2.10}$$

The perturbation of the shape also leads to a perturbation of the principle moments of inertia of the cross-sections. We have defined the slender beam to be small in two dimensions and elongated in the third. Like before, we now look at infinitesimal cross-sections orthogonal to the z-axis. The tensor of inertia J of such an infinitesimal cross-section in a fixed coordinate system whose origin is located at its center is defined by

$$J_{ij} \quad = \quad \int\limits_{A(x_3)} \rho(\delta_{ij} x_k x_k - x_i x_j) \, dx_1 \, dx_2 \, dx_3. \tag{2.11}$$

By using the fact that the center is located at the origin ($x_3 = 0$) and by the decomposi-

tion of the area $A(x_3)$ into the circular part A_0 and the perturbed part A_1 we obtain

$$J_{31} = J_{32} = 0,$$

$$J_{33} = \int_{A(x_3)} \rho x_\alpha x_\alpha \, dx_1 \, dx_2 \, dx_3 =: \rho I_p(x_3) \, dx_3 + \int_{A_1(x_3)} \rho(x_1^2 + x_2^2) \, dx_1 \, dx_2 \, dx_3,$$

$$J_{12} = - \int_{A(x_3)} \rho x_1 x_2 \, dx_1 \, dx_2 = - \int_{A_1(x_3)} \rho x_1 x_2 \, dx_1 \, dx_2 \, dx_3 := -\rho \Delta I_{12} \, dx_3,$$

$$J_{11} = \int_{A(x_3)} \rho x_2^2 \, dx_1 \, dx_2 \, dx_3 =: \rho I_a(x_3) \, dx_3 + \int_{A_1(x_3)} \rho x_2^2 \, dx_1 \, dx_2 \, dx_3,$$

$$J_{22} = \int_{A(x_3)} \rho(x) x_1^2 \, dx_1 \, dx_2 \, dx_3 =: \rho I_a(x_3) \, dx_3 + \int_{A(x_3)} \rho x_1^2 \, dx_1 \, dx_2 \, dx_3.$$

We see that J_{11}, J_{22}, and J_{33} can be expressed in terms of a the circular cross-sections area moments of inertia, the diametral moment I_a and the polar moment I_p, respectively, and small perturbations caused by the shape perturbation R_1. Hence the inertia tensor of the cross-section has the following form

$$J = \rho \begin{pmatrix} I_a + \Delta I_{11} & -\Delta I_{12} & 0 \\ -\Delta I_{12} & I_a + \Delta I_{22} & 0 \\ 0 & 0 & I_p + \Delta I_{33} \end{pmatrix} dz. \tag{2.12}$$

The coordinate systems spanned by the cross-section's principal axis of inertia $(e_1(z), e_2(z), e_3(z))$ in which I is diagonal depend on z. However, from $J_{31} = J_{32} = 0$ we can deduce that the third principal axis e_3 is always collinear with the z-axis. After diagonalization of the tensor, let the principal moments of inertia be J_1, J_2 and $J_3 = J_{33}$ and let principal area moments be I_1, I_2 and I_3. We then have $J_i = \rho I_i \, dz$. Due to the small variations in shape, the diametral moments I_1 and I_2 differ only by small perturbations ΔI_i from the diametral area moment $I_a = \pi R^4/4$ of a perfect disk. We will assume that

$$I_1 = I_a + \Delta I, \quad \text{and} \quad I_2 = I_a - \Delta I. \tag{2.13}$$

This assumption can be fulfilled by adapting the radius R in such a way that a perfect disk of radius R has an area moment equal to the mean of I_1 and I_2. The polar area moment for a circular cross-section with uniform density distribution is $I_p = \pi R^4/2$.

2.2   Potential Energy of the Rotating Beam

We will now derive an expression for the elasic energy stored in a deformed rotating beam. In order to describe deformations of the reference configuration $\mathcal{D}$ we define the displacement field $u : \mathcal{D} \to \mathbb{R}^3$. This vector field u describes the translation of a

point x of the reference configuration to its new position $\tilde{x}$, i.e. for all $x \in \mathcal{D}$ we have

$$\tilde{x} = x + u(x). \tag{2.14}$$

In the following we will assume that the displacement of the beam is small. This assumption leads to the classical Euler-Bernoulli beam theory which can be found in many textbooks. In (Landau & Lifschitz, 1983) it is derived by physical reasoning, in (Trabucho & Viaño, 1995) the displacement field is derived by strict asymptotic analysis based on a variational formulation and using only the two assumptions that the overall displacement is small and that two dimensions of the beam are small. Shear effects can be neglected for slender beams. The shaft of the turbocharger we want to model has a slenderness ratio $s = L/R \approx 70$ for which it is sufficient to use Euler-Bernoulli-theory. The inclusion of such shear effects would lead to Timoshenko beam theory (Han *et al.*, 1999) which is not studied in further detail in this work. A continuous rotating Timoshenko beam model can be found in (Eshleman & Eubanks, 1969) and in (Nelson, 1980) where also a finite element discretization for such beams is presented.

First we consider the displacement field $(u_1, u_2, u_3) : \mathcal{D} \to \mathbb{R}^3$ obtained from Euler-Bernoulli theory in the rotating frame of the bodies principal axis of inertia. In the absence of axial forces it can be described (Trabucho & Viaño, 1995) by

$$u_1(x, y, z) = d_1(z), \quad u_2(x, y, z) = d_2(z), \quad u_3(x, y, z) = x\partial_z d_1 + y\partial_z d_2. \tag{2.15}$$

Cross-sections orthogonal to the center line stay planar and orthogonal to the center line after deformation. The displacement of the center line is hence sufficient to describe the whole displacement of the beam. If the displacement is small, the elastic energy of a bent Euler-Bernoulli beam is given (Landau & Lifschitz, 1983) by

$$U_e = \frac{1}{2} \int_0^L EI_1(\partial_{zz} d_1)^2 + EI_2(\partial_{zz} d_2)^2 \, dz. \tag{2.16}$$

Here E is Young's modulus. I_1 and I_2 are the cross-sectional diametral moments of inertia.

If we assume that the beam rotates about its center line with constant angular velocity ω we can transform the above expression to a fixed coordinate system in which the deformation of the centerline is described by the functions u for the deformation in the x-direction and by v for the deformation in the y-direction. We have

$$\begin{pmatrix} d_1 \\ d_2 \end{pmatrix} = A(\omega t) \begin{pmatrix} u \\ v \end{pmatrix}. \tag{2.17}$$

If we denote by $'$ the derivative with respect to z, we obtain from (2.16)

$$
U_e = \frac{1}{2} \int_0^L EI_1(\cos \omega t u'' + \sin \omega t v'')^2 + EI_2(-\sin \omega t u'' + \cos \omega t v'')^2 \, dz
$$

$$
= \frac{1}{2} \int_0^L E\Big((I_1 \cos^2 \omega t + I_2 \sin^2 \omega t)u'' + (I_2 \cos^2 \omega t + I_1 \sin^2 \omega t)v''
$$

$$
+ 2(I_1 - I_2)u''v'' \cos \omega t \sin \omega t\Big) dz
$$

$$
= \frac{1}{2} \int_0^L EI_a(u''^2 + v''^2) + E\Delta I\Big((u''^2 - v''^2)\cos 2\omega t + 2u''v'' \sin 2\omega t\Big) dz. \qquad (2.18)
$$

If the rotor is also subject to gravity (or other static loads which are given by a potential) we have to add the potential to the elastic energy (2.18)

$$
U = U_e + U_{\text{pot}} = U_e + \int_0^L \mu g v \, dz. \qquad (2.19)
$$

where the second equation is for gravity acting in the $-y$-direction and g denotes the gravitational acceleration.

2.3   Kinetic Energy of the Rotating Beam

Euler-Bernoulli theory states that planar cross-sections of the undistorted beam which are orthogonal to the center line stay planar and orthogonal to the center line also in the bent state. Our derivation of the kinetic energy of the rotating beam is based upon this observation.

In the unbent reference state each point in the beam is described by its position along the axis of the rotor (z-coordinate) and its position on the cross-section orthogonal to the center line at the point's z-coordinate. The position of the center relative to the z-axis is denoted by $r_0(z, t)$ and the center line has the coordinates (r_0, z). In the unbent state therefore $r_0 = 0$. At each point on the z-axis we choose the principal axes of inertia of the cross-section $e_1(z, t), e_2(z, t)$ and the normal vector $e_3(z, t)$ as moving orthonormal basis for that cross-section. As stated above this normal vector is always collinear with the tangent vector of the center line. Using the sum convention the position of the material point relative to the center line is given by $r = \xi_\alpha e_\alpha(z, t)$. Repeated Greek indices are summed over 1 and 2, and repeated Roman indices are summed over 1, 2, and 3.

The new position $X(x, t)$ of a material point x at time t is given by the displacement $r_0(z, t)$ of the center point transverse to the z-axes and the position relative to the center

point

$$X(x,t) = r_0(z,t) + \xi_\alpha e_\alpha(z,t).$$ (2.20)

The cross-section in which the point x lies in the undistorted beam remains rigid and orthogonal to the center line. The position of the point on the disk is given by $\xi_\alpha e_\alpha(z,t)$ in terms of the rotating coordinate system. The disk rotates with the angular velocity $\Omega(z,t)$ about the momentary axis of rotation spanned by $\Omega = \Omega_i e_i$.

The kinetic energy of the beam is given by the integral over the velocities in each point

$$T = \frac{1}{2} \int_{\mathcal{D}} \rho(x)(\partial_t X(x,t))^2 \, dx^3.$$ (2.21)

Using the above assumptions on the deformation we obtain by integration over the cross-sections

$$
\begin{aligned}
T \quad &= \quad \frac{1}{2} \int_{\mathcal{D}} \rho(x)(\dot{r}_0(z,t) + \Omega(z,t) \times \xi_i e_i(z,t))^2 \, dx^3 \\
&= \quad \frac{1}{2} \int_{\mathcal{D}} \rho(x)(\dot{r}_0(z,t) \cdot \dot{r}_0(z,t) + 2\dot{r}_0(z,t) \cdot (\Omega(z,t) \times \xi_i e_i(z,t)) \\
&\qquad + (\Omega(z,t) \times \xi_i e_i(z,t)) \cdot (\Omega(z,t) \times \xi_i e_i(z,t))) \, dx^3 \\
&= \quad \frac{1}{2} \int_{\mathcal{D}} \rho(x)(\|\dot{r}_0(z,t)\|^2 + 2(\dot{r}_0(z,t) \times \Omega(z,t)) \cdot \xi_i e_i(z,t) \\
&\qquad + (\Omega_1 \xi_2 - \Omega_2 \xi_1)^2 + (\xi_1^2 + \xi_2^2)\Omega_3) \, dx^3 \\
&= \quad \frac{1}{2} \int_0^L \mu(\dot{u}^2 + \dot{v}^2) + 2\mu \dot{r}_0 \cdot (\Omega \times r_g(z,t)) + I_1\Omega_1^2 + I_2\Omega_2^2 + I_3\Omega_3^2 \, dz
\end{aligned}
$$ (2.22), (2.23)

$$=: \quad \int_0^L T_t + T_{\text{unb}} + T_{\text{rot}} \, dz,$$ (2.24)

where we used the property of the e_i being the principal axis of inertia of the disk. The energy splits into three parts. The first term in (2.23) gives the translational kinetic energy T_t. The term containing the eccentricity $r_g(z,t)$ of the cross-section appears when integrating the second term in the third line. It gives the rotational energy stored in the rotation of the center of mass of the cross-section about the center line and is denoted by T_{unb}. The third term gives the rotational energy T_{rot} of the inclined disk. Starting with the last term we will now derive expressions for the rotational energy in terms of the displacement and the inclination of the center line. To do so, we have to express the momentary angular velocity Ω in such terms. This can be achieved by introducing Euler angles describing the postion of the disk.

The position of the cross-section relative to the origin is given by the Euler angles (γ, β, ϕ) (Nelson & McVaugh, 1976). The three angles describe three successive rotations
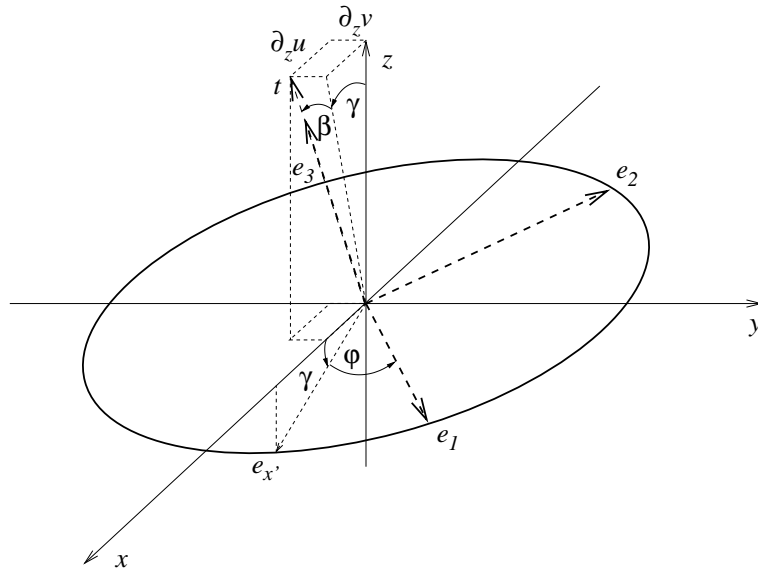
Figure 2.2: Euler angles γ, β and ϕ describe the orientation of the rotating disk.

of the disk whose principal axis of inertia (e_1, e_2, e_3) are assumed to be initially collinear with the space coordinate system (e_x, e_y, e_z). The first rotation leaves the y-axis fixed and rotates the disk by the angle γ about this axis. The second rotation leaves the image $e_{x'}$ of the vector e_x fixed and rotates the disk by β. The third rotation which corresponds to the spin of the disk rotates the coordinate system about the image of e_z under the first two equations by the angle ϕ.

From Figure 2.2 we see that the momentary angular velocity is given by

$$\Omega = \dot{\gamma} e_y + \dot{\beta} e_{x'} + \dot{\phi} e_3. \tag{2.25}$$

In this equation e_y is the unit vector in y-direction, e_3 is the normal vector to the plane (and also spans a principal axis of inertia), and $e_{x'}$ is the unit vector along the image of the x-axis after the first rotation. From (2.25) we can obtain the expression for the current angular velocity in terms of the Euler angles. The detailed calculations of what follows are given in the Appendix A where we obtain

$$\begin{align}
\Omega_1 &= \dot{\gamma} \sin \varphi \cos \beta + \dot{\beta} \cos \varphi, \tag{2.26} \\
\Omega_2 &= \dot{\gamma} \cos \varphi \cos \beta - \dot{\beta} \sin \varphi, \tag{2.27} \\
\Omega_3 &= -\dot{\gamma} \sin \beta + \dot{\varphi}, \tag{2.28}
\end{align}$$

and for the third term in the integral from Equation (2.23) which gives the rotational

energy of the infinitesimal cross-section

$$T_{\mathrm{rot}} = \frac{1}{2}\left(I_1\Omega_1^2 + I_2\Omega_2^2 + I_3\Omega_3^2\right) = \frac{I_a}{2}\left(\dot{\gamma}^2\cos^2\beta + \dot{\beta}^2\right)$$
$$+ \frac{I_p}{2}\left(\dot{\varphi}^2 - 2\sin\beta\dot{\gamma}\dot{\varphi} + \sin^2\beta\dot{\gamma}\right) \tag{2.29}$$
$$+ \frac{\Delta I}{2}\left((\dot{\beta}^2 - \dot{\gamma}^2\cos^2\beta)\cos 2\varphi + 2\dot{\beta}\dot{\gamma}\cos\beta\sin 2\varphi\right).$$

We now use the assumption that the total deformation and hence also the inclination of the beam is small. Using $\gamma \approx u'$, $\beta \approx -v'$ and $\phi = \omega t$ as derived in Appendix A, by dropping second order terms we get

$$2T_{\mathrm{rot}} \approx I_a(\dot{u}'^2 + \dot{v}'^2) + I_p\left(\omega^2 + 2\omega\dot{u}'v'\right)$$
$$+ \Delta I\left((\dot{v}'^2 - \dot{u}'^2)\cos 2\omega t - 2\dot{u}'\dot{v}'\sin 2\omega t\right). \tag{2.30}$$

The second term from the integral in (2.23) evaluates to

$$T_{\mathrm{unb}} = 2\mu\dot{r}_0 \cdot (\Omega \times r_g(z,t)) = 2\mu(-\dot{u}\Omega_3 r_{G,2} + \dot{v}\Omega_3 r_{G,1})$$
$$= 2\mu(-\dot{u}(\dot{\varphi} - \dot{\gamma}\sin\beta)r_{g,2} + \dot{v}(\dot{\varphi} - \dot{\gamma}\sin\beta)r_{g,1})$$
$$\approx 2\mu\omega(\dot{v}r_{g,1} - \dot{u}r_{g,2}). \tag{2.31}$$

Here again the terms $v'r_{g,2}$ and $u'r_{g,2}$ are of second order and are therefore dropped.

Combining (2.23) with (2.30) and (2.31) we finally obtain the expression for the kinetic energy we will use in the following.

$$T = \frac{1}{2}\int_0^L \mu(\dot{u}^2 + \dot{v}^2) + 2\mu\omega(\dot{v}r_{g,1} - \dot{u}r_{g,2})$$
$$+ I_a(\dot{u}'^2 + \dot{v}'^2) + I_p\left(\omega^2 + 2\omega\dot{u}'v'\right)$$
$$+ \Delta I\left((\dot{v}'^2 - \dot{u}'^2)\cos 2\omega t - 2\dot{u}'\dot{v}'\sin 2\omega t\right)\, dz. \tag{2.32}$$

Common Euler-Bernoulli beam theory does not include the rotatory inertia term $I_a(\dot{u}'^2 + \dot{v}'^2)$ and the gyroscopic term $I_p\left(\omega^2 + 2\omega\dot{u}'v'\right)$. The rotatory inertia term would also appear in the non-rotating case. The beam theory which includes this rotatory inertia term is called Rayleigh beam (Han *et al.*, 1999) and is considered in this work.

2.4 Euler-Lagrange Equations

The derivation of the equation of motion is based on Hamilton's principle (José & Saletan, 1998). The equations of motion are the Euler-Lagrange equations of the action functional

$$S = \int_{t_0}^{t_1} L(q, \dot{q}, \nabla q, \nabla^2 q, t, x). \tag{2.33}$$

The Lagrangian L depends on the functions q and their temporal and spatial derivatives. It is worth noting that higher order derivatives are allowed which leads to a more general formulation of the Euler-Lagrange equations. The Lagrangian is given by

$$L = T - U,$$

where T is the kinetic energy and U the potential energy of the system under consideration. In continuum mechanics the Lagrangian is calculated from a Lagrangian density

$$L = \int_{\Omega} \mathcal{L}(q, \dot{q}, \nabla q, \nabla^2 q, t, x) = \int_{\Omega} \mathcal{T} - \mathcal{U}$$

which is again calculated from the densities of the kinetic and the potential energy respectively.

The Euler-Lagrange equations in the continuum case do not lead to ordinary differential equations as it is the case for Lagrangians describing systems of point masses, but to partial differential equations. The generalized Euler-Lagrange equations for functionals involving higher order derivatives are

$$\frac{\partial \mathcal{L}}{\partial q_i} - \sum_{j=1}^{n+1} \frac{d}{dy_j} \frac{\partial \mathcal{L}}{\partial(\partial_{y_j} q_i)} + \sum_{j,k=1}^{n+1} \frac{d^2}{dy_j dy_k} \frac{\partial^2 \mathcal{L}}{\partial(\partial_{y_j} \partial_{y_k} q_i)} = 0, \tag{2.34}$$

where $y = (t, x)$. Depending on the problem one also obtains natural boundary conditions.

The dissipation of energy by viscous damping can be accounted for by adding the Rayleigh dissipation function F_R to the Lagrangian density $\mathcal{L}$

$$F_R(\dot{q}) = \frac{1}{2} c \|\dot{q}\|^2$$

with the distributed damping parameter c. The Euler-Lagrange equations are then modified as follows (see e.g. (José & Saletan, 1998; Yamamoto & Ishida, 2001))

$$\frac{\partial \mathcal{L}}{\partial q_i} - \sum_{j=1}^{n+1} \frac{d}{dy_j} \frac{\partial \mathcal{L}}{\partial(\partial_{y_j} q_i)} + \sum_{j,k=1}^{n+1} \frac{d^2}{dy_j dy_k} \frac{\partial^2 \mathcal{L}}{\partial(\partial_{y_j} \partial_{y_k} q_i)} - \frac{\partial F_R}{\partial_t q_i} = 0. \tag{2.35}$$

In the previous sections we have derived formulas for the kinetic and the potential energy (cf. Eqs. (2.32) and (2.19)) of a rotating shaft with 2 distinct area moments of inertia I_1 and I_2 differing by $2\Delta I$ and eccentricity r_G of the center of gravity. In the following we will assume that the two diametral moments of inertia are equal, i.e. that $\Delta I = 0$.

The Lagrangian is thus given by

$$L = \frac{1}{2} \int\limits_0^L \mu(\dot{u}^2 + \dot{v}^2) + 2\mu\omega(\dot{v}r_{g,1} - \dot{u}r_{g,2}) + I_a(\dot{u}'^2 + \dot{v}'^2) + I_p\left(\omega^2 + 2\omega\dot{u}'v'\right)$$

$$- EI_a(u''^2 + v''^2) - 2\mu gv + c(\dot{u}^2 + \dot{v}^2)\, dz. \tag{2.36}$$

The derivatives with respect to the generalized coordinates are:

$$\frac{\partial \mathcal{L}}{\partial u} = 0, \qquad\qquad\qquad\qquad \frac{\partial \mathcal{L}}{\partial v} = -\mu g, \tag{2.37}$$

$$\frac{d}{dt}\frac{\partial \mathcal{L}}{\partial \dot{u}} = \mu\ddot{u} - \mu\omega\dot{r}_{g,2}, \qquad\qquad \frac{d}{dt}\frac{\partial \mathcal{L}}{\partial \dot{v}} = \mu\ddot{v} + \mu\omega\dot{r}_{g,1}, \tag{2.38}$$

$$\frac{d}{dz}\frac{\partial \mathcal{L}}{\partial u'} = 0, \qquad\qquad\qquad \frac{d}{dz}\frac{\partial \mathcal{L}}{\partial v'} = \omega(I_p\dot{u}')', \tag{2.39}$$

$$\frac{d^2}{dzdt}\frac{\partial \mathcal{L}}{\partial \dot{u}'} = (I_a\ddot{u}')' + \omega(I_p\dot{v}')', \qquad \frac{d^2}{dzdt}\frac{\partial \mathcal{L}}{\partial \dot{v}'} = (I_a\ddot{v}')', \tag{2.40}$$

$$\frac{d^2}{dz^2}\frac{\partial \mathcal{L}}{\partial u''} = -(EI_a u'')'', \qquad\qquad \frac{d^2}{dz^2}\frac{\partial \mathcal{L}}{\partial v''} = -(EI_a v'')'', \tag{2.41}$$

$$\frac{\partial F_R}{\partial \dot{u}} = c\dot{u}, \qquad\qquad\qquad \frac{\partial F_R}{\partial \dot{v}} = c\dot{v}. \tag{2.42}$$

Using the generalized Euler-Lagrange equations 2.35 we obtain

$$(EI_a u'')'' + \mu\ddot{u} - (I_a\ddot{u}')' - \omega(I_p\dot{v}')' + c\dot{u} \;\; = \;\; \mu\omega\dot{r}_{g,2}, \tag{2.43}$$

$$(EI_a v'')'' + \mu\ddot{v} - (I_a\ddot{v}')' + \omega(I_p\dot{u}')' + c\dot{v} \;\; = \;\; -\mu\omega\dot{r}_{g,1} - \mu g, \tag{2.44}$$

and by using the expression (2.9) for the unbalance we can replace the time derivatives on the right hand side to obtain the equation of motion for the shaft:

$$(EI_a u'')'' + \mu\ddot{u} - (I_a\ddot{u}')' - \omega(I_p\dot{v}')' + c\dot{u} = \mu\omega^2(r_{G,1}\cos\omega t - r_{G,2}\sin\omega t), \tag{2.45}$$

$$(EI_a v'')'' + \mu\ddot{v} - (I_a\ddot{v}')' + \omega(I_p\dot{u}')' + c\dot{v} = \mu\omega^2(r_{G,1}\sin\omega t + r_{G,2}\cos\omega t) - \mu g. \tag{2.46}$$

Additionally, from the variation of the Lagrangian we obtain the natural boundary conditions on $\{0, L\} \times [0, T]$

$$I_a\ddot{u}' + \omega I_p\dot{v}' - (EI_a u'')' = 0, \tag{2.47}$$

$$I_a\ddot{v}' - \omega I_p\dot{u}' - (EI_a v'')' = 0, \tag{2.48}$$

$$EI_a u'' = 0, \tag{2.49}$$

$$EI_a v'' = 0. \tag{2.50}$$

This system of equations together with the initial conditions

$$u(z, 0) = u_0(z), \qquad \dot{u}(z, 0) = u_1(z), \tag{2.51}$$

$$v(z, 0) = v_0(z), \qquad \dot{v}(z, 0) = v_1(z), \tag{2.52}$$

describes the motion of a free shaft without bearings. The two equations (2.45) and (2.46) are coupled and one sees that the coupling vanishes for $\omega = 0$, i.e. when the

beam is not rotating the vibrations in x and y directions are mutually independent. The antisymmetric coupling reflects the gyroscopic moments in the rotating beam which are caused by changes of the angular momentum vector $I_p\omega$ due to the whirling of the rotor (Yamamoto & Ishida, 2001).

In Section 2.6 we will show how bearings can be included into the model generally and in Chapter 5 we will derive a detailed model for the forces exerted by oil lubricated journal bearings. The natural boundary conditions (2.47) and (2.48) show the absence of shearing forces at the ends of the beam, while the boundary conditions (2.49) and (2.50) stand for the absence of bending moments. We see that a harmonic forcing term appears on the right hand side of Equations (2.45) and (2.46) which depends linearly on the eccentricity of the center of mass and grows quadratically with the angular velocity. This forcing is called static unbalance excitation (Gasch & Pfützner, 1975; Yamamoto & Ishida, 2001). It is called static because the eccentricity of the center of mass can be detected also when the rotor is at rest, in contrast to dynamic unbalance which is caused by angular misalignment of flywheels as described in the following section. The quadratic dependence of the unbalance on the angular velocity makes balancing very important for fast rotating bodies, such as the rotors used in turbomachinery. The technique of balancing is described in (Yamamoto & Ishida, 2001) for continuous and rigid rotors with different kinds of unbalance.

2.5   Modifications for Rigid Disks

The rotor of a turbocharger consists not only of the shaft but also of the compressor wheel and of the turbine wheel. The vibration of the blades and the gasdynamic interaction of either of them shall be neglected in this work. Furthermore the vibrations of the wheel structure are negligible as the eigenfrequencies are much higher than the driving frequency and are not excited. It is therefore common in studies of rotor-dynamics to model the wheels as rigid disks which are attached to the elastic shaft (Yamamoto & Ishida, 2001; Vance, 1988; Childs, 1993).

As we have seen before, a cross-section of a Rayleigh beam remains planar and can be considered rigid. Its dynamics can be described by four variables: x- and y-displacement u and v and the two inclination angles $\gamma \approx u'$ and $\beta \approx -v'$. In contrast to the above, the rigid disks which model the fly wheels are not necessarily perpendicular to the shaft axis and so-called dynamic unbalance excitation can occur (Yamamoto & Ishida, 2001). In Figure 2.3 such a situation is depicted. The Euler angles β, γ, and φ describing the position of the body system relatively to the space system are defined as above. The disk is attached at the axial coordinate z_d and is initially inclined to the shaft center line by the angle τ with phase η. When the center line inclines by the
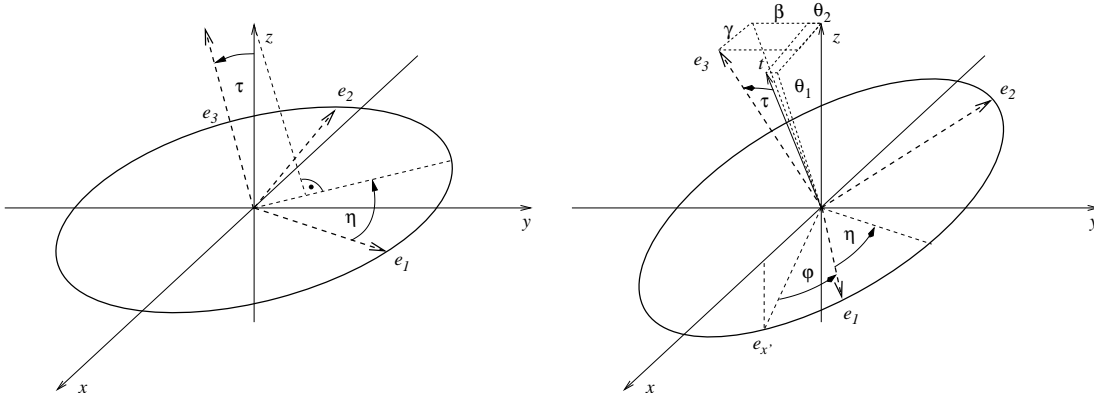
Figure 2.3: Dynamic unbalance: The disk is initially inclined to the shaft center line by the angle τ with phase η (left). During movement (right) the position of the tangential vector t relative to the body coordinate system e_1, e_2, e_3 remains constant.

angles θ_1 and θ_2 away from the z-axis the following relations hold to first order

$$u'(z_d) \approx \theta_1 \quad = \quad \gamma + \tau \cos(\phi + \eta), \tag{2.53}$$

$$v'(z_d) \approx -\theta_2 \quad = \quad -\beta + \tau \sin(\phi + \eta). \tag{2.54}$$

We plug these relations into the Equation (2.29) for the rotational energy of a rotating disk in terms of the Euler angles and we obtain after dropping second order terms in τ

$$
\begin{aligned}
2T_{\text{rot}} = &I_a \left(\dot{u}'^2 + \dot{v}'^2 + 2\omega\tau(\dot{u}' \sin(\omega t + \eta) - \dot{v}' \cos(\omega t + \eta)) \right) \\
&+ I_3 \left(\omega^2 + 2\omega\dot{u}'v' - 2\omega\tau(\dot{u}' \sin(\omega t + \eta) - \omega v' \sin(\omega t + \eta)) \right) \\
&+ \Delta I \left((\dot{v}'^2 - \dot{u}'^2) \cos 2\omega t - 2\dot{u}'\dot{v}' \sin 2\omega t \right) \\
&+ 2\tau\omega\Delta I \left(\dot{u}' \sin(\omega t - \eta) - \dot{v}' \cos(\omega t - \eta) \right).
\end{aligned}
\tag{2.55}
$$

Furthermore the disks also contribute to the kinetic energy stored in transversal motion. This contribution is not influenced by the misalignment τ, but only by the eccentricity of the center of mass r_g as in Equation 2.32 where we have to replace mass density μ by mass m_d

$$2T_{\text{t}} = m_d(\dot{u}(z_d)^2 + \dot{v}(z_d)^2) + 2m_d\omega(\dot{v}(z_d)r_{g,1}^d - \dot{u}(z_d)r_{g,2}^d). \tag{2.56}$$

Adding the two contributions (2.55) and (2.56) yields the total kinetic energy of the disk

$$T_d = T_{\text{t}} + T_{\text{rot}}. \tag{2.57}$$

Since the disk is considered not elastic, only its weight contributes to the potential energy

$$U_d = m_d g v(z_d). \tag{2.58}$$

Hence the Lagrangian of the disk results as

$$L_d = T_d - U_d \tag{2.59}$$

which has to be added to the Lagrangian of the shaft (2.36) to obtain the Lagrangian for the composite system. Note that the Lagrangian of the disk only depends on the displacement and the inclination of the centerline at the position z_d and is not given by an integral.

However it can be included into the analytic formulation of Section 2.4 by splitting up the integration interval at the points z_{d_i}. We obtain additional interface conditions between the different parts of the shaft. Furthermore we have to demand continuity of the functions u and v and their first spatial derivatives u' and v' in the points z_{d_i} Consider the combined Lagrangian

$$ L = \int\limits_0^L \mathcal{L} + \sum_{i=1}^{N_d} L_{d_i}, \tag{2.60} $$

where $\mathcal{L}$ is the Lagrangian density of the continuous shaft (2.36). L_{d_i} is the Lagrangian of the ith rigid disk fixed in z_{d_i}, which is only depending on deflection and inclination in that point. Variation of the action functional (2.33) yields the same partial differential equations (2.45) and (2.46) on each interval $I_i = [z_i, z_{i+1}]$ as for the case without disks. The additional interface conditions at z_{d_i} are

$$ \left[I_a \ddot{u}' + \omega I_p \dot{v}' - (EI_a u'')' \right]_{z_{d_i}} = m_{d_i} \ddot{u}(z_{d_i}) - m_{d_i} \omega \ddot{r}_{g,2}^{d_i}, \tag{2.61} $$

$$ \left[I_a \ddot{v}' - \omega I_p \dot{u}' - (EI_a v'')' \right]_{z_{d_i}} = m_{d_i} \ddot{v}(z_{d_i}) + m_{d_i} \omega \ddot{r}_{g,1}^{d_i} - m_{d_i} g, \tag{2.62} $$

$$ [EI_a u'']_{z_{d_i}} - I_a^{d_i} \ddot{u}'(z_{d_i}) - \omega I_p^{d_i} \dot{v}'(z_{d_i}) = (I_a^{d_i} - I_p^{d_i}) \omega^2 \tau_{d_i} \cos(\omega t + \eta_{d_i}), \tag{2.63} $$

$$ [EI_a v'']_{z_{d_i}} - I_a^{d_i} \ddot{v}'(z_{d_i}) + \omega I_p^{d_i} \dot{u}'(z_{d_i}) = (I_a^{d_i} - I_p^{d_i}) \omega^2 \tau_{d_i} \sin(\omega t + \eta_{d_i}). \tag{2.64} $$

The notation $[u]_z$ stands for the jump of u at z, i.e. $[u]_z = \lim\limits_{x \searrow z} u(x) - \lim\limits_{x \nearrow z} u(x)$.

We see that the inertial force of the disk and the static unbalance forcing term add to the shearing force between two adjacent sections, while the additional moments exerted by the disk due to gyroscopic effects and dynamic unbalance add to the bending moments. The additional forcing term in the moment balance (2.63) and (2.64) is the already mentioned dynamic unbalance excitation which depends on the angle of misalignment τ and also grows quadratically with the angular velocity. In contrast to the static unbalance, misalignment can only be detected when the rotor is rotating because the gyroscopic effects appear only during movement.

2.6 Bearings

As mentioned before we will derive a detailed model for oil lubricated journal bearings in Chapter 5. Here we describe for reasons of completeness how to include bearings into the continuous model of the rotating shaft in a more abstract way. The system

(2.45)-(2.48) as it is written in Section 2.4 is not statically determined, i.e. it remains unchanged under rigid body transformations since linear transformations are in the kernel of the corresponding differential operator. The introduction of bearings solves this problem and leads to the existence of a unique solution of our system as we shall see in Chapter 3.

We shall consider two bearings which support the rotating shaft. They are located at two disctinct axial positions $a, b \in [0, L]$ along the rotor. Each of the bearings reacts on the movement of the shaft by reaction forces f_b and reaction moments t_b which we consider to be localized to the position of the bearing, i.e. we neglect the axial dimension of the bearing. Hence, the support forces and moments in the two distinct points $\{a, b\} \subset [0, L]$ are concentrated point forces.

Here, as in Section 2.5, the bearing forces are added as transmission conditions for the forces at their respective postions. For this we define $I_1 = [0, z_{b_1}]$, $I_2 = [z_{b_1}, z_{b_2}]$, and $I_3 = [z_{b_2}, L]$. Hence on each I_i we have

$$(EI_a u'')'' + \mu\ddot{u} - (I_a \ddot{u}')' - \omega(I_p \dot{v}')' + c\dot{u} = \mu\omega^2(r_{G,1} \cos\omega t - r_{G,2} \sin\omega t), \tag{2.65}$$

$$(EI_a v'')'' + \mu\ddot{v} - (I_a \ddot{v}')' + \omega(I_p \dot{u}')' + c\dot{v} = \mu\omega^2(r_{G,1} \sin\omega t + r_{G,2} \cos\omega t) - \mu g. \tag{2.66}$$

In addition to the boundary conditions (2.47) - (2.50) at $z = 0$ and $z = L$, we get the force and moment transmission conditions at z_{b_1} and z_{b_2}:

$$\left[-I_a \ddot{u}' - \omega I_p \dot{v}' + (EI_a u'')' \right]_{z_{b_i}} = f_{b_i,1}, \tag{2.67}$$

$$\left[-I_a \ddot{v}' + \omega I_p \dot{u}' + (EI_a v'')' \right]_{z_{b_i}} = f_{b_i,2}, \tag{2.68}$$

$$\left[-EI_a u'' \right]_{z_{b_i}} = t_{b_i,1}, \tag{2.69}$$

$$\left[-EI_a v'' \right]_{z_{b_i}} = t_{b_i,2}. \tag{2.70}$$

As an example, the bearing response force function for linear spring and damper support with stiffness k and damping coefficient c is

$$\begin{pmatrix} f_{b,1}(u, v, \dot{u}, \dot{v}) \\ f_{b,2}(u, v, \dot{u}, \dot{v}) \end{pmatrix} = \begin{pmatrix} -ku - c\dot{u} \\ -kv - c\dot{v} \end{pmatrix}. \tag{2.71}$$

For other kinds of support the response function f_b may be chosen differently, however throughout this work they are considered as concentrated point forces. Furthermore, we will not consider bearings such as spiral springs which exert moments on the shaft, therfore $t_{b_i} = 0$ for the rest of this work. As we will see later (cf. Sec. 5), the nonlinear bearing forces of the oil lubricated bearing forces also respond only to the displacement and not to the inclination of the shaft.

2.7   Complex Formulation of Equation of Motion

The number of equations of motion can be reduced by introducing a complex-valued notation using $\mathbb{C} \sim \mathbb{R}^2$. For this we set

$$w = u + iv, \quad F_b = f_{b,1} + if_{b,2}, \quad f_{\text{unb}} = r_{G,1} + ir_{G,2}, \quad f_{\text{grav}} = -i\mu g, \qquad (2.72)$$

and obtain by adding Equations (2.65) and (2.65)

$$\mu\ddot{w} - (I_a\ddot{w}')' + i\omega(I_p\dot{w}')' + c\dot{w} + (EI_a w'')'' = f_{\text{grav}} + \mu\omega^2 f_{\text{unb}}e^{i\omega t}. \qquad (2.73)$$

Analogously we obtain

$$\left[-I_a\ddot{w}' + i\omega I_p\dot{w}' + (EI_a w'')'\right]_{z_{b_i}} = F_b, \qquad (2.74)$$

$$[EI_a w'']_{z_{b_i}} = 0, \qquad (2.75)$$

from the boundary conditions (2.47)-(2.50). This formulation reflects nicely the symmetries and antisymmetries of the original equation. Furthermore it reduces notably the notational effort and will therefore be used in Chapter 3 where we prove existence of solutions to Equation (2.73).

Chapter 3

Existence of Solutions

In this chapter we want to examine the existence of solutions of the equation of motion for a rotating beam. The equation has been derived in Section 2.6 of Chapter 2. The equation for the deflection $u(t, x) \in \mathbb{C}$ of the beam at point $x \in \Omega = [0, L]$ at time $t \in [0, T]$ is

$$\mu u_{tt} - (I_a u_{ttx})_x + i\omega(I_p u_{tx})_x + (EI_a u_{xx})_{xx} = g \quad \text{in } (0, T) \times \Omega, \tag{3.1}$$

$$EI_a u_{xx} = 0 \quad \text{on } (0, T) \times \partial\Omega, \tag{3.2}$$

$$\left(I_a u_{ttx} - i\omega I_p u_{tx} - (EI_a u_{xx})_x\right) = 0 \quad \text{on } (0, T) \times \partial\Omega, \tag{3.3}$$

$$u(0, x) = u_0(x) \quad \text{and} \quad u_t(0, x) = u_1(x) \quad \text{for } x \in \Omega, \tag{3.4}$$

where $g : [0, T] \times \Omega \to \mathbb{C}$ is a periodic driving force. Supporting the shaft at the two distinct interior points $\{a, b\} \subset \Omega$ leads transmission conditions for the moments and the forces at the location of the support:

$$[EI_a u_{xx}]_{x_j} = 0 \qquad\qquad\qquad \text{for } (t, x_j) \in (0, T) \times \{a, b\}, \tag{3.5}$$

$$\left[\left(I_a u_{ttx} - i\omega I_p u_{tx} - (EI_a u_{xx})_x\right)\right]_{x_j} = f(u(t, x_j), u_t(t, x_j)) \quad \text{for } (t, x_j) \in (0, T) \times \{a, b\}, \tag{3.6}$$

where $f : \mathbb{C}^2 \to \mathbb{C}$ gives the reaction forces of the bearings depending on deflection and velocity of the beam and $[.]_z$ denotes the jump of the term at that point. The coefficients μ, I_p, I_a, and E are considered to be in $L^\infty(\Omega)$ and do not depend on time. Additionally they are strictly positive, i.e. there are constants such that

$$0 < \underline{\mu} \le \mu(x) \le \overline{\mu} < \infty,$$

$$0 < \underline{I_p} \le I_p(x) \le \overline{I_p} < \infty,$$

$$0 < \underline{I_a} \le I_a(x) \le \overline{I_a} < \infty,$$

$$0 < \underline{E} \le E(x) \le \overline{E} < \infty,$$

for almost every $x \in \Omega$. Furthermore $\omega > 0$ is constant.

We will first prove the existence of solutions for the case of linear support functions corresponding to spring support using Galerkin's method (Evans, 1998; Zeidler, 1990). In a second step we will consider nonlinear support as it is the case for the fluid film bearings. Throughout the chapter, C will denote a generic positive real constant.

3.1   Existence for Linear Support

In the case of linear support the reaction forces in the support are as follows

$$f(u(x,t), u_t(x,t)) = -ku(x,t), \tag{3.7}$$

where $k > 0$ is a constant.

Multiplication of Equation (3.1) by $\bar{\varphi} \in H^2(\Omega)$ (the overbar denoting the complex conjugate) and partial integration leads to the following weak formulation:

$$\int_0^L \left[\mu u_{tt}\bar{\varphi} + I_a u_{ttx}\bar{\varphi}_x - i\omega I_p u_{tx}\bar{\varphi}_x + EI_a u_{xx}\bar{\varphi}_{xx} \right] dx + k(u(a)\bar{\varphi}(a) + u(b)\bar{\varphi}(b)) = \int g\bar{\varphi}dx \tag{3.8}$$

for all $\varphi \in H^2(\Omega)$. By the Sobolev embedding theorem $H^2(\Omega) \hookrightarrow C^1(\Omega)$ continuously for one-dimensional Ω and every element in H^2 is equal to a continuously differentiable function after changing it on a subset of measure 0. Therefore the evaluation of u at the points a and b is possible.

We can simplify the weak formulation (3.8) by introducing three sesquilinear forms. These are

$$a : H^2(\Omega) \times H^2(\Omega) \to \mathbb{C}, \tag{3.9}$$

$$a(u,v) = \int_0^L EI_a(x)u_{xx}\bar{v}_{xx}dx + k(u(a)\bar{v}(a) + u(b)\bar{v}(b)), \tag{3.10}$$

which takes into account all terms related to stiffness, and

$$m : H^1(\Omega) \times H^1(\Omega) \to \mathbb{C}, \tag{3.11}$$

$$m(u,v) = \int_0^L \mu(x)u\bar{v} + I_a(x)u_x\bar{v}_x dx, \tag{3.12}$$

which takes all the inertia terms, and

$$b : H^1(\Omega) \times H^1(\Omega) \to \mathbb{C}, \tag{3.13}$$

$$b(u,v) = -i\omega \int_0^L I_p(x)u_x\bar{v}_x dx, \tag{3.14}$$

which is the gyroscopic term. Equation (3.8) then reads as

$$m(u_{tt}, v) + b(u_t, v) + a(u, v) = (g, v)_{L^2(\Omega)}. \tag{3.15}$$

It follows directly from the boundedness and the strict positivity of the coefficients μ and I_a that the form $m(.,.)$ defines a scalar product on $H^1(\Omega)$ which is equivalent to the standard scalar product in the sense that the induced norms are equivalent.

Definition 3.1. Let $m(.,.)$ be the sesquilinear form defined in (3.11). We equip the space $H^1(\Omega)$ with the equivalent scalar product $(u, v)_m = m(u, v)$ for $u, v \in H^1(\Omega)$ to obtain the space

$$H^1_m(\Omega) := (H^1(\Omega), (.,.)_m = m(.,.)). \tag{3.16}$$

From the bounds on $\mu(x)$ and $I_a(x)$ we can immediately deduce:

Proposition 3.2. *The identity* id $: H^1(\Omega) \to H^1_m(\Omega)$ *is a continuous bijection with continuous inverse.*

In the following we do not consider the usual Gelfand triple with $L^2(\Omega)$ as pivot space but the triple

$$H^2(\Omega) \subset H^1_m(\Omega) = H^1_m(\Omega)' \subset H^2(\Omega)', \tag{3.17}$$

where we identify $H^1_m(\Omega)$ with its dual and embed it into $H^2(\Omega)'$ by

$$\langle u, v \rangle_{H^2(\Omega)' \times H^2(\Omega)} = (u, v)_m = m(u, v) \quad \text{for} \quad u \in H^1_m(\Omega), \; v \in H^2(\Omega). \tag{3.18}$$

The sesquilinear form $a(.,.)$ is examined in the following lemma.

Lemma 3.3. *Let* $u, v \in H^2(\Omega)$, $\Omega = [0, L] \subset \mathbb{R}^1$ *bounded,* $a, b \in \Omega$ *with* $0 \le a < b \le L$, $0 < \underline{\rho} < \rho(x) < \overline{\rho} < \infty$ *for almost every* $x \in \Omega$ *and* $k > 0$. *The sesquilinear form*

$$a(u, v) = \int_0^L \rho(x) u_{xx} \bar{v}_{xx} dx + k(u(a)\bar{v}(a) + u(b)\bar{v}(b)) \tag{3.19}$$

is continuous and coercive.

Proof. We have

$$|a(u, v)| \le \overline{\rho} \left(\int_0^L |u_{xx}|^2 dx \right)^{\frac{1}{2}} \left(\int_0^L |v_{xx}|^2 dx \right)^{\frac{1}{2}} + 2k\|u\|_\infty \|v\|_\infty \le C\|u\|_{H^2} \|v\|_{H^2} \tag{3.20}$$

by Hölder's inequality and the boundedness of ρ for the first term and from the continuos embedding of $H^2(\Omega)$ into $C^1(\Omega)$ for the second term. Thus $a(u, v)$ is continuous.

For $u \in H^2(\Omega)$ we obtain by applying the triangular and Hölder's inequality

$$
\begin{aligned}
|u(x)|^2 &= \left| u(a) + \int_a^x u_x(t)dt \right|^2 \leq 2|u(a)|^2 + 2\left| \int_a^x u_x(t)dt \right|^2 \\
&\leq 2|u(a)|^2 + 2\left(\int_a^x |u_x(t)|dt \right)^2 \leq 2|u(a)|^2 + 2|x-a|\left(\int_a^x |u_x(t)|^2dt \right) \\
&\leq 2|u(a)|^2 + 2L\|u_x\|^2_{L^2(\Omega)}
\end{aligned}
$$

and hence by integration over Ω

$$
\|u\|_{L^2(\Omega)} \leq 2L|u(a)|^2 + 2L^2\|u_x\|^2_{L^2(\Omega)}. \tag{3.21}
$$

From the generalized Poincaré equation (B.1) from the appendix we get the following estimate for the first derivative by setting $B = [a,b]$ and $\bar{u}_{xB} = \frac{1}{|B|}\int_\Omega u_x(s)ds$:

$$
\begin{aligned}
\|u_x\|^2_{L^2(\Omega)} &\leq 2\|u_x - \bar{u}_{x,B}\|^2_{L^2(\Omega)} + 2\|\bar{u}_{x,B}\|^2_{L^2(\Omega)} \tag{3.22} \\
&\leq 2\|u_x - \bar{u}_{x,B}\|^2_{L^2(\Omega)} + \frac{2}{|B|^2}\left(\int_B u_x(y)dy \right)^2 \tag{3.23} \\
&\leq 2\frac{C}{|B|}\|u_{xx}\|^2_{L^2(\Omega)} + \frac{4|\Omega|}{|B|^2}(|u(a)|^2 + |u(b)|^2). \tag{3.24}
\end{aligned}
$$

From these two estimates for $\|u\|_{L^2(\Omega)}$ and $\|u_x\|_{L^2(\Omega)}$ we obtain the coercitivity of the sesquilinear form:

$$
\begin{aligned}
\|u\|^2_{H^2(\Omega)} &= \|u\|^2_{L^2(\Omega)} + \|u_x\|^2_{L^2(\Omega)} + \|u_{xx}\|^2_{L^2(\Omega)} \tag{3.25} \\
&\leq \|u_{xx}\|^2_{L^2(\Omega)} + 2L|u(a)|^2 + (2L^2+1)\|u_x\|^2_{L^2(\Omega)} \tag{3.26} \\
&\leq C\|u_{xx}\|^2_{L^2(\Omega)} + C'(|u(a)|^2 + |u(b)|^2) \tag{3.27} \\
&\leq C(\underline{\rho}\|u_{xx}\|^2_{L^2(\Omega)} + k(|u(a)|^2 + |u(b)|^2)) \tag{3.28} \\
&\leq Ca(u,u). \tag{3.29}
\end{aligned}
$$

$\square$

The properties of the forms can be used to give some a priori estimates on the weak solution.

Lemma 3.4. *The solution of the linear Equation (3.8) fulfills the following a priori estimates:*

$$
\begin{aligned}
\|u\|_{L^\infty(0,T;H^2(\Omega))} &+ \|u_t\|_{L^\infty(0,T;H^1_m(\Omega))} + \|u_{tt}\|_{L^2(0,T;H^2(\Omega)')} \\
&\leq C\left(\|g\|_{L^2(0,T;L^2(\Omega))} + \|u_0\|_{H^2(\Omega)} + \|u_1\|_{H^1(\Omega)} \right). \tag{3.30}
\end{aligned}
$$

Proof. Using u_t as test function in Equation (3.8), we obtain

$$\int_\Omega (\mu u_{tt}\bar{u}_t + I_a u_{ttx}\bar{u}_{tx} - i\omega I_p u_{tx}\bar{u}_{tx} + EI_a u_{xx}\bar{u}_{txx})dx + k(u(a)\bar{u}_t(a) + u(b)\bar{u}_t(b)) = \int g\bar{u}_t dx. \quad (3.31)$$

With sesquilinear forms used in Eq. (3.15) this can be written in a simplified manner

$$m(u_{tt}, u_t) + b(u_t, u_t) + a(u, u_t) = (g, u_t)_{L^2(\Omega)}. \quad (3.32)$$

Adding the complex conjugate of the equation and observing that

$$\begin{aligned}
\frac{d}{dt}m(u_t, u_t) &= \frac{d}{dt}\int_\Omega (\mu u_t \bar{u}_t + I_a u_{tx}\bar{u}_{tx})\, dx \\
&= \int_\Omega (\mu\,(u_{tt}\bar{u}_t + u_t \bar{u}_{tt}) + I_a\,(u_{ttx}\bar{u}_{tx} + u_{tx}\bar{u}_{ttx}))\, dx \\
&= m(u_{tt}, u_t) + \overline{m(u_{tt}, u_t)},
\end{aligned}$$

and analogously

$$\frac{d}{dt}a(u, u) = a(u, u_t) + \overline{a(u, u_t)},$$

and that

$$b(u_t, u_t) + \overline{b(u_t, u_t)} = 0,$$

we get

$$\frac{d}{dt}\left(m(u_t, u_t) + a(u, u)\right) = (g, u_t)_{L^2(\Omega)} + \overline{(g, u_t)}_{L^2(\Omega)}. \quad (3.33)$$

Using the Hölder inequality and $\|u_t\|_{L^2(\Omega)} \le \|u_t\|_{H^1(\Omega)} < Cm(u_t, u_t)$ and $0 \le a(u, u)$ we get

$$\frac{d}{dt}\left(m(u_t, u_t) + a(u, u)\right) \le C(\|g\|_{L^2(\Omega)} + m(u_t, u_t) + a(u, u)). \quad (3.34)$$

We apply Gronwall's inequality (B.3) with $\eta(t) = m(u_t, u_t) + a(u, u)$, $\phi(t) = C$ and $\psi(t) = C\|g(t)\|_{L^2(\Omega)}$ and obtain the a priori estimate

$$m(u_t, u_t) + a(u, u) \le e^{Ct}\left[m(u_1, u_1) + a(u_0, u_0) + C\int_0^t \|g(t)\|_{L^2(\Omega)}\right]. \quad (3.35)$$

From the equivalence of $a(.,.)$ to the standard scalar product on $H^2(\Omega)$ (shown in lemma 3.3) we obtain the estimate for the norms for almost all $t \in [0, T]$

$$\|u\|_{H^2(\Omega)} + \|u_t\|_{H^1_m(\Omega)} \le C\left(\|g\|_{L^2(0,T;L^2(\Omega))} + \|u_0\|_{H^2(\Omega)} + \|u_1\|_{H^1_m(\Omega)}\right). \quad (3.36)$$

To get an estimate on $\|u_{tt}\|_{L^2(0,T;H^2(\Omega)')}$ we use the continuity of $m(.,.)$, $b(.,.)$ and $a(.,.)$. We observe that for $v \in H^2(\Omega)$

$$\begin{aligned}
|\langle u_{tt}, v\rangle| &= |(u_{tt}, v)_{H^1_m(\Omega)}| = |m(u_{tt}, v)| & (3.37) \\
&= |(g, v)_{L^2(\Omega)} - a(u, v) - b(u_t, v)| & (3.38) \\
&\le \left(\|g\|_{L^2(\Omega)} + C\|u\|_{H^2(\Omega)} + C'\|u_{tx}\|_{L^2(\Omega)}\right)\|v\|_{H^2(\Omega)}. & (3.39)
\end{aligned}$$

Here we used the equivalence of $m(.,.)$ to the standard scalar product in the first line, the Equation (3.15) in the second, and the continuity of $a(.,.)$ and $b(.,.)$ in the third line. From this we deduce that

$$\|u_{tt}\|_{H^2(\Omega)'} \leq C\left(\|g\|_{L^2(\Omega)} + \|u\|_{H^2(\Omega)} + \|u_t\|_{H^1_m(\Omega)}\right) \tag{3.40}$$

and after integration from 0 to T we obtain

$$\|u_{tt}\|^2_{L^2(0,T;H^2(\Omega)')} = \int_0^T \|u_{tt}\|^2_{H^2(\Omega)'} \tag{3.41}$$

$$\leq C\left(\|g\|^2_{L^2(0,T;L^2(\Omega))} + \|u_0\|^2_{H^2(\Omega)} + \|u_1\|^2_{H^1_m(\Omega)}\right) \tag{3.42}$$

using the above estimates (3.36) for $\|u\|_{H^2(\Omega)}$. This completes the proof. $\qquad\square$

Now we have all the ingredients to prove the existence of a weak solution of the linear problem.

Theorem 3.5. *Let a, m, b be the bilinear forms defined in (3.10),(3.11) and (3.14) and let $g \in L^2(0,T;L^2(\Omega))$.*

There exists a weak solution of initial/boundary-value problem (3.1)-(3.4) with linear support function f as in (3.7), i.e. we can find a function

$$u \in L^\infty(0,T;H^2(\Omega)), \quad \text{with} \quad u' \in L^\infty(0,T;H^1_m(\Omega)) \quad \text{and} \quad u'' \in L^2(0,T;H^2(\Omega)') \tag{3.43}$$

that fulfills

$$\langle u_{tt}, v \rangle + b(u_t, v) + a(u, v) = (g, v)_{L^2(\Omega)} \tag{3.44}$$

for all $v \in H^2(\Omega)$ and for almost all $t \in [0,T]$. Furthermore u satisfies the initial conditions:

$$u(0) = u_0 \in H^2(\Omega) \quad \text{and} \quad u_t(0) = u_1 \in H^1_m(\Omega). \tag{3.45}$$

Proof. We use Galerkin's method to construct a weak solution. For this we choose a basis of $\{w^k\}_k \subset H^2(\Omega)$ to construct approximate solutions.

Since $H^2(\Omega)$ is dense in $H^1_m(\Omega)$ and therefore also span($\{w^k\}_k$), we can find coefficients α_{kn} and β_{kn} such that

$$u_{n0} = \sum_{k=1}^n \alpha_{kn} w^j \to u_0 \quad \text{in} \quad H^2(\Omega), \tag{3.46}$$

$$u_{n1} = \sum_{k=1}^n \beta_{kn} w^j \to u_1 \quad \text{in} \quad H^1_m(\Omega). \tag{3.47}$$

We want to construct for each $n \in \mathbb{N}$ approximate solutions of the form

$$u^n(t) = \sum_{j=0}^n d_n^j(t) w^j \tag{3.48}$$

to the problems projected onto the subspace spanned by n of the testfunctions w^k

$$m(u_{tt}^n, w^k) + b(u_t^n, w^k) + a(u^n, w^k) = \left(g, w^k\right)_{L^2(\Omega)} \quad \text{for all} \quad k = 1, \dots, n, \tag{3.49}$$

where the coefficients fulfill the initial conditions

$$d_n^j(0) = \alpha_{nk} \quad \text{and} \quad d_n^{j\prime}(0) = \beta_{nk}. \tag{3.50}$$

If the solution has the form (3.48) we can put it into the equation and obtain a system of n linear differential equations for the coefficients $d_n^j : [0, T] \to \mathbb{R}$

$$\sum_{j=0}^n \left[d_n^{j\prime\prime}(t) m(w^j, w^k) + d_n^{j\prime}(t) b(w^j, w^k) + d_n^j a(w^j, w^k) \right] = \left(g, w^k\right)_{L^2(\Omega)} \tag{3.51}$$

for all $k = 1, \dots, n$. It can be written in matrix form

$$M d_n'' + B d_n' + A d_n = g_n, \tag{3.52}$$

where the matrices are given by $M_{k,j} = m(w^j, w^k)$, $B_{k,j} = b(w^j, w^k)$, $A_{k,j} = a(w^j, w^k)$, and $g_n = ((g, w^1), \dots, (g, w^n))^T$. This system can be solved uniquely because the matrix M is nonsingular if the $\{w^k\}_k$ are linearly independent. This follows from the fact that $m(., .)$ is a scalar product on $H_m^1(\Omega)$ (cf. Lemma B.3 in the appendix). We therefore have a unique solution vector $d_n \in C^2(0, T; \mathbb{R}^n)$ fulfilling the initial conditions (3.50).

The approximate solutions clearly also fulfill for all n the a priori estimate (3.30) we have proved in Lemma 3.4. Therefore the sequence of approximate solutions $\{u^n\}_n$ is bounded in $L^2(0, T; H^2(\Omega))$, $\{u_t^n\}$ is bounded in $L^2(0, T; H^1(\Omega))$ and $\{u_{tt}^n\}$ is bounded in $L^2(0, T; H^2(\Omega)')$. By the theorem of Banach-Alaoglu-Bourbaki (Brezis, 1999) we therefore find a weakly convergent subsequence $\{u^{n_k}\}_k$ and $u \in L^2(0, T; H^2(\Omega))$ with $u_t \in L^2(0, T; H^1(\Omega))$ and $u_{tt} \in L^2(0, T; H^2(\Omega)')$, such that

$$\begin{aligned}
u^{n_k} &\rightharpoonup u \quad \text{weakly in} \quad L^2(0, T; H^2(\Omega)), \\
u_t^{n_k} &\rightharpoonup u_t \quad \text{weakly in} \quad L^2(0, T; H^1(\Omega)), \\
u_{tt}^{n_k} &\rightharpoonup u_{tt} \quad \text{weakly in} \quad L^2(0, T; H^2(\Omega)').
\end{aligned} \tag{3.53}$$

Now we consider a test function $v = \sum_{k=1}^l \xi_k(t) w^k \in C^1(0, T; H^2(\Omega))$ with smooth $\xi_k(t)$. The weak convergence (3.53) implies for $n_k > l$

$$\left| \int_0^T \langle u_{tt}, v \rangle + b(u_t, v) + a(u, v) - (g, v)_{L^2(\Omega)} dt \right|$$

$$\leq \underbrace{\left| \int_0^T \left\langle u_{tt} - u_{tt}^{n_k}, v \right\rangle + b(u_t - u_t^{n_k}, v) + a(u - u^{n_k}, v) dt \right|}_{\to 0 \quad \text{by (3.53)}}$$

$$+ \underbrace{\int_0^T \left| m(u_{tt}^{n_k}, v) + b(u_t^{n_k}, v) + a(u^{n_k}, v) - (g, v)_{L^2(\Omega)} \right| dt}_{=0 \quad \text{by (3.49)}}. \tag{3.54}$$

As $\{w^j\}_j$ has been chosen dense in $H^2(\Omega)$, functions of the form of the test function v are dense in $L^2(0,T;H^2(\Omega))$ and hence Equation (3.54) remains valid for all $v \in L^2(0,T;H^2(\Omega))$. Furthermore it follows that for almost all $t \in [0,T]$ (3.44) is fulfilled for all $v \in H^2(\Omega)$.

It remains to show that the initial conditions are fulfilled. For this we note first that from $u \in L^\infty(0,T;H^2(\Omega))$, $u' \in L^\infty(0,T;H_m^1(\Omega))$ and $u'' \in L^2(0,T;H^2(\Omega)')$ we can conclude that $u \in C(0,T;H_m^1(\Omega))$ and $u_t \in C(0,T;H_m^1(\Omega)')$ (Evans, 1998). We choose a function $\psi \in C^2(0,T;\mathbb{R})$ with $\psi(T) = \psi'(T) = 0$ and set $v = \psi w^k \in C^2(0,T;H^2(\Omega))$. We can then deduce from Equation (3.54) by partial integration over t that

$$\int_0^T \langle u, v_{tt}\rangle + b(u_t, v) + a(u, v)\, dt - \psi(0)m(u_t(0), w^k) + \psi'(0)m(u(0), w^k) = \int_0^T (g, v)_{L^2(\Omega)}\, dt$$

and from (3.49) that

$$\int_0^T \langle u^{n_k}, v_{tt}\rangle + b(u_t^{n_k}, v) + a(u^{n_k}, v)\, dt$$

$$- \psi(0)m(u_t^{n_k}(0), w^k) + \psi'(0)m(u^{n_k}(0), w^k) = \int_0^T (g, v)_{L^2(\Omega)}\, dt.$$

From these two equations we can deduce by (3.53) that for all w^k from our basis:

$$\lim_{n_k \to \infty} \psi(0)m(u_t^{n_k}(0), w^k) - \psi'(0)m(u^{n_k}(0), w^k) = \psi(0)m(u_t(0), w^k) - \psi'(0)m(u(0), v_t(0)).$$

But above we have chosen the projected initial conditions (3.50) such that in $H_m^1(\Omega)$

$$u_t^{n_k}(0) = \sum_{j=1}^{n_k} \beta_{kn} w^j \to u_1$$

and therefore by continuity of $m(.,.)$ and the arbitrariness of $\psi(0)$

$$m(u_1, w^k) = \lim_{n_k \to \infty} m(u_t^{n_k}(0), w^k) = m(u_t(0), w^k) \quad \text{for all} \quad k. \tag{3.55}$$

Analogously we have chosen $u^{n_k} = \sum_{j=1}^{n_k} \beta_{kn} w^j \to u_0$ in $H^2(\Omega)$ and hence

$$m(u_0, w^k) = \lim_{n_k \to \infty} m(u^{n_k}(0), w^k) = m(u(0), w^k) \quad \text{for all} \quad k. \tag{3.56}$$

From the density of span($\{w^k\}_k$) in $H_m^1(\Omega)$ we get the equalities

$$u_0 = u(0) \quad \text{and} \quad u_1 = u_t(0) \quad \text{for almost all} \quad x \in \Omega. \tag{3.57}$$

This finishes our proof. $\square$

Remark 3.6. Uniqueness of the solution can be shown using the technique in (Evans, 1998), Chapter 7.2, Theorem 4. There, the test function

$$v(t) = \begin{cases} \int_t^s u(\tau)\,d\tau & 0 \le t \le s \\ 0 & s \le t \le T \end{cases} \qquad (3.58)$$

is used to show that the only weak solution of the homogeneous hyperbolic equation with zero initial conditions is indeed $u \equiv 0$.

Remark 3.7. The regularity of the solution can be improved by taking $g \in H^1(0, T; L^2(\Omega))$, $u_0 \in H^3(\Omega)$ and $u_1 \in H^2(\Omega)$. Differentiation of the equation of motion (3.1) and the boundary/transmission conditions with respect to time and testing with u_{tt} yields

$$u \in L^\infty(0, T; H^3(\Omega)),\ u' \in L^\infty(0, T; H^2(\Omega)),\ u'' \in L^\infty(0, T; H^1_m(\Omega)),\ u''' \in L^\infty(0, T; H^2(\Omega)').$$
$$(3.59)$$

The proof is analogous to (Evans, 1998), Chapter 7.2, Theorem 5. In particular this regularity yields $u \in C^0(0, T; H^2(\Omega))$ and $u' \in C^0(0, T; H^1_m(\Omega))$, which is needed in the next section.

3.2   Existence for Nonlinear Support

In this section we want to extend our existence result from the previous section to nonlinear support functions, more precisely to support functions that model hydrodynamic bearings. We prove short time existence of solutions to the nonlinear equations using local Lipschitz continuity and a fixed point argument.

The support functions are derived in Chapter 5. Their detailed form is not important here and we will write them in the following convenient way.

$$f : \mathbb{C}^2 \supset B_{c_r}(0) \times \mathbb{C} \to \mathbb{C}, \qquad (3.60)$$
$$(x + iy, v + iw) \mapsto e^{i\gamma}(f^n(r, \dot{r}, \dot{\gamma}) + if^t(r, \dot{r}, \dot{\gamma})),$$

where

$$r = \sqrt{x^2 + y^2},\ \gamma = arg(x + iy),\ \dot{r} = v\cos\gamma + w\sin\gamma,\ \dot{\gamma} = (w\cos\gamma - v\sin\gamma)/r. \quad (3.61)$$

The functions f^n and f^t give the normal and tangential forces acting on the rotating beam in the bearing. Their special form is given in Equations (5.159) and (5.160) in Section 5.5.1. For $r < c_r$ the functions f^n and f^t are locally Lipschitz-continuous as can be seen from the analytical expressions in Section 5.5.1. For $r \to c_r$ however $e^{-i\gamma}f^n \to -\infty$, so that we do not have a global Lipschitz-constant for f. The local Lipschitz condition is the essential ingredient in the proof of the following existence theorem for the equation of motion with nonlinear support funcitons.

Theorem 3.8. *Let f be a locally Lipschitz, nonlinear support function as in (3.60). Let $a, b \in \Omega = [0, L]$ and let the coefficients μ, I_a, I_p, $EI_a \in L^\infty(\Omega)$ be strictly positive. Furthermore let $g \in H^1(0, T; L^2(\Omega))$ and let $u_0 \in H^3(\Omega)$ with $|u_0(a)|$, $|u_0(b)| < c_r$, and $u_1 \in H^2(\Omega)$.*

There exists a short time weak solution to the initial/boundary value problem (3.1)-(3.4) with support function f, i.e. there is a $T > 0$ and

$$u \in C^0(0, T; H^2(\Omega)), \quad with \quad u' \in C^0(0, T; H^1_m(\Omega)), \tag{3.62}$$

such that for all $v \in H^2(\Omega)$ and for almost all $t \in [0, T]$

$$\int_0^L \left[\mu u_{tt}\bar{v} + I_a u_{ttx}\bar{v}_x - i\omega I_p u_{tx}\bar{v}_x + EI_a u_{xx}\bar{v}_{xx} \right] dx - \sum_{x_i \in \{a,b\}} f(u(x_i), u_t(x_i))\bar{v}(x_i) = \int g\bar{v}dx. \tag{3.63}$$

Furthermore u satisfies the initial conditions:

$$u(0) = u_0 \in H^3(\Omega) \quad and \quad u_t(0) = u_1 \in H^2(\Omega). \tag{3.64}$$

Proof. In the proof we will consider the nonlinear equation as a perturbation of the linear case. In order to apply Banach's theorem we will show that the solution operator of a regularized linear equation with fixed nonlinearity on the right hand side is indeed a contraction. The unique fixed point will then be a solution to the nonlinear problem.

Since f fulfills a local Lipschitz condition we find $\delta > 0$, such that for $x_i \in \{a, b\}$

$$|f(\xi, \zeta) - f(\xi', \zeta')| \leq L(|\xi - \xi'| + |\zeta - \zeta'|) \quad and \quad \xi, \xi' \in B_{c_r}(0) \tag{3.65}$$

for all $\xi, \xi' \in B_\delta(u_0(x_i))$ and $\zeta, \zeta' \in B_\delta(u_1(x_i))$.

Let $k > 0$ be a constant. We define the bilinear forms a, m, b as in (3.10), (3.11), and (3.14) using k as coefficient for the form a:

$$a(u, v) = \int_\Omega EI_a u_{xx}\bar{v}_{xx} \, dx + k \sum_{x_i \in \{a,b\}} u(x_i)\bar{v}(x_i). \tag{3.66}$$

We can then rewrite the equation of motion (3.63).

$$\langle u_{tt}, v\rangle + b(u_t, v) + a(u, v) = (g, v)_{L^2} - \sum_{x_i \in \{a,b\}} f(u(t, x_i), u_t(t, x_i))\bar{v}(x_i) + ku(t, x_i)\bar{v}(x_i) \tag{3.67}$$

such that it resembles the linear equation in Theorem 3.5. Fixing the function u on the right hand side and solving the resulting linear equation yields the operator on which we will apply the fixed point theorem.

Consider the Banach space

$$X = \{u \in C^0(0, T; H^2(\Omega)) \,|\, u' \in C^0(0, T; H^1_m(\Omega))\} \tag{3.68}$$

with the norm

$$\|u\|_X = \sup_{0 \le t \le T} \|u\|_{H^2(\Omega)} + \sup_{0 \le t \le T} \|u'\|_{H^1_m(\Omega)}. \tag{3.69}$$

We will use Banach's theorem on the following closed subset $M \subset X$

$$M = \{u \in X \mid |u(t, x_i) - u_0(x_i)| \le \delta, \ |u'(t, x_i) - u_1(x_i)| \le \delta \quad \text{for } 0 \le t \le T, \ x_i \in \{a, b\}\}. \tag{3.70}$$

The operator $A : M \to M$ is then defined as follows: For a given $u \in M$ we define a linear equation by

$$\langle w_{tt}, v \rangle + b(w_t, v) + a(w, v) = (g, v)_{L^2} - \sum_{x_i \in \{a,b\}} f(u(t, x_i), u_t(t, x_i))\bar{v}(x_i) + ku(x_i)\bar{v}(x_i) \tag{3.71}$$

which has a unique weak solution $w \in X$. From the proof of Theorem 3.5 and from Remark 3.7 we know that $w \in C^0(0, T; H^2(\Omega))$ and $w' \in C^0(0, T; H^1_m(\Omega))$ and that the initial conditions are fulfilled. By eventually reducing $T > 0$ we can therefore assure that $|w(x_i) - u_0(x_i)| \le \delta$ and $|w'(x_i) - u_1(x_i)| \le \delta$. Hence $w \in M$ and we set

$$Au = w. \tag{3.72}$$

Now we show that A is a contraction. Choose $u, \tilde{u} \in M$ and set $w = Au$, $\tilde{w} = A\tilde{u}$ and $\Delta w = w - \tilde{w}$. For notational convenience we set $u_i = u(t, x_i)$, $w_i = w(t, x_i)$, etc. Analogously to the proof of the a-priori estimate in Lemma 3.4 we test (3.71) with $\overline{w'}$ and $\overline{\tilde{w}'}$ and the complex conjugated equation with w' and $\tilde{w}'$. Substraction then yields

$$\frac{d}{dt}\Big(m(\Delta w', \Delta w') + a(\Delta w', \Delta w')\Big)$$

$$\le \sum_{x_i \in \{a,b\}} \Re\left(\Big(f(u_i, u'_i) - f(\tilde{u}_i, \tilde{u}'_i) + k(u_i - \tilde{u}_i)\Big)\Delta w'_i\right)$$

$$\le \sum_{x_i \in \{a,b\}} \frac{1}{2}\Big(|f(u_i, u'_i) - f(\tilde{u}_i, \tilde{u}'_i)|^2 + k^2|u_i - \tilde{u}_i|^2\Big) + |\Delta w'_i|^2$$

$$\le \sum_{x_i \in \{a,b\}} \frac{1}{2}\left(L^2\Big(|u_i - \tilde{u}_i| + |u'_i - \tilde{u}'_i|\Big)^2 + k^2|u_i - \tilde{u}_i|^2\right) + |\Delta w'_i|^2$$

$$\le \sum_{x_i \in \{a,b\}} (L^2 + k^2)|u_i - \tilde{u}_i|^2 + L^2|u'_i - \tilde{u}'_i|^2 + |\Delta w'_i|^2$$

$$\le C\Big(\|u - \tilde{u}\|^2_{H^2(\Omega)} + \|u' - \tilde{u}'\|^2_{H^1_m(\Omega)} + m(\Delta w', \Delta w') + a(\Delta w, \Delta w)\Big).$$

The last estimate is due to the Sobolev embeddings of $H^2(\Omega)$ and $H^1_m(\Omega)$ into $C^1(\Omega)$ and $C^0(\Omega)$, respectively. As in the proof of Lemma 3.4 we can now apply Gronwall's inequality to conclude

$$\sup_{0 \le t \le T}(\|\Delta w'\|^2_{H^1_m(\Omega)} + \|\Delta w\|^2_{H^2(\Omega)}) \le e^{CT}T \sup_{0 \le t \le T}(\|u - \tilde{u}\|^2_{H^2(\Omega)} + \|u' - \tilde{u}'\|^2_{H^1_m(\Omega)}). \tag{3.73}$$

This is equivalent to

$$\|Au - A\tilde{u}\|_X \le CT^{\frac{1}{2}}\|u - \tilde{u}\|_X, \tag{3.74}$$

and by choosing $T > 0$ sufficiently small we can make A a contraction. This yields the existence of a fixed point in M and hence a short time solution of the nonlinear equation. $\square$

For simpler nonlinear support functions like e.g. $f(u) = -e^{i\gamma}|u|^3$ one could also prove long time existence, because global a-priori estimates can be derived easily, since $\frac{d}{dt}|u|^4 = f(u)\bar{u}' + \bar{f}(u)u'$. The complicated nature of the support function for hydrodynamic bearings does not permit such a simple approach. However, since the forces are always restoring a proof for global existence should still be possible, but is not in the scope of this work.

Chapter 4

Finite Element Discretization

In Chapter 2 we have derived the equations of motion (2.45) and (2.46) of a homogenous, isotropic, rotating beam by the Lagrangian formalism. We are now going to use the variational formulation of the equations of motion (2.36) to derive approximative equations by the finite element method. The derivation is based on (Yamamoto & Ishida, 2001) which is itself based on (Nelson & McVaugh, 1976). Good introductions to the use of the finite element method in engineering can also be found in the books (Kikuchi, 1986) and (Meirovitch, 1986). For the mathematical background see e.g. (Rannacher, 2000; Rannacher, 2001; Braess, 2007; Strang & Fix, 1973).

4.1   Variational Formulation

We derive the finite element formulation for a rotating Rayleigh beam to which several rigid disks are attached and which rotates in bearings. For this, consider the equations of motion (2.45) and (2.46) for $u, v \in H^2(\Omega)$ together with boundary conditions at $z_{p_1} = 0$ and $z_{p_{N+1}} = L$ and transmission conditions at the points $z_{p_i} \in \mathring{\Omega} = (0, L)$, $i = 2, \ldots N$ to model the point forces f_p and moments m_p occuring at the positions of rigid disks and and bearings

$$(EI_a u'')'' + \mu \ddot{u} - (I_a \ddot{u}')' - \omega(I_p \dot{v}')' + c\dot{u} = f_{\mathrm{unb},1}, \tag{4.1}$$

$$(EI_a v'')'' + \mu \ddot{v} - (I_a \ddot{v}')' + \omega(I_p \dot{u}')' + c\dot{v} = f_{\mathrm{unb},2} - \mu g, \tag{4.2}$$

$$\left[I_a \ddot{u}' + \omega I_p \dot{v}' - (EI_a u'')' \right]_{z_{p_i}} = f_{p_i,1}, \tag{4.3}$$

$$\left[I_a \ddot{v}' - \omega I_p \dot{u}' - (EI_a v'')' \right]_{z_{p_i}} = f_{p_i,2}, \tag{4.4}$$

$$[EI_a u'']_{z_{p_i}} = t_{p_i,1}, \tag{4.5}$$

$$[EI_a v'']_{z_{p_i}} = t_{p_i,2}. \tag{4.6}$$

The notation $[g]_z$ denotes the jump of g at point z. To obtain a variational formulation we multiply 4.1 with the test function $\eta \in H^2(\Omega)$ and (4.2) with the test function $\xi \in H^2(\Omega)$. Partial integration over $\Omega = [0, L]$ then yields

$$\int_\Omega EI_a u'' \eta'' + \mu \ddot{u} \eta + I_a \ddot{u}' \eta' + \omega I_p \dot{v}' \eta' + c \dot{u} \eta \, dz$$

$$+ \sum_{i=1}^{N} \left((EI_a u'')' \eta - (EI_a u'') \eta' - I_a \ddot{u}' - \omega I_p \dot{v}' \right) \Big|_{z_{p_i}}^{z_{p_{i+1}}} = \int_\Omega f_{\text{unb},1} \eta \, dz, \qquad (4.7)$$

$$\int_\Omega EI_a v'' \xi'' + \mu \ddot{v} \xi + I_a \ddot{v}' \xi' - \omega I_p \dot{u}' \xi' + c \dot{v} \xi \, dz$$

$$+ \sum_{i=1}^{N} \left((EI_a v'')' \eta - (EI_a v'') \eta' - I_a \ddot{v}' + \omega I_p \dot{u}' \right) \Big|_{z_{p_i}}^{z_{p_{i+1}}} = \int_\Omega (f_{\text{unb},2} - \mu g) \xi \, dz. \qquad (4.8)$$

The boundary terms that appear here, also appear in (4.3) - (4.6) and can therefore be replaced with the corresponding forces and moments

$$\int_\Omega EI_a u'' \eta'' + \mu \ddot{u} \eta + I_a \ddot{u}' \eta' + \omega I_p \dot{v}' \eta' + c \dot{u} \eta \, dz$$

$$+ \sum_{i=1}^{N+1} \left(f_{p_i,1}(z_{p_i}) \eta(z_{p_i}) + t_{p_i,1} \eta'(z_{p_i}) \right) = \int_\Omega f_{\text{unb},1} \eta \, dz, \qquad (4.9)$$

$$\int_\Omega EI_a v'' \xi'' + \mu \ddot{v} \xi + I_a \ddot{v}' \xi' - \omega I_p \dot{u}' \xi' + c \dot{v} \xi \, dz$$

$$+ \sum_{i=1}^{N+1} \left(f_{p_i,2}(z_{p_i}) \eta(z_{p_i}) + t_{p_i,2} \eta'(z_{p_i}) \right) = \int_\Omega (f_{\text{unb},2} - \mu g) \xi \, dz. \qquad (4.10)$$

Adding the two equations we obtain the variational formulation of our equation

$$\int_\Omega \begin{bmatrix} \eta \\ \xi \end{bmatrix}^T \begin{bmatrix} \mu & \\ & \mu \end{bmatrix} \begin{bmatrix} \ddot{u} \\ \ddot{v} \end{bmatrix} + \begin{bmatrix} \eta' \\ \xi' \end{bmatrix}^T \begin{bmatrix} I_a & \\ & I_a \end{bmatrix} \begin{bmatrix} \ddot{u}' \\ \ddot{v}' \end{bmatrix} + \begin{bmatrix} \eta \\ \xi \end{bmatrix}^T \begin{bmatrix} c & \\ & c \end{bmatrix} \begin{bmatrix} \dot{u} \\ \dot{v} \end{bmatrix}$$

$$+ \begin{bmatrix} \eta'' \\ \xi'' \end{bmatrix}^T \begin{bmatrix} EI_a & \\ & EI_a \end{bmatrix} \begin{bmatrix} u'' \\ v'' \end{bmatrix} + \begin{bmatrix} \eta' \\ \xi' \end{bmatrix}^T \begin{bmatrix} & \omega I_p \\ -\omega I_p & \end{bmatrix} \begin{bmatrix} \dot{u}' \\ \dot{v}' \end{bmatrix} dz \qquad (4.11)$$

$$+ \sum_{i=1}^{N+1} \begin{bmatrix} \eta(z_{p_i}) \\ \xi(z_{p_i}) \end{bmatrix}^T \begin{bmatrix} f_{p_i,1} \\ f_{p_i,2} \end{bmatrix} + \begin{bmatrix} \eta'(z_{p_i}) \\ \xi'(z_{p_i}) \end{bmatrix}^T \begin{bmatrix} t_{p_i,1} \\ t_{p_i,2} \end{bmatrix} = \int_\Omega \begin{bmatrix} \eta \\ \xi \end{bmatrix}^T \begin{bmatrix} f_{\text{unb},1} \\ f_{\text{unb},2} - \mu g \end{bmatrix} dz.$$

4.2   System Matrices

We observe that the integral part of the functional on the left hand side of this equation is the sum of five functionals. We will now discuss the transformation of these functionals

in the finite element approximation. The five functionals are the translatory inertia functional

$$m_t(\ddot{u}, \ddot{v}, \eta, \xi) = \int_\Omega \begin{bmatrix} \eta \\ \xi \end{bmatrix}^T \begin{bmatrix} \mu & \\ & \mu \end{bmatrix} \begin{bmatrix} \ddot{u} \\ \ddot{v} \end{bmatrix} dz, \tag{4.12}$$

the rotatory inertia functional

$$m_r(\ddot{u}, \ddot{v}, \eta, \xi) = \int_\Omega \begin{bmatrix} \eta' \\ \xi' \end{bmatrix}^T \begin{bmatrix} I_a & \\ & I_a \end{bmatrix} \begin{bmatrix} \ddot{u}' \\ \ddot{v}' \end{bmatrix} dz, \tag{4.13}$$

the damping functional

$$c(\dot{u}, \dot{v}, \eta, \xi) = \int_\Omega \begin{bmatrix} \eta \\ \xi \end{bmatrix}^T \begin{bmatrix} c & \\ & c \end{bmatrix} \begin{bmatrix} \dot{u} \\ \dot{v} \end{bmatrix} dz, \tag{4.14}$$

the stiffness functional

$$k(u, v, \eta, \xi) = \int_\Omega \begin{bmatrix} \eta'' \\ \xi'' \end{bmatrix}^T \begin{bmatrix} EI_a & \\ & EI_a \end{bmatrix} \begin{bmatrix} u'' \\ v'' \end{bmatrix} dz, \tag{4.15}$$

and finally, the gyroscopic functional which introduces the coupling

$$g(\dot{u}, \dot{v}, \eta, \xi) = \int_\Omega \begin{bmatrix} \eta' \\ \xi' \end{bmatrix}^T \begin{bmatrix} & \omega I_p \\ -\omega I_p & \end{bmatrix} \begin{bmatrix} \dot{u}' \\ \dot{v}' \end{bmatrix} dz. \tag{4.16}$$

To derive approximative equations we chose a finite dimensional subspace $V_n \subset H^2(\Omega)$ and a basis $\{\tilde{w}_i\}_{i=1,\dots,n}$ of V_n. The vectors

$$\{w_i\}_{i=1,\dots,2n} = \left\{ \begin{bmatrix} \tilde{w}_i \\ 0 \end{bmatrix}, \begin{bmatrix} 0 \\ \tilde{w}_i \end{bmatrix} \right\} \tag{4.17}$$

then form a basis for $V_n \times V_n$. We are seeking solutions with separated variables of the form

$$\begin{bmatrix} u(z, t) \\ v(z, t) \end{bmatrix} = \sum_{i=1}^{2n} q_i(t) w_i(z) \tag{4.18}$$

which we will write in matrix notation as

$$\begin{bmatrix} u \\ v \end{bmatrix} = Wq, \tag{4.19}$$

where $q = (q_1, \dots, q_{2n})$ is the vector of the time dependent coefficients and $W = (w_1, \dots, w_{2n})$ is the matrix which has the basis vectors as columns. By putting (4.19) into (4.11) and using the w_i as test functions we obtain a system of $2n$ ordinary differential

equations for q. This is the explicit formulation of the Galerkin approximation in equation (3.52) in chapter 3.

$$\int_\Omega W^T \begin{bmatrix} \mu & \\ & \mu \end{bmatrix} W\ddot{q} + W'^T \begin{bmatrix} I_a & \\ & I_a \end{bmatrix} W'\ddot{q} + W^T \begin{bmatrix} c & \\ & c \end{bmatrix} W\dot{q}$$

$$+ W''^T \begin{bmatrix} EI_a & \\ & EI_a \end{bmatrix} W''q + W'^T \begin{bmatrix} & \omega I_p \\ -\omega I_p & \end{bmatrix} W'\dot{q}\, dz \tag{4.20}$$

$$+ \sum_{i=1}^N W(z_{p_i})^T \begin{bmatrix} f_{p_i,1} \\ f_{p_i,2} \end{bmatrix} + W'(z_{p_i})^T \begin{bmatrix} t_{p_i,1} \\ t_{p_i,2} \end{bmatrix} = \int_\Omega W^T \begin{bmatrix} f_{\text{unb},1} \\ (f_{\text{unb},2} - \mu g) \end{bmatrix} dz.$$

The integrals can be evaluated and yield the system matrices. Each of the functionals (4.12)-(4.16) defines a matrix which acts on the vector of coefficients q or its time derivatives. We have

$$m_t(W\ddot{q}, W) = \int_\Omega W^T \begin{bmatrix} \mu & \\ & \mu \end{bmatrix} W\ddot{q}\, dz = M^t \ddot{q}, \tag{4.21}$$

where

$$M^t_{i,j} = \int_\Omega \mu w_i^T w_j\, dz, \qquad\qquad\qquad i,j = 1,\dots,2n. \tag{4.22}$$

Analogously we obtain the matrices

$$M^r_{i,j} = \int_\Omega I_a w_i'^T w_j'\, dz, \qquad\qquad\qquad i,j = 1,\dots,2n, \tag{4.23}$$

$$C_{i,j} = \int_\Omega c w_i^T w_j\, dz, \qquad\qquad\qquad i,j = 1,\dots,2n, \tag{4.24}$$

$$K_{i,j} = \int_\Omega EI_a w_i''^T w_j''\, dz, \qquad\qquad\qquad i,j = 1,\dots,2n, \tag{4.25}$$

$$\tag{4.26}$$

which are all symmetric. The matrix defined by the gyroscopic functional is slightly more complicated, due to the coupling. By W_u we denote the first row of W, and by W_v we denote its second row. We have

$$g(W\dot{q}, W) = \int_\Omega \begin{bmatrix} W_u' \\ W_v' \end{bmatrix}^T \begin{bmatrix} & \omega I_p \\ -\omega I_p & \end{bmatrix} \begin{bmatrix} W_u' \\ W_v' \end{bmatrix} dz\dot{q} \tag{4.27}$$

$$= \int_\Omega \omega I_p \begin{bmatrix} -W_v' \\ W_u' \end{bmatrix}^T \begin{bmatrix} W_u' \\ W_v' \end{bmatrix} dz\dot{q} \tag{4.28}$$

$$= \int_\Omega \omega I_p (W_u'^T W_v' - W_v'^T W_u')\, dz\dot{q} = G\dot{q}, \tag{4.29}$$

where

$$G_{i,j} = \int\limits_{\Omega} \omega I_p(w_{i,u}'^T \tilde{w}_{j,v}' - w_{i,v}'^T w_{j,u}') \, dz, \quad i,j = 1,\ldots,2n. \tag{4.30}$$

In the approximate Equation (4.20) the sum

$$\sum_{i=1}^{N+1} W(z_{p_i})^T \begin{bmatrix} f_{p_i,1} \\ f_{p_i,2} \end{bmatrix} + W'(z_{p_i})^T \begin{bmatrix} t_{p_i,1} \\ t_{p_i,2} \end{bmatrix} \tag{4.31}$$

containing the transmission terms transforms into a vector that gives the projected forces and moments which might also depend on displacments and inclinations in the z_{p_i}. It can be further simplified if we chose the basis elements in an appropriate way (cf. Sec. 4.3). Also the integral of the unbalance forcing

$$f_{\mathrm{unb}} = \int\limits_{\Omega} W^T \begin{bmatrix} f_{\mathrm{unb},1} \\ f_{\mathrm{unb},2} \end{bmatrix} dz \tag{4.32}$$

yields a vector valued forcing term which in principle can be calculated explicitly if we know the value of the eccentricity along the shaft. This, unfortunately, is rarely the case and the unblance has to be estimated in practice. Analogously, only if the mass density μ is known we can calculate the gravity load explicity

$$f_{\mathrm{grav}} = \int\limits_{\Omega} W^T \begin{bmatrix} 0 \\ -\mu g \end{bmatrix} dz. \tag{4.33}$$

4.3   Explicite Choice of Approximating Space

Until now, we have left open the choice of the approximating subspace V_n and of the basis elements w_i. We will now give a derivation of the explicit system matrices based on (Yamamoto & Ishida, 2001) and (Nelson, 1980). For this the beam is decomposed into N sections of constant diameter, cross-section and material properties like density and Young's modulus. We will first derive the approximate equations for such a uniform beam element and then accumulate them into a system for the whole beam.

Now, let us consider the kth beam element bounded by z_k and z_{k+1} of lenght $l_k = z_{k+1} - z_k$. We want to describe the movement of the beam element by the nodal displacements (u_k, v_k) and (u_{k+1}, v_{k+1}) and the nodal inclination angles (β_k, γ_k) and $(\beta_{k+1}, \gamma_{k+1})$ in z_k and z_{k+1}, respectively, as shown in Figure 4.1. In the Appendix A it is shown that $\beta \approx -v'$ and $\gamma \approx u'$ (see also Section 2.3). The displacement in x-direction $u(z)$ is approximated by a cubic polynomial which is uniquely determined by the four values $(u_k, \gamma_k, u_{k+1}, \gamma_{k+1})$, and so is the displacement in y-direction $v(z)$ by $(v_k, \beta_k, v_{k+1}, \beta_{k+1})$. We can solve this interpolation problem with the use of the Hermite polynomials Ψ_i^k
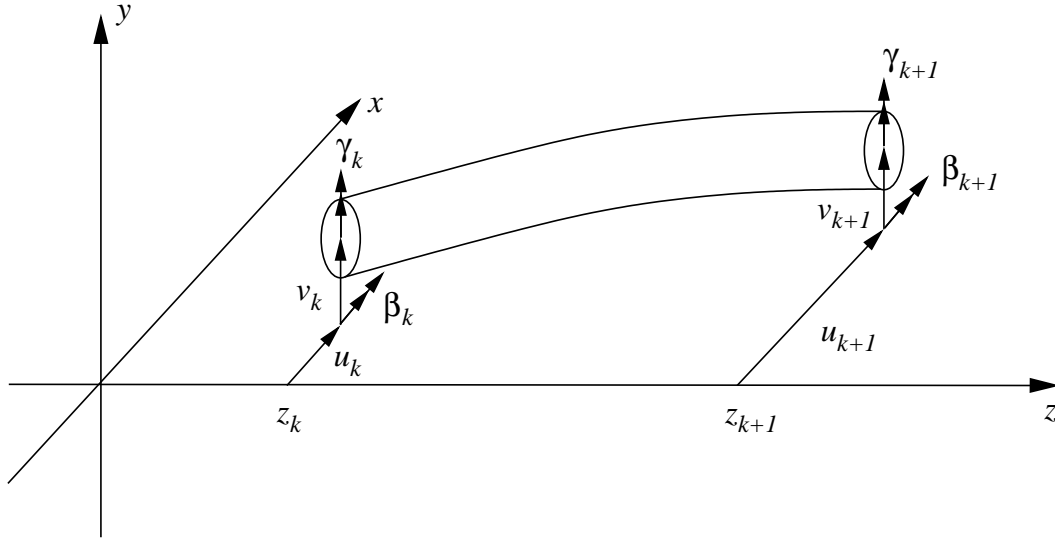
Figure 4.1: A single beam element is described by the nodal displacements (u_k, v_k) and u_{k+1}, v_{k+1} and the nodal inclination angles (β_k, γ_k) and $(\beta_{k+1}, \gamma_{k+1})$.

(Stoer & Bulirsch, 2002; Meirovitch, 1986)

$$\Psi_1(z) = 1 - 3\left(\frac{z - z_k}{l_k}\right)^2 + 2\left(\frac{z - z_k}{l_k}\right)^3, \tag{4.34}$$

$$\Psi_2(z) = (z - z_k)\left(1 - 2\left(\frac{z - z_k}{l_k}\right) + \left(\frac{z - z_k}{l_k}\right)^2\right), \tag{4.35}$$

$$\Psi_3(z) = 3\left(\frac{z - z_k}{l_k}\right)^2 - 2\left(\frac{z - z_k}{l_k}\right)^3, \tag{4.36}$$

$$\Psi_4(z) = l_k\left(-\left(\frac{z - z_k}{l_k}\right) + \left(\frac{z - z_k}{l_k}\right)^3\right), \tag{4.37}$$

and obtain the following representation for the displacements in $[z_k, z_{k+1}]$

$$u(z) = \Psi_1(z)u_k + \Psi_2(z)\gamma_k + \Psi_3(z)u_{k+1} + \Psi_4(z)\gamma_{k+1}, \tag{4.38}$$

$$v(z) = \Psi_1(z)v_k - \Psi_2(z)\beta_k + \Psi_3(z)v_{k+1} - \Psi_4(z)\beta_{k+1}. \tag{4.39}$$

Note that the Hermite polynomials are also the solutions of the static problem with unit displacement of one of the variables, e.g. Ψ_1 solves $EI_a u'''' = 0$ with boundary condition $u_k = 1$ and $\gamma_k = \gamma_{k+1} = u_{k+1} = 0$. In the engineering literature these interpolating functions are called shape functions.

We set

$$\tilde{q}_k = (u_k, v_k, \beta_k, \gamma_k, u_{k+1}, v_{k+1}, \beta_{k+1}, \gamma_{k+1})^T \tag{4.40}$$

and rewrite (4.38) and (4.39) in matrix form

$$\begin{bmatrix} u \\ v \end{bmatrix} = \begin{bmatrix} \Psi_1 & 0 & 0 & \Psi_2 & \Psi_3 & 0 & 0 & \Psi_4 \\ 0 & \Psi_1 & -\Psi_2 & 0 & 0 & \Psi_3 & -\Psi_4 & 0 \end{bmatrix} \tilde{q}_k = W_k \tilde{q}_k. \tag{4.41}$$

If we put this into equation (4.20), we obtain the system translatory mass matrix by calculating all the integrals in (4.21):

$$
M_k^t = \frac{\mu l_k}{420}
\begin{bmatrix}
156 & & & & & & & \\
0 & 156 & & & & \text{Sym.} & & \\
0 & -22l_k & 4l_k^2 & & & & & \\
22l_k & 0 & 0 & 4l_k^2 & & & & \\
54 & 0 & 0 & 13l_k & 156 & & & \\
0 & 54 & -13l_k & 0 & 0 & 156 & & \\
0 & 13l_k & -3l_k^2 & 0 & 0 & 22l_k & 4l_k^2 & \\
-13l_k & 0 & 0 & -3l_k^2 & -22l_k & 0 & 0 & 4l_k^2
\end{bmatrix}.
\tag{4.42}
$$

The other matrices are obtained by evaluating equations (4.23) - (4.30) and are given in the Appendix C. We obtain the equation of motion for one beam element

$$
M\ddot{\tilde{q}}_k + (G + C)\dot{\tilde{q}}_k + K\tilde{q}_k = F,
\tag{4.43}
$$

where the vector $F = f_{\text{unb}} + f_{\text{grav}}$ is the sum of unbalance forcing and gravity load. For a uniform element we can calculate the gravity load vector

$$
f_{\text{grav}} = -\frac{\mu g}{12} \left[0, 6l_k, -l_k^2, 0, 0, 6l_k, l_k^2, 0 \right]^T.
\tag{4.44}
$$

4.4   Rigid Disk Element Matrices

We now focus our attention on the discrete terms in the variational formulation (4.20) which give the virtual work of the forces and moments exerted by rigid disks. To facilitate notation we first consider only the Lagrangian of the rotating rigid disk at node k which we have derived in (2.59). Here again, we assume that the two cross-sectional moments of inertia are equal, i.e. $\Delta I = 0$

$$
\begin{aligned}
L =& \frac{I_a}{2} \left(\dot{\gamma}^2 + \dot{\beta}^2 + 2\omega\tau(\dot{\gamma}\sin(\omega t + \eta) + \dot{\beta}\cos(\omega t + eta)) \right) \\
&+ \frac{I_3}{2} \left(\omega^2 - 2\omega\dot{\gamma}\beta - 2\omega\tau(\dot{\gamma}\sin(\omega t + \eta) + \omega\beta\sin(\omega t + \eta)) \right) \\
&+ \frac{m_d}{2}(\dot{u}_k^2 + \dot{v}_k^2) + m_d\omega(\dot{v}_k r_{g,1}^d - \dot{u}_k r_{g,2}^d) - m_d g v_k.
\end{aligned}
\tag{4.45}
$$

Variation of the action functional with Rayleigh dissipation function $F_R = c(\dot{u}^2 + \dot{v}^2)$ leads to 4 ordinary differential equations for the nodal coordinates $q_k = (u_k, v_k, \beta_k, \gamma_k)$

$$
m_d\ddot{u}_k + c\dot{u}_k = m_d\omega^2(r_{G,1}\cos\omega t - r_{G,2}\sin\omega t),
\tag{4.46}
$$

$$
m_d\ddot{v}_k + c\dot{v}_k = m_d\omega^2(r_{G,1}\sin\omega t + r_{G,2}\cos\omega t) - m_d g,
\tag{4.47}
$$

$$
I_a\ddot{\beta}_k + \omega I_3\dot{\gamma}_k = \omega^2\tau(I_a - I_3)\sin(\omega t + \eta),
\tag{4.48}
$$

$$
I_a\ddot{\gamma}_k - \omega I_3\dot{\beta}_k = \omega^2\tau(I_a - I_3)\cos(\omega t + \eta).
\tag{4.49}
$$

We can rewrite this in matrix notation

$$M^d \ddot{q}_k + (C^d + G^d)\dot{q}_k = f^d_{unb} + f^d_{grav},$$ (4.50)

where the mass matrix M^d is given by

$$M^d = \begin{bmatrix} m & 0 & 0 & 0 \\ 0 & m & 0 & 0 \\ 0 & 0 & I_a & 0 \\ 0 & 0 & 0 & I_a \end{bmatrix},$$ (4.51)

the gyroscopic matrix G^d by

$$G^d = \omega \begin{bmatrix} 0 & 0 & 0 & 0 \\ 0 & 0 & 0 & 0 \\ 0 & 0 & 0 & I_3 \\ 0 & 0 & -I_3 & 0 \end{bmatrix},$$ (4.52)

and the damping matrix by

$$C^d = \begin{bmatrix} c & 0 & 0 & 0 \\ 0 & c & 0 & 0 \\ 0 & 0 & 0 & 0 \\ 0 & 0 & 0 & 0 \end{bmatrix}.$$ (4.53)

The vectors of unbalance forces f^d_{unb} and gravity f^d_{grav} are

$$f^d_{unb} = \begin{bmatrix} m_d \omega^2 (r_{G,1} \cos \omega t - r_{G,2} \sin \omega t) \\ m_d \omega^2 (r_{G,1} \sin \omega t + r_{G,2} \cos \omega t) \\ \omega^2 \tau (I_a - I_3) \sin(\omega t + \eta) \\ \omega^2 \tau (I_a - I_3) \cos(\omega t + \eta) \end{bmatrix} \quad \text{and} \quad f^d_{grav} = \begin{bmatrix} 0 \\ -m_d g \\ 0 \\ 0 \end{bmatrix}.$$ (4.54)

4.5   Assembling the Complete System

So far we have considered either one beam section with two nodes or a node to which a rigid disk is attached. We will now show how the elements can be combined to derive the approximative equation for the complete beam with N elements. Corresponding to the choice we have made in Section 4.3, we take V_n to be the space of continuously differentiable functions which are piecewise cubic polynomials

$$V_n = \{u \in C^1([0, L]) | u|_{[z_k, z_{k+1}]} \in P_3([z_k, z_{k+1}]),$$ (4.55)

which is dense in $H^2(\Omega)$ and has the dimension $2(N + 1)$. We set

$$q = (q_1, \ldots, q_{N+1}) = (u_1, v_1, \beta_1, \gamma_1, \ldots, u_{N+1}, v_{N+1}, \beta_{N+1}, \gamma_{N+1}),$$ (4.56)

where q_k is the vector of nodal coordinates for the kth node. We choose the position of the nodes such that the set of nodes includes the set of points where interface

conditions are given in equations (4.3)-(4.6). The individual element displacement vectors $\tilde{q}_k = (q_k, q_{k+1})$ can be obtained from this via $\tilde{q}_k = A_k q$ where

$$
A_k = \begin{bmatrix}
0 & 0 & \cdots & 0 & 1 & 0 & \cdots & 0 & 0 & \cdots & 0 \\
0 & 0 & \cdots & 0 & 0 & 1 & \cdots & 0 & 0 & \cdots & 0 \\
\vdots & & & & & & \ddots & & & & \vdots \\
0 & 0 & \cdots & 0 & 0 & 0 & \cdots & 1 & 0 & \cdots & 0
\end{bmatrix} \in \mathbb{R}^{8 \times 4(N+1)}. \tag{4.57}
$$

Here, $N + 1$ is the total number of nodes and the block with the identity matrix starts in the $4(k-1) + 1$th column. We define the continuously differentiable matrix function W on $[0, L]$ by

$$
W(z) = W_k(z)A_k \quad \text{for} \quad z \in I_k, \tag{4.58}
$$

where each W_k is defined as in equation (4.41) on the respective interval $[z_k, z_{k+1}]$. From the definition of the W_k it is clear that W is in $V_n \times V_n$. Hence the overall displacement is given by

$$
\begin{bmatrix} u \\ v \end{bmatrix} = Wq. \tag{4.59}
$$

In terms of Section 4.1, the columns of W are the basis elements $w_i \in V_n \times V_n$, $i = 1, \ldots, 4(N+1)$. They are chosen in such a way that in node k they have have either unit displacement ($w_{4(k-1)+1}$ and $w_{4(k-1)+2}$) or unit inclination ($w_{4(k-1)+3}$ and $w_{4(k-1)+4}$).

By putting the definition (4.58) of W into the variational formulation and the formulas for the system matrices (4.21) - (4.30), we obtain expressions for the complete system matrices

$$
\sum_{k=1}^{n-1} A_k^T \left(\int_{I_k} W_k^T \begin{bmatrix} \mu & \\ & \mu \end{bmatrix} W_k \ddot{q} + W_k'^T \begin{bmatrix} I_a & \\ & I_a \end{bmatrix} W_k' \ddot{q} + W_k^T \begin{bmatrix} c & \\ & c \end{bmatrix} W_k \dot{q} \right.
$$

$$
\left. + W_k''^T \begin{bmatrix} EI_a & \\ & EI_a \end{bmatrix} W_k'' q + W_k'^T \begin{bmatrix} & \omega I_p \\ -\omega I_p & \end{bmatrix} W_k' \dot{q} \, dz \right) A_k + F_p \tag{4.60}
$$

$$
= \sum_{k=1}^{n-1} A_k^T \int_{I_k} W_k^T \begin{bmatrix} f_{unb,1} \\ f_{unb,2} - \mu g \end{bmatrix} dz.
$$

The vector F_p gives the nodal forces and moments exerted by rigid disks or bearings. From the definition of the W_k we see that $W_k(z_{p_i}) \neq 0$ only for $z_{p_i} = z_k$ or $z_{p_i} = z_{k+i}$

$$
W_k(z_k) = \begin{bmatrix} 1 & 0 & 0 & 0 & 0 & 0 & 0 & 0 \\ 0 & 1 & 0 & 0 & 0 & 0 & 0 & 0 \end{bmatrix}, \tag{4.61}
$$

$$
W_k(z_{k+1}) = \begin{bmatrix} 0 & 0 & 0 & 0 & 1 & 0 & 0 & 0 \\ 0 & 0 & 0 & 0 & 0 & 1 & 0 & 0 \end{bmatrix}, \tag{4.62}
$$

$$
W_k'(z_k) = \begin{bmatrix} 0 & 0 & 0 & 1 & 0 & 0 & 0 & 0 \\ 0 & 0 & -1 & 0 & 0 & 0 & 0 & 0 \end{bmatrix}, \tag{4.63}
$$

$$
W_k'(z_{k+1}) = \begin{bmatrix} 0 & 0 & 0 & 0 & 0 & 0 & 0 & 1 \\ 0 & 0 & 0 & 0 & 0 & 0 & -1 & 0 \end{bmatrix}, \tag{4.64}
$$

and hence F_p can be written as

$$F_p = [f_{p_1,1}, f_{p_1,2}, t_{p_1,1}, t_{p_1,2}, \ldots, f_{p_n,1}, f_{p_n,2}, t_{p_n,1}, t_{p_n,2}]^T. \tag{4.65}$$

The bearing forces will be under consideration in Chapter 5. The disk forces have been considered in Section 4.4 and can be written as

$$\begin{bmatrix} f_{d_k,1} \\ f_{d_k,2} \\ t_{d_k,1} \\ t_{d_k,2} \end{bmatrix} = M_k^d \ddot{q}_k + (G_k^d + C_k^d)\dot{q}_k - f_{\text{unb},k}^d - f_{\text{grav},k}^d. \tag{4.66}$$

The complete mass matrix can hence be written as

$$M = \sum_{k=1}^{n-1} A_k^T M_k^s A_k + \sum_{k=1}^{n} B_k^T M_k^d B_k, \tag{4.67}$$

where M_k^s is the mass matrix of the kth element, analogously for the gyroscopic, damping and stiffness matrices and M_k^d is the mass matrix of the disk attached at the kth node. The matrix

$$B_k = \begin{bmatrix} 0 & \ldots & 0 & 1 & 0 & 0 & 0 & 0 & \ldots & 0 \\ 0 & \ldots & 0 & 0 & 1 & 0 & 0 & 0 & \ldots & 0 \\ 0 & \ldots & 0 & 0 & 0 & 1 & 0 & 0 & \ldots & 0 \\ 0 & \ldots & 0 & 0 & 0 & 0 & 1 & 0 & \ldots & 0 \end{bmatrix} \in \mathbb{R}^{4 \times 4N} \tag{4.68}$$

places the nodal matrices at the right position in the system matrix like the A_k do for the element matrices. Hence from (4.60) we get the equation of motion for the entire system

$$M\ddot{q} + (G + C)\dot{q} + Kq = F_{\text{unb}} + F_{\text{gr}} + F_{\text{bear}}, \tag{4.69}$$

where the matrices are defined as above and the force vectors are combined from the nodal and the element forces

$$
\begin{aligned}
F_{\text{unb}} &= F_{\text{unb}}^d + F_{\text{unb}}^s \tag{4.70} \\
&= [f_{\text{unb}}^{d_1}, \ldots, f_{\text{unb}}^{d_n}]^T + \sum_{k=1}^{n-1} A_k^T \int_{I_k} W_k^T \begin{bmatrix} f_{\text{unb},1} \\ f_{\text{unb},2} \end{bmatrix} dz, \tag{4.71} \\
F_{\text{gr}} &= F_{\text{grav}}^d + F_{\text{grav}}^s \tag{4.72} \\
&= [f_{\text{grav}}^{d_1}, \ldots, f_{\text{grav}}^{d_n}]^T + \sum_{k=1}^{n-1} A_k^T \int_{I_k} W_k^T \begin{bmatrix} 0 \\ -\mu(z)g \end{bmatrix} dz \tag{4.73} \\
&= \left[f_{\text{grav}}^{d_1}, \ldots, f_{\text{grav}}^{d_n} \right]^T - \sum_{k=1}^{n-1} A_k^T \frac{\mu g}{12} \left[0, 6l_k, -l_k^2, 0, 0, 6l_k, l_k^2, 0 \right]^T. \tag{4.74}
\end{aligned}
$$

The last equation only holds for uniform mass distribution in each element. The vector of bearing forces has the form

$$F_{\text{bear}} = \left[0, \ldots, 0, f_{b_1,1}, f_{b_1,2}, t_{b_1,1}, t_{b_1,2}, 0, \ldots, 0, f_{b_2,1}, f_{b_2,2}, t_{b_2,1}, t_{b_2,2}, 0, \ldots, 0 \right]^T. \tag{4.75}$$

The entries in the vector are at the postions of the bearing nodes. The special form of the bearing response functions depends on the mechanical properties of the bearing as described in Section 2.6 and in Chapter 5.

4.5.1 An Example
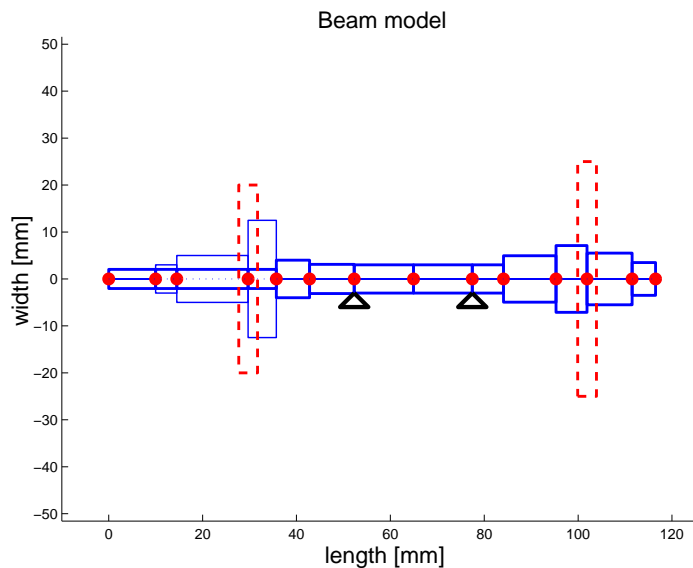
Figure 4.2: Detailed beam model of turbocharger: the rotor shaft is modelled with 13 finite elastic beam elements shown in blue, the turbine and impeller wheels are modelled as rigid disks and are shown with dashed red lines, and the positions of the bearings are indicated by the black triangles.

In Figure 4.2 a typical beam modell for a turbocharger is depicted. It consists of 13 elements and hence has 14 nodes. There are 2 rigid disks attached in node 4 and 12 respectivley (indicated by dashed lines), and the bearings (indicated by triangles) are located at node 7 and node 9. This model will be used later on for numerical simulations. A detailed description and all the paramters are given in the Appendix D.

4.6 Approximations for Unbalance Forcing

The unbalance force F_{unb} in equation (4.69) includes terms coming from the rigid disks and integral terms coming from an inhomogenous mass distribution along the shaft. In practice it is very difficult to estimate the inhomogenity which is usually also very small compared to the unbalance that is caused by the rigid disks. In the following the integral terms will therefore be neglected and only the static and dynamic unbalance caused by the misalignment of the rigid disks will be considered.

Furthermore the moments cause by the dynamic unbalance are replaced by pairs of forces located in neighbouring nodes. This formulation is equivalent (Yamamoto & Ishida, 2001) and facilitates notation. The unbalance force vector in node k is then characterized by its amplitude a_k and its phase ψ_k in the $x - y$-plane perpendicular to the shaft

$$
\begin{aligned}
f_{\text{unb},1} &= \omega^2 a_k \cos(\omega t + \psi_k), & (4.76)\\
f_{\text{unb},2} &= \omega^2 a_k \sin(\omega t + \psi_k). & (4.77)
\end{aligned}
$$

The amplitude a_k is calculated from the static unbalance and the force pairs replacing the dynamic unbalance. For static unbalance only we have

$$
a_k = m_d \|r_G\|, \tag{4.78}
$$

and for purely dynamic unbalance at node k we have

$$
a_{k-1} = a_{k+1} = \frac{\tau(I_p - I_3)}{z_{k+1} - z_{k-1}}. \tag{4.79}
$$

For the example from Section 4.5.1 the following constellation is considered where the dynamic unbalance dominates the static unbalance

$$
\begin{aligned}
a_3 &= 1.35 \times 10^{-7}\,kgm, & \psi_3 &= \pi, & (4.80)\\
a_5 &= 1.50 \times 10^{-7}\,kgm, & \psi_5 &= 0, & (4.81)\\
a_{11} &= 2.01 \times 10^{-7}\,kgm, & \psi_{11} &= 0, & (4.82)\\
a_{13} &= 2.07 \times 10^{-7}\,kgm, & \psi_{13} &= \pi. & (4.83)
\end{aligned}
$$

Chapter 5

Bearing Models

In the construction of turbomachinery, the bearings play an important role. Not only do they contain the moving parts in their designated position, but they also provide the necessary damping to prevent resonance catastrophes. In this chapter we derive models for oil lubricated journal bearings and the reaction forces they exert on the rotor.

In this work we consider plain journal bearings as they were used in the experiments conducted at the Toyota Central R&D Laboratories, whereas in commercial high-speed turbochargers usually floating ring bearings are used (San Andrés, 2006). The plain journal bearings (c.f. Figs. 5.2 and 5.3) have the advantage that they are relatively easy to model and that a closed form analytical solution of the pressure distribution is possible in some special cases. For more complicated bearing geometries this is no longer possible. The analytical formulation of the pressure distribution and hence also the bearing reaction forces allows for a faster numerical integration of the equation of motion of the rotor.

The derivation of bearing characteristics is an important branch of rotordynamics in particular since the discovery of lubricant induced instabilities, i.e. oil whirl (Newkirk & Taylor, 1925). The basic theory can be found in most textbooks on turbomachinery, e.g. in (Childs, 1993; Vance, 1988; Yamamoto & Ishida, 2001). It is based on Reynolds' equation for thin films of lubricant as we show in Section 5.1. The special case of long bearings was already studied by Sommerfeld (Sommerfeld, 1964). The special case of short bearings was introduced by Ocvirk (Childs, 1993). These two special cases allow for an analytical formulation of the bearing reaction forces and are therefore of great theoretical value. There is an extensive literature covering the calculation of bearing coefficients, i.e. the coefficients of the linearization of the bearing functions (Lund, 1987; Szeri, 1998). These coefficients can be used for the prediction of the onset of the lubricant induced instabilities (Muszynska, 1986; Muszynska, 1988; Crandall, 1995).

The evaluation of the model which was set up during the collaboration with TCRDL
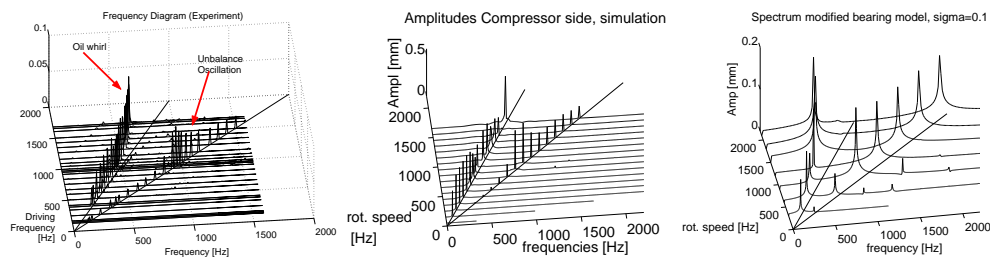
Figure 5.1: Comparison of experimental results (left) to simulations with Ocvirk short bearing approximation (center) and modified short bearing (right); a perturbation term as described in Sec. 5.2) yields a frequency shift of the oil whirl similar to the experimental results.

showed that already the common simple journal bearing model explains the main experimentally observed vibration phenomena quite well. The oil whirl, as well as the resonance of the bending mode occur at nearly the same frequencies as in the experiment as shown in the left and center diagram of Figure 5.1. The same holds for the computed amplitudes and mode shapes. The detailed results of the simulations are presented in Chapter 6, where also the comparison with the experimental data can be found.

However, in the course of the evaluation of the model it showed that the simple journal bearing model does not reproduce entirely correct the frequency of the subharmonic self-excited oscillation, i.e. the oil whirl. The simulation results and the experimental results differed, as can also be seen in Chapter 6. In the simulations the frequency of the subharmonic oscillation was close to half the driving frequency until the driving frequency reached twice the natural frequency of the beam. Then the frequency of the self-excited oscillation locks to the natural frequency of the beam and reaches very high amplitudes. The large amplitude oscillation is called oil whip. This transition behavior is common and also observed in (Muszynska, 1986; Muszynska, 1988; San Andrés, 2006).

In the experiments the ratio of whirl frequency to driving frequency shifts from $\frac{1}{2}$ to lower values in the driving frequency range above the first critical frequency of the beam. In order to describe this shift properly several other bearing models where considered and compared in simulations. Starting point is a modification of the pressure distribution function (cf. Section 5.2) which shows that the frequency of the self-excited oscillation can be directly influenced. Introduction of a perturbation which is quadratic in the angular velocity ω leads to a shift of the whirl ratio that is very similar to the one that is observed in the experiment (cf. Fig. 5.1).

In order to derive this perturbation from first principles the influence of second order corrections to Reynolds' equation is studied. As shown in 5.1.5 these inertia corrections lead to a quadratic dependence of the pressure distribution on the angular velocity. The

influence of inertia corrections on linearized bearing coefficients for journal bearings has been studied in (Nataraj *et al.*, 1994; Szeri, 1998; El-Shafei, 1995). A derivation of the second order correction terms for squeeze film dampers is shown in (Crandall & El-Shafei, 1993). The mathematical convergence theory for Reynolds theory is presented in (Nazarov, 1990; Bayada & Chambat, 1986; Duvnjak & Marušić-Paloka, 2000) for plain journal bearings with Newtonian lubricant and for thin films of non Newtonian liquids in (Bourgeat *et al.*, 1993; Duvnjak & Marušić-Paloka, 2000). The inertial effects are studied in (Assemien *et al.*, 1994)

The chapter is structured as follows. First we give the derivation of Reynolds' equation from the Navier-Stokes equation by an asymptotic expansion. The short bearing approximation is derived by giving a relation of the film thickness to the bearing length. This assumption of a relation between the two parameters is then also used to derive the second order correction terms. In Section 5.2 we give a motivation for the phenomenological perturbation term mentioned above. For completeness we list in Section 5.3 some other bearing models which were also considered during the project, such as finite length approximation, or Reynolds' equation with Reynolds' boundary conditions.

5.1 Derivation of Reynolds' Equation and Inertia Correction

We derive an equation for the pressure distribution inside a circular journal bearing. This is a hydrodynamic bearing where a circular shaft rotates inside a circular bearing casing and is supported by a thin layer of lubricant, usually oil in the case of the turbocharger. It is schematically shown in the Figures 5.2 and 5.3. The bearing casing is at rest. The rotation of the shaft creates a circular flow pattern by dragging along the fluid. This flow pattern causes the impedance of the bearing to loads on the shaft by causing higher pressures in narrowing regions of the bearing. This creates reaction forces that oppose the movement. The reaction forces can be calculated from the pressure distribution inside the bearing by integration over the bearing surface.

The radius R of the bearing and the radius R_j of the rotating shaft differ by a small distance c_r, the radial bearing clearance (cf. Figs. 5.2 and 5.3). The axial length of the bearing is called bearing width W. For small inclinations of the shaft the film thickness $h(\varphi)$ varies only with the circumferential angle φ and depends on the momentary position of the shaft's center Z which is considered to move with the velocity V_Z. The position of Z is given in polar coordinates by the eccentricity e and precession angle γ. The angular velocity of the shaft is denoted by ω. Note that in the figures the bearing clearance is exaggerated for illustration purposes. In the examined real turbocharger the clearance is 0.02 mm, while the radius of the shaft is 3 mm.

The derivation is based on an asymptotic expansion of the Navier-Stokes equations
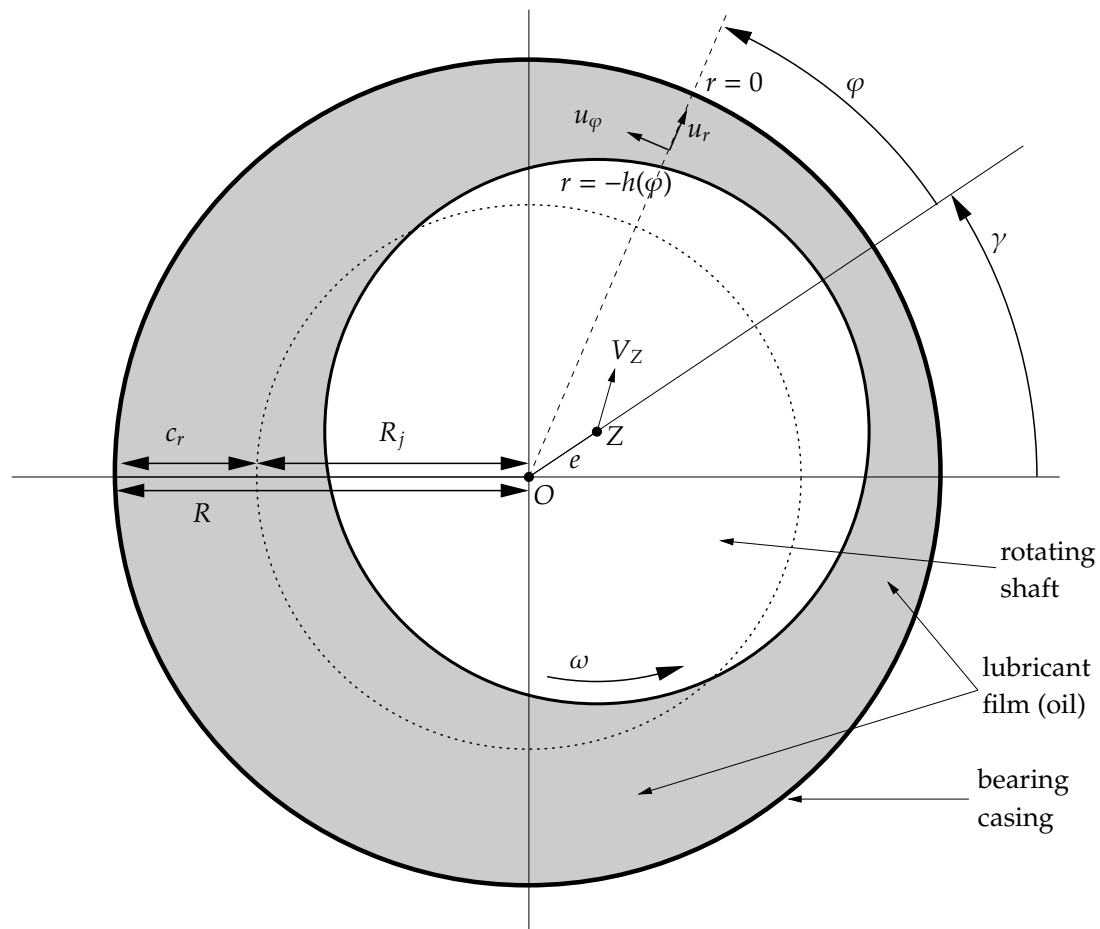
Figure 5.2: Sketch of simple journal bearing; view in axial direction; the radial bearing clearance c_r is exaggerated for illustration

with respect to the small parameter $\varepsilon = \frac{c_r}{R}$. This asymptotic expansion leads to approximations for the flow and the pressure in a thin film. The equation governing the pressure is called Reynolds' equation. We consider four cases in this work which differ by higher order terms and by the ratio of the bearing width W to the bearing radius R:

1. The classical Reynolds' equation: The ratio $\varepsilon = \frac{c_r}{R}$ is small, while the ratio $\delta = \frac{W}{R}$ is of order 1; no higher order terms are considered.

2. The short bearing approximation: the ratio $\delta = \frac{W}{R}$ is also small in addition to ε. To derive the approximate equations in one step we set $\varepsilon = K\delta^2$. Then the equations simplify even more and an analytical solution for the bearing forces can be obtained.

3. Reynolds' equation with inertia corrections: In the derivation of Reynolds' equation only terms of zeroth order in ε are considered. The inertia correction takes into account also terms of order ε^1.

Figure 5.3: Sketch of simple journal bearing; view in lateral direction

4. Short bearing with inertia corrections: As above the additional assumption of small δ and $\varepsilon = K\delta^2$ allows for further simplification and analytical solution for the pressure distribution also for the higher order terms.

We derive in detail the equations for the pressure distributions in these four cases in the following sections.

5.1.1 Scaling of the Navier Stokes Equations

The Navier-Stokes equations for an incompressible fluid (Ockendon & Ockendon, 1995) are given by

$$\partial_t \bar{u} + (\bar{u} \cdot \nabla)\bar{u} = -\nabla\bar{p} + \nu\Delta\bar{u}, \tag{5.1}$$

$$\operatorname{div} \bar{u} = 0. \tag{5.2}$$

The bearings have cylindrical geometry. Therefore we write (5.1) and (5.2) in cylindrical coordinates and non-dimensionalize them using the following variables. The dimensional variables carry an overbar, the non-dimensionalized ones carry a tilde:

$$\tau = \omega t, \ \tilde{r} = \frac{\bar{r}}{R}, \ \tilde{z} = \frac{\bar{z}}{R}, \ \tilde{\varphi} = \bar{\varphi}, \tag{5.3}$$

$$\tilde{u} = \frac{\bar{u}}{R\omega}, \ \tilde{p} = \frac{\bar{p}}{\rho R^2 \omega^2}, \ \tilde{\mathcal{R}} = \frac{R^2 \omega}{\nu}. \tag{5.4}$$

The non-dimensionalized NSE for an incompressible fluid in cylindrical coordinates then read as follows:

r-component:

$$\partial_\tau \tilde{u}_r \quad + \quad (\tilde{u}_r \partial_{\tilde{r}} \tilde{u}_r + \frac{\tilde{u}_\varphi}{\tilde{r}} \partial_{\tilde{\varphi}} \tilde{u}_r + \tilde{u}_z \partial_{\tilde{z}} \tilde{u}_r - \frac{\tilde{u}_\varphi^2}{\tilde{r}})$$

$$= \quad -\partial_{\tilde{r}} \tilde{p} + \frac{1}{\tilde{\mathcal{R}}} (\partial_{\tilde{r}}^2 \tilde{u}_r + \frac{\partial_{\tilde{r}} \tilde{u}_r}{\tilde{r}} + \partial_{\tilde{z}}^2 \tilde{u}_r + \frac{\partial_{\tilde{\varphi}}^2 \tilde{u}_r}{\tilde{r}^2} - \frac{\tilde{u}_r}{\tilde{r}^2} - \frac{2\partial_{\tilde{\varphi}} \tilde{u}_r}{\tilde{r}^2}), \qquad (5.5)$$

φ-component:

$$\partial_\tau \tilde{u}_\varphi \quad + \quad (\frac{\tilde{u}_r}{\tilde{r}} \tilde{u}_\varphi + \tilde{u}_r \partial_{\tilde{r}} \tilde{u}_\varphi + \frac{\tilde{u}_\varphi}{\tilde{r}} \partial_{\tilde{\varphi}} \tilde{u}_\varphi + \tilde{u}_z \partial_{\tilde{z}} \tilde{u}_\varphi)$$

$$= \quad -\frac{\partial_{\tilde{\varphi}} \tilde{p}}{\tilde{r}} + \frac{1}{\tilde{\mathcal{R}}} (\partial_{\tilde{r}}^2 \tilde{u}_\varphi + \frac{\partial_{\tilde{r}} \tilde{u}_\varphi}{\tilde{r}} + \partial_{\tilde{z}}^2 \tilde{u}_\varphi + \frac{\partial_{\tilde{\varphi}}^2 \tilde{u}_\varphi}{\tilde{r}^2} - \frac{\tilde{u}_\varphi}{\tilde{r}^2} + \frac{2\partial_{\tilde{\varphi}} \tilde{u}_r}{\tilde{r}^2}), \qquad (5.6)$$

z-component:

$$\partial_\tau \tilde{u}_z \quad + \quad (\tilde{u}_r \partial_{\tilde{r}} \tilde{u}_z + \frac{\tilde{u}_\varphi}{\tilde{r}} \partial_{\tilde{\varphi}} \tilde{u}_z + \tilde{u}_z \partial_{\tilde{z}} \tilde{u}_z)$$

$$= \quad -\partial_{\tilde{z}} \tilde{p} + \frac{1}{\tilde{\mathcal{R}}} (\partial_{\tilde{r}}^2 \tilde{u}_z + \frac{\partial_{\tilde{r}} \tilde{u}_z}{\tilde{r}} + \frac{\partial_{\tilde{\varphi}}^2 \tilde{u}_z}{\tilde{r}^2} + \partial_{\tilde{z}}^2 \tilde{u}_z), \qquad (5.7)$$

Continuity equation:

$$\partial_{\tilde{r}} \tilde{u}_r + \frac{\tilde{u}_r}{\tilde{r}} + \frac{\partial_{\tilde{\varphi}} \tilde{u}_\varphi}{\tilde{r}} + \partial_{\tilde{z}} \tilde{u}_z = 0. \qquad (5.8)$$

Two of the three dimensions of the problem are considered small compared to the radius of the bearing: the radial clearance c_r of the bearing and the axial length W of the film. We therefore introduce the following scalings of the nondimensionalized variables in Eqs. (5.5)-(5.8):

$$\varepsilon = \frac{c_r}{R}, \ \delta = \frac{W}{R}, \ r = \frac{\tilde{r} - 1}{\varepsilon}, \ z = \frac{\tilde{z}}{\delta}, \ \varphi = \tilde{\varphi},$$

$$u_r = \frac{\tilde{u}_r}{\varepsilon}, \ u_z = \frac{\tilde{u}_z}{\delta}, \ u_\varphi = \tilde{u}_\varphi, \ \mathcal{R} = \varepsilon \tilde{\mathcal{R}}, \ p = \mathcal{R} \frac{\varepsilon}{\delta^2} \tilde{p}.$$

The scaling for the axial coordinate *z* is chosen different from the scaling for the radial coordinate in order to obtain a limit for different ratios of these two dimensions. The scaling for the radial component includes a transformation such that $r = 0$ at the bearing casing and $r = -h(\varphi)$ on the journal surface. The differential operators in the new variables fulfill

$$\partial_{\tilde{r}} = \partial_r \frac{1}{\varepsilon}, \ \partial_{\tilde{z}} = \partial_z \frac{1}{\delta}.$$

Writing NSE in the new coordinates then yields

$$\partial_\tau \varepsilon u_r \quad + \quad \left(\varepsilon u_r (\frac{1}{\varepsilon} \partial_r \varepsilon u_r) + \frac{1}{1 + \varepsilon r} u_\varphi \partial_\varphi \varepsilon u_r + \delta u_z \frac{1}{\delta} \partial_z \varepsilon u_r - \frac{u_\varphi^2}{1 + \varepsilon r} \right)$$

$$= \quad -\frac{1}{\varepsilon} \partial_r \tilde{p} + \frac{1}{\tilde{\mathcal{R}}} \left(\frac{1}{\varepsilon^2} \partial_r^2 \varepsilon u_r + \frac{1}{1 + \varepsilon r} (\frac{1}{\varepsilon} \partial_r \varepsilon u_r) + \frac{1}{\delta^2} \partial_z^2 \varepsilon u_r \right.$$

$$+ \quad \left. \frac{1}{(1 + \varepsilon r)^2} \partial_\varphi^2 \varepsilon u_r - \frac{\varepsilon u_r}{(1 + \varepsilon r)^2} - \frac{2\partial_\varphi \varepsilon u_r}{(1 + \varepsilon r)^2} \right),$$

$$\partial_\tau u_\varphi \;+\; \left(\frac{\varepsilon u_r}{1+\varepsilon r}u_\varphi + \varepsilon u_r(\tfrac{1}{\varepsilon}\partial_r u_\varphi) + \frac{u_\varphi}{1+\varepsilon r}\partial_\varphi u_\varphi + \delta u_z\tfrac{1}{\delta}\partial_z u_\varphi\right)$$

$$=\; -\frac{1}{1+\varepsilon r}\partial_\varphi\tilde{p} + \frac{1}{\tilde{\mathcal{R}}}\left(\frac{1}{\varepsilon^2}\partial_r^2 u_\varphi + \frac{1}{1+\varepsilon r}(\tfrac{1}{\varepsilon}\partial_r u_\varphi) + \frac{1}{(1+\varepsilon r)^2}\partial_\varphi^2 u_\varphi + \frac{1}{\delta^2}\partial_z^2 u_\varphi\right.$$

$$+\;\left.\frac{2\partial_\varphi\varepsilon u_r}{(1+\varepsilon r)^2} - \frac{u_\varphi}{(1+\varepsilon r)^2}\right),$$

$$\partial_\tau\delta u_z \;+\; \left(\varepsilon u_r(\tfrac{1}{\varepsilon}\partial_r\delta u_z) + \frac{1}{1+\varepsilon r}u_\varphi\partial_\varphi\delta u_z + \delta u_z\tfrac{1}{\delta}\partial_z\delta u_z\right)$$

$$=\; -\frac{1}{\delta}\partial_z\tilde{p} + \frac{1}{\tilde{\mathcal{R}}}\left(\frac{1}{\varepsilon^2}\partial_r^2\delta u_z + \frac{1}{1+\varepsilon r}(\tfrac{1}{\varepsilon}\partial_r\delta u_z) + \frac{1}{\delta^2}\partial_z^2\delta u_z + \frac{1}{(1+\varepsilon r)^2}\partial_\varphi^2\delta u_z\right).$$

With the scaling for the Reynolds number $\mathcal{R} = \varepsilon\tilde{\mathcal{R}}$ we obtain:

$$\mathcal{R}\left(\partial_\tau u_r + u_r\partial_r u_r + \frac{1}{1+\varepsilon r}u_\varphi\partial_\varphi u_r + u_z\partial_z u_r - \frac{u_\varphi^2}{(1+\varepsilon r)\varepsilon}\right)$$

$$=\; -\frac{\mathcal{R}}{\varepsilon^2}\partial_r\tilde{p} + \left(\frac{1}{\varepsilon}\partial_r^2 u_r + \frac{1}{1+\varepsilon r}\partial_r u_r + \frac{\varepsilon}{\delta^2}\partial_z^2 u_r + \frac{\varepsilon}{(1+\varepsilon r)^2}\partial_\varphi^2 u_r\right.$$

$$-\;\left.\frac{\varepsilon}{(1+\varepsilon r)^2}u_r - \frac{2\partial_\varphi\varepsilon u_r}{(1+\varepsilon r)^2}\right),$$

$$\mathcal{R}\left(\partial_\tau u_\varphi + \frac{\varepsilon}{1+\varepsilon r}u_r u_\varphi + u_r\partial_r u_\varphi + \frac{u_\varphi}{1+\varepsilon r}\partial_\varphi u_\varphi + u_z\partial_z u_\varphi\right)$$

$$=\; -\frac{\mathcal{R}}{1+\varepsilon r}\partial_\varphi\tilde{p} + \left(\frac{1}{\varepsilon}\partial_r^2 u_\varphi + \frac{1}{1+\varepsilon r}\partial_r u_\varphi + \frac{\varepsilon}{(1+\varepsilon r)^2}\partial_\varphi^2 u_\varphi\right.$$

$$+\;\left.\frac{\varepsilon}{\delta^2}\partial_z^2 u_\varphi + \frac{2\partial_\varphi\varepsilon^2 u_r}{(1+\varepsilon r)^2} - \frac{\varepsilon u_\varphi}{(1+\varepsilon r)^2}\right),$$

$$\varepsilon\mathcal{R}\left(\partial_\tau u_z + u_r\partial_r u_z + \frac{1}{1+\varepsilon r}u_\varphi\partial_\varphi u_z + u_z\partial_z u_z\right)$$

$$=\; -\frac{\mathcal{R}\varepsilon}{\delta^2}\partial_z\tilde{p} + \left(\partial_r^2 u_z + \frac{\varepsilon}{1+\varepsilon r}\partial_r u_z + \frac{\varepsilon^2}{\delta^2}\partial_z^2 u_z + \frac{\varepsilon^2}{(1+\varepsilon r)^2}\partial_\varphi u_z\right).$$

Finally by introducing the scaling for the pressure $p = \mathcal{R}\frac{\varepsilon}{\delta^2}\tilde{p}$ and ordering by orders of ε and δ we get:

$$\partial_r u_r + \frac{\varepsilon}{1+\varepsilon r}u_r + \frac{1}{1+\varepsilon r}\partial_\varphi u_\varphi + \partial_z u_z = 0, \tag{5.9}$$

$$-\partial_r p = -\frac{\varepsilon^2}{\delta^2}\left(\partial_r^2 u_r + \mathcal{R}\frac{u_\varphi^2}{1+\varepsilon r}\right) \tag{5.10}$$

$$+\frac{\varepsilon^3}{\delta^2}\left(\mathcal{R}\left(\partial_\tau u_r + u_r\partial_r u_r + \frac{1}{1+\varepsilon r}u_\varphi\partial_\varphi u_\varphi + u_z\partial_z u_z\right) - \frac{1}{1+\varepsilon r}\partial_r u_r\right)$$

$$-\frac{\varepsilon^4}{\delta^4}\left(\partial_z^2 u_r\right)$$

$$-\frac{\varepsilon^4}{\delta^2}\left(\frac{\partial_\varphi^2 u_r - u_r - 2\partial_\varphi u_r}{(1+\varepsilon r)^2}\right),$$

$$\partial_r^2 u_\varphi = \frac{\delta^2}{1+\varepsilon r}\partial_\varphi p \tag{5.11}$$

$$+\varepsilon\left(\mathcal{R}\left(\partial_\tau u_\varphi + u_r\partial_r u_\varphi + \frac{u_\varphi}{1+\varepsilon r}\partial_\varphi u_\varphi + u_z\partial_z u_\varphi\right) - \frac{1}{1+\varepsilon r}\partial_r u_\varphi\right)$$

$$-\frac{\varepsilon^2}{\delta^2}\partial_z^2 u_\varphi$$

$$+\varepsilon^2\mathcal{R}\frac{u_\varphi u_r}{1+\varepsilon r}$$

$$-\varepsilon^2\frac{\partial_\varphi^2 u_\varphi + 2\varepsilon\partial_\varphi u_r - u_\varphi}{(1+\varepsilon r)^2},$$

$$\partial_r^2 u_z - \partial_z p = \varepsilon\left(\mathcal{R}\left(\partial_\tau u_z + u_r\partial_r u_z + \frac{u_\varphi}{1+\varepsilon r}\partial_\varphi u_z + u_z\partial_z u_z\right) - \frac{1}{1+\varepsilon r}\partial_r u_z\right)$$

$$-\frac{\varepsilon^2}{\delta^2}\partial_z^2 u_z \tag{5.12}$$

$$-\varepsilon^2\frac{\partial_\varphi^2 u_z}{(1+\varepsilon r)^2}.$$

5.1.2   Boundary Conditions

We impose the following no slip boundary conditions on our system. On the outer surface:

$$\tilde{u}_r = 0,\ \tilde{u}_\varphi = 0,\ \tilde{u}_z = 0 \quad \text{on } \Gamma_1 = \{\tilde{r} = 0,\ \tilde{\varphi} \in [0, 2\pi],\ \tilde{z} \in [0, W]\}, \tag{5.13}$$

and on the journal surface:

$$\tilde{u}_r = \tilde{V}_r(\varphi, t),\ \tilde{u}_\varphi = \tilde{V}_\varphi(\varphi, t),\ \tilde{u}_z = 0 \quad \text{on } \Gamma_2 = \{\tilde{r} = -\tilde{h}(\varphi, t),\ \tilde{\varphi} \in [0, 2\pi],\ \tilde{z} \in [0, W]\}, \tag{5.14}$$

and at the openings at both ends:

$$\tilde{p} = 0 \quad \text{on } \Gamma_3 \cup \Gamma_4 = \{\tilde{r} \in [-\tilde{h}(\varphi), 0],\ \tilde{\varphi} \in [0, 2\pi],\ \tilde{z} \in \{0, W\}\}. \tag{5.15}$$

The velocities $\tilde{V}_r(\varphi, t)$ and $\tilde{V}_\varphi(\varphi, t)$ of the journal surface and the oil film thickness $\tilde{h}(\varphi, t)$ can be expressed in terms of the position and velocity of the journal center (cf.
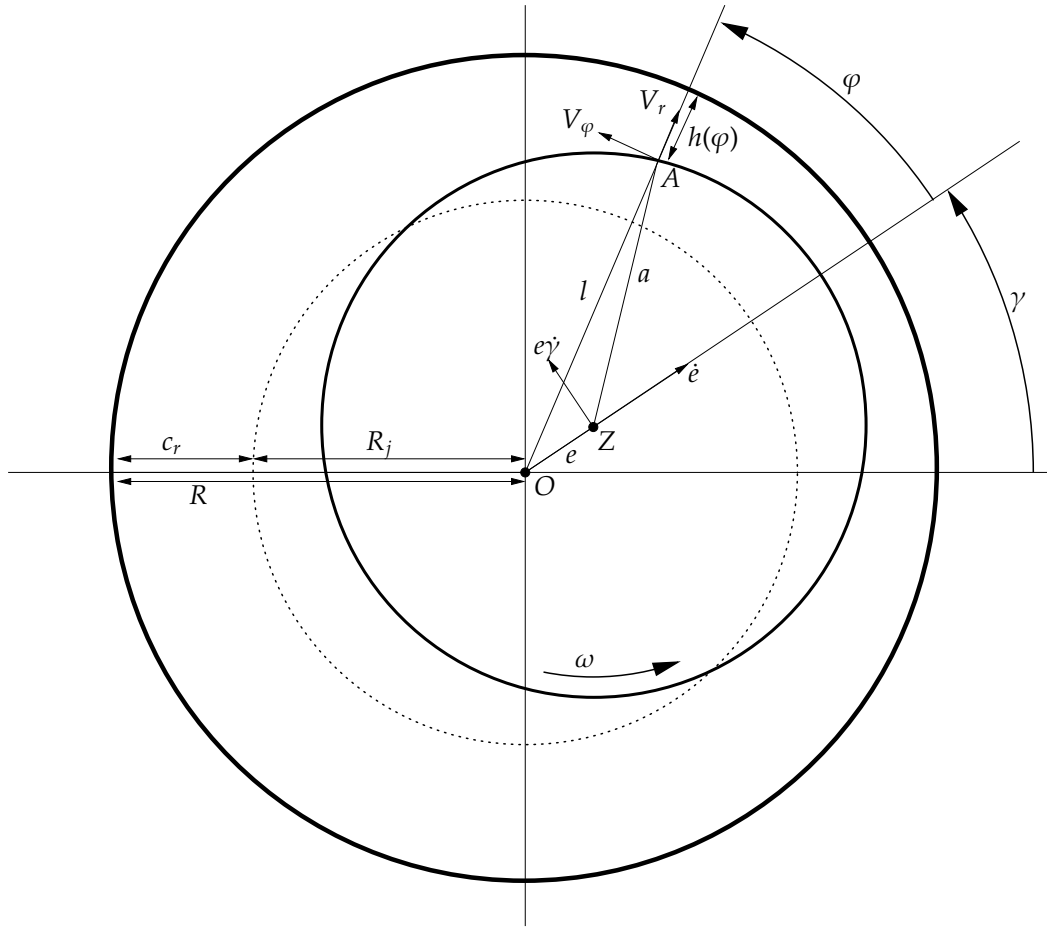
Figure 5.4: Sketch of simple journal bearing; view in axial direction

figure 5.4). Let E_e be the unit vector in the direction of the eccentricity $\tilde{e}$ and E_γ be the corresponding orthonormal unit vector in the tangential direction. The velocity $\tilde{V}_Z$ of the journal center can be written as

$$\tilde{V}_Z = \dot{\tilde{e}}E_e + \dot{\gamma}\tilde{e}E_\gamma.$$

Let E_r and E_φ be the local unit vectors at the point A. Then we have

$$E_e = \cos\varphi E_r - \sin\varphi E_\varphi,$$
$$E_\gamma = \sin\varphi E_r + \cos\varphi E_\varphi,$$

and from this

$$\tilde{V}_Z = (\dot{\tilde{e}}\cos\varphi + \dot{\gamma}\tilde{e}\sin\varphi)E_r + (\dot{\gamma}\tilde{e}\cos\varphi - \dot{\tilde{e}}\sin\varphi)E_\varphi.$$

Taking into concern the rotation of the shaft with with angular velocity ω we can write the velocity $\tilde{V}_A$ at point A as $\tilde{V}_A = \omega E_z \times a + \tilde{V}_Z$ where $a = -\tilde{e}E_e + lE_r$. We can determine

l from the relation

$$
\begin{aligned}
\|a\|^2 &= R_j^2 = l^2 + \tilde{e}^2 - 2l\tilde{e}\cos\varphi, \\
l_\pm &= \tilde{e}\cos\varphi \pm \sqrt{R_j^2 - \tilde{e}^2\sin^2\varphi}.
\end{aligned}
$$

Taking the positive solution $l = l_+$ we get

$$
\begin{aligned}
a &= -\tilde{e}E_e + (\tilde{e}\cos\varphi + \sqrt{R_j^2 - \tilde{e}^2\sin^2\varphi})E_r \\
&= -\tilde{e}\cos\varphi E_r + \tilde{e}\sin\varphi E_\varphi + (\tilde{e}\cos\varphi + \sqrt{R_j^2 - \tilde{e}^2\sin^2\varphi})E_r \\
&= \tilde{e}\sin\varphi E_\varphi + \sqrt{R_j^2 - \tilde{e}^2\sin^2\varphi}E_r.
\end{aligned}
$$

Hence

$$
\begin{aligned}
\tilde{V}_A &= \omega\tilde{e}\sin\varphi(E_z \times E_\varphi) + \omega\sqrt{R_j^2 - \tilde{e}^2\sin^2\varphi}(E_z \times E_r) \\
&\quad + (\dot{\tilde{e}}\cos\varphi + \dot{\gamma}\tilde{e}\sin\varphi)E_r + (\dot{\gamma}\tilde{e}\cos\varphi - \dot{\tilde{e}}\sin\varphi)E_\varphi \\
&= E_r(-\omega\tilde{e}\sin\varphi + \dot{\tilde{e}}\cos\varphi + \dot{\tilde{e}}\gamma\sin\varphi) \\
&\quad + E_\varphi(\omega\sqrt{R_j^2 - \tilde{e}^2\sin^2\varphi} - \dot{\tilde{e}}\sin\varphi + \dot{\gamma}\tilde{e}\cos\varphi) \qquad (5.16) \\
&= \tilde{V}_r E_r + \tilde{V}_\varphi E_\varphi. \qquad\qquad\qquad\qquad\qquad\qquad\qquad\qquad\qquad (5.17)
\end{aligned}
$$

For the film thickness $\tilde{h}$ we have

$$
\begin{aligned}
\tilde{h} &= R - l \\
&= R - \tilde{e}\cos\varphi - \sqrt{R_j^2 - e^2\sin^2\varphi} \\
&= R - \tilde{e}\cos\varphi - \sqrt{(R - c_r)^2 - e^2\sin^2\varphi}. \qquad (5.18)
\end{aligned}
$$

We now nondimensionalize and scale the boundary conditions in the same way as we did for the NSE:

$$
V_r = \frac{1}{\varepsilon}\frac{\tilde{V}_r}{R\omega}, \quad V_\varphi = \frac{\tilde{V}_\varphi}{R\omega}, \quad \kappa = \frac{1}{\varepsilon}\frac{\tilde{e}}{R} = \frac{\tilde{e}}{c_r}, \quad \tau = \omega t.
$$

The derivative with respect to τ will be denoted by '. From this and Eqs. (5.16) and (5.18) we deduce the following equations for V_r

$$
\begin{aligned}
c_r\omega V_r &= -\omega c_r\kappa\sin\varphi + \omega c_r\kappa'\cos\varphi + \omega c_r\kappa\gamma'\sin\varphi \\
V_r &= -\kappa\sin\varphi + \kappa'\cos\varphi + \kappa\gamma'\sin\varphi \qquad (5.19) \\
&= V_r^0,
\end{aligned}
$$

for V_φ

$$
\begin{aligned}
R\omega V_\varphi &= \omega \sqrt{R_j^2 - \tilde{e}^2 \sin^2 \varphi} - c_r \omega \kappa' \sin \varphi + \omega c_r \kappa \gamma' \sin \varphi \\
V_\varphi &= \sqrt{\frac{(R - c_r)^2}{R^2} - \frac{c_r^2}{R^2} \kappa^2 \sin^2 \varphi} - \varepsilon \kappa' \sin \varphi + \varepsilon \kappa \gamma' \cos \varphi \\
&= \sqrt{1 - 2\varepsilon + \varepsilon^2 - \varepsilon^2 \kappa^2 \sin^2 \varphi} - \varepsilon \kappa' \sin \varphi + \varepsilon \kappa \gamma' \cos \varphi \\
&= (1 - \varepsilon - \frac{1}{2}\varepsilon^2 \kappa^2 \sin^2 \varphi + O(\varepsilon^3)) - \varepsilon \kappa' \sin \varphi + \varepsilon \kappa \gamma' \cos \varphi \\
&= 1 + \varepsilon(-1 - \kappa' \sin \varphi + \kappa \gamma' \cos \varphi) - \varepsilon^2 \frac{1}{2} \kappa^2 \sin^2 \varphi + O(\varepsilon^3) \qquad (5.20) \\
&= V_\varphi^0 + \varepsilon V_\varphi^1 + O(\varepsilon^2),
\end{aligned}
$$

and for $h(\varphi, t)$

$$
\begin{aligned}
h(\varphi, t) &= \frac{\tilde{h}(\varphi)}{R} \frac{1}{\varepsilon} = \frac{\tilde{h}(\varphi)}{c_r} \\
&= \frac{1}{\varepsilon} - \kappa \cos \varphi - \sqrt{(\frac{1}{\varepsilon} - 1)^2 - \kappa^2 \sin^2 \varphi} \\
&= \frac{1}{\varepsilon} - \kappa \cos \varphi - (\frac{1}{\varepsilon} - 1 - \varepsilon \frac{1}{2} \kappa^2 \sin^2 \varphi + O(\varepsilon^2)) \\
&= 1 - \kappa \cos \varphi + \varepsilon \frac{1}{2} \kappa^2 \sin^2 \varphi + O(\varepsilon^2) \qquad (5.21) \\
&= h_0 + \varepsilon h_1 + O(\varepsilon^2).
\end{aligned}
$$

5.1.3   Reynolds' Equation and Short Bearing Approximation

We now want to solve the scaled NSE (5.9)-(5.12). We still have two free parameters in the equations which we will assume to be small in the following. $\varepsilon = \frac{c_r}{R}$ is the ratio of radial clearance c_r and bearing radius R and is a measure for the film thickness. It is considered small in all bearing theories. $\delta = \frac{W}{R}$ is the ratio of the bearing width W and the radius R. This parameter is considered small in the so called short bearing approximation. In the present model we have $\varepsilon \ll \delta \ll 1$. We therefore assume in the following relation between the two parameters

$$
\varepsilon = K\delta^2. \qquad (5.22)
$$

This leads to the following equations

$$
\begin{aligned}
-\partial_r p &= -K\varepsilon\left(\partial_r^2 u_r + \mathcal{R}\frac{u_\varphi^2}{1+\varepsilon r}\right) \\
&\quad + K\varepsilon^2\left(\mathcal{R}\left(\partial_\tau u_r + u_r\partial_r u_r + \frac{1}{1+\varepsilon r}u_\varphi\partial_\varphi u_\varphi + u_z\partial_z u_z\right) - \frac{1}{1+\varepsilon r}\partial_r u_r - K\partial_z^2 u_r\right) \\
&\quad -\varepsilon^3 K\left(\frac{\partial_\varphi^2 u_r - u_r - 2\partial_\varphi u_r}{(1+\varepsilon r)^2}\right), \\
\partial_r^2 u_\varphi &= \varepsilon\left(\frac{1}{K(1+\varepsilon r)}\partial_\varphi p - \frac{1}{1+\varepsilon r}\partial_r u_\varphi - K\partial_z^2 u_\varphi\right) \\
&\quad + \varepsilon\mathcal{R}\left(\partial_\tau u_\varphi + u_r\partial_r u_\varphi + \frac{u_\varphi}{1+\varepsilon r}\partial_\varphi u_\varphi + u_z\partial_z u_\varphi\right) \\
&\quad + \varepsilon^2\mathcal{R}\frac{u_\varphi u_r}{1+\varepsilon r} - \varepsilon^2\frac{\partial_\varphi^2 u_\varphi + 2\varepsilon\partial_\varphi u_r - u_\varphi}{(1+\varepsilon r)^2}, \\
\partial_r^2 u_z - \partial_z p &= \varepsilon\left(\mathcal{R}\left(\partial_\tau u_z + u_r\partial_r u_z + \frac{u_\varphi}{1+\varepsilon r}\partial_\varphi u_z + u_z\partial_z u_z\right) - \frac{1}{1+\varepsilon r}\partial_r u_z - K\partial_z^2 u_z\right) \\
&\quad -\varepsilon^2\frac{\partial_\varphi^2 u_z}{(1+\varepsilon r)^2},
\end{aligned}
$$

and

$$
\partial_r u_r + \frac{\varepsilon}{1+\varepsilon r}u_r + \frac{1}{1+\varepsilon r}\partial_\varphi u_\varphi + \partial_z u_z = 0.
$$

We expand u and p into a series in ε

$$
u^\varepsilon = u^0 + \varepsilon u^1 + O(\varepsilon^2) \quad\text{and}\quad p^\varepsilon = p^0 + \varepsilon p^1 + O(\varepsilon^2)
$$

and insert the series into the scaled equations above, keeping in mind that

$$
\frac{1}{1+\varepsilon r} = \sum_{n=0}^{\infty}(-\varepsilon r)^n.
$$

Collecting terms of same order in ε we get

$$
\varepsilon^0 : \qquad \partial_r p^0 = 0, \tag{5.23}
$$

$$
\partial_r^2 u_\varphi^0 = 0, \tag{5.24}
$$

$$
\partial_r^2 u_z^0 - \partial_z p^0 = 0, \tag{5.25}
$$

$$
\partial_r u_r^0 + \partial_\varphi u_\varphi^0 + \partial_z u_z^0 = 0, \tag{5.26}
$$

$$\varepsilon^1: \quad -\partial_r p^1 = -K(\partial_r^2 u_r^0 + \mathcal{R}(u_\varphi^0)^2), \tag{5.27}$$

$$\partial_r^2 u_\varphi^1 = \frac{\partial_\varphi p^0}{K} - \partial_r u_\varphi^0 - K\partial_z^2 u_\varphi^0$$

$$+ \mathcal{R}\left(\partial_\tau u_\varphi^0 + u_r^0 \partial_r u_\varphi^0 + u_\varphi^0 \partial_\varphi u_\varphi^0 + u_z^0 \partial_z u_\varphi^0\right), \tag{5.28}$$

$$\partial_r^2 u_z^1 - \partial_z p^1 = -\partial_r u_z^0 - K\partial_z^2 u_z^0$$

$$+ \mathcal{R}\left(\partial_\tau u_z^0 + u_r^0 \partial_r u_z^0 + u_\varphi^0 \partial_\varphi u_z^0 + u_z^0 \partial_z u_z^0\right), \tag{5.29}$$

$$\partial_r u_r^1 + u_r^0 - r\partial_\varphi u_\varphi^0 + \partial_\varphi u_\varphi^1 + \partial_z u_z^1 = 0. \tag{5.30}$$

The boundary conditions for the functions appearing in the expansions for the pressure and the velocity can be calculated from the boundary conditions for the NSE (5.13) - (5.15) and their expansions (5.19) - (5.21). From $u_r^\varepsilon(0, \varphi, z) = 0$ on the outer surface we deduce $u_r^0(0, \varphi, z) = u_r^1(0, \varphi, z) = 0$. Analogously $u_\varphi^0(0, \varphi, z) = u_\varphi^1(0, \varphi, z) = 0$ and $u_z^0(0, \varphi, z) = u_z^1(0, \varphi, z) = 0$. The boundary conditions at the inner surface $r = -h_\varepsilon$ are more interesting. For notational convenience the dependence of the velocities from z and φ are not explicitly written down in the next equations. We get

$$\begin{aligned}
V_r &= u_r^\varepsilon(-h_\varepsilon) \\
&= u_r^0(-h_0 - \varepsilon h_1 + O(\varepsilon^2)) + \varepsilon u_r^1(-h_0 - \varepsilon h_1 + O(\varepsilon^2)) + O(\varepsilon^2) \\
&= u_r^0(-h_0) - \varepsilon h_1 \partial_r u_r^0(-h_0) + \varepsilon u_r^1(-h_0) + O(\varepsilon^2).
\end{aligned}$$

From (5.19) we see that $V_r = V_r^0$ and therefore

$$\begin{aligned}
u_r^0(-h_0) &= V_r^0, \tag{5.31} \\
u_r^1(-h_0) &= h_1 \partial_r u_r^0(-h_0). \tag{5.32}
\end{aligned}$$

For u_φ^0, u_φ^1, u_z^0 and u_z^1 we derive in the same way that

$$\begin{aligned}
u_\varphi^0(-h_0) &= V_\varphi^0, \tag{5.33} \\
u_\varphi^1(-h_0) &= V_\varphi^1 + h_1 \partial_r u_\varphi^0(-h_0), \tag{5.34} \\
u_z^0(-h_0) &= 0, \tag{5.35} \\
u_z^1(-h_0) &= h_1 \partial_r u_z^0(-h_0). \tag{5.36}
\end{aligned}$$

In combination with these boundary conditions the equations (5.23) - (5.30) can be solved analytically which shall be done in the following sections.

5.1.4 Approximate Solution of Order ε^0

We start with the order ε^0. The first equation (5.23) tells us that the pressure does not depend on the radial variable r. Equations (5.24) and (5.25) can therefore be integrated over r using the boundary conditions at $r = 0$ and $r = -h_0$. We obtain the velocity profiles:

$$u^0_\varphi \quad = \quad -V^0_\varphi \frac{r}{h_0}, \tag{5.37}$$

$$u^0_z \quad = \quad \frac{r(r + h_0)}{2} \partial_z p^0. \tag{5.38}$$

From the continuity equation (5.26) we can calculate $\partial_r u^0_r$:

$$-\partial_r u^0_r = \partial_\varphi u^0_\varphi + \partial_z u^0_z = \partial_\varphi \left(-V^0_\varphi \frac{r}{h_0} \right) + \frac{r(r + h_0)}{2} \partial^2_z p^0. \tag{5.39}$$

We use again the fact that p^0 does not depend on r and integrate both sides with respect to r to eliminate the radial coordinate

$$-V^0_r \quad = \quad \int\limits_0^{-h_0(\varphi)} \partial_\varphi \left(-V^0_\varphi \frac{r}{h_0} \right) dr + \partial^2_z p^0 \left[\frac{1}{6} r^3 + \frac{h_0}{4} r^2 \right]_0^{-h_0} \tag{5.40}$$

$$= \quad \partial_\varphi \int\limits_0^{-h_0(\varphi)} \left(-V^0_\varphi \frac{r}{h_0} \right) dr + \left(V^0_\varphi \frac{h_0}{h_0} \right) \partial_\varphi h_0 + \frac{h^3_0}{12} \partial^2_z p^0 \tag{5.41}$$

$$= \quad \partial_\varphi \left(-V^0_\varphi \frac{h_0}{2} \right) + V^0_\varphi \partial_\varphi h_0 + \frac{h^3_0}{12} \partial^2_z p^0. \tag{5.42}$$

Leibniz' rule $\partial_\alpha \int_0^{g(\alpha)} f(x, \alpha)\, dx = \int_0^{g(\alpha)} \partial_\alpha f(x, \alpha)\, dx + f(g(\alpha), \alpha) \partial_\alpha g$ was used for interchanging derivation and integration. From this we get for the pressure

$$\partial^2_z p^0 \quad = \quad \frac{12}{h^3_0} \left(\frac{h_0}{2} \partial_\varphi V^0_\varphi + \frac{1}{2} V^0_\varphi \partial_\varphi h_0 - V^0_\varphi \partial_\varphi h_0 - V^0_r \right) \tag{5.43}$$

$$= \quad \frac{12}{h^3_0} \left(\frac{h_0}{2} \partial_\varphi V^0_\varphi - \frac{1}{2} V^0_\varphi \partial_\varphi h_0 - V^0_r \right). \tag{5.44}$$

Integration over z and using $p = 0$ for $z \in \{0, 1\}$ then yields

$$p^0 = \frac{6z(z - 1)}{h^3_0} \left(\frac{h_0}{2} \partial_\varphi V^0_\varphi - \frac{1}{2} V^0_\varphi \partial_\varphi h_0 - V^0_r \right). \tag{5.45}$$

To obtain the pressure profile in the lowest order in ε we finally use the ε^0-approximation V^0_r, V^0_φ and h_0 from (5.19) and (5.20) and (5.21).

$$h_0 = 1 - \kappa \cos \varphi, \quad V^0_\varphi = 1, \quad V^0_r = -\kappa \sin \varphi + \kappa' \cos \varphi + \kappa \gamma' \sin \varphi$$

and finally get

Statement 5.1. *The pressure solution for the zeroth order short bearing approximation corresponding to point 2 in the list in Section 5.1 is*

$$p^0 = 6z(z-1)\frac{\left(-\frac{1}{2}\kappa\sin\varphi + \kappa\sin\varphi - \kappa'\cos\varphi - \kappa\gamma'\sin\varphi\right)}{(1-\kappa\cos\varphi)^3} \tag{5.46}$$

$$= -6z(z-1)\frac{\left((\gamma'-\frac{1}{2})\kappa\sin\varphi + \kappa'\cos\varphi\right)}{(1-\kappa\cos\varphi)^3}. \tag{5.47}$$

Usually the short bearing approximation is obtained by first deriving Reynolds' equation for thin films and then in a second step assuming also smallness of the bearing width. Here, due to the special scaling it can be derived in one step. In Figure 5.5 the distributions for different values of κ, $\dot{\kappa}$ are depicted to give an idea of the geometric nature of the solutions.
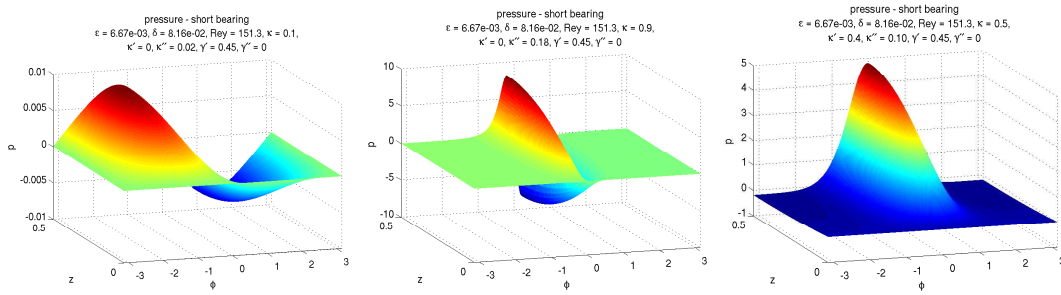

Figure 5.5: Zeroth order short bearing pressure distributions p_0 for varying values of κ and $\dot{\kappa}$; left: $\kappa = 0.1$, $\dot{\kappa} = 0$, middle: $\kappa = 0.9$, $\dot{\kappa} = 0$, right: $\kappa = 0.5$, $\dot{\kappa} = 0.4$.

For zero radial velocity the pressure distribution shows lower pressures in the region behind (in mathematically positive direction) the point of smalles film-thicknes and higher pressures in front of this bottle neck. For large eccentricities the region of large pressure variation is concentrated around this point of smallest film-thickness. These pressure differences sustain the circular whirling motion of the shaft. For nonzero radial velocity there appears a large pressure opposing the outward movement and avoiding collision.

From the solution for the pressure we can calculate the velocity profiles u_r^0, u_φ^0 and u_z^0 by (5.37), (5.38), and (5.39)

$$u_\varphi^0 = -\frac{r}{h_0}, \tag{5.48}$$

$$u_z^0 = \frac{r(r+h_0)}{2}\partial_z p^0 \tag{5.49}$$

$$= \frac{-6r(r+h_0)}{h_0^3}\left(z-\frac{1}{2}\right)\left(\left(\gamma'-\frac{1}{2}\right)\kappa\sin\varphi+\kappa'\cos\varphi\right),$$

$$u_r^0 = \int_0^r (-\partial_\varphi u_\varphi^0 - \partial_z u_z^0)\,d\rho$$

$$= \int_0^r -\frac{\rho}{h_0^2}\partial_\varphi h_0 - \frac{\rho(\rho+h_0)}{2}\partial_z^2 p^0\,d\rho$$

$$= \frac{r^2}{2h_0^2}\kappa\sin\varphi - \left(\frac{2r^3+3r^2 h_0}{h_0^3}\right)\left(\left(\gamma'-\frac{1}{2}\right)\kappa\sin\varphi+\kappa'\cos\varphi\right). \tag{5.50}$$

5.1.5   Approximate Solution of Order ε^1

The equations (5.27) - (5.30) for the order ε^1 have almost the same structure as the zeroth order approximation. The difference lies only in the right hand side terms which depend on the lower order solutions p^0 and u^0. To simplify the notation we define

$$
\begin{aligned}
T_\varphi^0(r,\varphi,z,\tau) &:= \frac{\partial_\varphi p^0}{K} - \partial_r u_\varphi^0 - K\partial_z^2 u_\varphi^0 \\
&\quad + \mathcal{R}\left(\partial_\tau u_\varphi^0 + u_r^0\partial_r u_\varphi^0 + u_\varphi^0\partial_\varphi u_\varphi^0 + u_z^0\partial_z u_\varphi^0\right), \tag{5.51} \\
T_z^0(r,\varphi,z,\tau) &:= -\partial_r u_z^0 - K\partial_z^2 u_z^0 \\
&\quad + \mathcal{R}\left(\partial_\tau u_z^0 + u_r^0\partial_r u_z^0 + u_\varphi^0\partial_\varphi u_z^0 + u_z^0\partial_z u_z^0\right). \tag{5.52}
\end{aligned}
$$

Equations (5.28) and (5.29) can then be rewritten as

$$\partial_r^2 u_\varphi^1 = T_\varphi^0, \tag{5.53}$$

$$\partial_r^2 u_z^1 - \partial_z p^1 = T_z^0. \tag{5.54}$$

From the equation for the pressure (5.27) and the solutions of lower order from the previous section we see that

$$\partial_r\partial_z p^1 = \partial_z\partial_r p^1 = K(\partial_z\partial_r^2 u_r^0 + \mathcal{R}\partial_z(u_\varphi^0)^2) = 0.$$

Therefore $\partial_z p^1$ does not depend on r and we can again use an analogous procedure like in the previous section to derive an equation for the pressure.

We integrate equation (5.54) twice over r and use the boundary conditions (5.36) to obtain

$$u_z^1 = \frac{r(r+h_0)}{2}\partial_z p^1 + \int_0^r\int_0^\rho T_z^0(s)\,ds\,d\rho + \frac{r}{h_0}\left(-h_1\partial_r u_z^0(-h_0) + \int_0^{-h_0}\int_0^\rho T_z^0(s)\,ds\,d\rho\right). \tag{5.55}$$

For u_φ^1 we have the boundary conditions $u_\varphi^1(0) = 0$ and $u_\varphi^1(-h_0) = V_\varphi^1 + h_1\partial_r u_\varphi^0(-h_0)$ (5.34). Hence the circumferential velocity v_φ^1 is given by

$$u_\varphi^1 = \int_0^r \int_0^\rho T_\varphi^0(s)\,ds\,d\rho + \frac{r}{h_0}\left(-V_\varphi^1 - h_1\partial_r u_\varphi^0(-h_0) + \int_0^{-h_0}\int_0^\rho T_\varphi^0(s)\,ds\,d\rho\right) \tag{5.56}$$

and does only depend on the boundary condition and known zeroth order terms.

For u_r^1 we have the boundary conditions $u_r^1(0) = 0$ and $u_r^1(-h_0) = h_1\partial_r u_r^0(-h_0)$ (5.32). By integrating the continuity equation (5.30) over r we then obtain

$$-h_1\partial_r u_r^0(-h_0) = \int_0^{-h_0} -\partial_r u_r^1\,dr \tag{5.57}$$

$$= \int_0^{-h_0}(u_r^0 - r\partial_\varphi u_\varphi^0)\,dr + \int_0^{-h_0}\partial_\varphi u_\varphi^1\,dr + \int_0^{-h_0}\partial_z u_z^1\,dr \tag{5.58}$$

$$= \int_0^{-h_0}(u_r^0 - r\partial_\varphi u_\varphi^0)\,dr + \int_0^{-h_0}\partial_\varphi u_\varphi^1\,dr + \partial_z^2 p^1\int_0^{-h_0}\frac{r(r+h_0)}{2}\,dr$$

$$+ \int_0^{-h_0}\int_0^r\int_0^\rho \partial_z T_z^0(s)\,ds\,d\rho\,dr$$

$$+ \int_0^{-h_0}\frac{r}{h_0}\left(-h_1\partial_z\partial_r u_z^0(-h_0) + \int_0^{-h_0}\int_0^\rho \partial_z T_z^0(s)\,ds\,d\rho\right)dr. \tag{5.59}$$

Here we used again that h_0 and h_1 do not depend on the axial coordinate z. Thus we have eliminated the radial coordinate again and we have

$$\partial_z^2 p^1 = \frac{12}{h_0^3}\left(-h_1\partial_r u_r^0(-h_0) - \int_0^{-h_0}(u_r^0 - r\partial_\varphi u_\varphi^0)\,dr\right.$$

$$- \int_0^{-h_0}\partial_\varphi u_\varphi^1\,dr - \int_0^{-h_0}\int_0^r\int_0^\rho \partial_z T_z^0(s)\,ds\,d\rho\,dr$$

$$\left.-\frac{h_0}{2}\left(-h_1\partial_z\partial_r u_z^0(-h_0) - \int_0^{-h_0}\int_0^\rho \partial_z T_z^0(s)\,ds\,d\rho\right)\right)$$

$$=: R(z,\varphi).$$

Using the zero boundary conditions for the pressure we can integrate the right hand side term and we get the following solution for the pressure in the order ε^1:

$$p^1(z,\varphi,\tau) = \int_0^z\int_0^\zeta R(s,\varphi)\,ds\,d\zeta - z\int_0^1\int_0^\zeta R(s,\varphi)\,ds\,d\zeta. \tag{5.60}$$

All the integrals on the right hand side exist and can be solved analytically. Hence the solution for the pressure p^1 can be computed explicitly and can be written in the following form

$$
\begin{aligned}
p^1 = {} & \mathcal{R}(\kappa')^2 \left(-\frac{51}{35h_0^2} z(z-1)\cos^2\varphi \right) \\
& + \mathcal{R}\kappa'\gamma' \left(-\frac{3}{70h_0^2} z(z-1)\sin\varphi(47\kappa\cos\varphi + 14) \right) \\
& + \mathcal{R}\kappa' \left(\frac{3}{35h_0^2} z(z-1)\sin\varphi(10\kappa\cos\varphi + 7) \right) \\
& + \kappa' \left(\frac{1}{2h_0^5} z(z-1)\Big(6h_0\kappa\sin^2\varphi(2\kappa\cos\varphi + 1) \right. \\
& \qquad \left. + \frac{(z^2 - z - 1)}{K}(-\kappa\cos^2\varphi + 2\kappa^2\cos^3\varphi + 3\kappa\sin^2\varphi - \cos\varphi)\Big) \right) \\
& + \mathcal{R}\kappa'' \left(-\frac{3}{5h_0} z(z-1)\cos\varphi \right) \\
& + \mathcal{R}\gamma'' \left(-\frac{3}{5h_0} z(z-1)\kappa\sin\varphi \right) \\
& + \mathcal{R}\gamma'^2 \left(-\frac{81}{70h_0^2} z(z-1)\kappa^2\sin^2\varphi \right) \\
& + \mathcal{R}\gamma' \left(\frac{1}{140h_0^2} z(z-1)\kappa \left(253\kappa\sin^2\varphi - 7\cos\varphi + 7\kappa\cos^2\varphi \right) \right) \\
& + \gamma' \left(\frac{1}{2h_0^5} z(z-1)\Big(6\kappa^2\sin\varphi h_0(\kappa\cos^2\varphi - \cos\varphi + 3\kappa\sin^2\varphi) \right. \\
& \qquad \left. + \frac{(z^2 - z - 1)}{K}\kappa\sin\varphi(3\kappa^2\sin^2\varphi - 1 - 4\kappa\cos\varphi + 5\kappa^2\cos^2\varphi)\Big) \right) \\
& + \mathcal{R} \left(-\frac{1}{140h_0^2} z(z-1)\kappa \left(-14\cos\varphi + 14\kappa\cos^2\varphi + 65\kappa\sin^2\varphi \right) \right) \\
& + \left(-\frac{1}{4h_0^5} z(z-1)\kappa\sin\varphi\Big(2h_0(5 - 10\kappa\cos\varphi + 5\kappa^2\cos^2\varphi + 9\kappa^2\sin^2\varphi) \right. \\
& \qquad \left. - \frac{(z^2 - z - 1)}{K}(3\kappa^2\sin^2\varphi - 1 - 4\kappa\cos\varphi + 5\kappa^2\cos^2\varphi)\Big) \right). \qquad (5.61)
\end{aligned}
$$

This rather inconveniently long expression can also be written in the form

$$
p_1 = \frac{z(z-1)}{h_0^5} \left(z(z-1)G + \sum_{i=0}^{4} H_i \right), \qquad (5.62)
$$

where the terms G and H_i are expression in terms of h_i, V_i, and p_0. They are given in Appendix E.1.

Statement 5.2. *The inertia correction for the short bearing pressure distribution has the following structure*

$$p^1 = F_0 + \mathcal{R}F_1 + \gamma'F_2 + \mathcal{R}\gamma'F_3 + \mathcal{R}(\gamma')^2F_4 + \mathcal{R}\gamma''F_5$$
$$+ \mathcal{R}\kappa''F_6 + \kappa'F_7 + \mathcal{R}\kappa'F_8 + \mathcal{R}\kappa'\gamma'F_9 + \mathcal{R}(\kappa')^2F_{10}, \tag{5.63}$$

where the F_j are rational functions of h, $\kappa\cos\varphi$ and $\kappa\sin\varphi$. The detailed formula is given in Equation (5.61). An alternative formulation is given in Appendix E.1. We call $p = p^0 + \varepsilon p^1$ the first order short bearing approximation. This approximation corresponds to point 4 in the list of bearings models in Section 5.1.

An analysis of the performed scalings shows that the term $\mathcal{R}F_1$ leads to an ω^2-dependence of the pressure

$$p = \frac{\varepsilon}{\delta^2}\mathcal{R}\tilde{p} = \frac{\varepsilon}{\delta^2}\mathcal{R}\frac{\bar{p}}{\rho R^2\omega^2}, \quad \mathcal{R} = \varepsilon\frac{R^2\omega}{\nu}.$$

The rescaled formula for the pressure is

$$\begin{aligned}
\bar{p} &= \frac{\rho R^2\omega^2\delta^2\nu}{\varepsilon^2 R^2\omega}p \\
&= \frac{\rho\nu\omega\delta^2}{\varepsilon^2}p \\
&\approx \frac{\rho\nu\omega}{K\varepsilon}(p^0 + \varepsilon p^1) \\
&= \frac{\rho\nu\omega}{K\varepsilon}p^0 + \frac{1}{K}\Big(\rho\nu\omega F_0 + \omega^2\rho Rc_rF_1 + \rho\nu\dot{\gamma}F_2 + \frac{\rho\nu\dot{\gamma}}{K}F_3 + \omega\rho Rc_r\dot{\gamma}F_4 \\
&\quad + \dot{\gamma}^2Rc_rF_5 + Rc_r\ddot{\gamma}F_6 + \rho Rc_r\ddot{\kappa}F_7 + \rho\nu\dot{\kappa}F_8 \\
&\quad + \frac{\rho\nu\dot{\kappa}}{K}F_9 + \omega\rho Rc_r\dot{\kappa}F_{10} + \rho Rc_r\dot{\kappa}\dot{\gamma}F_{11} + \rho Rc_r\dot{\kappa}^2F_{12}\Big).
\end{aligned}$$

In Figure 5.6 the inertia corrected pressure distributions for different parameter values are depicted. It can be seen in the lower line that for large values of W, i.e. small values of K, the first order solution differs significantly from the zeroth order solution. In these cases the validity of the short bearing approximation is in question and a solution without this approximation is needed.

5.1.6 Solution Without Short Bearing Approximation

The short bearing approximation is only valid for $\frac{W}{R}$-ratios up to 1 (Childs, 1993). For bearings with very high $\frac{W}{R}$-ratios the Sommerfeld or long bearing approximation is valid, but as most modern bearings do not have such high ratios this approximation is rarely used (San Andrés, 2006). In the case where neither approximation can be used, the classical Reynolds equation has to be solved numerically. We will now derive the
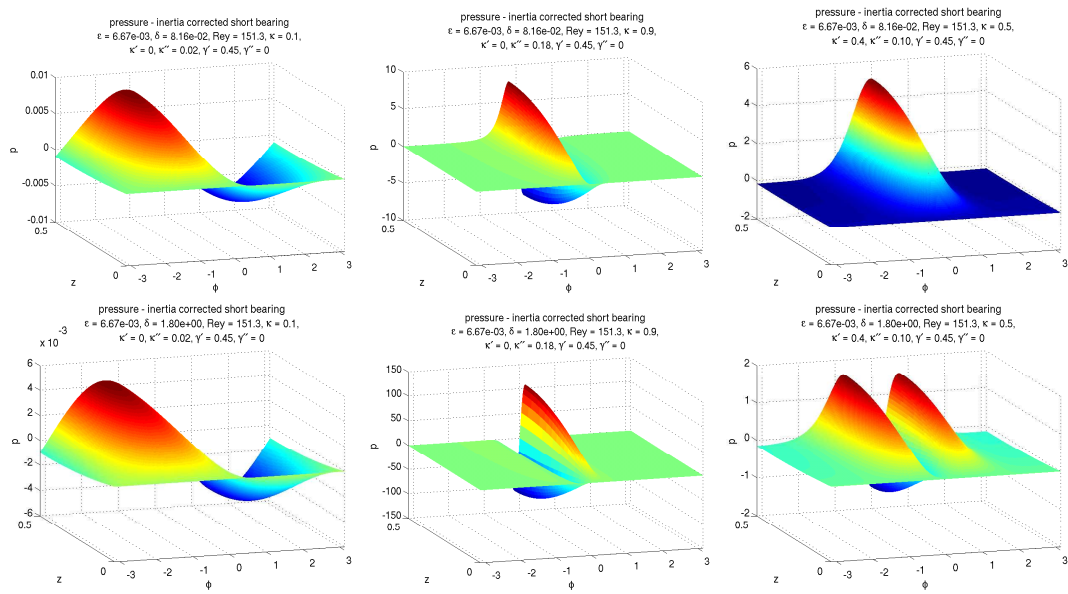
Figure 5.6: First order pressure distributions $p_0 + \varepsilon p_1$ for varying values of κ, $\dot{\kappa}$ and W; upper line: $W = 0.25$ ($K = 1$), lower line: $W = 5.4$ ($K = 0.002$); left: $\kappa = 0.1$, $\dot{\kappa} = 0$, middle: $\kappa = 0.9$, $\dot{\kappa} = 0$, right: $\kappa = 0.9$, $\dot{\kappa} = 0$.

equations for zeroth and first order in ε corresponding to the points 1 and 3 in the list in Section 5.1. In Section 5.4.1 we give a simple finite difference scheme for their solution.

In equations (5.9) - (5.12) we expand p and u again into series in ε and collect terms of the same order. Thus we get

$$\varepsilon^0 \ : \quad \partial_r p^0 = 0, \tag{5.64}$$

$$\partial_r^2 u_\varphi^0 - \delta^2 \partial_\varphi p^0 = 0, \tag{5.65}$$

$$\partial_r^2 u_z^0 - \partial_z p^0 = 0, \tag{5.66}$$

$$\partial_r u_r^0 + \partial_\varphi u_\varphi^0 + \partial_z u_z^0 = 0, \tag{5.67}$$

$$\varepsilon^1 : \qquad \partial_r p^1 = 0, \tag{5.68}$$

$$\partial_r^2 u_\varphi^1 - \delta^2 (\partial_\varphi p^1 - r \partial_\varphi p^0) = -\partial_r u_\varphi^0 \tag{5.69}$$
$$+ \mathcal{R} \left(\partial_\tau u_\varphi^0 + u_r^0 \partial_r u_\varphi^0 + u_\varphi^0 \partial_\varphi u_\varphi^0 + u_z^0 \partial_z u_\varphi^0 \right),$$

$$\partial_r^2 u_z^1 - \partial_z p^1 = -\partial_r u_z^0 + \tag{5.70}$$
$$+ \mathcal{R} \left(\partial_\tau u_z^0 + u_r^0 \partial_r u_z^0 + u_\varphi^0 \partial_\varphi u_z^0 + u_z^0 \partial_z u_z^0 \right),$$

$$\partial_r u_r^1 + u_r^0 - r \partial_\varphi u_\varphi^0 + \partial_\varphi u_\varphi^1 + \partial_z u_z^1 = 0. \tag{5.71}$$

To simplify the notation in the equations for the first order corrections we define the following terms which collect all lower order terms:

$$T_\varphi^0 = -\delta^2 r \partial_\varphi p^0 - \partial_r u_\varphi^0 + \mathcal{R} \left(\partial_\tau u_\varphi^0 + u_r^0 \partial_r u_\varphi^0 + u_\varphi^0 \partial_\varphi u_\varphi^0 + u_z^0 \partial_z u_\varphi^0 \right), \tag{5.72}$$
$$T_z^0 = -\partial_r u_z^0 + \mathcal{R} \left(\partial_\tau u_z^0 + u_r^0 \partial_r u_z^0 + u_\varphi^0 \partial_\varphi u_z^0 + u_z^0 \partial_z u_z^0 \right). \tag{5.73}$$

Analogously to Section 5.1.4 we use the fact that the pressure does not depend on the radial coordinate to integrate velocity equations over r

$$u_\varphi = \delta^2 \frac{r(r + h_0)}{2} \partial_\varphi p^0 - V_\varphi^0 \frac{r}{h_0}, \tag{5.74}$$

$$u_z = \frac{r(r + h_0)}{2} \partial_z p^0. \tag{5.75}$$

The boundary conditions remain the same as before. From the continuity equation we get

$$-\partial_r u_r^0 = \partial_\varphi u_\varphi^0 + \partial_z u_z^0, \tag{5.76}$$

and integration then yields

$$-V_r^0 = \int_0^{-h_0} \partial_\varphi u_\varphi^0 + \partial_z u_z^0 \, dr \tag{5.77}$$

$$= \frac{1}{12} \delta^2 \partial_\varphi (h_0^3 \partial_\varphi p^0) + \frac{1}{12} \partial_z (h_0^3 \partial_z p^0) + \frac{1}{2} V_\varphi^0 \partial_\varphi h^0 - \frac{h_0}{2} \partial_\varphi V_\phi^0. \tag{5.78}$$

The last term vanishes since $\partial_\varphi V_\phi^0 = 0$. We obtain the classical Reynolds equation, an elliptic equation for the zeroth order pressure p^0:

$$\delta^2 \partial_\varphi (h_0^3 \partial_\varphi p^0) + \partial_z (h_0^3 \partial_z p^0) = -12 (V_r^0 + \frac{1}{2} V_\varphi^0 \partial_\varphi h^0). \tag{5.79}$$

By means of the numerical methods described in Section 5.4.1 we can compute approximate solutions for this second order elliptical equation. For different parameter
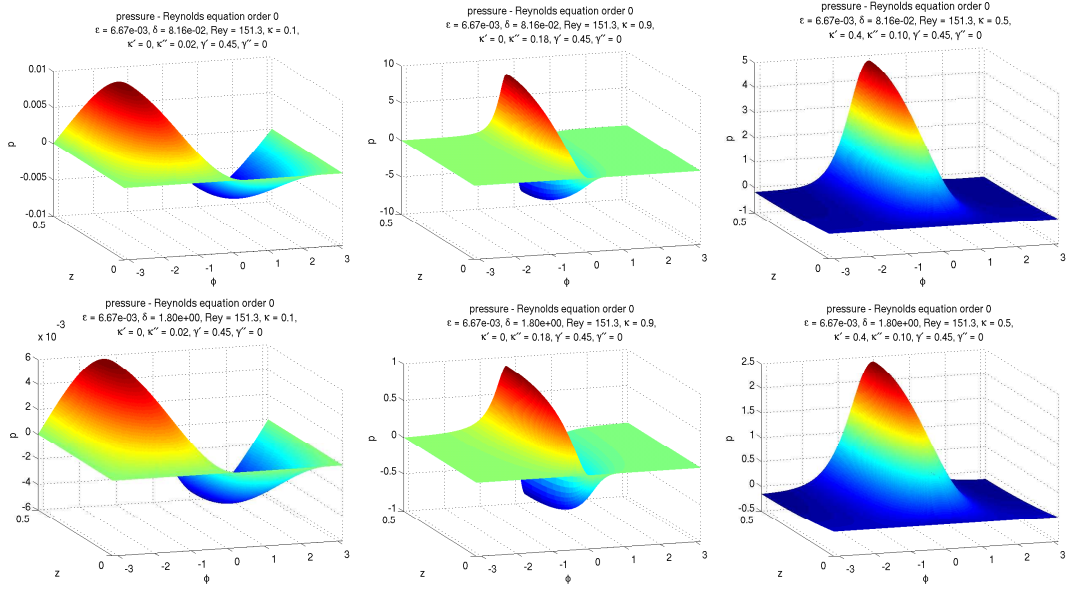
Figure 5.7: Solution p^0 of zeroth order Reynolds equation for varying values of κ, $\dot{\kappa}$, and W; upper line: $W = 0.25$ ($K = 1$), lower line: W=5.4 ($K = 0.002$); left: $\kappa = 0.1$, $\dot{\kappa} = 0$, middle: $\kappa = 0.9$, $\dot{\kappa} = 0$, right: $\kappa = 0.9$, $\dot{\kappa} = 0$.

values of κ, $\dot{\kappa}$, and bearing width W these are depicted exemplarily in Figure 5.7. The figures show similar behavior for different values of the bearing width in contrast to the behavior of the short bearing approximation in the previous section 5.1.5. Here we see zones of elevated pressure in front of the point of smallest film-thickness and reduced pressure behind this point. Note that the different scales are due the non-dimensionalization. In the scaled case with units the pressure is higher for the longer bearing, the scaling factor for the pressure being $\frac{\rho v \omega}{K \varepsilon} = \frac{\eta \omega W^2}{c_r^2}$.

For the first order equations we proceed analogously to obtain another elliptic equation for p^1. The right hand side of this equation however is more complicated due to the terms T_φ^0 and T_z^0. By integration of the equations for the velocities u_φ^1 and u_z^1 we get

$$u_\varphi^1 \;=\; \delta^2 \frac{r(r + h_0)}{2} \partial_\varphi p^1 + \int_0^r \int_0^s T_\varphi^0(t, \varphi, z, s)\, ds\, d\rho \tag{5.80}$$

$$+ \frac{r}{h_0} \left(-V_\varphi^1 - h_1 \partial_r u_\varphi^0(-h_0) + \int_0^{-h_0} \int_0^s T_\varphi^0(t, \varphi, z, s)\, ds\, d\rho \right), \tag{5.81}$$

$$u_z^1 = \frac{r(r+h_0)}{2}\partial_z p^1 + \int_0^r \int_0^s T_z^0(t,\varphi,z,s)\,ds\,d\rho \tag{5.82}$$

$$+\frac{r}{h_0}\left(-h_1\partial_r u_z^0(-h_0) + \int_0^{-h_0}\int_0^s T_z^0(t,\varphi,z,s)\,ds\,d\rho\right). \tag{5.83}$$

Using the continuity equation and integrating over r we obtain

$$-V_r^1 = \int_0^{-h_0} \partial_\varphi u_\varphi^1 + \partial_z u_z^1 + u_r^0 - r\partial_\varphi u_\varphi^0\,dr \tag{5.84}$$

$$= \frac{1}{12}\delta^2\partial_\varphi(h_0^3\partial_\varphi p^1) + \frac{1}{12}\partial_z(h_0^3\partial_z p^1) \tag{5.85}$$

$$+\int_0^{-h_0}\left(\partial_\varphi \int_0^r\int_0^s T_\varphi^0(t,\varphi,z,s)\,ds\,d\rho + \partial_z\int_0^r\int_0^s T_z^0(t,\varphi,z,s)\,ds\,d\rho\right)dr$$

$$+\int_0^{-h_0}\partial_\varphi\left[\frac{r}{h_0}\left(-V_\varphi^1 - h_1\partial_r u_\varphi^0(-h_0) + \int_0^{-h_0}\int_0^s T_\varphi^0(t,\varphi,z,s)\,ds\,d\rho\right)\right]dr$$

$$+\int_0^{-h_0}\partial_z\left[\frac{r}{h_0}\left(-h_1\partial_r u_z^0(-h_0) + \int_0^{-h_0}\int_0^s T_z^0(t,\varphi,z,s)\,ds\,d\rho\right)\right]dr$$

$$+\int_0^{-h_0}\left(u_r^0 - r\partial_\varphi u_\varphi^0\right)dr.$$

This is again an elliptic equation for p^1 with a rather complicated right hand side that depends only on the zeroth order solutions and the boundary conditions. The velocities u_r^0, u_φ^0 and u_z^0 can also be computed in terms of p_0. After some computations we obtain a right hand side that only depends on p_0, film thickness, and the boundary conditions

$$\delta^2\partial_\varphi^2 p^1 + \delta^2\frac{3\partial_\varphi h_0}{h_0}\partial_\varphi p^1 + \partial_z^2 p^1 = \Psi(p^0,h^0,h^1,V_\varphi^0,V_\varphi^1). \tag{5.86}$$

The the complete formula for Ψ is given in Appendix E.2. In the right hand side of this equation there appear time derivatives of h_0 and p^0. The time derivative of h_0 can easily be computed from (5.21) while the time derivative of the pressure needs the solution of an auxiliary partial differential equation. Differentiating the classical Reynolds equation (5.79) with respect to time we obtain

$$\delta^2\partial_\varphi^2\partial_t p^0 + \delta^2\frac{3\partial_\varphi h_0}{h_0}\partial_\varphi\partial_t p^0 + \partial_z^2\partial_t p^0 = -12\partial_t\left(\frac{(V_r^0 + \frac{1}{2}V_\varphi^0\partial_\varphi h_0)}{h_0^3}\right) \tag{5.87}$$

$$-\delta^2\partial_\varphi p^0(\frac{3\partial_\varphi\partial_t h_0}{h} + \frac{\partial_t h_0\partial_\varphi h_0}{h_0^2}).$$

This equation involves the same differential operator as Equations 5.79 and 5.86 and a modified right hand side with known lower order terms. To summarize the previous considerations we formulate the following statement.

Statement 5.3. *The pressure distribution in a circular hydrodynamic bearing with lubrication film thickness $h_0 = 1 - \kappa \cos \varphi$ is determined by three equations with the same differential operator*

$$L(\cdot) = \delta^2 \partial_\varphi^2(\cdot) + \delta^2 \frac{3\partial_\varphi h_0}{h_0} \partial_\varphi(\cdot) + \partial_z^2(\cdot), \tag{5.88}$$

and varying right hand sides

$$\varepsilon^0: \qquad\qquad L(p^0) = f_0(\kappa, \dot{\kappa}, \dot{\gamma}), \tag{5.89}$$

$$\varepsilon^1: \qquad\qquad L(p^1) = \Psi(\kappa, \dot{\kappa}, \dot{\gamma}, \ddot{\kappa}, \ddot{\gamma}, p^0, \nabla p^0, \nabla^2 p^0, \nabla^3 p^0, \nabla^2(\partial_t p^0)), \tag{5.90}$$

$$where \qquad L(\partial_t p^0) = \partial_t f_0 - \delta^2 \partial_\varphi p^0 \left(\frac{3\partial_\varphi \partial_t h_0}{h} + \frac{\partial_t h_0 \partial_\varphi h_0}{h_0^2}\right). \tag{5.91}$$

Here the p_i are scalar functions defined on $\Omega = (0,1) \times (0,2\pi)$. The boundary conditions are

$$p^i(\varphi, 0) = p^i(\varphi, 1) = 0 \qquad\qquad for\ \varphi \in (0, 2\pi), \tag{5.92}$$

$$p^i(0, z) = p^i(2\pi, z) \qquad\qquad for\ z \in (0, 1). \tag{5.93}$$

The parameters κ, γ, $\dot{\kappa}$, $\dot{\gamma}$, etc. are given by the current shaft position and velocity in polar coordinates. The function f_0 is given in Eq. (5.79), while a detailed expression for Ψ can be found in the Appendix E.2. The pressure distribution p^0 is called the zeroth order solution and correspondes to point 1 in the list in Section 5.1. The pressure distribution p^1 is called the inertia correction and we call $p = p^0 + \varepsilon p^1$ the first order solution to Reynolds' equation, corresponding to point 3 in the list.

The fact that we need the same differential operator in equations (5.89)-(5.91) simplifies the numerical solution because we only need one discretization. Furthermore we have to compute L^{-1} only once and can apply it subsequently to the three different right hand sides.

In Figure 5.8 we exemplarily depict different inertia corrected solutions $p^0 + \varepsilon p^1$. Compared to the corrections in the short bearing case (cf. Fig. 5.6) the corrections in this case are small. For both cases of W the geometry is very similar to the zeroth order case. In Section 5.6 we thoroughly compare the different pressure distributions and also give some numerical data that shows the convergence of the short bearing approximation to the solution of the full Reynolds equation in zeroth and first order.
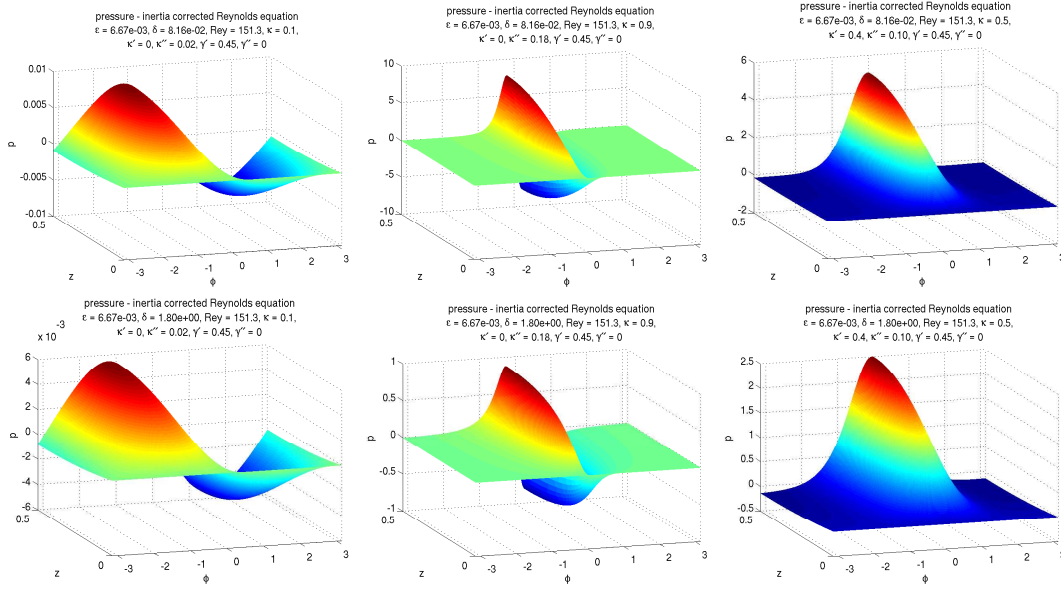
Figure 5.8: Inertia corrected solutions $p^0 + \varepsilon p^1$ of Reynolds equation for varying values of κ, $\dot{\kappa}$, and W; upper line: $W = 0.25$, lower line: $W = 5.4$; left: $\kappa = 0.1$, $\dot{\kappa} = 0$, middle: $\kappa = 0.9$, $\dot{\kappa} = 0$, right: $\kappa = 0.9$, $\dot{\kappa} = 0$.

5.1.7 Remark on Existence and Regularity

The existence of a weak solution of Reynolds' equation (5.79) is guaranteed by applying the Lax-Milgram Lemma to the continuous bilinear form

$$a : H \times H \rightarrow \mathbb{R}, \tag{5.94}$$

$$a(u, v) = \int_{\Omega} h_0^3 (\delta^2 \partial_\varphi u \partial_\varphi v + \partial_z u \partial_z v), \tag{5.95}$$

where u and v belong to the Hilbert space

$$H = H_{per}^{1,2} \cap \{f \mid T_{\Gamma_2} f = 0\} \tag{5.96}$$

with T_{Γ_2} being the trace operator onto the Dirichlet boundary

$$\Gamma_2 = \{(\varphi, z) \in \partial \Omega \mid z \in \{0, 1\}, \; \varphi \in [0, 2\pi]\}. \tag{5.97}$$

The film thickness h_0 is in $C^\infty(\bar{\Omega})$ and we have $0 < h_0 < 2$ on the whole of $\bar{\Omega}$, assuring continuity. Since on one part of the boundary the functions of H have prescribed value, the Poincaré inequality

$$\|u\|_{L^2} \leq C \|\partial_z u\|_{L^2} \leq C \|\nabla u\|_{L^2} \tag{5.98}$$

holds and the coercitivity $\beta \|u\|_{L^2}^2 \leq a(u, u)$ of the bilinear form is assured.

The right hand sides of the Reynolds' equations for the time derivative $\partial_t p_0$ and for the first order correction p_1 involve higher order derivatives of the zeroth order solution

p_0. Therefore some regularity considerations are required. The coefficient h_0 is in $C^\infty(\Omega)$ which gives us all the interior regularity we need (Evans, 1998). Because we can continuate it periodically, the Dirichlet boundary at $z = 0$ and $z = 1$ is in C^∞, so we also have regularity up to the boundary.

5.2   Phenomenological Correction of Pressure Function

In Section 5.1 we derived four bearing theories from first principles by asymptotic expansions of the Navier-Stokes equations. In Chapter 6 we see that simulations which only use the zeroth order approximations for the pressure do not reproduce the frequency of the oil whirl as observed in the experiments. The inertia corrections yield a small effect and lead to a reduced whirl frequency. However, the observed effect is still small compared to the experimental result. In the following we describe a simple fifth bearing model that is used to examine the influence of the pressure function on the whirl frequency. It is obtained by the following phenomenological considerations.

The pressure distribution of the short bearing solution is

$$\bar{p}^0 = -6\frac{\bar{z}}{W}\left(\frac{\bar{z}}{W} - 1\right)\frac{W^2\rho\nu}{c_r^2}\frac{\left((\dot{\gamma} - \frac{\omega}{2})\kappa\sin\varphi + \dot{\kappa}'\cos\varphi\right)}{(1 - \kappa\cos\varphi)^3}. \tag{5.99}$$

for $z \in [0, W]$. Using this pressure function in the calculation of the bearing forces during numerical integration of the equation of motion of the rotor, we observe a subharmonic instability with a frequency of approximately $\frac{\omega}{2}$.

To test the influence of the term $G = (\dot{\gamma} - \frac{\omega}{2})$ in the expression for p^0 on the frequency of the self excited oscillation we modify the term G and use the term

$$\tilde{G} = \left(\dot{\gamma} - \frac{\omega}{2} + s(\omega)\right) \tag{5.100}$$

instead. The shift function s has a strong influence on the subharmonic frequency. A linear term $s = \sigma\omega$ with $\sigma \in [0, \frac{1}{2}]$ leads to a linear frequency shift, while the correction function $s(\omega) = \sigma\omega^2$ introduces a quadratic dependence on ω into the pressure function. By tuning the coefficient σ it is possible to control the shift. Using the modified pressure distribution

$$\bar{p}^0 = -6\frac{\bar{z}}{W}\left(\frac{\bar{z}}{W} - 1\right)\frac{W^2\rho\nu}{c_r^2}\frac{\left((\dot{\gamma} - \frac{\omega}{2} + s(\omega))\kappa\sin\varphi + \dot{\kappa}'\cos\varphi\right)}{(1 - \kappa\cos\varphi)^3}, \tag{5.101}$$

to calculate the bearing reaction forces, the experimentally observed nonlinear frequency shift can be observed also in the numerical simulations shown in Chapter 6. Figure 5.9 depicts three pressure distributions for varying values of κ and $\dot{\kappa}$ for illustration. In Section 5.6 we compare this pressure distribution and the resulting bearing forces to the usual short-bearing approximation.
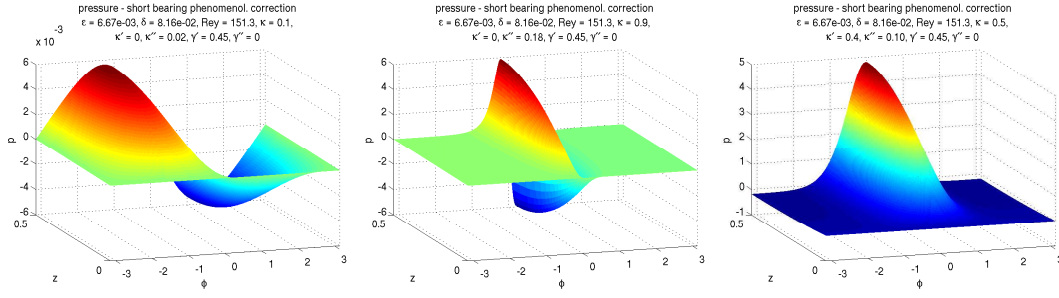
Figure 5.9: Phenomenologically corrected short bearing pressure distributions p_0 for varying values of κ and $\dot{\kappa}$; left: $\kappa = 0.1$, $\dot{\kappa} = 0$, middle: $\kappa = 0.9$, $\dot{\kappa} = 0$, right: $\kappa = 0.5$, $\dot{\kappa} = 0.4$.

The structure of the term G is explained in (Crandall, 1995). Recall the derivation of Reynolds' equation (cf. Sec. 5.1.4) where we obtained as principal flow pattern a Couette flow with a linear velocity profile growing from 0 on the bearing casing to $R\omega$ on the shaft. Integration of the continuity equation (5.26) over the radial coordinate and using the expression (5.38) for u_z^0 yields

$$
\begin{aligned}
-V_r^0 &= \int_0^{-h_0(\varphi)} \partial_\varphi u_\varphi^0(r,\varphi)\, dr + \int_0^{-h_0(\varphi)} \partial_z u_z^0(r,\varphi,z)\, dr \\
&= \partial_\varphi \int_0^{-h_0(\varphi)} u_\varphi^0(r,\varphi)\, dr + u(-h_0(\varphi),\varphi)\partial_\varphi h_0(\varphi) + \frac{h_0^3}{12}\partial_z^2 p^0 \\
&= -\partial_\varphi(h_0(\varphi)\overline{u_\varphi^0(\varphi)}) + V_\varphi^0 \partial_\varphi h_0(\varphi) + \frac{h_0^3}{12}\partial_z^2 p^0 \\
&= (V_\varphi^0 - \overline{u_\varphi^0(\varphi)})\partial_\varphi h_0(\varphi) - h_0(\varphi)\partial_\varphi \overline{u_\varphi^0(\varphi)} + \frac{h_0^3}{12}\partial_z^2 p^0,
\end{aligned}
$$

where $\overline{u_\varphi(\varphi)}$ is the radially averaged circumferential lubricant velocity.

In Section 5.1.1 we have rescaled time such that the angular velocity is of order $O(1)$. In order to show the appearance of the $\omega/2$-term, in the following paragraphs we go back to dimensionalized time. Hence $V_\varphi^0 = \omega$ and $V_r^0 = -\omega\kappa\sin\varphi + \dot{\kappa}\cos\varphi + \kappa\dot{\gamma}\sin\varphi$. Integration over z yields

$$
\begin{aligned}
p^0 &= \frac{6z(z-1)}{h^3}\left(-V_r^0 + (\overline{u_\varphi^0(\varphi)} - V_\varphi^0)\partial_\varphi h(\varphi) + h(\varphi)\partial_\varphi \overline{u_\varphi^0(\varphi)}\right) \\
&= \frac{6z(z-1)}{h^3}\left(\omega\kappa\sin\varphi - \dot{\kappa}\cos\varphi - \kappa\dot{\gamma}\sin\varphi + (\overline{u_\varphi^0(\varphi)} - \omega)\kappa\sin\varphi\right. \\
&\qquad\qquad \left. + (1 - \kappa\cos\varphi)\partial_\varphi \overline{u_\varphi^0(\varphi)}\right) \\
&= \frac{6z(z-1)}{h^3}\left((\overline{u_\varphi^0(\varphi)} - \dot{\gamma})\kappa\sin\varphi - \dot{\kappa}\cos\varphi + (1 - \kappa\cos\varphi)\partial_\varphi \overline{u_\varphi^0(\varphi)}\right). \quad (5.102)
\end{aligned}
$$

In the short bearing approximation the circumferential velocity has a linear Couette profile (cf. Eq. (5.37)) which rises from zero velocity on the casing to $V_\varphi^0 = \omega$ on the shaft

$$u_\varphi = \frac{r}{h(\phi)}\omega, \tag{5.103}$$

and hence the radially averaged circumferential velocity is

$$\overline{u_\varphi^0(\varphi)} = \frac{1}{2}\omega \tag{5.104}$$

and does not depend on φ. Therefore the last term in (5.102) vanishes and we get

$$p^0 = \frac{-6z(z-1)}{h^3}\left((\dot\gamma - \frac{\omega}{2})\kappa \sin\varphi + \dot\kappa \cos\varphi\right). \tag{5.105}$$

In (Muszynska, 1986; Muszynska, 1987; Muszynska, 1988) the fluid average circumferential velocity is identified as an important parameter for the onset and the frequency of the oil whirl. Experimental results are given which show a decrease of the average circumferential velocity for large eccentricities of the shaft. Hence

$$\tilde{G} = (\dot\gamma - \frac{\omega}{2} + s(\omega)) \tag{5.106}$$

can be interpreted as a direct change of the lubricants average circumferential velocity.

In Chapter 6 we see that this manipulation of the term $G = (\gamma' - \frac{1}{2})$ leads to a change in the subharmonic response frequency. This observation is also the motivation for the derivation of the inertia correction. As shown in Section 5.1.5 the inclusion of first order corrections leads to an ω^2-dependence of the pressure and hence the bearing forces.

5.3   Alternative Bearing Models

Several other modifications of the bearing model were also tested for their ability to reproduce the experimental results, especially the frequency shift of the oil whirl. As the simulations in Chapter 6 show, it was not possible to reproduce the shift by any of them. We describe them here for completeness.

5.3.1   The Finite Bearing

In the short bearing theory the axial pressure distribution is approximated by a parabolic profile of order 2. Another possibility is to assume a separation of the variables and approximate the axial pressure distribution by a parabolic function of order m (Inagaki, 2002):

$$p(\varphi, \zeta) = (1 - (2\zeta - 1)^m)v(\varphi). \tag{5.107}$$

If we plug this into equation (5.79) and integrate both sides with respect to ζ from 0 to 1, we obtain

$$\delta^2 \frac{m}{m+1}\left(3h^2 h_\varphi v_\varphi + h^3 v_{\varphi\varphi}\right) - 4mh^3 v = -12\left(G\sin\varphi + E\cos\varphi\right), \tag{5.108}$$

where we set $E = \kappa'$ and $G = \kappa(\gamma' - \frac{1}{2})$. It is possible to simplify this equation by setting $w = h^2 v$. Inserting this into equation (5.108) one gets:

$$hw_{\varphi\varphi} - h_\varphi w_\varphi - (2h_{\varphi\varphi} + ah)w = -12b\left(G\sin\varphi + E\cos\varphi\right), \tag{5.109}$$

where $a = 4\frac{(m+1)}{\delta^2}$ and $b = \frac{(m+1)}{m\delta^2}$. Expanding w into a Fourier series and neglecting terms of order 3 and higher one gets an approximation of the solution:

$$w = \sum_{n=0}^{2} K_n \cos(n\varphi) + \sum_{n=1}^{2} C_n \sin(n\varphi), \tag{5.110}$$

where

$$
\begin{aligned}
K_0 &= \frac{-24\kappa bE}{3a\kappa^2 - 4a - 4 - 6\kappa^2}, \\
K_1 &= \frac{-48bE}{3a\kappa^2 - 4a - 4 - 6\kappa^2} = \frac{2}{\kappa}K_0, \\
K_2 &= \frac{-24\kappa bE(a-2)}{(3a\kappa^2 - 4a - 4 - 6\kappa^2)(a+4)} = K_0\frac{(a-2)}{(a+4)}, \\
C_1 &= \frac{-48bG}{a\kappa^2 - 4a - 2\kappa^2 - 4}, \\
C_2 &= \frac{-24\kappa bG(a-2)}{(a\kappa^2 - 4a - 2\kappa^2 - 4)(a+4)} = \frac{\kappa}{2}C_1\frac{(a-2)}{(a+4)}.
\end{aligned}
$$

Having this, the approximate pressure function is

$$p = (1 - (2\zeta - 1)^m)\frac{w}{h^2}. \tag{5.111}$$

Figure 5.10 show the pressure distributions for varying values of κ, $\dot{\kappa}$, and W. The geometry is most notably different for small eccentricities ($\kappa = 0.1$). In Section 5.6 we compare the resulting forces. The finite bearing approximation proposed here underestimates the pressure in most cases, leading to too small bearing forces. This is due to the large error made by truncating the Fourier series. This approximation is therefore not considered in the numerical simulations in Chapter 6.

5.3.2 Reynolds' Boundary Conditions

In the calculation of the bearing forces in Section 5.5 the so-called Gümbel boundary conditions are used. They provide a simple cavitation model by setting the pressure to zero where negative pressure occurs. In our search for an oilfilm model that reproduces the frequency shift the use of these simplified boundary conditions appeared
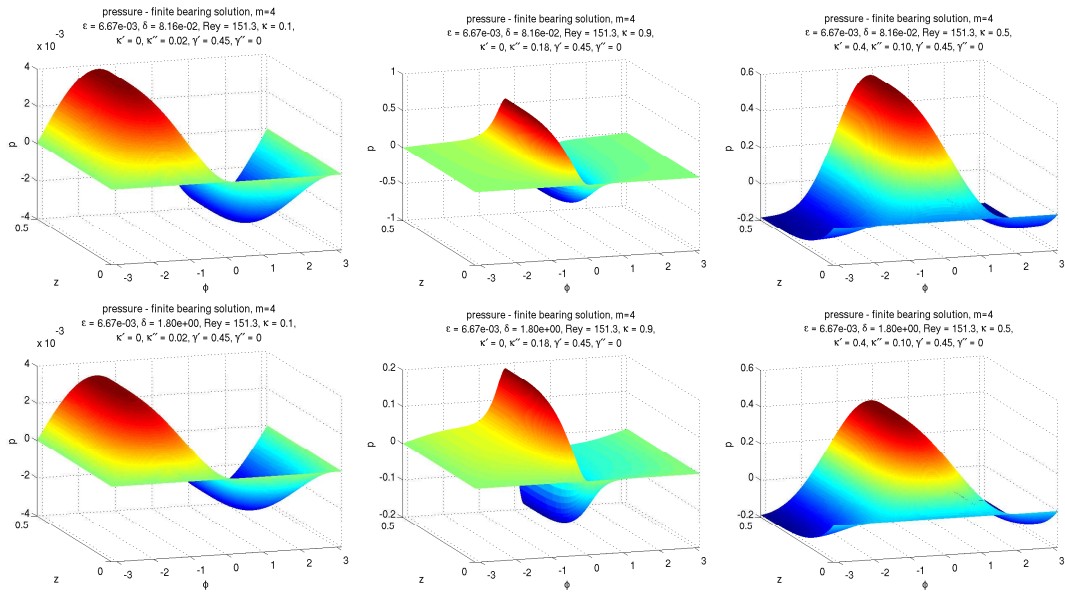
Figure 5.10: Finite bearing pressure distributions p_0 for varying values of κ, $\dot{\kappa}$, and W; upper line: $W = 0.25$, lower line: $W = 5.4$; left: $\kappa = 0.1$, $\dot{\kappa} = 0$, middle: $\kappa = 0.9$, $\dot{\kappa} = 0$, right: $\kappa = 0.5$, $\dot{\kappa} = 0.4$.

to be another possible explanation. A more realistic cavitation model is given by Reynolds' boundary conditions (Yamamoto & Ishida, 2001). So we reformulate the nondimensional Reynolds' equation (5.79)

$$\delta^2 \partial_\varphi \left(h^3 \partial_\varphi \bar{p} \right) + \partial_\zeta \left(h^3 \partial_\zeta \bar{p} \right) = -12 \left((\gamma' - \frac{1}{2}) \kappa \sin \varphi + \kappa' \cos \varphi \right) \qquad (5.112)$$

using Reynolds' boundary conditions

$$p(0, z) = p(2\pi, \zeta) \quad \forall \zeta \in [0, 1], \qquad (5.113)$$

$$p(\varphi, 0) = p(\varphi, 1) = 0 \quad \forall \varphi \in [0, 2\pi], \qquad (5.114)$$

$$p \geq 0, \qquad (5.115)$$

which leads to a free boundary problem for the pressure. The third boundary condition is responsible for the free boundary problem structure because it does not fix the point of oilfilm rupture.

This kind of problem can be solved numerically by a projection method like projective successive overrelaxation (PSOR) (Deuflhard & Hohmann, 1993). Simply spoken, in this method one computes the solution for the unconstrained problem and then projects the solution on the subspace containing the feasible functions, that is the subspace of positive functions in our case. In Section 5.4.1.3 we describe the method in detail and give the appropriate choice of iteration matrices which assure convergence. In Figure 5.11 the pressure distribution is again shown for varying parameter values.
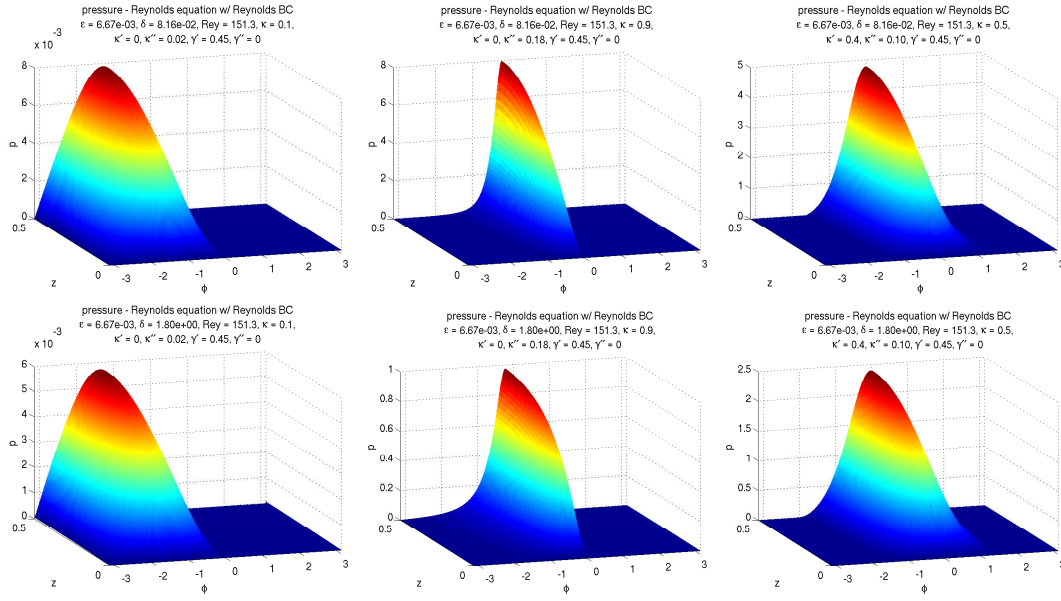
Figure 5.11: Pressure distributions p_0 computed with Reynolds' boundary conditions for varying values of κ, $\dot{\kappa}$, and W; upper line: $W = 0.25$, lower line: $W = 5.4$; left: $\kappa = 0.1$, $\dot{\kappa} = 0$, middle: $\kappa = 0.9$, $\dot{\kappa} = 0$, right: $\kappa = 0.5$, $\dot{\kappa} = 0.4$.

5.4 Numerical Schemes for Reynolds' Equation

In the previous section a variety of different bearing models were given. For some of them it is possible to give analytical solutions, e.g. for the short bearing approximation (5.47). Others involve the solution of partial differential equations, i.e. Reynolds' equation with different right hand sides for the zeroth and first order approximation (5.79) and (5.86) and the iterative solution of this equation with other boundary conditions by the PSOR method in section 5.3.2. In this work three different methods have been used to solve these PDEs which we will describe in the following. The differential operator in all three cases is given by

$$\tilde{L}(\cdot) = \delta^2 \partial_\varphi \left(h_0^3(\varphi) \partial_\varphi(\cdot) \right) + h_0^3(\varphi) \partial_z^2(\cdot). \tag{5.116}$$

The operator $\tilde{L}$ above is given in divergence form and therefore useful in the weak formulation of the problem which is used later for the finite element discretization. The software package `deal.II` (Bangerth *et al.*, 2007; Bangerth *et al.*, 2008) is used for the discretization and the setup of the linear equations.

The film thickness h_0 depends only on the circumferential angle φ. Therefore we can also divide $\tilde{L}$ by h_0^3 and by δ^2 to obtain the operator L which allows for an easier discretization by finite differences

$$L(\cdot) = \partial_\varphi^2(\cdot) + \frac{1}{\delta^2} \partial_z^2(\cdot) + \frac{3\partial_\varphi h_0}{h_0} \partial_\varphi(\cdot). \tag{5.117}$$

5.4.1 Finite Differences for Reynolds' Equation

5.4.1.1 5-point Laplacian and Second Order Approximation

A very simple discretization of L can be calculated by applying the five-point discretization of the Laplace operator and central differences for the first order derivative. We obtain

$$
\delta^2 \frac{3\kappa \sin \varphi_i}{1 - \kappa \cos \varphi_i} \frac{1}{2\Delta_\varphi} \Big(p(\varphi_{i+1}, \zeta_j) - p(\varphi_{i-1}, \zeta_j) \Big)
$$

$$
+ \quad \delta^2 \frac{1}{\Delta_\varphi^2} \Big(p(\varphi_{i+1}, \zeta_j) + p(\varphi_{i-1}, \zeta_j) - 2p(\varphi_i, \zeta_j) \Big)
$$

$$
+ \quad \frac{1}{\Delta_\zeta^2} \Big(p(\varphi_i, \zeta_{j+1}) + p(\varphi_i, \zeta_{j-1}) - 2p(\varphi_i, \zeta_j) \Big)
$$

$$
= \quad \frac{-12\Big((\gamma' - \frac{1}{2})\kappa \sin \varphi_i + \kappa' \cos \varphi_i\Big)}{(1 - \kappa \cos \varphi_i)^3}, \tag{5.118}
$$

where $\varphi_i = i\Delta_\varphi$, $i = 1, \ldots, N$ and $\varphi\zeta = j\Delta_\zeta$, $j = 1, \ldots, M$.

We set

$$
p_{i,j} = p(\varphi_i, \zeta_j),
$$

$$
g_i = \frac{3\kappa \sin \varphi_i}{1 - \kappa \cos \varphi_i},
$$

$$
f_i = \frac{1}{\delta^2} \frac{-12\Big((\gamma' - \frac{1}{2})\kappa \sin \varphi_i + \kappa' \cos \varphi_i\Big)}{(1 - \kappa \cos \varphi_i)^3},
$$

and

$$
d = \frac{\Delta_\varphi^2}{\Delta_\zeta^2 \delta^2}.
$$

From this we get

$$
\frac{1}{\Delta_\varphi^2}(p_{i+1,j} + p_{i-1,j} + d(p_{i,j+1} + p_{i,j-1}) - 2(1 + d)p_{i,j}) + \frac{1}{2\Delta_\varphi} g_i(p_{i+1,j} - p_{i-1,j}) = f_i.
$$

The periodic boundary condition $p(0, z) = p(2\pi, z)$ leads to the following special relations:

$$
\partial_\varphi p_{1,j} \quad \approx \quad \frac{1}{2\Delta_\varphi}(p_{2,j} - p_{N,j}),
$$

$$
\partial_\varphi p_{N,j} \quad \approx \quad \frac{1}{2\Delta_\varphi}(p_{1,j} - p_{N-1,j}).
$$

So the discretized equation can be written in matrix form as

$$
Cp = Ap + \Delta_\varphi Bp = F \tag{5.119}
$$

with

$$A = \begin{pmatrix} L_1 & dI & & \\ dI & L_1 & \ddots & \\ & \ddots & \ddots & dI \\ & & dI & L_1 \end{pmatrix}, \text{ where } L_1 = \begin{pmatrix} -2-2d & 1 & & 1 \\ 1 & \ddots & \ddots & \\ & \ddots & \ddots & 1 \\ 1 & & 1 & -2-2d \end{pmatrix},$$

$$B = \frac{1}{2}\begin{pmatrix} L_2 & & & \\ & L_2 & & \\ & & \ddots & \\ & & & L_2 \end{pmatrix}, \text{ where } L_2 = \begin{pmatrix} g_1 & & & \\ & g_2 & & \\ & & \ddots & \\ & & & g_{N-1} \end{pmatrix} \cdot \begin{pmatrix} 0 & 1 & & -1 \\ -1 & 0 & \ddots & \\ & \ddots & \ddots & 1 \\ 1 & & -1 & 0 \end{pmatrix},$$

and $(f_1, \dots, f_N)$ M-times repeated to form the right hand side

$$F = \Delta_\varphi^2 (f_1, \dots, f_N, \dots, f1, \dots, f_N)^T.$$

Since the 5-point-Laplacian and the central differences both are second order approximations this discretization also is of second order.

5.4.1.2   9-point-Laplacian and 4th Order Approximation

The 9-point-Laplacian on a uniform grid with step-size h

$$\Delta_h^{(9)} u_h = \frac{1}{6h^2} \left(4u_{i\pm1,j} + 4u_{i,j\pm1} + u_{i\pm1,j\pm1} - 20u_{i,j} \right) \tag{5.120}$$

yields a fourth order approximation for the Poisson equation after a modification of the right hand side (Rannacher, 2000) using the well known 5-point Laplacian

$$\tilde{f} = f + \frac{1}{12} h^2 \Delta_h^{(5)} f. \tag{5.121}$$

To apply this to a discretization of the differential operator L of Reynolds' equation (5.117) with different step-sizes h_1 and h_2 in each direction we modify the discretization. We set

$$L_1 = \theta p_{i,j} + \alpha p_{i\pm1,j} + \beta p_{i,j\pm1} + \gamma p_{i\pm1,j\pm1} \tag{5.122}$$

with

$$\gamma = \frac{h_1^2 + \delta^2 h_2^2}{12\delta^2 h_1^2 h_2^2}, \tag{5.123}$$

$$\alpha = \frac{1 - 2\gamma h_1^2}{h_1^2}, \tag{5.124}$$

$$\beta = \frac{1 - 2\gamma h_2^2 \delta^2}{h_2^2 \delta^2}, \tag{5.125}$$

$$\theta = -2(\alpha + \beta + 2\gamma). \tag{5.126}$$

Furthermore we set

$$L_2 = \frac{g_i}{12h_1} \left(p_{i-2,j} - 8p_{i-1,j} + 8p_{i+1,j} - p_{i+2,j} \right), \tag{5.127}$$

where $g_i = \frac{3\partial_\varphi h_0(\varphi_i)}{h_0(\varphi_i)}$, and

$$L_3 = \frac{1}{12} \left(-4p_{i,j} + p_{i\pm 1,j} + p_{i,j\pm 1} \right) \tag{5.128}$$

to come to the following result.

Proposition 5.4. *Let p be the solution of*

$$L(p) = F \tag{5.129}$$

where L is given by (5.117) and $F = \frac{f}{\delta^2 h_0^3}$. We then have

$$L_1 p + (I - L_3)L_2 p - (I - L_3)F = O(h^4), \tag{5.130}$$

i.e. the consistency order is $\tau = 4$.

Proof. Taylor expansion and substitution of Equation (5.129) show that

$$L_1 p = \partial_\varphi^2 p + \frac{1}{\delta^2} \partial_z^2 p + \frac{1}{12}(h_1^2 \partial_\varphi^2 + h_2^2 \partial_z^2)(F - g\partial_\varphi p) + O(4), \tag{5.131}$$

$$L_2 p = g\partial_\varphi p + O(4). \tag{5.132}$$

Furthermore, for any $\pi \in C^4$ we have

$$L_3 \pi = \frac{1}{12}(h_1^2 \partial_\varphi^2 + h_2^2 \partial_z^2)\pi + O(4). \tag{5.133}$$

Hence the result follows.   □

The computational effort can be reduced by using the symmetry in the z-direction. We take Dirichlet conditions at $z = 0$ and symmetry conditions at $z = \frac{1}{2}$. In the φ-direction we take periodic boundary conditions. The vector of unknowns is

$$p = (p_{0,1}, p_{1,1}, \ldots, p_{N-1,1}, p_{0,2}, \ldots, p_{N-1,M})^T \tag{5.134}$$

where the first index i of $p_{i,j}$ stands corresponds to the grid in φ-direction and the second index to the grid in z-direction. Using the above scheme we obtain the following system matrices

$$L_1 = \begin{pmatrix} A & B & & \\ B & A & \ddots & \\ & \ddots & \ddots & B \\ & & 2B & A \end{pmatrix}, \tag{5.135}$$

where

$$
A = \begin{pmatrix} \theta & \alpha & & \alpha \\ \alpha & \theta & \ddots & \\ & \ddots & \ddots & \alpha \\ \alpha & & \alpha & \theta \end{pmatrix}, \quad \text{and} \quad B = \begin{pmatrix} \beta & \gamma & & \gamma \\ \gamma & \beta & \ddots & \\ & \ddots & \ddots & \gamma \\ \gamma & & \gamma & \beta \end{pmatrix},
$$

and

$$
L_2 = \frac{1}{12h_1} Id_M \otimes C, \tag{5.136}
$$

where

$$
C = \begin{pmatrix} g_1 & & & \\ & g_2 & & \\ & & \ddots & \\ & & & g_{N-1} \end{pmatrix} \cdot \begin{pmatrix} 0 & 8 & -1 & & 1 & -8 \\ -8 & 0 & 8 & -1 & & 1 \\ & \ddots & \ddots & \ddots & \ddots & \\ 8 & -1 & & 1 & 8 & 0 \end{pmatrix},
$$

and

$$
(I - L_3) = \frac{1}{12} \begin{pmatrix} D & Id_N & & Id_N \\ Id_N & D & \ddots & \\ & \ddots & \ddots & Id_N \\ & & 2Id_N & D \end{pmatrix}, \quad \text{where } D = \begin{pmatrix} 8 & 1 & & 1 \\ 1 & 8 & \ddots & \\ & \ddots & \ddots & 1 \\ 1 & & 1 & 8 \end{pmatrix}.
$$

As already mentioned in the derivation (cf. Section 5.1.6), the solution of Reynolds' equation and its inertia correction requires the solution of three PDEs with identical differential operator and varying right hand side. Therefore it is advantageous to use a direct solution method like LU-decomposition for the corresponding linear equation, since the decomposition of the system matrix can be stored and used three times consecutively. In our case we use the LU-decomposition for sparse matrices which is implemented in the software package UMFPACK (Davis, 2004; Davis, 2007) and which is included in MATLAB. Comparison with iterative methods like `bicgstab` or `gmres` showed a slight advantage of the sparse LU-decomposition in the required computational time.

In the solution process the matrices for the discretized operator L_1, L_2, and L_3 are set up and the LU-decomposition is computed. Then the solution p^0 of the zeroth order of Reynolds' equation is computed with the right hand side

$$
f_0 = \frac{-12\left((\gamma' - \frac{1}{2})\kappa \sin \varphi_i + \kappa' \cos \varphi\right)}{\delta^2 h_0^3}. \tag{5.137}
$$

The right hand side of the equation for $\partial_t p^0$ involves spatial derivatives of p^0 (cf. (5.87)) and the one for p^1 involves higher order derivatives of p^0 and of $\partial_t p_0$ (cf. (E.9)).

Due to the periodicity of the solution we can compute higher order approximations of the φ-derivatives also at the boundary by prolongation. In order to compute the z-derivatives, we use the differential equation to calculate second order derivatives, while the first and third derivative are computed by finite differences.

The solution of the linear equations give an approximation to the pressure distribution

$$p = p^0 + \varepsilon p^1. \tag{5.138}$$

The resulting forces on the rotating shaft are computed by numerical integration of the pressure distribution.

5.4.1.3   Projection Method for Constrained Problem

In Section 5.3.2 the positivity contstraints to Reynolds' equation known as Reynolds' boundary conditions are introduced as an alternative bearing model. The projective successive overrelaxation method (PSOR) can be used to solve this free boundary problem (Deuflhard & Hohmann, 1993). The PSOR algorithm for the constrained problem works as follows. The matrix $C = A + \Delta_\varphi B$ from Eq. (5.119) is decomposed into a diagonal, a lower and an upper triangular matrix $C = D + L + R$. We set $Q = D + \rho L$, $S = (1 - \rho)D - \rho R$ and $\tilde{F} = \rho F$. In every iteration step k we solve:

$$Q\tilde{p}^k = Sp^{k-1} + \tilde{F}, \tag{5.139}$$
$$p^k = \max(\tilde{p}^k, 0), \tag{5.140}$$

where the first step is the usual successive overrelaxation step and the second step is the projection on the subspace of positive functions. For a choice of $\rho \in [1, 2]$ this procedure converges to the solution of the free boundary problem because the SOR converges (Deuflhard & Hohmann, 1993) and the projection does not increase the spectral radius of the iteration mapping. Due to the fact that we have to solve the free boundary problem in every time step the numerical integration becomes very slow. The simulation results in Chapter 6 show no significant effect on the frequency of the self-excited oscillation.

5.4.2   Finite Element Approximation

The pressure distribution inside the bearings shows large variations in the circumferential φ-direction in a small interval around $\varphi = 0$ and almost no variation elsewhere. In order to resolve this with finite differences a very small stepsize has to be chosen, which increases the computational cost. To overcome this problem a finite element approach with local refinement is used alternatively to improve the speed of the calculations. The theory of finite elements for elliptic equations is well developed and can be found in textbooks like (Braess, 2007; Ciarlet, 1978; Brenner & Scott, 1994; Strang &

Fix, 1973) or in (Rannacher, 2000). We use the finite element software library `deal.II` (Bangerth *et al.*, 2007; Bangerth *et al.*, 2008).

The weak formulations of the three Reynolds equations for zeroth order pressure p^0 (derived from Eq. (5.79)), its time derivative $\partial_t p^0$ (from (5.87)), and first order pressure p^1 (cf. (5.85)) are

$$-\iint_\Omega \frac{1}{12} h_0^3 \tilde{\nabla} p^0 \tilde{\nabla} \psi \, d\varphi \, dz \qquad = -\iint_\Omega f \psi \, d\varphi \, dz, \tag{5.141}$$

$$-\iint_\Omega \frac{1}{12} h_0^3 \tilde{\nabla} \partial_t p^0 \tilde{\nabla} \psi \, d\varphi \, dz \qquad = -\iint_\Omega \partial_t f \psi \, d\varphi \, dz + \iint_\Omega \partial_t h_0^3 \tilde{\nabla} p^0 \tilde{\nabla} \psi \, d\varphi \, dz, \tag{5.142}$$

$$-\iint_\Omega \frac{1}{12} h_0^3 \tilde{\nabla} p^1 \tilde{\nabla} \psi \, d\varphi \, dz \qquad = \iint_\Omega \left(-W_0 \psi + W_\varphi \partial_\varphi \psi + W_z \partial_z \psi \right) d\varphi \, dz, \tag{5.143}$$

where

$$W_0 = h_1 \partial_r u_r^0(-h_0) + \partial_\varphi h_0 \left(V_\varphi^1 + h_1 \partial_r u_\varphi(-h_0) \right) - u_r^0 + r \partial_\varphi u_v p h^0,$$

$$W_\varphi = \int_0^{-h_0} \int_0^r \int_0^s T_\varphi^0(\rho, \varphi, z) \, d\rho \, ds \, dr + \frac{1}{2} h_0 \left(-V_\varphi^1 - h_1 \partial_r u_\varphi(-h_0) + \int_0^{-h_0} \int_0^r T_\varphi^0(\rho, \varphi, z) \, d\rho \, dr \right),$$

$$W_z = \int_0^{-h_0} \int_0^r \int_0^s T_z^0(\rho, \varphi, z) \, d\rho \, ds \, dr + \frac{1}{2} h_0 \left(-h_1 \partial_r u_z(-h_0) + \int_0^{-h_0} \int_0^r T_z^0(\rho, \varphi, z) \, d\rho \, dr \right).$$

Here we use the notations from Section 5.1.6 and additionally $\tilde{\nabla}$ denotes the operator $\tilde{\nabla} = (\frac{1}{\delta} \partial_\varphi, \partial_z)^T$. ψ is a test function.

In `deal.II` we use second order quadratic elements and Gaussian quadrature with 3 quadrature points in each direction. The local refinement is done following a-posteriori error estimation with the built-in Kelly-estimator which measures the local error of the solution of the Poisson problem by integrating over the jump of the gradients along the faces of each cell (Bangerth *et al.*, 2008). The treatment of the periodic boundary conditions is not trivial since it must be kept track of the hanging nodes at different levels of refinement along periodic boundary. This is done following the suggestions of (Bangerth, 2002) by recursively checking the refinement of adjacent elements along the periodic boundary and interpolating hanging nodes in case of different refinement levels.

We want to use the same discretization of the differential operator for the three different equations. Therefore, we first compute the solution of the zeroth order Equation (5.141) on a relatively coarse grid that has been 3 times globally refined and which has 64 nodes. Then we subsequently refine 9 times locally by applying the a-posteriori error estimation and refining the 30% of the cells with highest local error, while coarsening the lowest 3%. The obtained system matrix is then also used to solve Equations

cycles	DOF	I_1	I_2	DOF	I_1	I_2
	$\kappa = 0.7$			$\kappa = 0.98$		
3	1126	-0.181363	0.0735314	1093	-2.05621	0.348900
4	2253	-0.183821	0.0737043	2225	-2.19322	0.348822
5	4262	-0.184569	0.0736962	4639	-2.21716	0.353029
6	8021	-0.184602	0.0737123	8831	-2.22607	0.354908
7	15674	-0.184642	0.0737650	16042	-2.22823	0.355328
8	29621	-0.184649	0.0737705	31122	-2.22937	0.355737
9	55805	-0.184641	0.0737767	58818	-2.22937	0.355813
10	105926	-0.184637	0.0737791	115497	-2.22968	0.355882
11	200516	-0.184635	0.0737798	216140	-2.22975	0.355925
12	378415	-0.184634	0.0737802	407322	-2.22978	0.355933

Table 5.1:   Values of the bearing integrals converge with increasing number of local refinement cycles for $\kappa = 0.7$ and slower for $\kappa = 0.98$. The slow convergence is due to cut-off of the negative part of the solution.

(5.142) and (5.143). In Chapter 6 the numerical solution of the equation of motion of a rotating, elastic shaft supported by hydrodynamic bearings requires the solution of the three equations (5.141)-(5.143) in every time-step. The system matrix depends on the thickness h_0 of the lubricant film and has to be updated in every timestep. If we solve the three systems in every time step, the direct LU-decomposition for sparse matrices from the UMFPACK library is faster than the usual iterative solvers, because it has to be done only once in the first linear equation and can be reused to solve the second and the third. The process can still be accelerated by using the fact that during several time-steps of the ode-solver the system matrix does not change drastically. If we use the LU-decomposition as a preconditioner for e.g. the cg-solver for some time steps the convergence of the iterative solver is very good, since we use a matrix close to the inverse as preconditioner. We recompute the LU-decomposition as soon as the iterative solver makes more than a prescribed number of iteration steps (in the numerical examples shown later this is 10). The number of necessary refinement cylces is determined by examining the convergence of the bearing integrals

$$I_1 = \int_\Omega p \cos \varphi \, dr \, d\varphi, \quad I_2 = \int_\Omega p \sin \varphi \, dr \, d\varphi, \quad (5.144)$$

for different values of κ as shown in Table 5.1. There it can be seen, that 10 refinements lead to a reasonably small error ($\approx 1e - 4$) in the intgrals. The resulting mesh and a series of solutions p_0, p_1, and $\partial_t p_0$ is shown in Figure 5.12. The package `VisIt` is used here for the visualization of mesh and surfaces.

The process of local refinement takes up a lot of computation time, therefore we restrain it to those time-steps when a new Jacobian matrix for the implicit solver is computed.
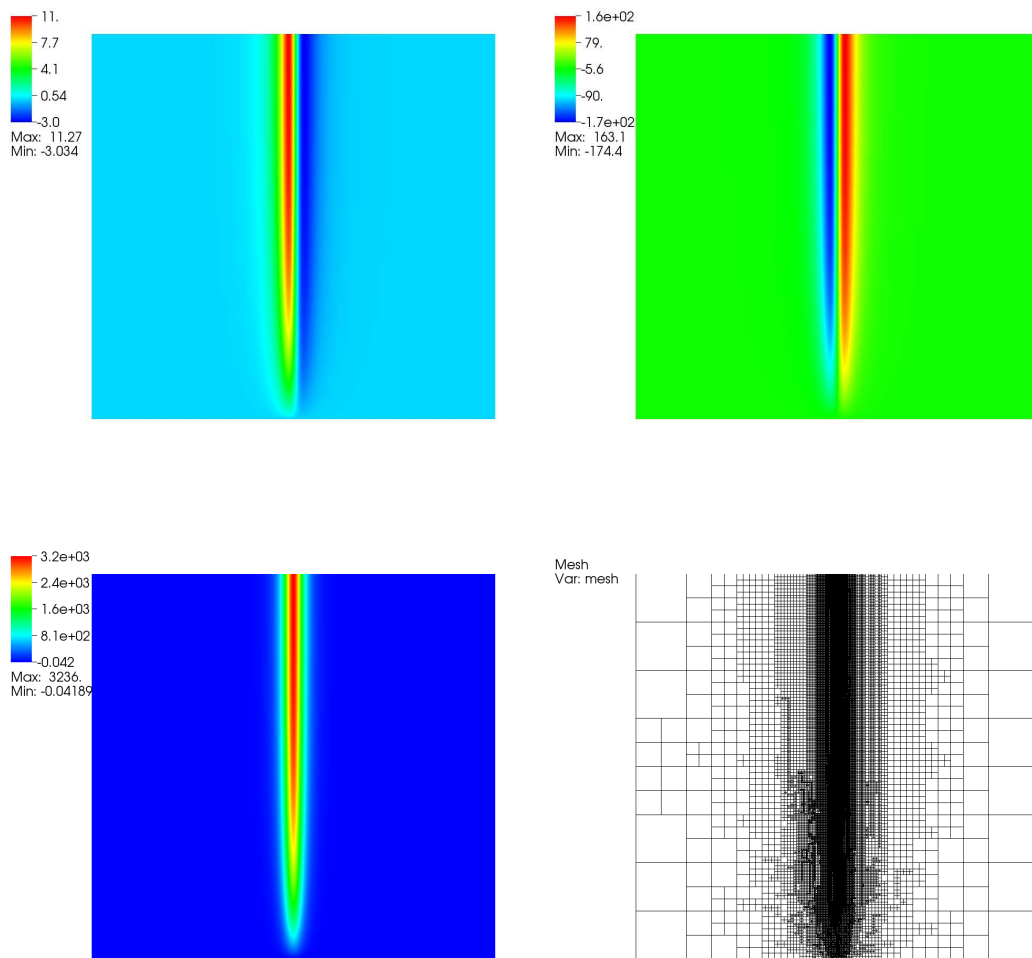
Figure 5.12: Solutions and mesh computed with `deal.II` after 11 refinement cylces; upper left: p_0, upper right: p_1, lower left: $\partial_t p_0$, lower right: mesh. The domain shown is $[-\pi, \pi] \times [0, \frac{1}{2}]$.

The zone of large variation in the pressure distribution is located most of the time around the line $\varphi = 0$ (cf. Figure 5.12), so there is always a fine grid around this line, even if the pressure distribution changes slightly. Since a new Jacobian is computed each time the error gets large and convergence is slow, this is a good heuristic for the timing of the recomputation of the grid.

5.5   Calculation of Bearing Forces

Having calculated the pressure distribution in the journal bearing we can now compute the force acting on the journal center. Negative pressures lead to cavitation in the oil film. A very simple but popular cavitation model are the so called Gümbel boundary conditions which are often used in the rotordynamics literature (Childs, 1993; Yamamoto & Ishida, 2001; San Andrés, 2006). When calculating the force by integration of the pressure over the journal surface only the domain where the pressure is positive is considered. The above mentioned Reynolds' boundary conditions are a more complicated and computationally more expensive model.

For all the lubrication models proposed in this chapter the resulting bearing forces are computed by integrating the positive part of the pressure over the bearing surface.

$$
F_{\text{bear}} = \begin{pmatrix} F_N \\ F_T \end{pmatrix} = \int_{\Omega} \bar{p}^+ \nu \, d\sigma = - \int_0^{2\pi} \int_0^W \bar{p}^+ \begin{pmatrix} \cos \varphi \\ \sin \varphi \end{pmatrix} R \, d\varphi \, dz. \tag{5.145}
$$

The analytical formulation of the pressure distribuation in the short bearing approximation also allows for the analytical computation of these integrals.

5.5.1   Analytical Solution for the Lowest Order in Short Bearing Approximation

The surface integral for the lowest order approximation can be solved analytically using Sommerfeld's variable transformation (Lang & Steinhilper, 1978). The (dimensional) normal and tangential forces are computed from the (dimensional) pressure $\bar{p}$ by

$$
F_N = - \int_0^W \int_0^{2\pi} (\bar{p}(\varphi, \bar{z}/W))^+ \cos \varphi R \, d\varphi \, d\bar{z}, \tag{5.146}
$$

$$
F_T = - \int_0^W \int_0^{2\pi} (\bar{p}(\varphi, \bar{z}/W))^+ \sin \varphi R \, d\varphi \, d\bar{z}. \tag{5.147}
$$

A variable transformation $z = \bar{z}/W$ leads to an integral over the nondimensional pressure.

$$
F_N = - \frac{WR\rho\nu\omega}{K\varepsilon} \int_0^1 \int_0^{2\pi} (p^0)^+ \cos \varphi \, d\varphi \, dz, \tag{5.148}
$$

$$
F_T = - \frac{WR\rho\nu\omega}{K\varepsilon} \int_0^1 \int_0^{2\pi} (p^0)^+ \sin \varphi \, d\varphi \, dz. \tag{5.149}
$$

The pressure distribution obtained from the short bearing approximation to Reynolds' equation (cf. Eq. (5.47) in Sec. 5.1.4) can be written in a complex notation, which shows the positive pressure region in a more distinctive way

$$p^0 = -6z(z-1)\frac{\left((\gamma' - \frac{1}{2})\kappa \sin\varphi + \kappa' \cos\varphi\right)}{(1 - \kappa\cos\varphi)^3} \tag{5.150}$$

$$= \frac{-6z(z-1)}{(1 - \kappa\cos\varphi)^3}\Re\left(\left(\kappa' - i\left(\gamma' - \frac{1}{2}\right)\kappa\right)e^{i\varphi}\right) \tag{5.151}$$

$$= \frac{-6z(z-1)}{(1 - \kappa\cos\varphi)^3}\sqrt{\kappa'^2 + \left(\left(\gamma' - \frac{1}{2}\right)\kappa\right)^2}\,\Re\left(e^{i(\varphi+\psi)}\right). \tag{5.152}$$

The phase angle ψ is defined by

$$\psi = \arg\left(\dot{\kappa} - i\left(\dot{\gamma} - \frac{1}{2}\right)\kappa\right). \tag{5.153}$$

Hence $p^0(\varphi, z) > 0$ if the real part of the complex number $e^{i(\varphi+\psi)}$ is positive, i.e.

$$\mathrm{Re}\left(e^{i(\varphi+\psi)}\right) > 0 \quad \Leftrightarrow \quad \varphi + \psi \in \left[-\frac{\pi}{2}, \frac{\pi}{2}\right]. \tag{5.154}$$

So the integration in Eqs. (5.148) and (5.149) runs from

$$\varphi_1 = -\frac{\pi}{2} - \psi \quad \text{to} \quad \varphi_2 = \frac{\pi}{2} - \psi, \tag{5.155}$$

as the first two terms in (5.152) are all positive since $0 < \kappa < 1$.

One can now integrate the equations (5.148) and (5.149) using Sommerfeld's variable transformation

$$1 - \kappa\cos\varphi = \frac{1 - \kappa^2}{1 - \kappa\cos\theta}. \tag{5.156}$$

However, the calculations are lengthy and can be found in Appendix F. The integration boundaries transform as follows:

$$\theta_1 = \arctan(\kappa - \cos\varphi_1, -\sqrt{1 - \kappa^2}\sin\varphi_1), \tag{5.157}$$

$$\theta_2 = \arctan(\kappa - \cos\varphi_2, -\sqrt{1 - \kappa^2}\sin\varphi_2). \tag{5.158}$$

With these boundaries the integrals result in

$$F_N = -\frac{W^3 R\rho\nu\omega}{c_r^2}\left(A_1\kappa' - A_2(\gamma' - \frac{1}{2})\kappa\right), \tag{5.159}$$

$$F_T = -\frac{W^3 R\rho\nu\omega}{c_r^2}\left(A_3(\gamma' - \frac{1}{2})\kappa - A_2\kappa'\right), \tag{5.160}$$

$$\tag{5.161}$$

where

$$A_1 = \frac{(\kappa^2 + \frac{1}{2})(\theta_2 - \theta_1) - 2\kappa(\sin\theta_2 - \sin\theta_1) + \frac{1}{4}(\sin 2\theta_2 - \sin 2\theta_1)}{(1 - \kappa^2)^{\frac{5}{2}}}, \tag{5.162}$$

$$A_2 = \frac{-\kappa(\cos\theta_2 - \cos\theta_1) + \frac{1}{4}(\cos 2\theta_2 - \cos 2\theta_1)}{(1 - \kappa^2)^2}, \tag{5.163}$$

$$A_3 = \frac{(2(\theta_2 - \theta_1) - \sin 2\theta_2 + \sin 2\theta_1)}{4(1 - \kappa^2)^{\frac{3}{2}}}. \tag{5.164}$$

This nice analytical formulation allows for a much faster numerical solution of the equation of motion, since the numerical evaluation of the surface integrals is computationally much more expensive.

5.5.2   Calculation of Bearing Forces for Inertia Corrected Pressure

The (dimensional) normal and tangential forces are computed from the (dimensional) pressure $\bar{p}$ by

$$F_N = -\int_0^W \int_0^{2\pi} (\bar{p}(\varphi, \bar{z}/W))^+ \cos\varphi R \, d\varphi \, d\bar{z}, \tag{5.165}$$

$$F_T = -\int_0^W \int_0^{2\pi} (\bar{p}(\varphi, \bar{z}/W))^+ \sin\varphi R \, d\varphi \, d\bar{z}. \tag{5.166}$$

The same variable transformation for $\bar{z}$ like in Section 5.5.1 leads to an integral over the nondimensional pressure

$$F_N = -\frac{\rho v \omega \delta^2}{\varepsilon^2} \int_0^1 \int_0^{2\pi} (p(\varphi, z))^+ \cos\varphi R \, d\varphi \, W \, dz \tag{5.167}$$

$$= -\frac{WR\rho v \omega \delta^2}{\varepsilon^2} \int_0^1 \int_0^{2\pi} \left(-6z(z-1)\frac{\Psi(\varphi)}{h_0^3} \right.$$

$$\left. + \varepsilon \frac{1}{h_0^5} \left(z^2(z-1)^2 G(\varphi) + z(z-1)\sum_{i=0}^4 H_i(\varphi) \right) \right)^+ \cos\varphi \, d\varphi \, dz$$

$$= -\frac{WR\rho v \omega}{K\varepsilon} \int_0^{2\pi} \left(\frac{\Psi(\varphi)}{h_0^3} + \varepsilon \frac{1}{h_0^5} \left(\frac{1}{30} G(\varphi) - \frac{1}{6}\sum_{i=0}^4 H_i(\varphi) \right) \right)^+ \cos\varphi \, d\varphi, \tag{5.168}$$

$$F_T = -\frac{\rho v \omega \delta^2}{\varepsilon^2} \int_0^1 \int_0^{2\pi} (p(\varphi, z))^+ \sin\varphi R \, d\varphi \, W \, dz \tag{5.169}$$

$$= -\frac{WR\rho v \omega}{K\varepsilon} \int_0^{2\pi} \left(\frac{\Psi(\varphi)}{h_0^3} + \varepsilon \frac{1}{h_0^5} \left(\frac{1}{30} G(\varphi) - \frac{1}{6}\sum_{i=0}^4 H_i(\varphi) \right) \right)^+ \sin\varphi \, d\varphi. \tag{5.170}$$

The integration along the z-axis can easily be computed while the solution of the φ-integral is rather complicated and therefore done numerically.

5.5.3 Order Improvement for Numerical Integration

The computation of the bearing reaction forces (5.148) and (5.149) can be done analytically in the simple case of the short bearing approximation (cf. Sec. 5.5.1). Already in the case of short bearing approximation with inertia correction the analytical solution of the involved integrals becomes too complicated. When the full Reynolds equation (with or without inertia correction) is solved numerically with the methods in Sections 5.4.1.2 and 5.4.2, the computation of the bearing forces also requires the numerical solution of the integrals

$$F_N = -\frac{WR\rho\nu\omega}{K\varepsilon} \int_0^1 \int_0^{2\pi} (p)^+ \cos\varphi \, d\varphi \, dz, \tag{5.171}$$

$$F_T = -\frac{WR\rho\nu\omega}{K\varepsilon} \int_0^1 \int_0^{2\pi} (p)^+ \sin\varphi \, d\varphi \, dz, \tag{5.172}$$

which are not linear in the pressure distribution because of the truncation of the negative part. Furthermore we want to use the given grid points for the quadrature having computed the values there already.

As can be seen in Sec. 5.1 the solution of Reynolds equation show periodic behavior with sign-change in the circumferential φ-direction and parabolic shape in the axial z-direction without sign-changes for most values of z on the grid. We first compute all the integrals with respect to z and then use the resulting sequence on the φ-grid to approximate the integral in the φ-direction. In the case of a uniform grid which we have for a finite differences discretization (cf. Sec. 5.4.1) we can compute the integrals using Simpson's rule and the error is of order 4 in the grid sizes h_1 or h_2 (Stoer & Bulirsch, 2002) in those cases where no sign-changes occur. The truncation of the negative part leads to a problem in the computation of the integrals essentially because of the loss of differentiability. In the following we describe a work-around for this problem.

For sufficiently differentiable functions f the accumulated trapezoidal rule

$$T_h = \frac{1}{2}h(f(a) + f(b)) + h \sum_{i=1}^{N-1} f(a + ih) \tag{5.173}$$

can be corrected to yield an accuracy of order h^4 where $h = (b - a)/N$ and $\xi \in (a, b)$

$$I(f) = T_h - h^2 \frac{f'(b) - f'(a)}{12} + h^4 \frac{b - a}{720} f^{(4)}(\xi). \tag{5.174}$$

For periodic functions the derivatives at the end-points are equal and the trapezoidal rule is always of order 4 (Stoer & Bulirsch, 2002).

Since the zeros of the pressure distribution are not necessarily located at grid-points, the application of the trapezoidal rule to the truncated pressure $(p)^+$ has no longer order 4. Figure 5.13 shows that the truncation entails the inclusion of the triangular
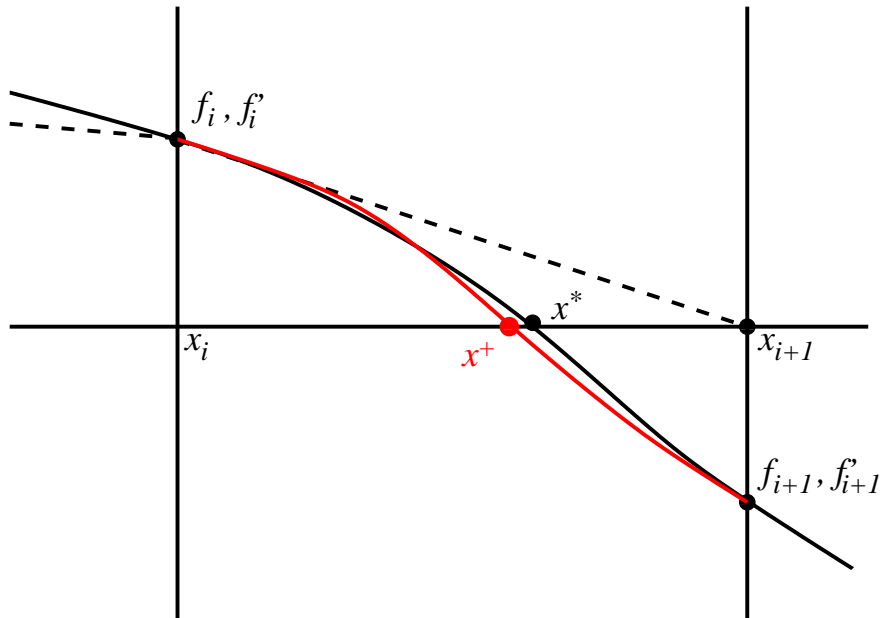

Figure 5.13: Correction of the quadrature by integration of an interpolant

area below the dashed line into the trapezoidal sum, while the exact integral only includes the area below the black curve up to its zero at x^*. This can be overcome by approximating the positive part of the integral on the cell in which the sign change occurs with the help of an interpolant, which is shown in red. This leads again to an error of order h_1^4. In detail we do the following to correct the approximation of the integral. We therefore determine the intervals where sign changes occur and do the following steps for all of them:

- compute derivatives f_i' and $f_i' + 1$ with central differences,

- compute the coefficients of the interpolating cubic Hermite polynomial H_3 which are given by

$$a_0 = f_i, \quad a_1 = f_i', \quad a_2 = \frac{-3f_i + 3f_{i+1}}{h} - \frac{2f_i' + f_{i+1}'}{h^2}, \quad a_3 = \frac{f_i' + f_{i+1}'}{h^2} + \frac{2f_i - 2f_{i+1}}{h^3},$$
(5.175)

- find the zero x^+ of polynomial H_3 that lies in $[x_i, x_{i+1}]$,

- compute the integrals of the interpolant from the boundaries of the interval to

the zero

$$I_1 = \int_{x_i}^{x^+} H_3(x)\, dx = (((\frac{a_3}{4}x^+ + \frac{a_2}{3})x^+ + \frac{a_1}{2})x^+ + a_0)x^+,$$

$$I_2 = \int_{x^+}^{x_{i+1}} H_3(x)\, dx = h(\frac{f_i + f_{i+1}}{2} + h\frac{f'_i - f'_{i+1}}{12}) - I_1,$$

- correct the trapezoidal sum T_h over the whole interval $[0, 2\pi]$ by

$$I_h = T_h + \begin{cases} -\frac{h f_i}{2} - \frac{h^2 f'_i}{12} + I_1 & \text{if} \quad f_i > 0, \\ -\frac{h f_{i+1}}{2} + \frac{h^2 f'_{i+1}}{12} + I_2 & \text{if} \quad f_{i+1} > 0. \end{cases} \tag{5.176}$$

Proposition 5.5. *The resulting approximation to the integral is of order 4, i.e. $|I - I_h| = O(h^4)$.*

Proof. Outside the intervals where sign changes occur the approximation order of the corrected trapezoidal sum is 4 (cf. Eq. (5.174)). We need to give an estimate for the error of the above procedure inside these intervals.

Let f_i, f'_i, f_{i+1} and f'_{i+1} be the function values and derivatives at the boundary of the interval (x_i, x_{i+1}) of length h. The interpolation error of the Hermite interpolation is given by (Stoer & Bulirsch, 2002)

$$|f(x) - H_3(x)| \leq \frac{1}{4!}\|f^{(iv)}\|_\infty \left|(x - x_i)^2 (x - x_{i+1})^2\right|. \tag{5.177}$$

With this the error of the integrals of the truncated functions can be estimated.

$$|I - I_h| = |\int_{x_i}^{x_{i+1}} (f^+ - H_3^+)\, dx| \leq \int_{x_i}^{x_{i+1}} |(f^+ - H_3^+)|\, dx \leq \int_{x_i}^{x_{i+1}} |(f - H_3)|\, dx \leq C\|f^{(iv)}\|_\infty h^5. \tag{5.178}$$

Hence the integral of the interpolant up to its zero is a sufficient approximation to the truncated function f inside the intervals where sign changes occur. □

When calculating the pressure distribution on a uniform grid by finite difference we use this method to correct the integration. Numerical results show that the computation time is not drastically increased while convergence is faster. In Figure 5.14 we compare the convergence of the above method to the convergence of the simple trapezoidal rule for the integration of the functions

$$f = \left(\frac{\sin(\varphi - \alpha)}{(1 - c\cos(\varphi))^3}\right)^+ \cos(\varphi),$$

and

$$g = \left(\frac{\sin(\varphi - \alpha)}{(1 - c\cos(\varphi))^3}\right)^+ \sin(\varphi),$$

which occur in the computation of the bearing forces. The relative errors of the corrected method converge much faster to zero than those of the trapezoidal method.
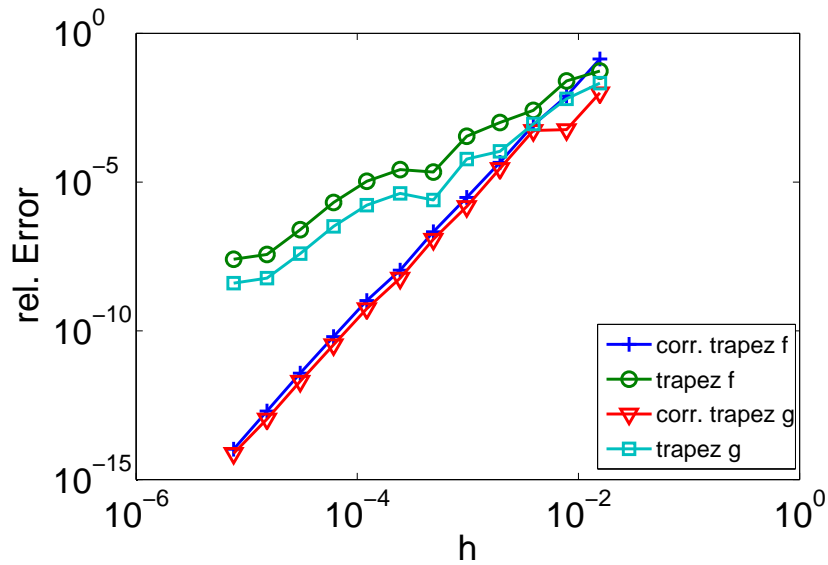
Figure 5.14: Error of the numerical quadrature: Corrected trapezoidal method shows faster convergence than trapezoidal method .

5.6   Numerical Results and Comparison of Bearing Properties

In the previous sections different models for the pressure distribution in a plain journal bearing and numerical methods to compute them were introduced. In this section we compare the results and take a look at the bearing reaction forces caused by the movement of the shaft in the lubricant.

5.6.1   Convergence Considerations for Short Bearing Approximation

In Section 5.1 Reynolds' equation is derived as a thin film approximation to the Navier-Stokes equations. The short bearing approximation additionally considers the axial dimension of the bearing being small. We introduce the additional relation $\varepsilon = K\delta^2$ where $\varepsilon = \frac{c_r}{R}$ is the ratio of radial bearing clearance c_r to bearing radius R and $\delta = \frac{W}{R}$ the ratio of bearing width W to radius. By letting them simultaneously become small the convergence of the solution of Reynolds' equation (in two variables) to the short bearing approximation can be observed. Figure 5.15 shows the relative difference between the solutions of Reynolds' equation p_r^i and the short bearing approximation p_s^i in the L^2-Norm

$$\text{error} = \frac{\|p_r - p_s\|_{L^2}}{\|p_r\|_{L^2}} \tag{5.179}$$

for the zeroth and the first order. The error is shown in dependence of ε for a fixed ratio of $K = \frac{c_r R}{W^2} = 1$ which corresponds to a very short bearing. As expected from Section 5.1 the convergence rate is roughly quadratic for the first order approximation and linear
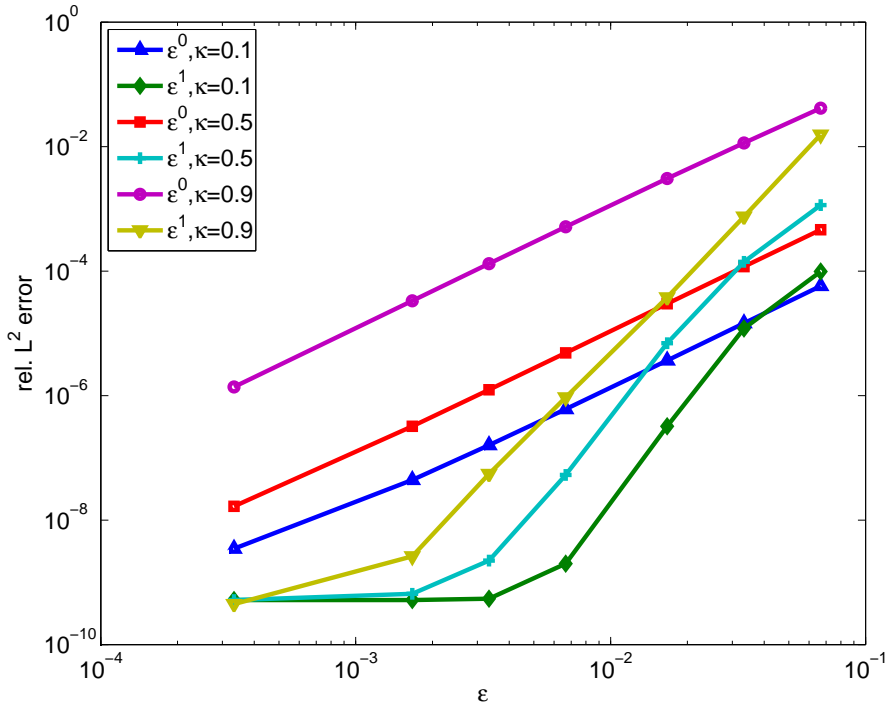
Figure 5.15: The relative difference $\frac{\|p_r - p_s\|_{L^2}}{\|p_r\|_{L^2}}$ between the solutions of Reynolds' equation and the short bearing approximation for zeroth and first order and for different eccentricity values; the ratio of clearance to the square of width is constant $K = \frac{\varepsilon}{\delta^2} = 1$.

in ε for the zeroth order approximation. The validity for different eccentricity ratios is also demonstrated in the figure. However, for large eccentricities the convergence becomes poorer.

Since the bearings used in practice usually do not fulfill this special ratio $K = \frac{c_r R}{W^2} = 1$, it is also necessary to examine the convergence behavior for different ratios in order to know the limits of usability of the approximation. In Figure 5.16 the relative error in dependence of δ is depicted for several values of ε. In the zeroth order approximation the ratio K does not appear in the expression for the pressure (5.47), so there is no difference in the convergence of the zeroth order solutions for different ε and only the one for $\varepsilon = \frac{c_r}{R} = 0.0067$ is depicted. We have convergence of the solutions of Reynolds' equation to the short bearing approximation for decreasing $\delta = \frac{W}{R}$, the convergence being better for small ε and also better for the first order equation than for the zeroth order. However, it can also be seen, that for large δ, i.e. longer bearings of a width to radius ratio of 1 or larger, the short bearing solution differs largely from the solution of Reynolds equation no matter how small ε. Here the difference is bigger for the first order equation than for the zeroth order. This corresponds with (Childs, 1993) and (San Andrés, 2006) where is stated that the short bearing approximation is valid only for $\frac{W}{R}$-ratios smaller than 1.
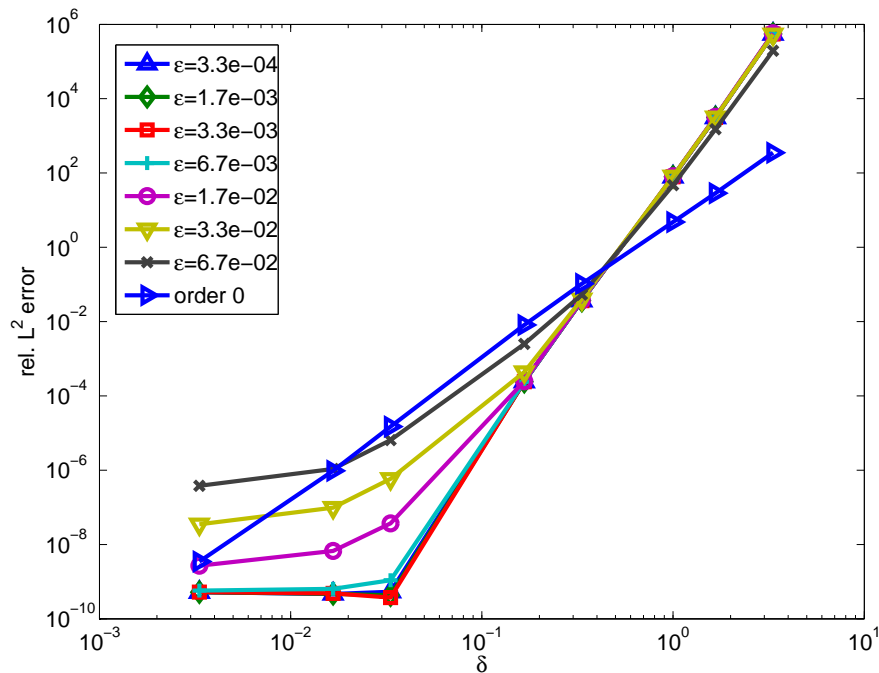
Figure 5.16: The relative difference $\frac{\|p_r - p_s\|_{L^2}}{\|p_r\|_{L^2}}$ between the solutions of Reynolds' equation and the short bearing approximation (order ε^0 and order ε^1) for varying width and different values of ε; the relative eccentricity is $\kappa = 0.9$.

5.6.2   Comparison of Pressure Distributions and Resulting Forces

The surface plots in the Figures 5.5 - 5.11 depict the pressure distributions arising from the solution of Reynolds' equation, the short bearing approximation and alternative bearing models, as derived in the Sections 5.1 - 5.3. The comparison of the various pressure distributions is facilitated by looking at the z-averaged pressure distributions as shown in Figure 5.17. It can be seen clearly that for the very short bearing (first line: $W = 0.24$ mm, $K = 1$) and for the short bearing (second line: $W = 1$ mm, $K = 0.06$) the z-averaged pressure distributions are almost identical with slightly larger differences for larger eccentricities. The only exception is the finite bearing approximation (5.111), which underestimates the pressure in all cases and is therefore not considered in the simulations in Chapter 6. For the medium sized bearing as it is used in the turbocharger of TCRDL the first order short bearing approximations shows drastically different behavior than the first order solution of Reynolds' equation, as seen in the convergence considerations in the last section. While the zeroth order approximation overestimates the pressure, the correction term (5.61) in this case becomes larger than the zeroth order solution and therefore dominates the pressure distribution, leading to a physically wrong solution where the pressure is negative in front of the point of smallest film thickness.
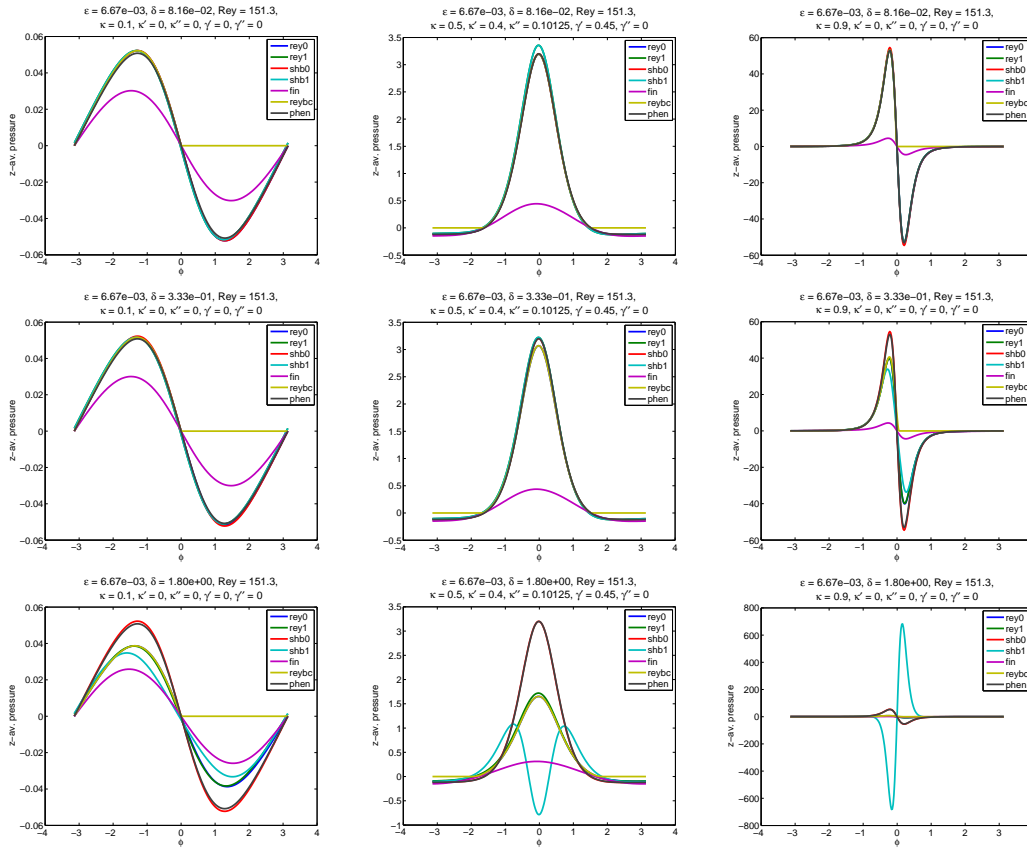
Figure 5.17: *z*-averaged pressure distributions from solutions to Reynolds' equation (*rey0*, *rey1*), short bearing approximation(*shb0*, *shb1*), finite bearing (*fin*), Reynolds' equation with free boundary conditions (*reybc*), and the phenomenological correction (*phen*): First line: very short bearing (*W* = 0.24, *K* = 1); second line: short bearing (*W* = 1, *K* = 0.06); third line: medium sized bearing (*W* = 5.4, *K* = 0.002); in each column different values of κ, $\dot{\kappa}$, and $\dot{\gamma}$ are used.

This affects also the bearing reaction forces as shown in Figure 5.18. We depict the normal force along the line from the center of the bearing to center of the shaft and the orthogonal tangential force in dependence of the eccentricity κ for a rotating shaft with rotational frequency $\nu = 1400$ Hz and whirling with an angular velocity of $\dot{\gamma} = 0.4\omega$. In the three columns of the figure different bearing lengths are considered, all other parameters being equal. Again it can be seen that for a long bearing (*W* = 5.4 mm) the first order solution shows a drastically different behavior due to the large difference of the pressure distributions shown in Figure 5.17. This also leads to a totally different dynamic behavior of the shaft as can be seen in the simulations in Chapter 6.

The forces arising from the solutions of Reynolds' equation only show little differences. In Figure 5.19 surface plots of the bearing forces arising from the zeroth order short bearing approximation are shown exemplarily in dependence of κ and $\dot{\gamma}$ for $\dot{\kappa} = 0$, and *W* = 1. The forces are zero for $\dot{\gamma} = \frac{1}{2}$. This is the case for the zeroth order Reynolds'
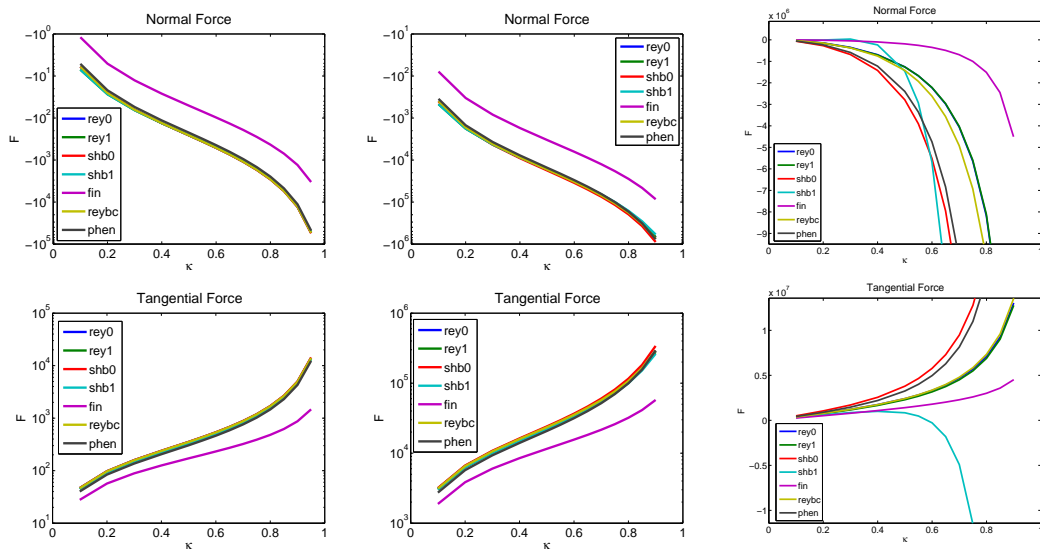
Figure 5.18: Normal and tangential forces acting on a rotating shaft (rot. frequency ν = 1400 Hz) orbiting the bearing center on a circular orbit of radius κ; the angular velocity is $\dot{\gamma} = 0.4\omega$; the other parameters are R = 3 mm, c_r = 0.02 mm, Reynolds number $\mathcal{R}$ = 152; the bearing width varies from the left to the right: W = 0.245 mm, W = 1 mm, and W = 5.4 mm. Depicted are the forces resulting from the solutions to Reynolds' equation (*rey0*, *rey1*), short bearing approximation (*shb0*, *shb1*), finite bearing (*fin*), Reynolds' equation with free boundary conditions (*reybc*), and the phenomenological correction (*pheno*). The right column is not in logarithmic scale due to the sign changes of the first order short bearing approximation *shb1*.
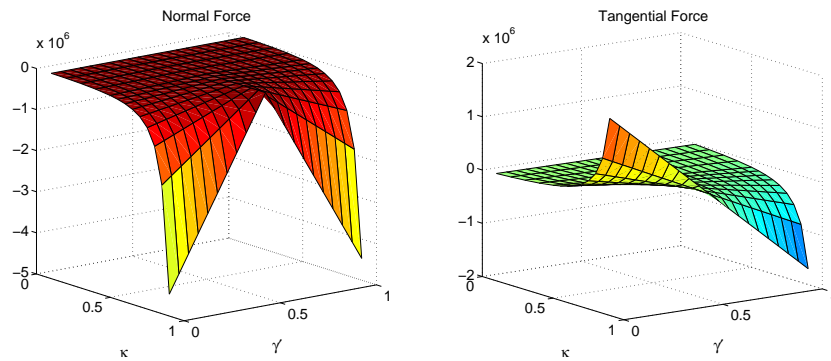
Figure 5.19: Surface plots of normal and tangential force computed for zeroth order short bearing approximation for varying κ and $\dot{\gamma}$ with fixed $\dot{\kappa} = 0$, $W = 1$.

equation as well.

For the short bearings the first order approximations differ only a little from the zeroth order approximations. They are however not identical and especially the tangential force of the first order solution is smaller than that of the zeroth order solution. In view of the question for the rotor self excited whirl frequency the behavior of the tangential

force is of special interest, since it accelerates or decelerates the rotor along the circular whirling orbit. For the first order solutions the zero of the tangential force moves to lower values of $\dot{\gamma}$ as shown in the Figure 5.20 which backs the hypothesis that the inertia correction leads to a reduction of the whirl frequency.
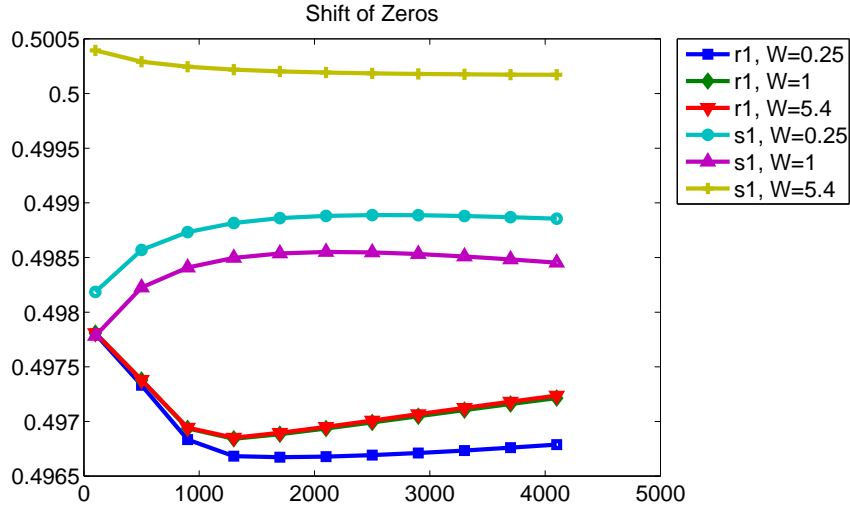

Figure 5.20: Approximate value of $\dot{\gamma}$ for which the tangential force vanishes in dependence of ω for $\kappa = 0.9$, $\dot{\kappa} = 0$.

The phenomenological correction of the zeroth order short bearing approximation (5.101) also shows similar behavior. In Figure 5.21 we depict the normal and the tangential force for $W = 1$, $\dot{\gamma} = 0.4$, and $\dot{\kappa} = 0$, in dependence of κ and the correction parameter σ for a linear correction $s(\omega) = \sigma\omega$.
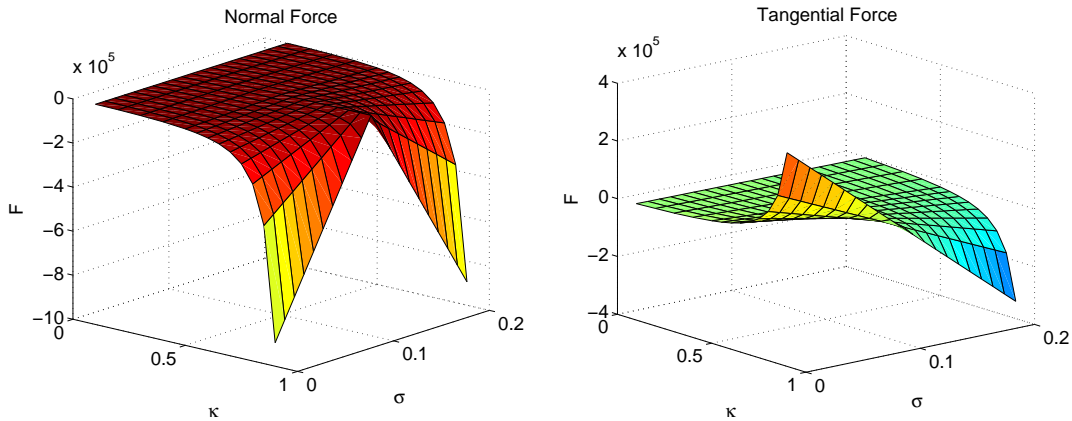

Figure 5.21: Normal and tangential force from phenomenological pressure correction in dependence of κ and σ.

From Equation (5.101) it is easy to see that the parameter σ shifts the zero of the tangential force. In the figure the tangential force is zero for $\sigma = 0.1$. Hence we can use

the shift parameter to control for which value of $\dot{\gamma}$ the tangential force vanishes, e.g. in the linear case

$$\dot{\gamma} + \sigma = \frac{1}{2} \quad \Rightarrow \quad f_t = 0. \tag{5.180}$$

5.7   Conclusions

In view of the convergence results and the comparison of the resulting forces we can draw the following conclusions.

- For very short and short bearings the solution of Reynolds equation converges to the derived short bearing approximation and yields a model for the pressure distribution that is easier and faster computable.

- The first order short bearing approximation can be used for very short bearings ($K \approx 1$), while for medium sized bearings the first order Reynolds equation should be the model of choice for the pressure distribution in the plain journal bearing.

- The numerical evidence points to an influence of the inertia correction on the whirling frequency via a change in the zero of the tangential force. This influence on the tangential force is also present for the phenomenological correction to the short bearing approximation

- The finite bearing approximation underestimates the pressure and the forces and will therefore not be considered for the direct numerical simulations.

- The free boundary problem for zeroth order Reynolds equation with Reynolds boundary conditions yields solutions that are similar to those with Gümbel conditions, however the computation time is considerably larger. In Chapter 6 we see that there is no influence on the whirling frequency.

The derivation of the bearing model is an important part of the modelling of the rotor-bearing system as the influence on the dynamics is considerable. It is therefore naturally an intensively studied field with a large variety of models around. We do not seek completeness here, which would be beyond the scope of this work, but we want to show in the following that already the relatively simple models presented here lead to complex dynamic behavior. The methods we will use in Chapters 6 and 7 can then also be applied to more complicated bearing that e.g. involve turbulence, surface roughness, or variable viscosity.

Chapter 6

Direct Numerical Simulation and Experimental Results

In the previous chapters we have derived the various parts of a model for rotating beams constrained by simple journal bearings. In Chapter 2 a PDE model was derived for the lateral motion of a continuous Rayleigh beam. In Chapter 4 we have used the finite element method to discretize the equations and we have arrived at an ODE system for the nodal displacement of the beam. In Chapter 5 the model for the reaction forces of the oil lubricated bearings has been derived from the Navier-Stokes equations by asymptotic analysis. In the present chapter we combine these results to obtain finally the equations of motion for the rotating beam, and we solve these with numerical integration methods. The results of the simulations are compared to the experiments performed at the Toyota Central Research and Development Laboratories (TCRDL). As we shall see, the equations of motion are either a stiff system of ordinary differential equations if no inertia correction is applied, or an implicit system if the inertia correction is used in the bearing model. Therefore appropriate implicit methods such as backward differentiation formulas (BDF) (Hairer & Wanner, 1996) or numerical differentiation formulas (NDF) (Shampine & Reichelt, 1997; Shampine, 2002) have to be used.

6.1   Equations of Motion

The equations of motion for a rotating beam are a system of ordinary differential equations for the nodal displacement of the beam elements used for the discretization of the rotor as in Equation (4.69).

The state space is $\mathbb{R}^{4(N+1)}$, where N is the number of finite beam elements. The state

vector is

$$x = (x_1, \ldots, x_{4(N+1)}) \tag{6.1}$$

$$= (q_1, \ldots, q_{N+1}) = (u_1, v_1, \beta_1, \alpha_1, \ldots, u_{N+1}, v_{N+1}, \beta_{N+1}, \alpha_{N+1}), \tag{6.2}$$

where u_k and v_k are the lateral displacements in node k, and β_k and α_k the inclinations as shown in Section 4.3 of Chapter 4. For small displacements we have approximately $\beta_k \approx -v_k'$ and $\alpha_k \approx u_k'$ (cf. Appendix A). Furthermore, we need the following notations which facilitate the formulation of the equations of motion. The polar coordinates of the nodal displacement are

$$r_k = \sqrt{u_k^2 + v_k^2}, \quad \gamma_k = \arg(u_k + iv_k). \tag{6.3}$$

The nodal lateral displacements at the bearing nodes are denoted by $x_{b_i} = (u_{b_i}, v_{b_i})^T$. The vector $x_b = (u_{b_1}, v_{b_1}, u_{b_2}, v_{b_2})^T$ contains the displacements at all the bearing nodes.

As seen in the previous chapters the rotating shaft is subject to several external forces. First, there are constant loads, such as gravity, which we will denote in the following by F_{gr}. Second, there are time-periodic forces $F_{unb}(t)$ due to the unbalance of the rotor, as given in (4.76) and (4.77) with nodal unbalance amplitude a_k and phase ψ_k. They have the following structure

$$F_{unb}(t) = \omega^2 \begin{pmatrix} a_1 \cos(\omega t + \psi_1) \\ a_1 \sin(\omega t + \psi_1) \\ 0 \\ \vdots \\ a_{N+1} \cos(\omega t + \psi_{N+1}) \\ a_{N+1} \sin(\omega t + \psi_{N+1}) \\ 0 \\ 0 \end{pmatrix}. \tag{6.4}$$

Third, there are the bearing reaction forces. Depending on the bearing model the system is either explicit or implicit.

6.1.1 Explicit Case

When no inertia correction is applied, i.e. the zeroth order short bearing approximation (Eqs. (5.159), (5.160)) or the zeroth order solution to Reynolds equation (Eq. (5.145)) are used as models for the pressure distribution in the bearings, the equation of motion (4.69) is explicit. It is also explicit for the alternative bearing models proposed in Section 5.3, like the phenomenological model, the finite bearing approximation, and the solution with Reynolds boundary conditions. In these cases the bearing reaction force F_{bear} has the following form

$$F_{bear}(x_b) = \left(0, \ldots, f_{b_1,1}(x_{b_i}, \dot{x}_{b_i}), f_{b_1,2}(x_{b_1}, \dot{x}_{b_1}), 0, \ldots, f_{b_2,1}(x_{b_1}, \dot{x}_{b_i}), f_{b_2,2}(x_{b_2}, \dot{x}_{b_2}), 0, \ldots, 0\right)^T. \tag{6.5}$$

It is computed from the normal and the tangential forces at the bearing nodes b_i, $i \in \{1, 2\}$, by

$$\begin{pmatrix} f_{b_i,1} \\ f_{b_i,2} \end{pmatrix}(x_{b_i}, \dot{x}_{b_i}) = T(\gamma_{b_i}) \begin{pmatrix} f_n(r_{b_i}, \dot{r}_{b_i}, \dot{\gamma}_{b_i}) \\ f_t(r_{b_i}, \dot{r}_{b_i}, \dot{\gamma}_{b_i}) \end{pmatrix}, \tag{6.6}$$

where $T(\gamma)$ is the two-dimensional rotation matrix

$$T(\gamma) = \begin{pmatrix} \cos\gamma & -\sin\gamma \\ \sin\gamma & \cos\gamma \end{pmatrix}. \tag{6.7}$$

Combining the above, we finally obtain the equation of motion which can be written in second order form as

$$M\ddot{x} + (\omega G + C)\dot{x} + Kx = F_{\text{gr}} + F_{\text{unb}}(t) + F_{\text{bear}}(x_b, \dot{x}_b), \tag{6.8}$$

or in first order form with $y = (\dot{x}, x)^T$

$$\begin{pmatrix} M & \\ & I \end{pmatrix}\dot{y} = \begin{pmatrix} -(\omega G + C) & -K \\ I & 0 \end{pmatrix}y + \begin{pmatrix} F_{\text{gr}} + F_{\text{unb}}(t) + F_{\text{bear}}(y_b) \\ 0 \end{pmatrix}. \tag{6.9}$$

6.1.2 Implicit Case

When the inertia corrected lubrication models (Eq. (5.63) or (5.90)) are used, the bearing reaction forces additionally depend on the acceleration of the shaft at the bearing node. We have

$$F_{\text{bear}} = \Big(0, \ldots, 0, f_{b_1,1}(x_{b_1}, \dot{x}_{b_1}, \ddot{x}_{b_1}), f_{b_1,2}(x_{b_1}, \dot{x}_{b_1}, \ddot{x}_{b_1}), 0, \ldots$$
$$\ldots, 0, f_{b_2,1}(x_{b_2}, \dot{x}_{b_2}, \ddot{x}_{b_2}), f_{b_2,2}(x_{b_2}, \dot{x}_{b_2}, \ddot{x}_{b_2}), 0, \ldots, 0\Big)^T \tag{6.10}$$

with

$$\begin{pmatrix} f_{b_i,1} \\ f_{b_i,2} \end{pmatrix}(x_{b_i}, \dot{x}_{b_i}, \ddot{x}_{b_i}) = T(\gamma_{b_i}) \begin{pmatrix} f_n(r_{b_i}, \dot{r}_{b_i}, \dot{\gamma}_{b_i}, \ddot{r}_{b_i}, \ddot{\gamma}_{b_i}) \\ f_t(r_{b_i}, \dot{r}_{b_i}, \dot{\gamma}_{b_i}, \ddot{r}_{b_i}, \ddot{\gamma}_{b_i}) \end{pmatrix}. \tag{6.11}$$

This leads to an implicit equation of motion

$$M\ddot{x} + (\omega G + C)\dot{x} + Kx = F_{\text{gr}} + F_{\text{unb}}(t) + F_{\text{bear}}(x_b, \dot{x}_b, \ddot{x}_b), \tag{6.12}$$

which we can be rewritten in first order form

$$\begin{pmatrix} M & \\ & I \end{pmatrix}\dot{y} = \begin{pmatrix} -(\omega G + C) & -K \\ I & 0 \end{pmatrix}y + \begin{pmatrix} F_{\text{gr}} + F_{\text{unb}}(t) + F_{\text{bear}}(y_b, \dot{y}_b) \\ 0 \end{pmatrix}. \tag{6.13}$$

By introducing the projection P_b onto the components of the state space describing the lateral displacement of the bearing nodes and the dummy variable a

$$P_b \ddot{x} = \ddot{x}_b = a, \tag{6.14}$$

we can rewrite this implicit equation as a differential-algebraic equation of degree 1 with singular mass matrix.

$$\begin{pmatrix} M & 0 & 0 \\ 0 & I & 0 \\ P_b & 0 & 0 \end{pmatrix} \begin{pmatrix} \ddot{x} \\ \dot{x} \\ \dot{a} \end{pmatrix} = \begin{pmatrix} -(\omega G + C) & -K & 0 \\ I & 0 & 0 \\ 0 & 0 & -I \end{pmatrix} \begin{pmatrix} \dot{x} \\ x \\ a \end{pmatrix} + \begin{pmatrix} F_{\mathrm{gr}} + F_{\mathrm{unb}}(t) + F_{\mathrm{bear}}(x_b, \dot{x}_b, a) \\ 0 \\ 0 \end{pmatrix}. \tag{6.15}$$

6.1.3   Simple Model

Additionally, as in (Hollis & Taylor, 1986), a very simple model can be used for examination of the influence of the bearing function on the dynamics. We consider a rotating cylinder of mass M of the same length as a journal bearing. The forces acting on the cylinder are the bearing forces, unbalance forcing, gravity and eventually some viscous damping with damping coefficient $D \geq 0$. With $x \in \mathbb{R}^2$ being the vector of lateral displacement, the equation of motion for the lateral displacement is

$$M\ddot{x} + D\dot{x} = \begin{pmatrix} F_{\mathrm{bear},1} \\ F_{\mathrm{bear},2} - Mg \end{pmatrix} + f_{\mathrm{unb}}\omega^2 \begin{pmatrix} \cos \omega t \\ \sin \omega t \end{pmatrix}. \tag{6.16}$$

One can interpret this as a model describing just the motion of the bearing node subject to the bearing forces and an additional periodic forcing, but without interaction with the neighboring nodes. Depending on the lubrication model, Equation (6.16) can be either explicit or implicit.

6.2   Numerical Methods

In the previous section we stated equations of motion that arise from our models. All these equations show the characteristics of stiff equations (Hairer & Wanner, 1996). Especially the spectrum of the Jacobian is very stretched out over the negative half plane. In Figure 6.1, we exemplarily depict the eigenvalues of the Jacobian of the explicit system (6.8) using a 13 element beam as in Section 4.5.1 and the short bearing lubrication model (5.159), (5.160). We see that it has eigenvalues of large absolute value on the negative real axis as well as close to the imaginary axis. Therefore the use of A-stable implicit methods is appropriate, where the whole negative half plane is in the region of stability (Hairer & Wanner, 1996). Semiexplicite equations of the form (6.15) can be solved by Matlab's `ode15s` solver or Hairer and Wanner's `RADAU5` (Hairer
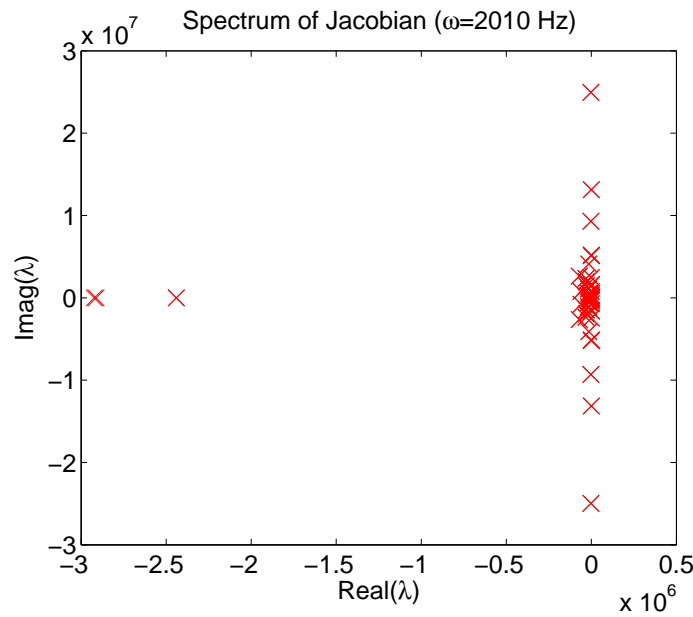
Figure 6.1: Spectrum of the Jacobian of the explicit system (6.8) for a 13 element beam model with short bearing lubrication model at $\omega = 2010$ Hz. Most of the eigenvalues are located along the imaginary axis with a small negative real part and a few eigenvalues have large negative real parts, which leads to the stiffness of the equations.

& Wanner, 1996), among others. The implicit equation can be solved with Matlab's `ode15i`. The code `DASPK` can be used to solve both variants.

In this work, we mainly apply Matlab's `ode15s` code and the code `DASPK`, which is a successor of the popular code `DASSL`. `DASPK` uses backward differentiation formulas (BDF) of variable order for the integration of stiff differential(-algebraic) systems. These implicit multistep methods are described in (Brenan *et al.*, 1989) and also in (Deuflhard & Bornemann, 1994). `DASPK` can also compute consistent initial conditions. The `DASPK` routine is included in the free software Octave (Eaton, 2002) which is mostly compatible with Matlab.

The code `ode15s` used in Matlab is described in (Shampine & Reichelt, 1997). It uses numerical differentiation formulas (NDF) which are a modification of the BDF having an additional free parameter that can be used to either enlarge the region of stability while maintaining the truncation error, or to reduce the error while keeping the size of the region of stability close to the one of the BDF. In `ode15s` the second target is chosen leading to smaller regions of stability. For order 2, however, both methods are A-stable. When using `ode15s` it is necessary to set the maximal order of the method to 2, since otherwise numerical instabilities occur. `ode15s` can compute consistent initial conditions.

In both codes the user can supply a routine for the Jacobian matrix of the system, which

is otherwise computed by finite differences. The computation of the bearing reaction forces can be computationally expensive, especially when the Reynolds equation has to be solved to compute them. This makes the computation of the Jacobian by finite differences expensive although the non-linearity only appears in a few (4) components and depends only on the coordinates of the bearing nodes. We therefore supply a routine that makes use of the special structure of the system to compute the Jacobian more efficiently. For this, we compute the matrices

$$
K_{b_i} = \begin{pmatrix} \frac{\partial f_{b_i,1}}{\partial x_{b_i,1}} & \frac{\partial f_{b_i,1}}{\partial x_{b_i,2}} \\ \frac{\partial f_{b_i,2}}{\partial x_{b_i,1}} & \frac{\partial f_{b_i,2}}{\partial x_{b_i,2}} \end{pmatrix}, \tag{6.17}
$$

$$
C_{b_i} = \begin{pmatrix} \frac{\partial f_{b_i,1}}{\partial \dot{x}_{b_i,1}} & \frac{\partial f_{b_i,1}}{\partial \dot{x}_{b_i,2}} \\ \frac{\partial f_{b_i,2}}{\partial \dot{x}_{b_i,1}} & \frac{\partial f_{b_i,2}}{\partial \dot{x}_{b_i,2}} \end{pmatrix}, \tag{6.18}
$$

$$
M_{b_i} = \begin{pmatrix} \frac{\partial f_{b_i,1}}{\partial \ddot{x}_{b_i,1}} & \frac{\partial f_{b_i,1}}{\partial \ddot{x}_{b_i,2}} \\ \frac{\partial f_{b_i,2}}{\partial \ddot{x}_{b_i,1}} & \frac{\partial f_{b_i,2}}{\partial \ddot{x}_{b_i,2}} \end{pmatrix}, \tag{6.19}
$$

using central differences. These are subsequently added to the corresponding components of the matrix of the constant linear part of Equations (6.9) or (6.13), respectively, and to the mass matrix of (6.13)

$$
J = \begin{pmatrix} -(\omega G + C) & -K \\ I & 0 \end{pmatrix} + \begin{pmatrix} C_b & K_b \\ 0 & 0 \end{pmatrix}, \tag{6.20}
$$

$$
B = \begin{pmatrix} M & \\ & I \end{pmatrix} - \begin{pmatrix} -M_b & \\ & 0 \end{pmatrix}, \tag{6.21}
$$

where

$$
K_b = \begin{pmatrix} \ddots & & & & \\ & K_{b_1} & & & \\ & & \ddots & & \\ & & & K_{b_2} & \\ & & & & \ddots \end{pmatrix} \tag{6.22}
$$

is zero except for the blocks K_{b_1} and K_{b_2} which are located at the indices corresponding to the variables describing the lateral displacement of the bearing nodes. C_b and M_b are formed analogously. While still using finite differences to approximate the derivative of the non-linearity, we can hence reduce the number of necessary computations of the bearing forces to 24 regardless of the dimension of the system. Both, the Jacobian J and the mass matrix B are sparse. The use of the sparsity pattern and other sparse matrix routines in Matlab also leads to a considerable speed-up of the computations.

6.3 Analysis of Experimental Results

Simulations have been done for several different parameter sets. These sets reflect the different set-ups used in the experiments at TCRDL using the turbocharger rotor similar to the one depicted in Figure 6.2, but without floating ring bearings. The experiments have been carried out in 2002 at TCRDL by Mizuho Inagaki. The standard
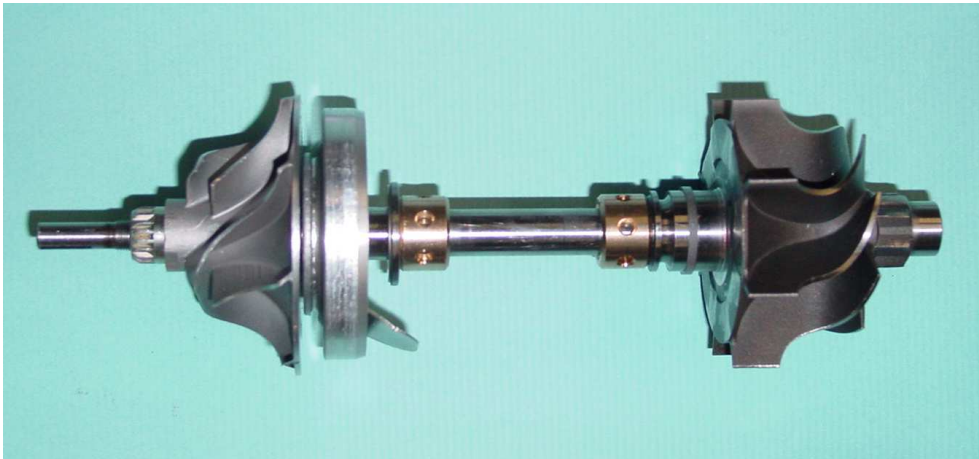
Figure 6.2: The rotor of a turbocharger used in the experiments at TCRDL. It consists of the shaft, the compressor (left) and the turbine wheel (right). The bearing positions are indicated here by the two floating rings (golden color). The experiments were done for plain journal bearings without floating rings.
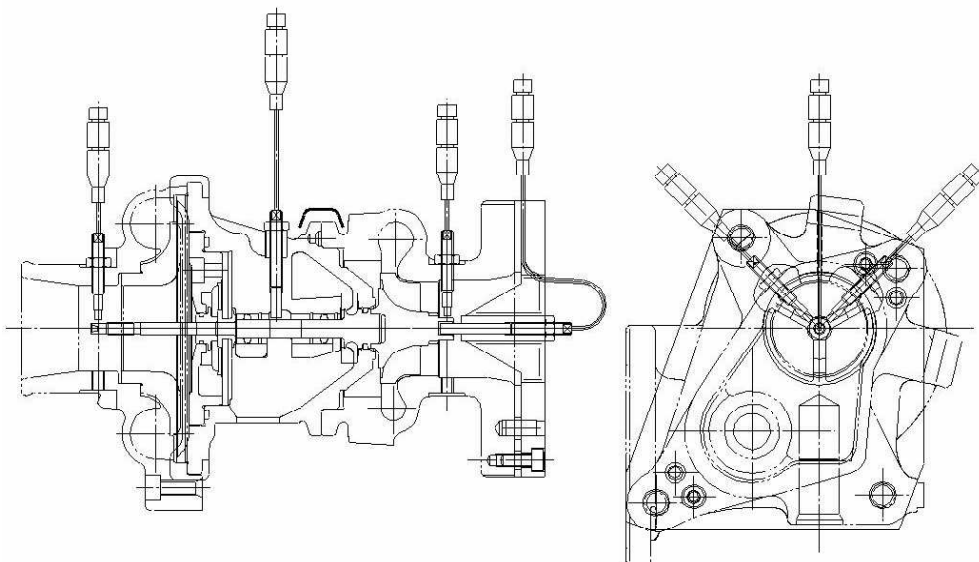

Figure 6.3: Positions of eddy current sensors measuring lateral *x*-*y*-displacement at three points along the shaft (impeller, middle, turbine) and axial displacement at the right end.
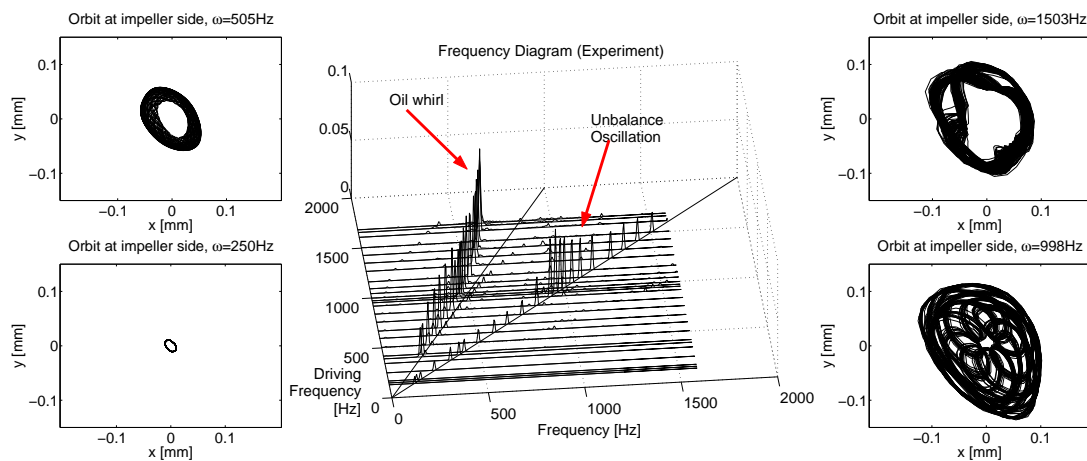
Figure 6.4: Experimental results: Waterfall diagram of the response spectrum of rotor for varying driving frequencies (center); orbits of impeller end of rotor for 4 different driving frequencies (left and right). Mainly two kinds of vibration occur in the examined frequency range: the subharmonic oil whirl and the synchronous unbalance oscillation of a bending mode.

experimental case used two bearings of 5.4 mm width, 0.02 mm radial clearance, 80°C oil pan temperature and an oil supply pressure of 0.001 Pa. The dimensions of the rotor and the unbalance condition are given in the Appendix D. During the experiments the rotor is driven by pressurized air at a given rotational velocity. The lateral displacement in x- and y-direction is measured by eddy current sensors at three positions along the rotor. Additionally, the axial displacement is measured at one end. The sensor positions are shown in Figure 6.3.

The results of the measurements with the above experimental set-up are shown in Figure 6.4. In the central waterfall diagram for each rotational speed ω (y-axis) the power spectrum of the motion of the impeller is plotted with the observed frequencies ν along the x-axis. The two diagonals indicate the $\nu = \omega$ and $2\nu = \omega$ lines. To the left and to the right of the waterfall diagram orbits of the impeller end of the rotor are plotted for four different rotational frequencies. One observes increasingly complex behavior. In Chapter 7 an analysis of the Poincaré sections of the orbits also reveals quasiperiodic behavior.

In the waterfall diagram it can be seen that above a threshold of about 400 Hz there are mainly two frequencies present in the power spectrum, while there is only one present below 400 Hz. The one frequency always present is equal to the driving frequency, which is due to a harmonic response to unbalance forcing. Around 1000 Hz there is a peak with large amplitudes, which is caused by the resonance of the first bending mode of the rotor. The other frequency is a subharmonic, large amplitude vibration which sets in above 500 Hz. Around the resonance of the bending mode the amplitude of this mode drops, only to increase again above the critical speed of 1000 Hz. This
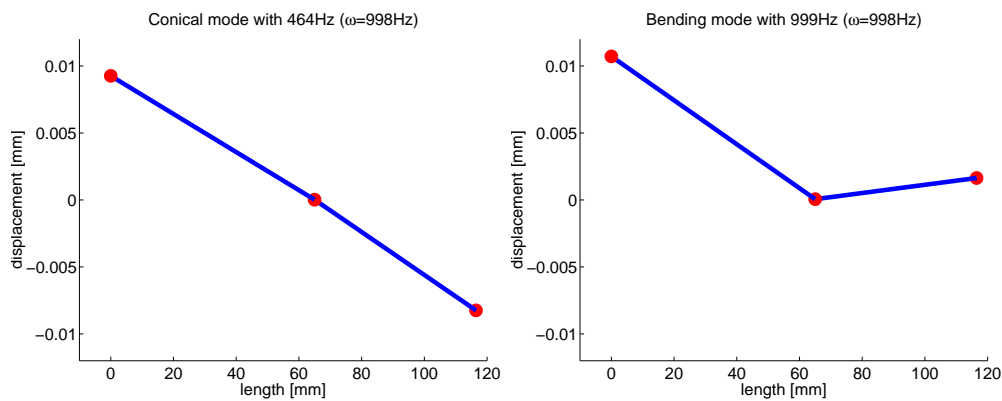
Figure 6.5: The running modes measured in experiment (set-up 1) are an allmost rigid conical mode (left) and a bending mode (right). Red markers indicate the measuring positions, points in between are unknown.

phenomenon is known as entrainment. The subharmonic vibration is called oil whirl, as it is a rotor instability which is caused by the oil-lubricated bearings. This instability has been known for a long time (Newkirk & Taylor, 1925) and has been investigated thoroughly in (Muszynska, 1986; Muszynska, 1988; Crandall, 1995; Hollis & Taylor, 1986) among others. In Figure 6.4, but also in Figure 6.6 below, one can see that the whirl frequency is about half the driving frequency for rotational speeds below the critical speed of 1000 Hz. For higher rotational speeds the frequency of the oil whirl still increases, but no longer linearly. The ratio of whirl frequency to rotational speed drops from $\frac{1}{2}$ at 500 Hz to approximately $\frac{2}{5}$ at 1500 Hz and one observes a shift away from the $\frac{\omega}{2}$-line.

The running mode shapes can also be calculated from the experimental data. They are shown in Figure 6.5. There are two main running modes at a rotational speed of 998 Hz: a conical mode of the subharmonic oil whirl with a frequency of less than half the rotor speed and a bending mode synchronous with the rotation.

As mentioned above several experiments with varying parameters were carried out. The experimental parameters are given in Table 6.1. In Figure 6.6 the Campbell diagrams for 4 different situations are depicted. In these diagrams, the *x*-coordinate of the centers of the circles gives the response frequency, the *y*-coordinate the driving frequency, and the radii of the represent the amplitudes of the underlying Fourier modes.

The comparison of the cases 1 and 2 shows that a variation of the unbalance parameter has little influence on the occurrence and the frequency of the oil whirl. In case 2, the amplitudes of the oil whirl are smaller, while the entrainment is more pronounced. The measurements in case 3 and 4 show that the oil whirl is suppressed by a reduction the bearing clearance or the bearing width. However, these modifications lead to
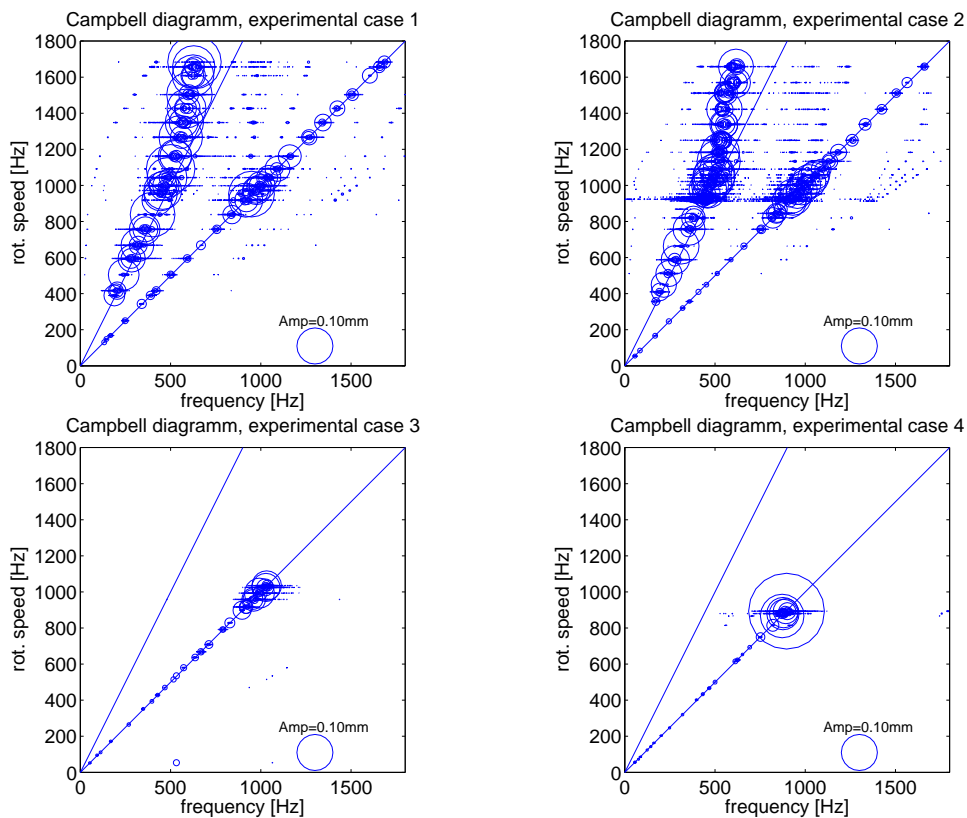
Figure 6.6: Campbell diagram showing amplitudes (radius of circles) and frequency (position of center) of the oscillations at impeller side for 4 different experimental set-ups. For the experimental parameters see Table 6.1. Circles on the diagonal are due to harmonic response, circles to the left of the line indicating half-frequency response are due to self-excited vibration.

larger unbalance oscillations in the resonance region of the bending mode. These large oscillations caused the limitation of these two experiments to the speed region below 60000 RPM (1000 Hz), since bearing failures and extreme noise occurred.

Case	rad. clearance	bearing width	unbalance [10^{-7}kgm],[rad]			
#	[mm]	[mm]	a_3, ψ_3	, a_5, ψ_5	a_{11}, ψ_{11}	a_{13}, ψ_{13}
1	0.02	5.4	1.35, π	1.50, 0	2.01, 0	2.07, π
2	0.02	5.4	0.64, 0	0.75, 0	0.98, π	1.09, π
3	0.01	5.4	1.35, π	1.50, 0	2.01, 0	2.07, π
4	0.02	3.8	1.35, π	1.50, 0	2.01, 0	2.07, π

Table 6.1: Experimental parameters for the results shown in Figure 6.6.
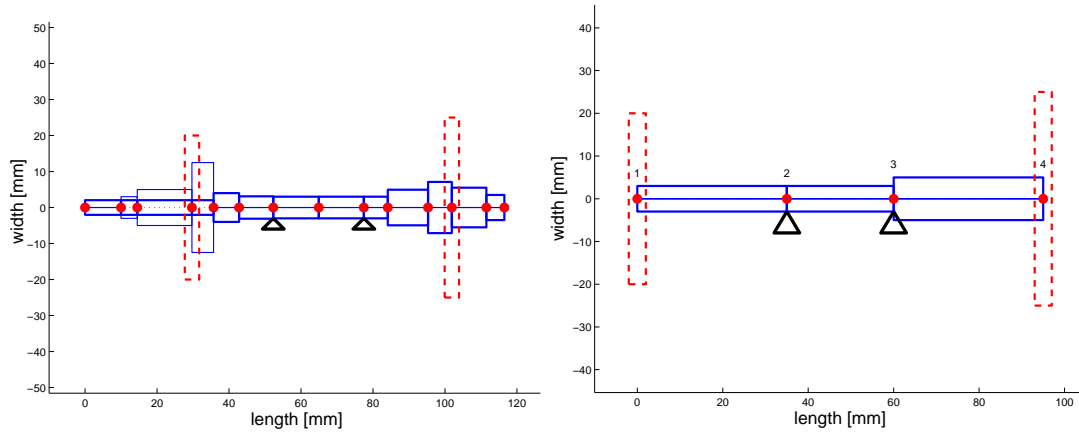
Figure 6.7: A detailed 13 element beam model (left) and a less detailed 3 element beam model (right) used in numerical simulations. The 3 element model is also used in the investigation of oil-film influence and numerical bifurcation analysis. The rigid discs modelling impeller and turbine are shown in red dashed lines and the positions of the bearings are indicated by the black triangles.

6.4   Simulations for Large Rotor Model

In the joint research project with TCRDL direct numerical simulations were performed for several rotor models of varying element number. These were a larger model with 13 beam elements (cf. Section 4.5.1) that was also considered for shape optimization in (Strauß, 2005), as well as a smaller model with 4 beam elements that is also used in the investigation of the influence of the lubrication model in Section 6.5 and in the bifurcation analysis in Chapter 7.

The analytic formulation of the bearing reaction forces in the short bearing approximation allows for their fast computation. This reduces the computation time for direct numerical simulation considerabely. The 13 element rotor model is depicted again in Figure 6.7 with the positions of the short bearings indicated by triangles. The bearing and unbalance parameters are chosen as in the experimental case 1 (cf. Table 6.1) with a dynamic viscosity of $\eta = 0.049$ Pas. The integration of Equation (6.9) with bearing force functions given by the zeroth order short bearing approximation (5.159) and (5.160) is done by applying `ode15s` with maximal order set to 2 and a relative tolerance of 10^{-2}. The only remaining free parameter that is not known from the experiment is the viscous damping coefficient that is used in the damping matrix C in Equation (6.9). It is set to 9 Ns/m in this simulation.

The results are shown in Figure 6.8 and one can see from the waterfall diagram that the main dynamical features of the experiment are reproduced. The complexity of the orbits increases with the rotational speed and also the amplitudes are only slightly larger than in experiment. Entrainment can be observed around a rotational speed
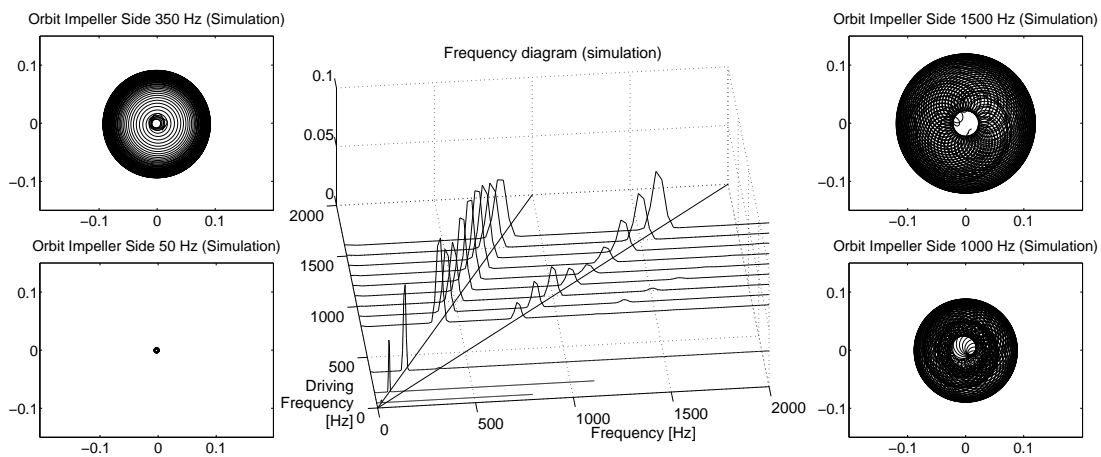
Figure 6.8: Simulated orbits and waterfall diagram for 13 element beam model and parameters as in experimental set-up 1 with external damping coefficient 9 Ns/m. The main experimentally observed vibration effects of subharmonic oil whirl and synchronous unbalance vibration are captured in the model.
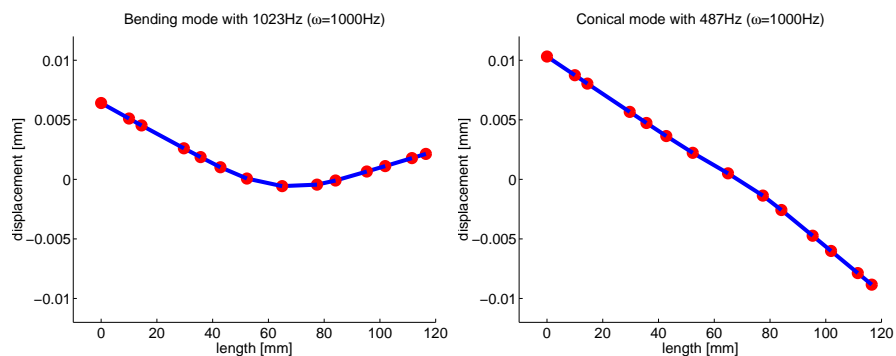

Figure 6.9: The running modes from simulation with ext. damping coefficient 9 Ns/m are similar to those from the experiment. Associated to the subharmonic oil whirl is an allmost rigid conical mode, while the harmonic part has the curved shape of a first bending mode.

of 1000 Hz where the first resonance of the harmonic response occurs. The running modes can also be calculated and are shown in Figure 6.9. In good agreement with the experiments the subharmonic mode is a conical mode, while the harmonic response consists of a bending mode.

There are however two differences between the simulations and the experiments. In the simulations there appears a second peak in the harmonic response, which is caused by the resonance of a second bending mode. This can not be observed in the experiments. Furthermore, the ratio of the oil whirl frequency and the driving frequency remains constant $\frac{1}{2}$ and the shift to lower frequency ratios does not occur. This phenomenon will be addressed later in Section 6.5.
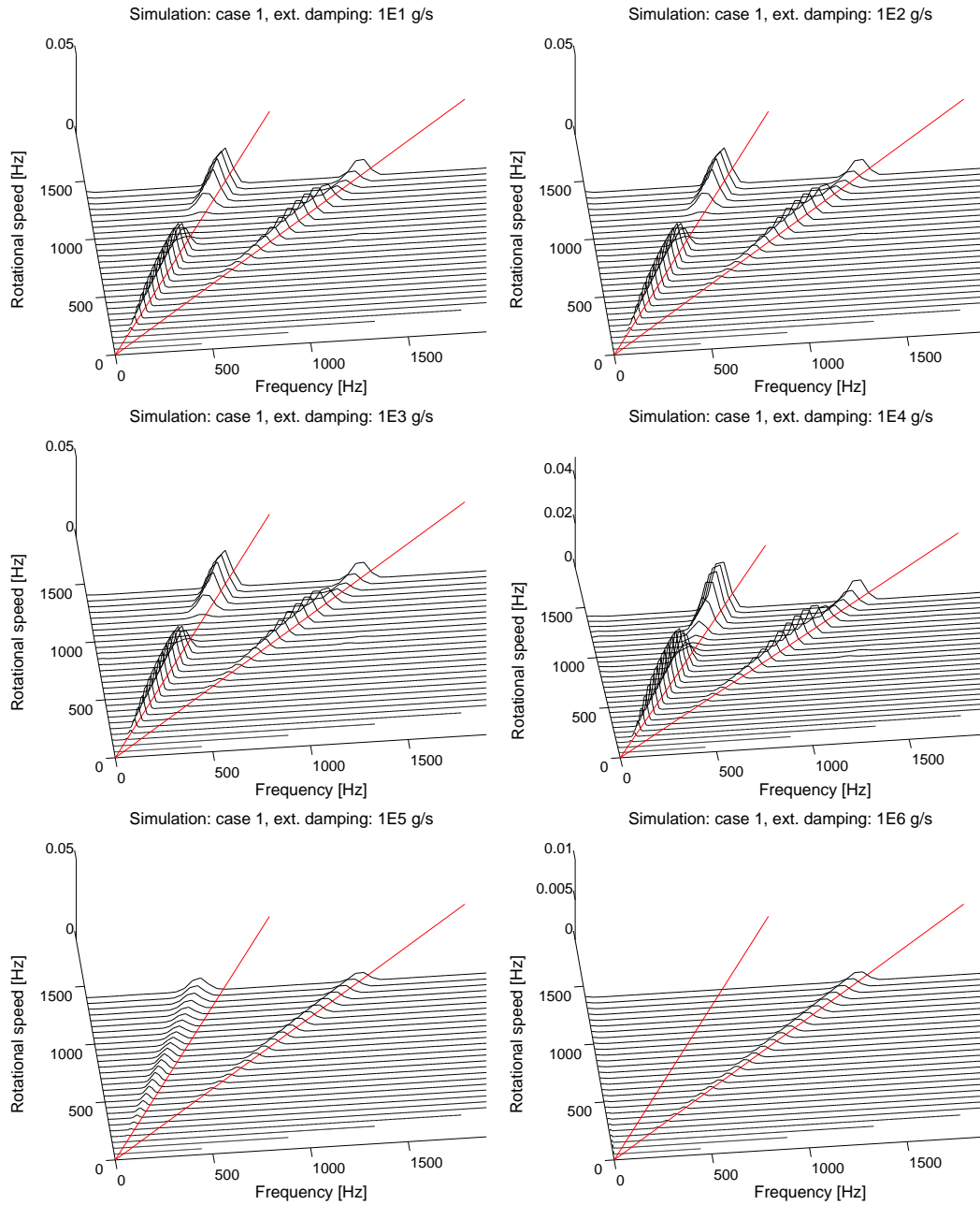
Figure 6.10: Waterfall diagrams for simulations using the same set-up as in the experimental case 1; external damping coefficient is varying from 10^{-2} Ns/m to 10^3 Ns/m. For small external damping the entrainment effect for driving frequencies around 1000 Hz is strongly developed, while for higher damping the self-excited oscillation can be completely suppressed. For $D = 10^3$ Ns/m (lower left) the subharmonic part of the response is shifted slightly to lower frequencies, i.e. to the left of the $\frac{1}{2}\omega$-line.

In order to further evaluate the model and to find an appropriate external damping parameter more simulations with this model have been carried out. The external damping coefficient is varied from 10^{-2}Ns/m to 10^4Ns/m to study its influence. The

results are shown in waterfall diagrams in Fig. 6.10. Note that significant features of the experiment such as the half-frequency oil whirl, harmonic unbalance resonance and entrainment are reproduced. The variation of the damping coefficient shows that the oil whirl instability can be completely suppressed by increasing the viscous damping. Furthermore the frequency ratio of oil whirl to driving frequency can also be influenced. In the central panel of the lower row the ratio of the two frequencies is still constant, but slightly less than $\frac{1}{2}$. It can be said that the external damping plays a big role. Its influence is examined in more detail in Chapter 7 where continuation methods are used to determine the exact values for which the oil whirl is suppressed. The frequency shift seems to depend not only on the external damping but also on the lubrication model used. This will be investigated partly in the next section.
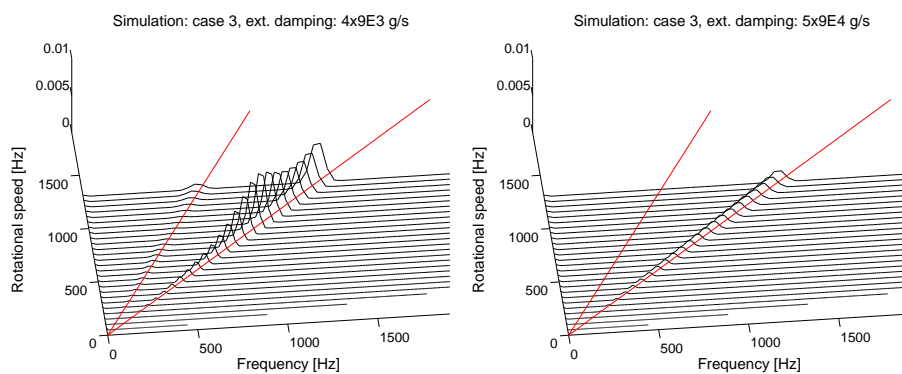
Figure 6.11: Simulation results with higher viscosity η = 0.2188 Pas; external damping 36 Ns/m (left) and 450 Ns/m (right): the higher viscosity leads to a stronger damping and to the suppression of the self-excited part of the vibration response; stronger damping also suppresses the harmonic part.
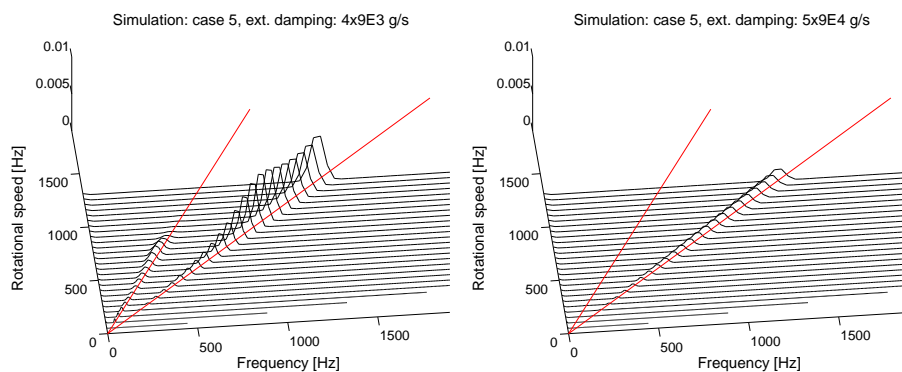
Figure 6.12: Simulation results with reduced radial bearing clearance c_r = 0.01 mm: the subharmonic part of the response is suppressed for frequencies above 1000 Hz for external damping of 36 Ns/m (left); for external damping of 450 Ns/m (right) it vanishes completely.

The figures 6.11, 6.12 and 6.13 show results from simulations done with different parameter values, such as higher viscosity, smaller radial clearance or smaller bearing
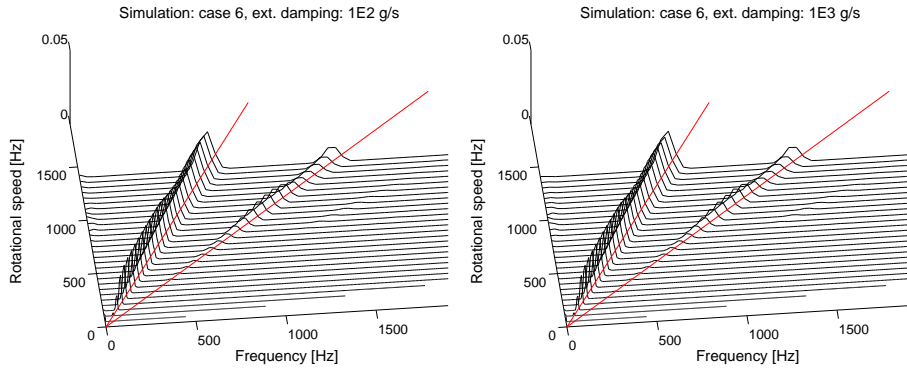
Figure 6.13: Simulation results with reduced bearing length $B = 3.8$ mm; external damping 0.1 Ns/m (left) and 1 Ns/m (right). For both damping values the subharmonic response is quite large in contrast to the experiment.

length. In all of these simulations we can observe self-excited oscillations and unbalance oscillation. Entrainment is also present for smaller external damping. Especially the effect of the reduction of the bearing clearance is reproduced very well. For both values of the damping parameter the oil whirl is almost entirely suppressed. In contrast to that, in the simulations the reduction of the bearing width leads to oil whirl with an even larger amplitude, while the corresponding experiment shows no self-excited oscillations. This result could be due to a stronger influence of the oil-inlet which is neglected in the model, due to inclination of the shaft, or also due to a rotor damaged by previous experiments.

6.5   Influence of Oilfilm Model on Dynamics

In the last section the simulations of the larger 13 beam element model with short bearing lubrication model already showed quite good agreement with the experimental data. The main difference between the calculated and the measured power spectrum is the shift of the frequency of the oil whirl away from the line $v = \frac{\omega}{2}$. The results in Figure 6.10 show that increased damping leads to such a shift but also to the suppression of the oil whirl.

6.5.1   Simulations with Phenomenological Bearing Model

From looking at the equations for the bearing reaction forces of the short bearing (5.159) and (5.160), we see that the forces vanish for value of $\dot{\gamma} = \frac{\omega}{2}$ and $\dot{\kappa} = 0$. This leads to the reasonable conjecture, that the whirl frequency can be influenced by the lubrication model. The phenomenological model proposed in Section 5.2 is a simple modification of the short bearing lubrication model. In Section 5.2 the factor $\frac{\omega}{2}$ is identified as the
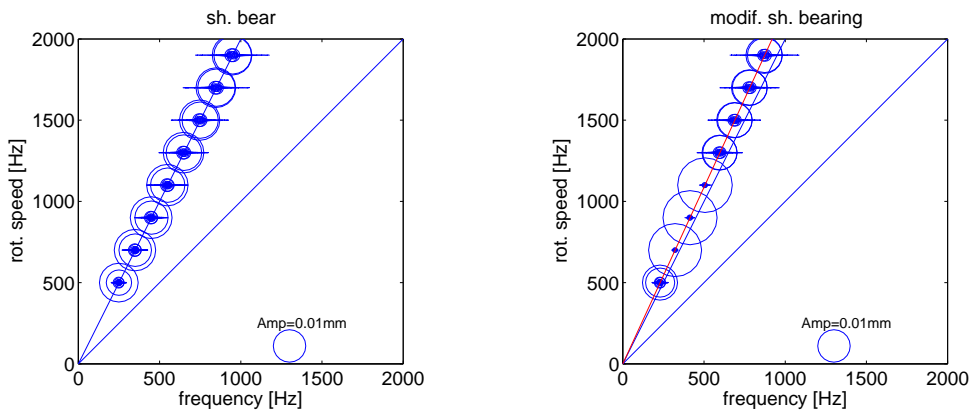
Figure 6.14: Modified bearing function leads to frequency shift; left: short bearing solution ($s \equiv 0$), right: $\frac{\omega}{2}$-term changed to 0.46ω ($s = 0.04\omega$) in Eq. (6.23); blue: lines $\nu = \omega$ and $\nu = \frac{\omega}{2}$, red: ($\nu = 0.46\omega$)-line coincides with actual frequency of self-excited oscillation ($D = 0.001$, $M = 100$, $f_{\text{unb}} = 2.3 \cdot 10^{-7}$).

lubrication fluid's average circumferential velocity and a correction term is introduced that changes this velocity. The resulting pressure function then looks as follows

$$\bar{p}^0 = -6 \frac{\bar{z}}{W} \left(\frac{\bar{z}}{W} - 1 \right) \frac{W^2 \rho \nu}{c_r^2} \frac{\left((\dot{\gamma} - \frac{\omega}{2} + s(\omega))\kappa \sin \varphi + \dot{\kappa}' \cos \varphi \right)}{(1 - \kappa \cos \varphi)^3}. \tag{6.23}$$

As a first test for this phenomenological model we integrate the simple model (6.16) using first short bearing approximation and second the corrected pressure from (6.23) with $s(\omega) = 0.04\omega$. The comparison of the results depicted in Figure 6.14 shows that the linearly shifted peaks of the self-excited oscillation of the corrected model lie on the $\nu = \frac{2.3\omega}{5}$ line, while the peaks for the uncorrected model lie on the $\nu = \frac{\omega}{2}$ line. This clearly indicates a direct influence of the correction on the whirl frequency.

To further investigate the influence of the modification term $s(\omega)$ we simulate a smaller rotor model with 3 beam elements as depicted in Figure 6.7 using the phenomenologically corrected short bearing pressure function (6.23) with a quadratic correction term $s = \sigma \frac{\omega^2}{\omega_0}$. The sole reason for introducing $\omega_0 = 1000$ Hz into the term is to normalize it, so that not too small values of σ have to be used.

In Figure 6.15 the Campbell diagrams a depicted for varying values of $\sigma \in [0, 0.2]$. For small values of σ the spectrum is similar to the uncorrected one in the top left corner. All diagrams show the presence of a harmonic response with a resonance around 900 Hz. The line $\nu = \omega$ on which the circles of the harmonic part lie and the line $\nu = \frac{\omega}{2}$ are indicated in blue. The circles indicating the self-excited oscillation are always located on the curves $\nu = \frac{\omega}{2} - \frac{\sigma \omega^2}{\omega_0}$ which are depicted in red. As σ grows, the red lines, and hence the peaks of the self-excited oscillation, bend away more and more from the blue line $\nu = \frac{\omega}{2}$, a behavior similar to the experiment. Additionally it can be observed that the large amplitude oscillation which is present at 1800 Hz for $\sigma = 0$, is pushed
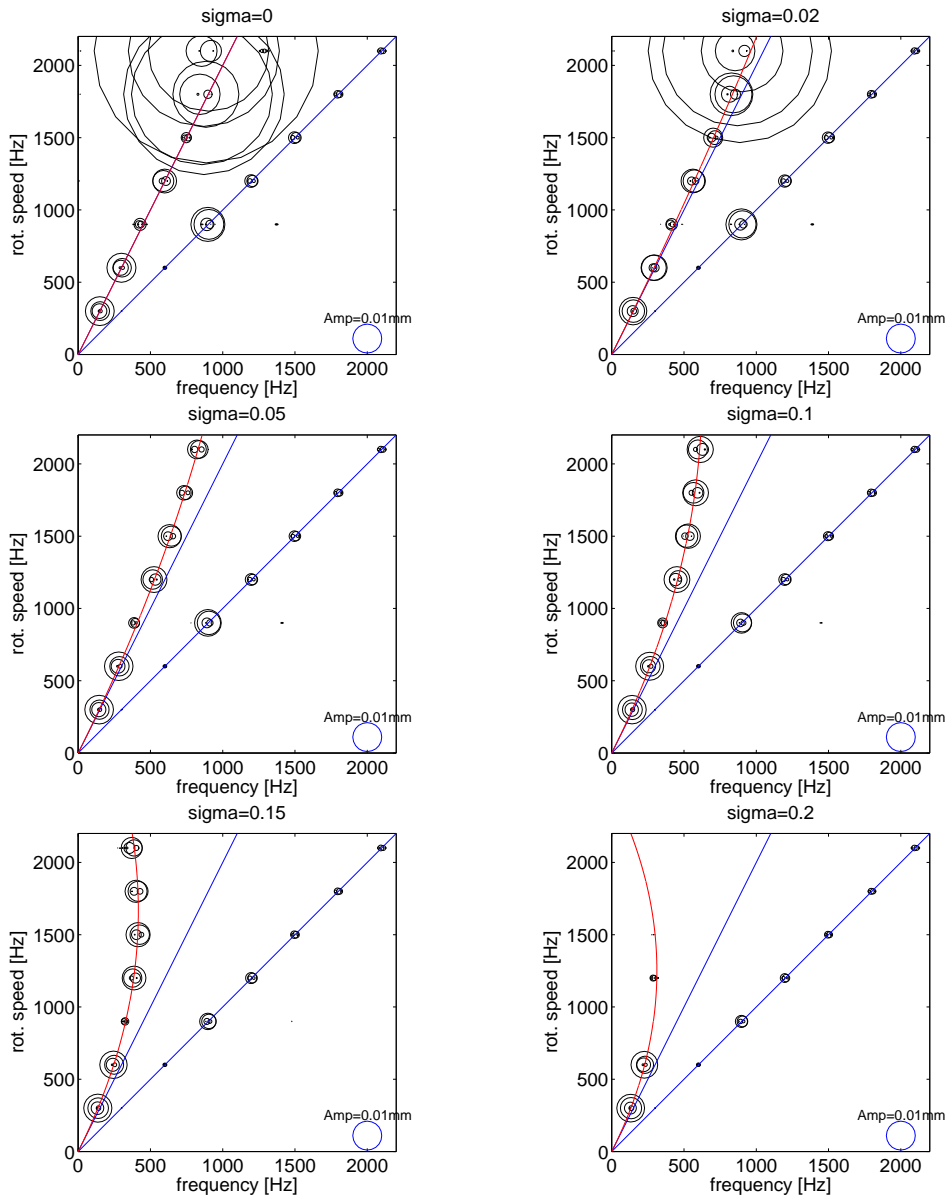
Figure 6.15: Campbell diagrams for simulation of small beam model with phenomenological correction of short bearing. σ is the tuning parameter. The subharmonic part of the response allways lies on the curve $v(\omega) = \frac{\omega}{2} - s(\omega) = \frac{\omega}{2} - \frac{\sigma\omega^2}{\omega_0}$ with $\omega_0 = 2\pi \cdot 1000\frac{rad}{s}$.

towards higher frequencies and finally out of the range of simulated rotational speeds.

This illustrates again the important influence of the lubrication model on the whole dynamics. In (Crandall, 1995) it is shown by considering force equilibria that the onset frequency of the oil-whip, the large amplitude oscillation which starts in our example at around 1800 Hz, is double the eigenfrequency of the first bending mode. In (Muszynska, 1986) the fluid's average circumferential velocity is identified as additional critical speed. The coalescence of these two critical speeds leads to this harmful

phenomenon that is the oil-whip. In this case the self-excited vibration forces the bending oscillation causing the large amplitudes.

6.5.2 Varying the Lubrication Model

The last section has shown the importance of the lubrication model and especially of the average circumferential fluid velocity for the dynamical behavior of the rotor-bearing system. In Chapter 5 we have derived several bearing models which are more realistic than the short bearing approximation. In order to reproduce the experimentally observed shift of the ratio of the whirl frequency to the driving frequency these models have tested with the small 3 beam element rotor model which has 32 degrees of freedom (DOF), as well as with the simple model with 4 degrees of freedom (6.16).

According to (Childs, 1993) and (Yamamoto & Ishida, 2001) the zeroth order short bearing approximation is valid for ratios of bearing length to bearing radius $\frac{W}{R} < 1$. The bearings of the turbocharger of which the vibration behavior was examined in the experiments has a ratio $\frac{W}{R} = \frac{5.4}{3}$ and so the short bearing approxmation tends to give erroneous results. As a first step it is therefore interesting to investigate the behavior of the rotor when the bearing reaction forces are computed from the solution of Reynolds equation itself without the simplification of assuming a short bearing. Furthermore the choice of the boundary conditions which serve as a simple cavitation model could influence the vibration behavior. Two sets of boundary conditions described in more detail in Sections 5.3.2 and 5.5 are under consideration in the following simulations:

- the Gümbel boundary conditions prescribe the periodicity of the pressure in the circumferential direction and environment pressure ($p = 0$) at the bearing ends. After the solution the pressure is set to zero in the regions where it is negative.

- the Reynolds' boundary conditions additionally demand that $p \geq 0$ inside the domain which leads to a free boundary problem whose solution is quite time consuming and which has to solved every time the bearing forces are evaluated.

6.5.2.1 Simulations with Reynolds' Boundary Conditions

Since the solution of the free boundary boundary problem with the PSOR algorithm (cf. Section 5.4.1.3) is very time consuming, the simulations for this lubrication model are done with the 4 DOF model (6.16). Matlab's `ode15s` is used as integrator and the 5-point Laplacian (cf. Sec. 5.4.1) is used for the discretization of Reynolds' equation. This computational setup leads to very long computation times which definitely could be improved a lot by applying more sophisticated numerical methods. However, the results of this simple numerical experiment imply that the influence of the Reynolds' boundary conditions on the vibrations is neglectable. The frequency response is shown
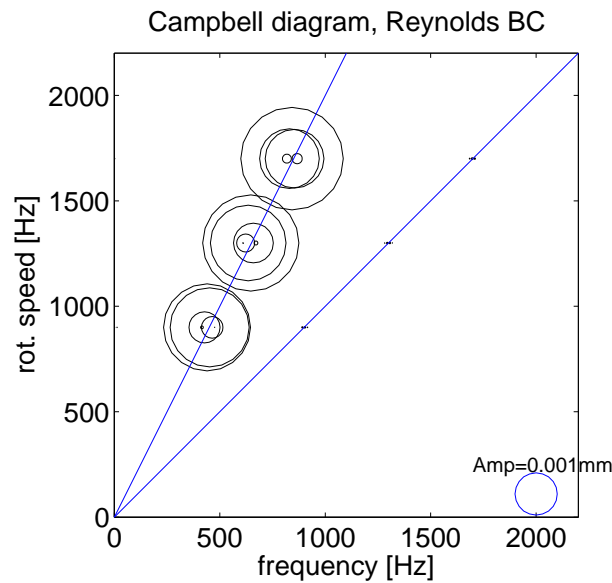
Figure 6.16: Spectrum from simulation of simple model (6.16) with Reynolds' boundary condition the lubrication equation shows no shift of subharmonic response.

in Figure 6.16 for a few driving frequencies. The parameters used in this simulation are $D = 0.5 \frac{\text{Ns}}{\text{m}}$, $u = 2.1 \cdot 10^{-7} \, \text{kg}\,\text{m}$ and $M = 0.1 \, \text{kg}$. The results show no significant shift of the subharmonic response.

6.5.2.2   Reynolds' Equation With/Without Inertia Correction

Although they provide a cruder cavitation model, the Gümbel conditions allow for a faster evaluation of the bearing forces, which accelerates the computation. In the following simulations Reynolds' equation with Gümbel boundary condition is used in the two variants derived in Section 5.1.6. We compare the solutions of the explicit model (6.9), that uses the zeroth order Reynolds' equation (5.89), with those of the implicit model (6.13), where the first order inertia corrected version of Reynolds' equation (5.89) is used. For the rotor itself the smaller 3 element model is used in both cases with the parameters as given in Appendix D.2. For the explicit model Matlab's `ode15s` solver for stiff problems is used. For the implicit model the solver routine `DASPK` is called from an `octave` script. The partial differential equations for the evaluation of the pressure distribution in each step are solved with the `deal.II` package as described in Section 5.4.2. The computations are again quite time consuming. The most critical part is the computation of the pressure distribution from Reynolds' equation. As we have seen in Sections 5.4.2, many degrees of freedom are needed to compute the bearing forces with sufficient accurateness. Less accuracy in the finite element solver often leads to failure in the ode solvers, which in that case run into discontinuities leading to nonconvergence of the underlying Newton method.
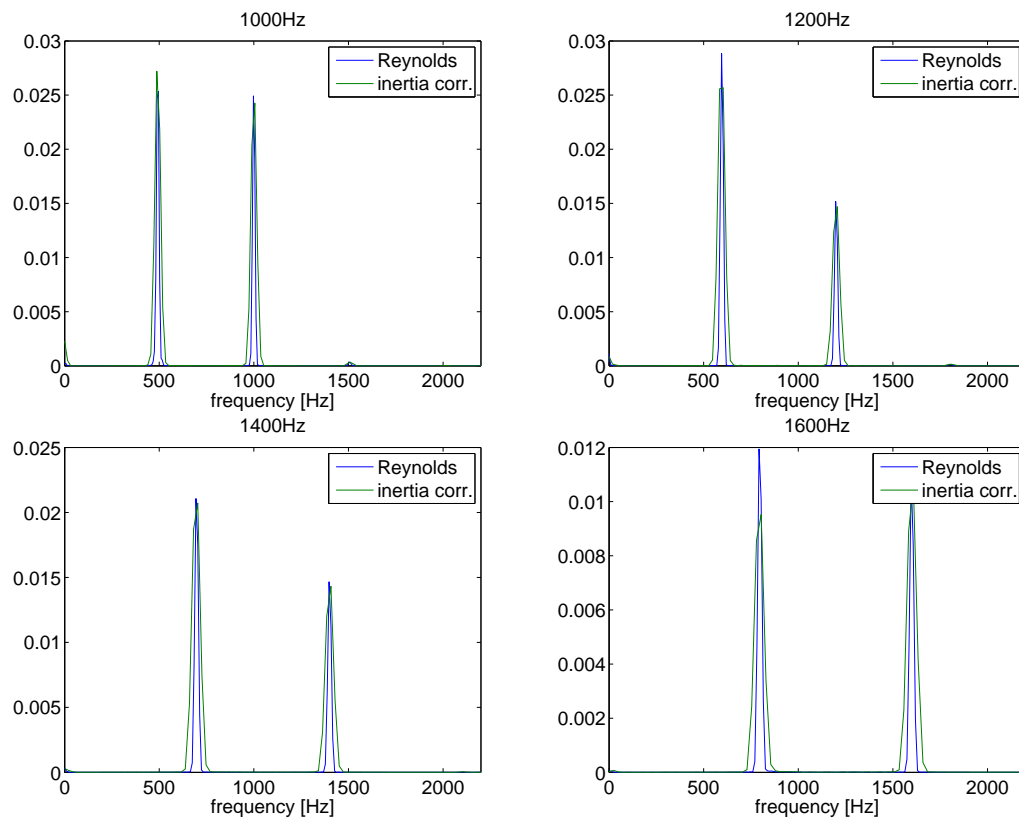
Figure 6.17: 3 element beam mode: comparison of the spectra of simulation results with zeroth order (blue) and first order (green) Reynolds' equation. No significant frequency shift of the subharmonic can be observed.

The results are shown in Figure 6.17. The power spectrum of the rotor vibration taken from the orbit of the turbine is shown for four different rotational speeds from the region in which the frequency shift is observed in the experiment. The blue peaks show the frequency response of the explicit system with zeroth order Reynolds' equation. The green peaks show the response of the implicit system with the inertia corrected version of Reynolds' equation. A frequency shift which is as significant as in the experiment cannot be observed. Computations over a longer time interval which allow for a better frequency resolution in the spectra are not done, since a significant frequency comparable to the one observed in experiment would be visible at this scale and the calculation time (in the order of several days for one rotational velocity) is prohibitively long.

6.5.2.3 Simulations Using Inertia Corrected Short Bearing Approximation

Faster computations are possible when we use the short bearing approximation which allows for an analytic formula for the pressure distribution in the case of inertia cor-
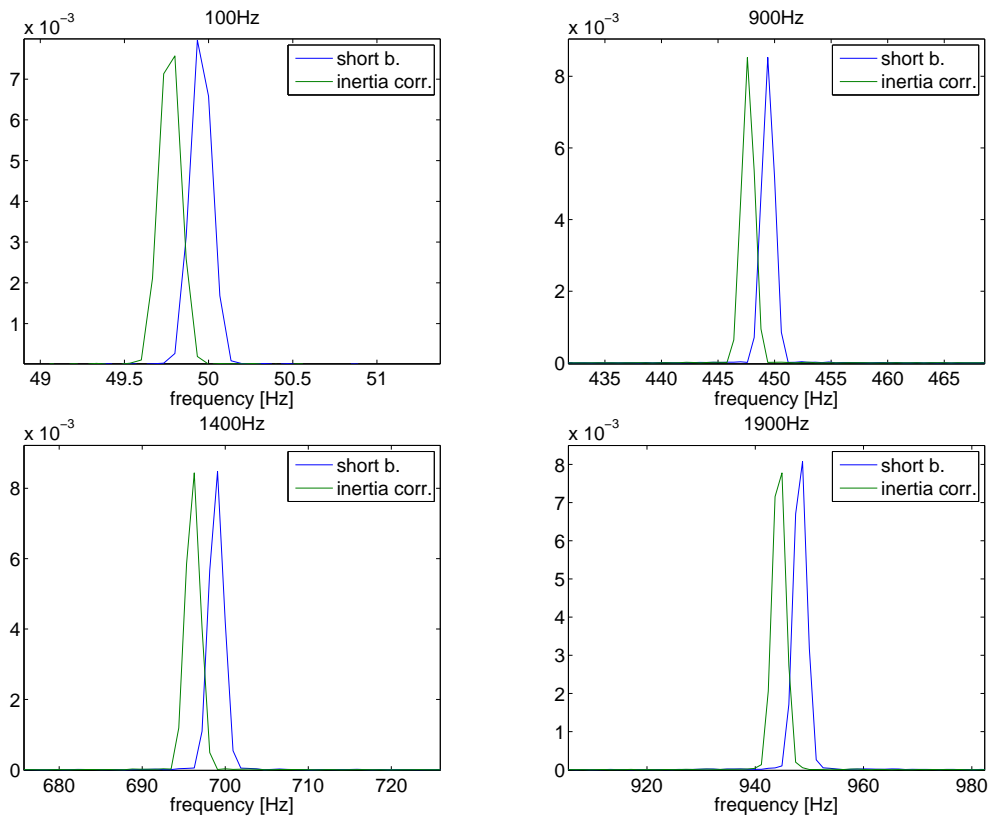
Figure 6.18: Comparison of subharmonic responses of simple model (6.16) for classical short bearing (blue) and inertia corrected short bearing (green). A frequency shift toward lower frequencies of about 1% compared to response of uncorrected system can be observed.

rected pressure, as well as in the case of zeroth order approximation. In Section 5.6 it is demonstrated that bearing parameters similar to those form the experiment ($R = 3$ mm, $W = 5.4$ mm, $c_r = 0.02$ mm) lead to erroneous results in the pressure distribution especially for the inertia corrected pressure. To evaluate the influence of the inertia correction on the frequency of the oil whirl, the simple model (6.16) is simulated ($M = 1$ g, $D = 1e − 3$g/s, $u = 3e − 7$gmm) with both lubrication models (5.47) and (5.63) and a bearing configuration for which the short bearing approximation and the inertia correction are valid ($R = 3$ mm, $W = 0.25$ mm, $c_r = 0.02$ mm). DASPK is used for time integration in both cases, the explicit case using the zeroth order short bearing approximation and the implicit case using inertia corrected first order short bearing approximation.

The results of these simulations are depicted in Figure 6.18. They show that the subharmonic response of the inertia corrected model (green) displays a frequency shift to the response of the model using the classical short bearing approximation (blue). The shift, however, is not of the same magnitude as observed in the experiments, but it is relatively small. Compared to the subharmonic response of the uncorrected

model with its $\frac{\omega}{2}$-response, the response of the inertia corrected system is between 0.5% and 1% lower. This clearly shows that the inertia correction has an influence on the self-excited oscillation, but it also indicates that the large frequency shift observed in experiment can not be fully explained by this correction.

6.6   Conclusions from the Simulations

To conclude this chapter we summarize here the results and comment on the quality of the proposed model.

- The simulations show that the presented beam model together with the short bearing approximation for the hydrodynamic bearings reproduces the dynamical behavior of the turbocharger quite well. In good agreement with the experimental results it exhibits the harmonic unbalance response, the self-excited subharmonic oscillation known as oil whirl, and the same vibration modes.

- In the model with short bearing the dependence on parameters such as bearing width, radial clearance, and oil viscosity is similar to the experimental response to parameter variation.

- The external damping constant is a parameter unknown in experiment. Its influence can be used to suppress the self-excited oscillation and to influence its frequency.

- The frequency of the oil whirl can be influenced by varying the lubricant's average circumferential velocity. By introducing a phenomenological correction term into the short bearing approximation it is possible to prescribe the frequency of this self-excited oscillation.

- The ratio of oil whirl frequency to forcing frequency differs between experiment and simulation. The variation of the lubrication model does not have a large effect on this ratio. The use of zeroth order Reynolds' equation neither with Gümbel boundary conditions, nor with Reynolds' boundary conditions instead of the short bearing approximation leads to a reduction of the whirl-forcing ratio.

- The inertia correction of Reynolds equation also leads to no significant shift of the whirl-forcing ratio, while the computation time is considerably longer due to the required solution of 3 partial differential equations in each time step.

- The inertia correction of the short bearing approximation has a small influence on the frequency of the oil whirl. The ratio of oil whirl frequency to forcing frequency is close to $\frac{1}{2}$ for the uncorrected classical short bearing approximation. For the inertia corrected short bearing approximation the ratios drops by approximately 1%.

These results suggest that the short bearing approximation is a good compromise for simulations where the computation time is critical, such as e.g. in an shape optimization framework. The inclusion of the phenomenological correction for the circumferential lubricant velocity allows to reproduce a measured frequency behavior of a certain bearing type without detailed modeling of the bearing, and without the computational effort of solving partial differential equations in each time or optimization step.

However, the determination of the overall frequency response of the system by direct numerical simulation is somewhat inefficient, since it is first necessary to compute also the transient behavior at the beginning and to determine the end of the transient region. Secondly the accuracy of the Fourier spectra depends on the length of the simulated interval. In order to compute the frequency response more efficiently, continuation methods seem to be more appropriate which follow the periodic orbit in parameter space and which do not require the computaition of transients. Such methods are introduced and applied to the above models in the following Chapter 7.

Chapter 7

Numerical Bifurcation Analysis

The direct numerical simulation of the model equations is a popular approach for the investigation of systems response. By solving multiple initial value problems it allows for validation of the model equations over a broader parameter range and also for the classification of solutions. However, as we have seen in Chapter 6, the direct numerical simulation can be very time consuming, not only because transient behavior has to be accounted for, but also due to long data sets being necessary for the subsequent analysis of the solution with e.g. Fourier analysis.

Numerical continuation and bifurcation methods are an useful and efficient alternative. These techniques not only provide efficient means of computing certain types of solutions, but also allow the detection and classification of bifurcations, i.e. qualitative changes of the solution. They are therefore better suited for extensive parameter studies. Bifurcation theory is a very broad and flourishing field. We refer to the textbooks (Chow & Hale, 1982; Kuznetsov, 2004; Nayfeh, 2000; Nayfeh & Balachandran, 1995; Wiggins, 1990) and the references there for more information on bifurcation theory. There are some well-established software-packages for the computation of equilibria and periodic solutions such as AUTO (Doedel *et al.*, 2000), CONTENT (Kuznetsov & Levitin, 1997), or MATCONT (Dhooge *et al.*, 2004). These packages provide methods for detecting pitchfork, transcritical, period-doubling, and Neimark-Sacker bifurcations. Furthermore, loci of such bifurcations can be computed in a two-parameter plane.

In this chapter the software-package AUTO 2000 (Doedel *et al.*, 2000) is used to study the parameter dependency and the bifurcation behavior of equilibria and also of periodic solutions of the equations that model the dynamics of a fast rotating body in hydrodynamic bearings. Additionally, a method proposed in (Schilder & Peckham, 2007) and implemented in the package TORCONT (Schilder, 2004) is used to continue the quasi-periodic solutions which also have been observed in the direct numerical simulations and in the experiments.

7.1   Short Overview of Continuation Methods and Bifurcation Theory

Continuation methods are based on the Implicit Function theorem (Chow & Hale, 1982). For a given solution $(x_0, \lambda_0) \in X \times \Lambda$ of an equation

$$F(x, \lambda) = 0 \qquad\qquad\qquad (7.1)$$

with a Fréchet differentiable function $F : X \times \Lambda \to Z$, where X and Z are Banach spaces, and the parameter set Λ is an open set in a Banach space, the boundedness of the derivative $D_x F$ asserts the existence of a a function $x^*(\lambda)$ that parametrizes the solutions in a neighborhood of (x_0, λ_0), i.e. for (x, λ) in that neighborhood we have $F(x, \lambda) = 0$ iff $x = x^*(\lambda)$. In points where the differentiability condition fails the qualitative behavior of the solutions can change. These points are called bifurcation points.

In this chapter we will mainly come across two types of bifurcations: the Hopf bifurcation and the Neimark-Sacker or torus bifurcation. The two bifurcations are closely related, since both are occurring at the onset of self-excited vibrations. The Hopf bifurcation describes the bifurcation of a periodic orbit from a branch of equilibrium solutions, while the torus bifurcation describes the bifurcation of an invariant torus from a branch of periodic orbits leading to the appearance of a second frequency in the solution.

The Hopf bifurcation theorem (Guckenheimer & Holmes, 1983; Kuznetsov, 2004) states that generically, if an ordinary differential equation $\dot{x} = f(x, \mu)$, $x \in \mathbb{R}^n, \mu \in \mathbb{R}$ has an equilibrium at (x_0, μ_0) at which a pair of complex conjugate eigenvalues of the Jacobian $D_x f(x, \mu_0)$ crosses the imaginary axes transversally, there exists a family of periodic orbits close to the equilibrium towards one side of the bifurcation value of the parameter, i.e. for $\mu > \mu_0$ or for $\mu < \mu_0$. The stability of the equilibrium changes in μ_0 and the periodic orbit is always of a different stability type than the equilibrium on its side of the bifurcation value.

The Neimark-Sacker bifurcation is the equivalent bifurcation for fixed points of maps. It occurs when the one-parameter family of maps $f_\mu : x \mapsto f_\mu(x)$ has a fixed point (x_0, μ_0) at which the Jacobian $D_x f_{\mu_0}$ has a pair of complex conjugate eigenvalues $\lambda, \bar{\lambda}$ which cross the unit circle transversally at μ_0. Furthermore, the additional non-resonance conditions $\lambda^n \neq 1$ for $n = 1, 2, 3, 4$ are required. If these conditions are fulfilled there exists an invariant circle of the map f_μ on one side of the bifurcation value. This is of particular importance for the bifurcation of limit cycles of ordinary differential equations. The stability of a limit cycle is given by the Floquet multipliers, which are the eigenvalues of the stroboscopic or Poincaré map of the cycle. The limit cycle corresponds to a fixed point of the Poincaré map and if a pair of multipliers crosses the unit circle, this fixed point undergoes a Neimark-Sacker bifurcation and an invariant circle

of the Poincaré map appears. This invariant circle corresponds to a two-dimensional invariant torus that bifurcates from the limit cycle. Under the additional assumption of normal hyperbolicity the torus persists for small parameter changes (Fenichel, 1971). The dynamics on this invariant torus can either be periodic or quasi-periodic. The periodic case is structurally stable, while the quasi-periodic flow can be destroyed by arbitrarily small parameter variations. However the measure of the set of parameter values where quasiperiodic behavior on the torus can occur is non-zero and there is hence a non-zero probability to observe it (Wiggins, 1990).

The Implicit Function theorem is the foundation for the numerical continuation methods that are used in the following. The solutions that are continued can have different natures. In the case of equilibrium solutions of an ordinary differential equation $\dot{x} = f(x, \lambda)$ with $f : \mathbb{R}^n \times \mathbb{R} \rightarrow \mathbb{R}^n$, starting from a known equilibrium (x_0, λ_0) with $f(x_0, \lambda_0) = 0$ and nonsingular Jacobian, a Newton-type method can be used to compute a nearby equilibrium, the existence of which is guaranteed by the above theorem.

The case of the continuation of periodic solutions of a differential equation can be regarded as an infinite dimensional analogon of the above. Consider the function F going from the space of continuously differentiable functions to R^{2n+1}, and mapping a function φ on the residual of the boundary value problem

$$F : C^1([0, 1]) \times \mathbb{R} \times \Lambda \rightarrow R^{2n+1}, \tag{7.2}$$

$$F(\varphi, T, \lambda) = \begin{pmatrix} \dot{\varphi} - Tf(\varphi, \lambda) \\ \varphi(1) - \varphi(0) \\ \Psi(\varphi) \end{pmatrix}. \tag{7.3}$$

Then a zero of F is a solution to the boundary value problem, i.e. a periodic solution of the original equation. The first component of F is the differential equation, the second is the boundary condition which asserts periodicity, and the third is a phase condition which chooses on particular solution out of the possible shifted ones. Differentiability conditions on analogous to the equilibrium case then allow a continuation in parameter space.

A detailed overview of the numerical methods used in AUTO can be found in (Beyn *et al.*, 2002; Doedel *et al.*, 1991a; Doedel *et al.*, 1991b; Kuznetsov, 2004). AUTO uses pseudo-arclength continuation (Keller, 1977) which allows the continuation also around folds. The system $F(x, \lambda) = 0$, $\lambda \in \mathbb{R}$ with a zero in (x_0, λ_0) is augmented with an additional equation which fixes the stepsize along the solution branch

$$F(x_1, \lambda_1) = 0, \tag{7.4}$$

$$(x_1 - x_0)x' + (\lambda_1 - \lambda_0)\lambda' - \Delta s = 0, \tag{7.5}$$

where (x_0, λ_0) is the current position on the branch, (x_1, λ_1) the unknown next point, and $(x', \alpha'$ the normalized tangent vector of the branch in (x_0, λ_0). The advantage of this formulation is, that the Jacobian of the left hand side is always nonsingular as long

as the solution is regular, i.e. the Jacobian $DF = (DF_x, DF_\lambda)$ of the original equation has rank n and only one solution branch passes through the solution (Beyn *et al.*, 2002). Bifurcations are detected by test functions which have zeros at the bifurcation points, e.g. the determinant of the Jacobian of the augmented system (7.4) and (7.5) is used as test function for a branch point. In AUTO the real part of the complex eigenvalue with smallest absolute value of the real part is used as test function for Hopf bifurcation points.

The computation of invariant tori is currently an active area of research. An overview of recent contributions can be found in the introduction of (Schilder *et al.*, 2005). The recently developed package TORCONT (Schilder, 2004) is used for the continuation in invariant tori with quasiperiodic solutions in Section 7.7.3. The technique is based on the computation of a Fourier approximation of the invariant circle of the Poincaré map. More details and references are given in Section 7.7.2.

7.2   Reformulations of Equations of Motion

The equations of motion for rotordynamical systems are derived in Chapters 2 to 5. They are an explicit system of ordinary differential equations

$$M\ddot{x} + (\omega G + C)\dot{x} + Kx = F_{\mathrm{gr}} + F_{\mathrm{unb}}(t) + F_{\mathrm{bear}}(x_b, \dot{x}_b), \tag{7.6}$$

if the bearing force function does not depend on the nodal acceleration of the bearing nodes. In first order form it reads

$$\begin{pmatrix} M & \\ & I \end{pmatrix}\dot{y} = \begin{pmatrix} -(\omega G + C) & -K \\ I & 0 \end{pmatrix}y + \begin{pmatrix} F_{\mathrm{gr}} + F_{\mathrm{unb}}(t) + F_{\mathrm{bear}}(y_b) \\ 0 \end{pmatrix}. \tag{7.7}$$

If the bearing force function does depend on the nodal acceleration, the system becomes implicit

$$M\ddot{x} + (\omega G + C)\dot{x} + Kx = F_{\mathrm{gr}} + F_{\mathrm{unb}}(t) + F_{\mathrm{bear}}(x_b, \dot{x}_b, \ddot{x}_b). \tag{7.8}$$

The first order form is

$$\begin{pmatrix} M & \\ & I \end{pmatrix}\dot{y} = \begin{pmatrix} -(\omega G + C) & -K \\ I & 0 \end{pmatrix}y + \begin{pmatrix} F_{\mathrm{gr}} + F_{\mathrm{unb}}(t) + F_{\mathrm{bear}}(y_b, \dot{y}_b) \\ 0 \end{pmatrix}. \tag{7.9}$$

From Chapter 4 we recall that the mass matrix M is symmetric and positive definite, the damping matrix C and the stiffness matrix K are symmetric and positive semidefinite, and the gyroscopic matrix G is skew-symmetric. F_{gr} is a static load (e.g. gravity), F_{bear} is the nonlinear bearing reaction force, and $F_{\mathrm{unb}} = u\omega^2 \cos(\omega t + \psi)$ is the periodic unbalance forcing.

7.2.1   Transformations for AUTO and Internal Newton Method

For the software AUTO, the user has to supply a file which returns the right hand side of an explicit, autonomous, ordinary differential equation for given state vector and parameters. As described in the AUTO user manual (Doedel *et al.*, 2000) the transformation of a non-autonomous periodically forced system like (7.7) to an autonomous system can be done by coupling a nonlinear oscillator unidirectionally to the original system, like e.g. the Hopf normal form

$$\dot{x} = x + \omega y - x(x^2 + y^2), \tag{7.10}$$
$$\dot{y} = -\omega x + y - y(x^2 + y^2), \tag{7.11}$$

which has the asymptotically stable solution $x = \sin(\omega t)$, $y = \cos(\omega t)$. The periodic forcing term $f_{\text{unb}} = u \cos \omega t$ in (7.7) can then be replaced by $f_{\text{unb}} = uy$ to obtain an autonomous system.

For a given state vector y the user supplied right hand side function has to return $\dot{y}$. It is however not possible to transform (7.9) analytically into an explicit expression for $\dot{y}_b$, the variables describing deflection and velocity at the bearing nodes. In order to apply AUTO to (7.9), we have to solve the equation for $\dot{y}$ numerically. This is possible by applying an internal Newton method. Since the nonlinearity is only in the bearing nodes this can be done relatively efficiently by a decomposition into variables which affect and are affected directly by the nonlinearity and variables that are only affected by the linear term. For this we separate y and $\dot{y}$ into those variables y_1 and $\dot{y}_1$ that describe displacements and velocities at the bearing and those variables y_2 and $\dot{y}_2$ that describe the rest. By rearranging the system matrices we can put (7.9) in the following form

$$\begin{pmatrix} M_{11} & M_{12} \\ M_{21} & M_{22} \end{pmatrix} \begin{pmatrix} \dot{y}_1 \\ \dot{y}_2 \end{pmatrix} = \begin{pmatrix} A_{11} & A_{12} \\ A_{21} & A_{22} \end{pmatrix} \begin{pmatrix} y_1 \\ y_2 \end{pmatrix} + \begin{pmatrix} F_{\text{bear}}(y_1, \dot{y}_1) \\ 0 \end{pmatrix} + \begin{pmatrix} G_1 \\ G_2 \end{pmatrix} \tag{7.12}$$

$$= \begin{pmatrix} F_{\text{bear}}(y_1, \dot{y}_1) \\ 0 \end{pmatrix} + \begin{pmatrix} R_1 \\ R_2 \end{pmatrix}, \tag{7.13}$$

where A and G are the respective permutations of

$$\tilde{A} = \begin{pmatrix} -(\omega G + C) & -K \\ I & 0 \end{pmatrix}, \quad \tilde{G} = \begin{pmatrix} F_{\text{gr}} + F_{\text{unb}}(t) \\ 0 \end{pmatrix}, \tag{7.14}$$

and

$$R_1 = A_{11} y_1 + A_{12} y_2 + G_1, \tag{7.15}$$
$$R_2 = A_{21} y_1 + A_{22} y_2 + G_2. \tag{7.16}$$

We can eliminate $\dot{y}_2$ from the first line of Equation (7.12) by using

$$\dot{y}_2 = (M_{22})^{-1} R_2 - (M_{22})^{-1} M_{21} \dot{y}_1 \tag{7.17}$$

and obtain the following low-dimensional equation for $\dot{y}_1$

$$(M_{11} - M_{12}(M_{22})^{-1}M_{21})\dot{y}_1 = \begin{pmatrix} F_{\text{bear}}(y_1, \dot{y}_1) \\ 0 \end{pmatrix} + R_1 - M_{12}(M_{22})^{-1}R_2. \qquad (7.18)$$

This equation has to be solved numerically with Newton's method. The iteration matrix is

$$J = M_{11} - M_{12}(M_{22})^{-1}M_{21} - M_b, \qquad (7.19)$$

where the Jacobian M_b of F_{bear} with respect to $\dot{y}_1$ is approximated by central finite differences. The result of the last successful step is a good starting value for the internal Newton method, in practice leading to convergence after a few iteration steps. This internal Newton method is less numerically efficient than solving the implicit equation directly, because one ends up in doing two Newton methods: one every time the right hand side is evaluated, and one in AUTO's continuation procedure. But since AUTO does not allow implicit equations, this is a reasonable work-around, especially since generally only very few internal iterations are needed.

7.2.2 Formulation in Co-Rotating Frame

So far we considered the equation of motion (7.6) in a fixed frame coordinate system. The transformation to a co-rotating frame however yields some further insight into the dynamics of the system. Let $q_i = (u_i, v_i, \beta_i, \alpha_i)$ be the nodal coordinates in the fixed frame as above and p_i the coordinates in a frame that is rotating about the z-axis with rotational speed ω. Then

$$q_i = \begin{pmatrix} T(\omega t) & \\ & T(\omega t) \end{pmatrix} p_i, \quad \text{where} \quad T(\omega t) = \begin{pmatrix} \cos \omega t & -\sin \omega t \\ \sin \omega t & \cos \omega t \end{pmatrix}. \qquad (7.20)$$

Setting

$$P = \begin{pmatrix} T(\omega t) & & \\ & \ddots & \\ & & T(\omega t) \end{pmatrix} \quad \text{and} \quad H = \begin{pmatrix} 0 & -1 & & & \\ 1 & 0 & & & \\ & & \ddots & & \\ & & & 0 & -1 \\ & & & 1 & 0 \end{pmatrix}, \qquad (7.21)$$

and substituting $q = Pp$ in (7.6) we obtain the following equation for y:

$$M\ddot{p} + (2\omega MH + G + C)\dot{p} + (K - \omega^2 M + \omega GH + \omega CH)p = \tilde{F}_{\text{bear}}(p, \dot{p}) + F_{\text{gr}} \cos(\omega t) + \omega^2 F_{\text{unb}}. \qquad (7.22)$$

The bearing function F_{bear} in (7.6) only depends on the eccentricity r, the radial velocity $\dot{r}$ and the angular velocity $\dot{\gamma}$ of the journal center (cf. (5.159), (5.160))

$$F_b = \begin{pmatrix} F_{b,x} \\ F_{b,y} \end{pmatrix} = T(\gamma) \begin{pmatrix} F_n(r, \dot{r}, \dot{\gamma}) \\ F_t(r, \dot{r}, \dot{\gamma}) \end{pmatrix}. \qquad (7.23)$$

If we denote the polar coordinates in the co-rotating frame by e and ψ we have the following relations: $e = r$, $\dot{e} = \dot{r}$, $\gamma = \psi + \omega t$ and $\dot{\gamma} = \dot{\psi} + \omega$. Therefore the transformed bearing function $\tilde{F}_{\text{bear}}$ in (7.22) has the following form

$$
\begin{aligned}
\tilde{F}_{\text{bear}} &= T^{-1}(\omega t)F_{\text{bear}}(q, \dot{q}) = T^{-1}(\omega t)T(\gamma)\begin{pmatrix} F_n(r, \dot{r}, \dot{\gamma}) \\ F_t(r, \dot{r}, \dot{\gamma}) \end{pmatrix} && (7.24) \\
&= T^{-1}(\omega t)T(\omega t)T(\psi)\begin{pmatrix} F_n(e, \dot{e}, \dot{\psi} + \omega) \\ F_t(e, \dot{e}, \dot{\psi} + \omega) \end{pmatrix} && (7.25) \\
&= T(\psi)\begin{pmatrix} F_n(e, \dot{e}, \dot{\psi} + \omega) \\ F_t(e, \dot{e}, \dot{\psi} + \omega) \end{pmatrix}. && (7.26)
\end{aligned}
$$

In the implicit case the transformed bearing function is of the form

$$
\tilde{F}_{\text{bear}} = \begin{pmatrix} F_n(e, \dot{e}, \dot{\psi} + \omega, \ddot{\psi}) \\ F_t(e, \dot{e}, \dot{\psi} + \omega, \ddot{\psi}) \end{pmatrix}. \tag{7.27}
$$

The formulation in the co-rotating can sometimes be more convenient than the fixed frame version as the harmonic unbalance forcing transforms to a constant term and the formerly static gravity load term becomes an harmonic forcing term. In the absence of gravity load (e.g. in a vertical rotor) or any other constant load the analysis of the dynamics is therefore simpler because the system is autonomous. Periodic orbits of the
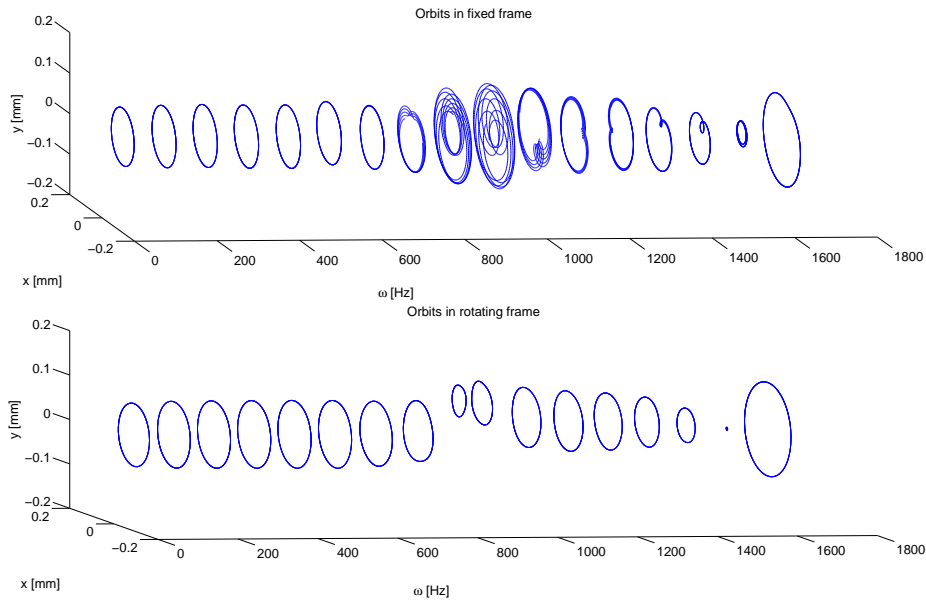


Figure 7.1: Comparison of simulated orbits seen in fixed frame of coordinates (top) and co-rotating frame (bottom); quasi-periodic orbits in the fixed frame become periodic orbits in the co-rotating frame of reference.

system with unbalance forcing in the static coordinate system transform to equilibria in the co-rotating frame and invariant tori transform to periodic orbits. This can be

seen from the following considerations. Let

$$x = ae^{i\omega_0 t} + be^{i\omega_1 t} \tag{7.28}$$

be a quasi-periodic signal with the two basic frequencies ω_0 and ω_1. The transformed signal in a rotating frame with ω_0 then has the form

$$z = e^{-i\omega_0 t} x = a + be^{i(\omega_1 - \omega_0)t}. \tag{7.29}$$

Hence a periodic solution with frequency ω_0 (i.e. $b = 0$) will transform to a constant solution, while the term with frequency ω_1 is transformed into another periodic term with the frequency $\omega_1 - \omega_0$. In Section 7.8 the period length T_{rot} of a solution to the equation of motion in the co-rotating frame of coordinates is computed with AUTO. To calculate the basic frequency ω_1 in the fixed frame of coordinates for $\omega_1 < \omega_0$, we use

$$T_{rot} = \frac{2\pi}{\omega_0 - \omega_1} \quad \Leftrightarrow \quad \omega_1 = \omega_0 - \frac{2\pi}{T_{rot}}. \tag{7.30}$$

Hence if $\omega_1 = \frac{\omega_0}{2}$ the period is $T_{rot} = \frac{4\pi}{\omega_0}$, and if $T_{rot} < \frac{4\pi}{\omega_0}$, the subharmonic frequency is also reduced $\omega_1 < \frac{\omega_0}{2}$, as it is observed experimentally for the oil whirl.

The simplification achieved through the transformation is illustrated in Figure 7.1, where we see a comparison of simulation results of a system without gravity load in the fixed frame and in the co-rotating frame for varying rotational speed. The orbits in the lower graph, seen in the co-rotating frame, are much simpler. Neglecting gravity is also justified in our example for large rotational speeds, because F_{gr} becomes small compared to unbalance above frequencies of approximately 500 Hz as can be seen later in this chapter.

7.3   Linear Stability Analysis

As a first step in the bifurcation analysis we perform a linear stability analysis of the rotor-bearing system. From the equations of motion (7.7) and (7.9) we see that in the absence of the constant load, i.e. $f_{grav} = 0$, and of the unbalance forcing ($f_{unb} = 0$), there exists an equilibrium in the origin. For non-vanishing constant load $f_{grav} \neq 0$ the equilibrium is no longer in the origin. If the bearing function is complicated one has to calculate it numerically. The real parts of the eigenvalues of the Jacobian of the right hand side of the equation of motion evaluated at the equilibrium point give its linear stability. The computation of the zeros of the right hand side can be complicated if the system is large, i.e. if many beam elements are considered. However, since nonlinearity is brought into the system only by the bearing function which itself only depends on the nodal coordinates of at the bearing positions, a decomposition of the equation of motion can be used to facilitate the numerical computation of the equilibrium.

From (7.6) we see that the condition for an equilibrium in x^* is

$$0 = Kx^* + F_{\text{gr}} + F_{\text{bear}}(x_b^*, 0). \tag{7.31}$$

K is the stiffness matrix of the beam, its null space is spanned by the rigid body motions of the beam (cf. Eq. 4.25), and therefore $Kx^r = 0$ for a rigid translation x^r of the beam. Hence we can decompose the equilibrium position x^* into a rigid translation x^r and a elastic bending deflection x^e with fixed zero deflection at the bearing nodes ($x_b^e = 0$):

$$x^* = x^r + x^e. \tag{7.32}$$

Substituting this into (7.31), the forces in the bearings are then given by

$$F_{\text{bear}}(x_b^r) = -Kx^e + F_{\text{gr}}. \tag{7.33}$$

Ordering K and x^e in such a way that the zero components of x^e are in the first rows we can write the last equation in more details:

$$- \left(\begin{array}{c|c} K_1 & K_2 \\ \hline K_3 & K_4 \end{array} \right) \left(\begin{array}{c} 0 \\ \tilde{x}^e \end{array} \right) + \left(\begin{array}{c} F_{\text{gr},1} \\ F_{\text{gr},2} \end{array} \right) = \left(\begin{array}{c} F_{\text{bear}}(x^r) \\ 0 \end{array} \right). \tag{7.34}$$

From this we can calculate the bending deflection

$$\tilde{x}^e = K_4^{-1} F_{\text{gr},2} \tag{7.35}$$

and the resulting bearing forces by elimination of x^e from the equation

$$\begin{aligned} F_{\text{bear}}(x_b^r) &= -K_2 \tilde{x}^e + F_{\text{gr},1} & \text{(7.36)} \\ &= -K_2 K_4^{-1} F_{\text{gr},2} + F_{\text{gr},1} & \text{(7.37)} \\ &= \tilde{F}. & \text{(7.38)} \end{aligned}$$

Then the rigid translation in each of the bearings can be calculated by solving numerically the nonlinear equation

$$F_{\text{bear}}(x_b^r) = \tilde{F}, \tag{7.39}$$

e.g. with a Newton type method. The entire rigid translation x^r is calculated from the translations at the bearings x_b^r by linear interpolation. The lateral shaft deflection in equilibrium is then given by adding again the rigid translation and the bending deflection.

Since (7.39) decomposes even further into two two-dimensional problems, one for each bearing, this reduced problem is much easier to solve than the direct problem (7.31), also for large systems with many finite elements.

Knowing the equilibrium position, the bearing stiffness and damping coefficients, as well as the derivative with respect to the nodal acceleration $\ddot{x}_b$ in the case of the implicit system (7.9)

$$K_{\text{oil}} = (\frac{\partial F_{\text{bear},i}}{\partial x_{b,j}})_{i,j}, \tag{7.40}$$

$$C_{\text{oil}} = (\frac{\partial F_{\text{bear},i}}{\partial \dot{x}_{b,j}})_{i,j}, \tag{7.41}$$

$$M_{\text{oil}} = (\frac{\partial F_{\text{bear},i}}{\partial \ddot{x}_{b,j}})_{i,j}, \tag{7.42}$$

can be determined by calculating the central difference quotients of the oil film forces around the equilibrium as in Equation (6.17) in Section 6.2.

With these coefficients one can do a linear stability analysis of the equilibrium position by analyzing the linearized right hand side of the equation of motion without periodic forcing

$$
\begin{aligned}
\dot{y} &= \begin{pmatrix} -(M - M_{\text{oil}})^{-1}(\omega G + C + C_{\text{oil}}) & -(M - M_{\text{oil}})^{-1}(K + K_{\text{oil}}) \\ I & 0 \end{pmatrix} y \\
&= By.
\end{aligned}
\tag{7.43}
$$

Note that in the case of the explicit equation of motion (7.7) $M_{\text{oil}} = 0$. The eigenvalues of the matrix B in Eq. (7.43) determine the stability of the equilibrium. By computing the equilibria and the corresponding eigenvalues for varying values of the rotational velocity, dependence of the equilibria's stability on this parameter can be studied. Using the old equilibrium as a starting value for the Newton iteration of the next one is a good guess and leads to fast convergence. If all eigenvalues have negative real part, the system is linearly stable and for small forcing the expected response is harmonic. If one or more eigenvalues have positive real part, the corresponding equilibrium is unstable and self-excited oscillations may occur. A Hopf bifurcation occurs at a given parameter value, if a pair of two eigenvalues crosses the imaginary axes transversally at this parameter (Wiggins, 1990).

7.3.1   Hopf Bifurcation at Onset of Oil Whirl

Like in Chapter 6 we mainly study two models of a turbocharger, a larger one with thirteen beam elements resulting in an equation of motion with 112 dimensions and a smaller one with only three beam elements whose equation of motion has only 32 dimensions (cf. Fig. 6.7).

For rotational speeds between 10 Hz and 2010 Hz we calculate the equilibria of the large model with 13 finite beam elements and the corresponding eigenvalues of the Jacobian. In Figure 7.2 the real and the imaginary parts of the eigenvalues are plotted
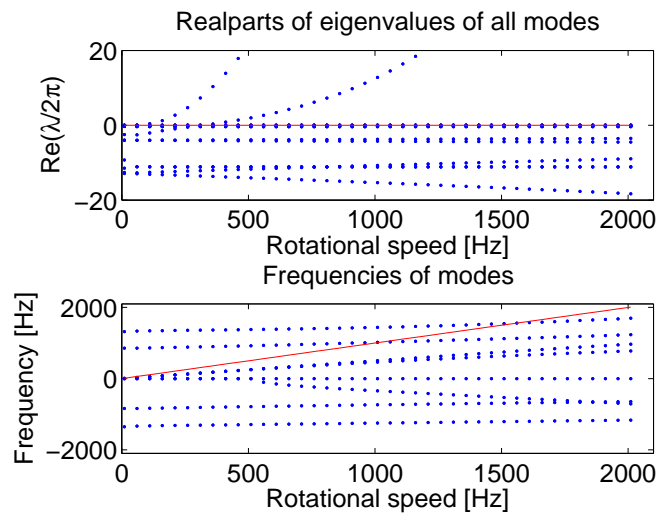
Figure 7.2: Plot of the eigenvalues of the linearized dynamical system for the 13 beam element model. Top: Real parts. Bottom: Frequencies of the eigenmodes given by the imaginary parts divided by 2π. Two eigenmodes subsequently lose stability at driving frequencies of around 100 and around 350 Hz, respectively.

in dependency of the rotational velocity ω. In the upper plot we see that two curves cross the zero line, one around 100 Hz and one at about 350 Hz, which indicates some vibration modes becoming unstable. In the lower plot the red line indicates the forcing frequency. Crossings of the red line with blue eigenvalue curves indicate driving frequencies where harmonic resonances occur. This is in agreement with the simulation results shown in Figure 6.8 in Section 6.4, where a harmonic resonance of the first bending mode appears at 1000Hz and a second harmonic resonance peak is observed around 1600 Hz. In Figure 7.3 the orbits of the eigenvalues in the complex plane are shown. One can see the pair of eigenvalues crossing the imaginary axis into the positive half plane. This shows numerically the presence of a Hopf bifurcation at the onset of the oil whirl.

This linear stability analysis is common in rotordynamics and is used e.g. in (San Andrés, 2006) or (Childs, 1993) to predict the stability of rotordynamic systems. However in the presence of self-excited oscillations, the linear stability analysis can lead to wrong conclusions, since we perform it along the then unstable equilibrium which is not observed in the physical reality. Nevertheless, the correct perdiction of the resonance peaks shows that the solutions with self-excited oscillation are still reasonably close to the equilibrium, such that a linear stability analysis makes sense.

For the smaller system we observe similar behavior as can be seen in Figure 7.4. Again two pairs of complex eigenvalues cross the imaginary axis. One pair at around 50 Hz and the other one around 300 Hz. In the lower figure on the left, one can see that again there is a harmonic resonance near 1000 Hz.
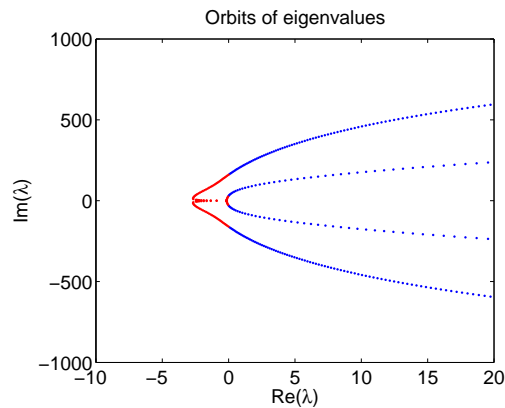
Figure 7.3: Close up of the origin of the complex plane with spectrum of the Jacobian of the 13 element model: two pairs of complex conjugate eigenvalues cross the imaginary axis indicating two subsequent Hopf bifurcations. Eigenvalues with negative real parts are plotted in red, eigenvalues with positve real parts in blue, for small ω both pairs start close to the origin in the negative half plane.
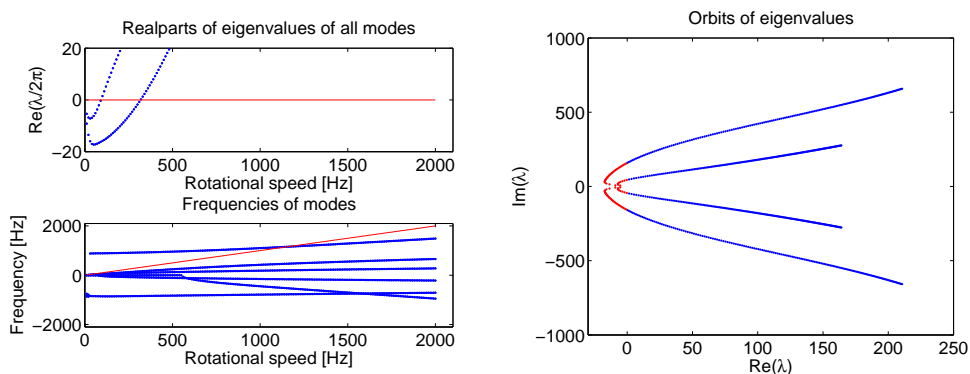
Figure 7.4: Results of linear stability analysis of 3 element model; left: plots of real and imaginary parts of the eigenvalues of the Jacobian; right: close-up of origin of the complex plane showing the orbits of 2 pairs of complex conjugate eigenvalues crossing the imaginary axis with varying ω. Eigenvalues with negative real part are plotted in red, those with positive real part in blue; for small ω both pairs start close to the origin in the negative half plane.

7.4 Numerical Bifurcation Analysis of Large Model

The software-package AUTO (Doedel *et al.*, 2000) has been developed to perform parameter continuation for a multitude of problems. In this section it is used to investigate closer the onset of instability of the larger, 112-dimensional model of the turbocharger (cf. 6.7) with 13 beam elements. Unfortunately the dimension of our problem makes it difficult to use AUTO for the calculation of the bifurcations the periodic orbits of our model (7.7) with unbalance forcing. This is mainly due to the
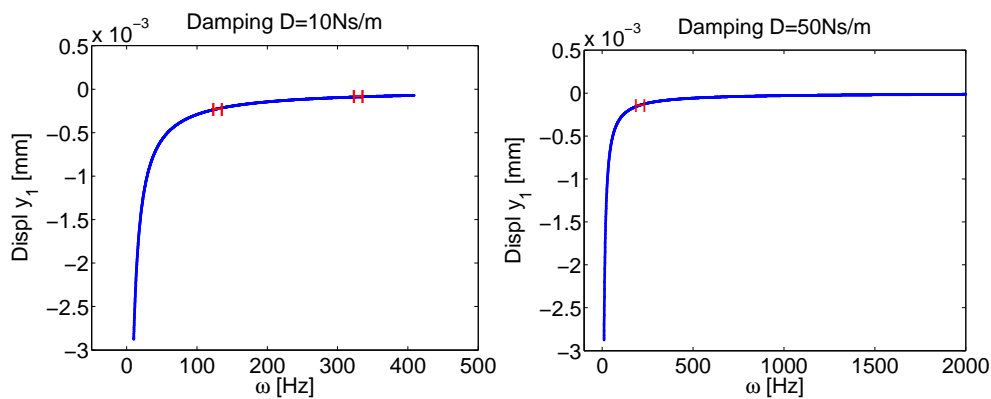
Figure 7.5: y-deflection at impeller side of the equilibrium state of the large model ($N = 112$) for varying rotational speed (x-axis) with lower (36 Ns/m;left) and higher (180Ns/m;right) damping factor and no unbalance forcing; to the right of the first Hopf bifurcation (H) the fixed point is unstable.

size and the stiffness of the problem and the resulting convergence problems for the Newton methods used in the algorithm. In the absence of unbalance it is possible to calculate the equilibrium and its stability for different damping factors and to locate the Hopf bifurcations which mark the onset of the oil whirl.
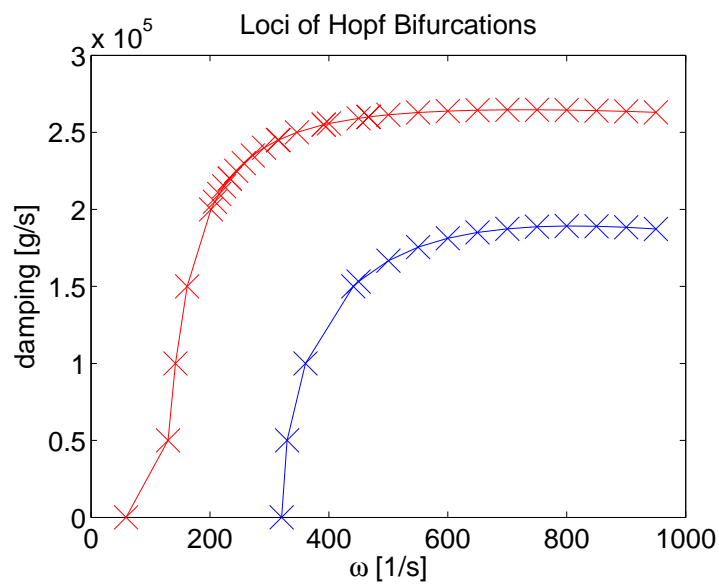
Figure 7.6: Curves of Hopf Bifurcations in the ω-D plane; above and left of the red curve the equilibrium is asymptotically stable; between the curves 2 unstable, below blue curve 4 unstable directions

The starting point for all continuations in the following is always the trivial equilibrium which exists in the absence of unbalance and static load ($F_{gr} = 0$ and $F_{unb} = 0$). For

increasing the F_{gr} this equilibrium becomes non trivial. The equilibrium branch is followed until F_{gr} reaches the same value it has in the simulations. Starting from this point, the equilibrium is now continued in the driving frequency from 10 Hz to 2000 Hz.

The results of the continuation are shown in the Figure 7.5 for two different external damping factors. Both graphs in the figure show the y-deflection of the rotor at the impeller side in the equilibrium state for a range of rotational speeds. The distance of the equilibrium from the origin decreases with increasing driving frequency. Several Hopf bifurcations are detected along the branches and marked with red H. As soon as the rotational speed passes the frequency of the first Hopf bifurcation the equilibrium solution becomes unstable and oil whirl occurs. For the lower value of the damping factor a second Hopf bifurcation is detected at a higher rotational speed. Note that for the higher damping (180Ns/m) the second Hopf bifurcation vanishes and that the onset of self-excited oscillation is pushed to higher frequencies. The parameters used to obtain the results in Figure 7.5 were the same as those used in the simulation shown in Figure 6.11, except for the unbalance excitation, which is neglected here.

The prediction of the onset of instability is of crucial importance for the design of the turbocharger and also of other rotors. A continuation of the first Hopf bifurcation in parameter space would yield a good tool for this purpose. However, the size of the system poses some problems to the numerical methods of AUTO and we encountered convergence problems when we tried this continuation. As an alternative it is possible to detect the loci of the Hopf bifurcations by several runs of AUTO which cover the parameter region of interest. For this we compute an equilibrium branch by continuating the starting solution in the damping parameter. From well chosen points on this branch we repeat the continuation in ω, and we can hence detect the location of the Hopf bifurcations on branches with different damping. For the results shown in Figure 7.6 such a search strategy was applied. Connecting the points of the first Hopf bifurcations (red) and those of the second Hopf bifurcations (blue) linearly we obtain a partition of the parameter space. In the left upper corner, above the red curve the equilibrium is asymptotically stable. Between the two curves there are 110 stable directions and 2 unstable ones. Below the blue curve there are 4 unstable directions. These results agree with our simulations in Section 6.4 (cf. Fig. 6.10) where the self-excited subharmonic vibration disappears for a large external damping factor D.

7.5   Numerical Bifurcation Analysis of Small System

As mentioned in Section 7.4 there are some convergence problems in AUTO for the large 112 dimensional system. To analyze the qualitative behavior in more detail we use again the smaller 3-element beam model for some calculations (cf. 6.7) which has be shown to have similar dynamical properties in Section 6.5. It consists only of 3 beam

elements with 2 disks attached at each end of the rotor and two journal bearings. The system therefore has 32 degrees of freedom (cf. Fig. 6.7). As explained in Section 7.2.1 2 more degrees of freedom have to be coupled to the system to make up for the periodic forcing, leading to a 34 dimensional system.

7.5.1   Unforced System in Fixed Frame of Coordinates

First we want to examine the bifurcation behavior of the equilibrium in the absence of unbalance forcing. For this we proceed exactly as above. Starting from the trivial equilibrium with small ω, the static load is increased until it reaches the value from the simulations. Then the driving frequency is increased and the equilibrium is continued until $\omega = 2000\,\text{Hz}$.
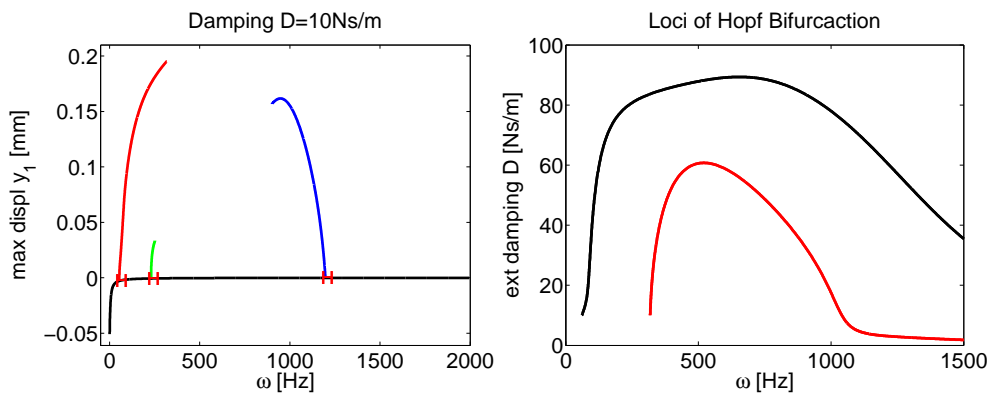

Figure 7.7: Bifurcations of equilibrium of small system. Left: 3 subsequent Hopf bifurcations (marked with H) are detected along equilibrium branch (black) for varying driving frequency; colored branches show the maximal amplitudes of the periodic orbits emerging at the Hopf points; only the leftmost one (red) is stable. Right: Locus curve of the Hopf bifurcations in the frequency-damping factor domain; the first Hopf bifurcation from the left picture lies on the black curve, the second and third Hopf bifurcations on the red curve at the intersection with $D = 10\,\text{Ns/m}$.

The results for the comparable smaller system are similar to the ones obtained for the larger system, but more detailed as shown in Figure 7.7. For the unforced system we observe three Hopf bifurcations from the equilibrium for rotational frequencies between 0 and 2000 Hz. It is possible to follow the periodic orbits emerging from the Hopf points. Unfortunately, there are again convergence problems for larger amplitudes of the periodic orbits, and they can not be continued through the whole frequency domain. Their maximal amplitude in the y-direction is shown in the colored branches in the left diagram. At the first point (lowest frequency) a supercritical Hopf bifurcation occurs and a stable periodic orbit branches off from the fixed point which is unstable from then on for all higher frequencies. The frequency of the stable periodic orbit is half the driving frequency as expected from the simulations. The two Hopf
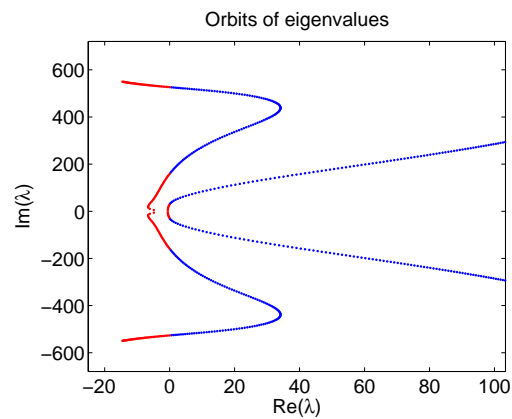
Figure 7.8: Results of linear stability analysis: trajectories of eigenvalues in the complex plane. One pair of eigenvalues crosses the imaginary axis twice with increasing driving frequency; first from negative (red) to positive (blue), and then back. For low driving frequencies both pairs are close to the origin.

points that are detected for higher rotational speeds seem to be linked by an unstable periodic orbit that emerges at the Hopf bifurcation in the middle and merges again with the unstable fixed point at the third Hopf point (higher frequency value). Since the calculations stop due to convergence problems it is not possible to link them in AUTO. However dimensional considerations indicate this, because the stable eigenspace of the fixed point has dimension 32 until the first Hopf bifurcation, dimension 30 between the first and the second one, the dimension decreases again to 28 between the second and third Hopf point and increases to 30 again for frequencies higher than at the third Hopf point. This periodic orbit is unstable, as already the periodic orbit emerging from the first Hopf point is stable and stays so. This conclusion is supported by a linear stability analysis. As can be seen from Fig. 7.8 one pair of eigenvalues crosses the imaginary axis twice, once in positive for a lower frequency and once in negative direction as the frequency increases. Another pair crosses the imaginary axis and stays in the right half-plane. The latter corresponds to the stable periodic orbit emerging at the first Hopf point, while the former corresponds to the unstable periodic orbit that exists between the second and third Hopf point.

This interpretation is also backed by the continuation of the loci of the Hopf bifurcation points. For this smaller system it is possible to track the locus curve in the two parameters damping factor and driving frequency. This is shown in the right diagram of Figure 7.7. The diagram shows the frequency-damping pairs at which the onset of self-excited oscillation occurs, i.e. the locus curve of first Hopf bifurcation (black), and those values of damping and frequency where the secondary Hopf bifurcation occurs. One can see that for a damping factor larger than approximately 90 Ns/m no Hopf bifurcation occurs anymore. This corresponds to the simulations in Section 6.4 and to the results of the bifurcation analysis for the large system (cf. Fig. 7.6), where for higher

damping factors no self-excited oscillation is observed. The second Hopf bifurcation is suppressed already for smaller values of the external damping factor. The frequencies where the red branch of Hopf bifurcations crosses the value $D = 10$ Ns/m in the right panel coincide with the frequencies of the second and third Hopf bifurcation in the left panel.

7.5.2 Forced System in Fixed Frame of Coordinates

In the presence of unbalance excitation the dynamics is slightly different. We start again with the trivial equilibrium for $F_{gr} = 0$ and $F_{unb} = 0$. As above, we trace the equilibrium when we increase F_{gr} to the value specified by the design of the rotor. As explained in Section 7.2.1 the non-autonomous forcing is replace by a two-dimensional oscillator with a stable limit cycle, that is unidirectionally coupled to the system. By increasing F_{unb} to the value specified in the design, we couple in the forcing. This has the effect that the equilibrium no longer exists. For rotational frequencies below the frequency of the first Hopf bifurcation, a stable periodic orbit takes its place. It has the same frequency as the forcing. AUTO allows for a continuation of the periodic orbit with the rotational frequency as continuation parameter. With rising rotational frequency the amplitude of the periodic orbit increases as expected from Equation (7.7) where the amplitude of F_{unb} grows quadratically in ω.
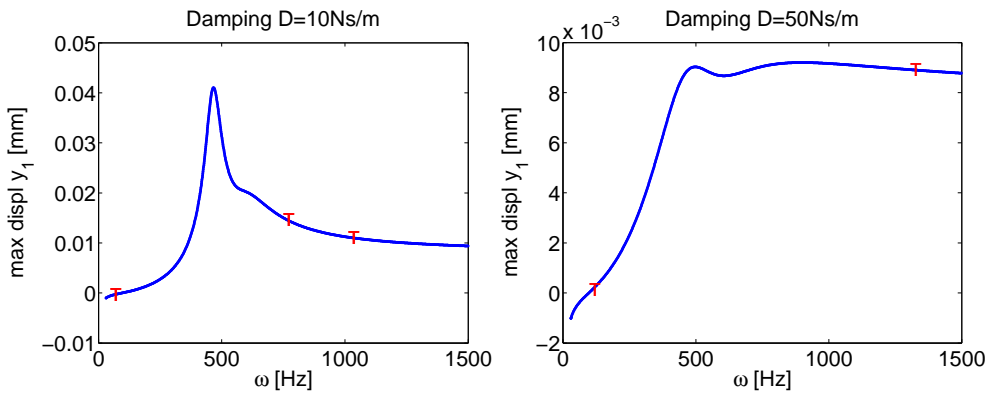
Figure 7.9: Frequency-response diagrams for the smaller system with unbalance excitation, at the leftmost torus bifurcation (T) this periodic orbit gets unstable and self excited oscillations appear which leads to a quasiperiodictours branching off; left: low damping, right: higher damping.

In Figure 7.9 the amplitude of this periodic orbit is depicted against the rotational frequency for two different values of the external damping factor D. For low damping we observe three torus bifurcations marked with a red T, while for the higher value only two of them are observed in the frequency range covered. An examination of the 34 Floquet multipliers that are computed by AUTO shows that all but one multiplier lie inside the unit circle and one is equal to 1. This shows that the periodic orbit

is asymptotically stable for driving frequencies lower than the one of the first torus bifurcation on the branch. At the first torus bifurcation a pair of Floquet multipliers with non-zero imaginary part leaves the unit circle, the periodic orbits gets unstable and a stable invariant torus bifurcates from it (Kuznetsov, 2004). At the second torus bifurcation another pair of Floquet multipliers leaves the unit circle. At the third torus bifurcation one pair reenters the unit circle. For higher external damping, the first torus point which is observed on the branch also marks a pair of Floquet multipliers leaving the unit circle. Again this has the consequence of a stable invariant torus bifurcating from the periodic orbit which is hence unstable. However, at the second torus bifurcation point this pair of multipliers returns into the unit circle and the periodic orbit regains its stability. There is no crossing of a second pair of multipliers detected. This behavior can be explained by looking at the Hopf bifurcation diagram on the right of Figure 7.7 which shows that the region of instability of the fixed point is like a tongue in the frequency-damping factor domain, i.e. for large damping as well as for very small and for very large frequencies the equilibrium is asymptotically stable. While this is not a proof for the situation in the forced case, the results of the averaging theorem (K., 1969; Guckenheimer & Holmes, 1983) suggest that the loci of the torus bifurcations show a similar behavior. This means that that the second torus bifurcation which is observed in the low damping case is suppressed in the higher damping case, and that the second torus bifurcation is the reversion of the first one.

Unfortunately it is not possible to follow the locus of the torus bifurcations themselves in the frequency-damping factor domain. Again, the relatively high dimension of the system leads to convergence problems in the Newton methods AUTO employs.

7.6   Fixed Frame vs. Co-Rotating Frame

As already shown in Section 7.2.2 a formulation in a coordinate frame co-rotating with angular velocity ω can be a simplification of the system (cf. Eq. (7.22)), if there is no constant load applied to the rotor. In this case the transformed system becomes autonomous, periodic orbits with period $T = \frac{2\pi}{\omega}$ become fixed points, and quasiperiodic solutions with one of the basic frequencies equal to ω become limit cycles. In the absence of a constant load, e.g. for a vertical rotor, this makes numerical continuation of these quasiperiodic solutions possible. However, since the trivial equilibrium is unstable in the absence of gravity, some preliminary continuations are necessary to reach a starting solution for continuation in the driving frequency. For this, starting from the trivial equilibrium, we increase the amplitude F_{unb} and follow the equilibrium branch. A Hopf bifurcation is detected along the branch for high values of the unbalance. The stable periodic orbit emerging from it is continued backwards in the forcing amplitude until the smaller value of F_{unb} used in the simulation is reached. This stable periodic orbit is the starting solution for a continuation in the driving frequency. Alternatively,

one could also start from a solution computed by direct numerical simulation. How-ever, the proposed method of reaching the starting solution by 2 continuation runs is faster, and we can also use the other solutions computed during the process for further continuation runs.
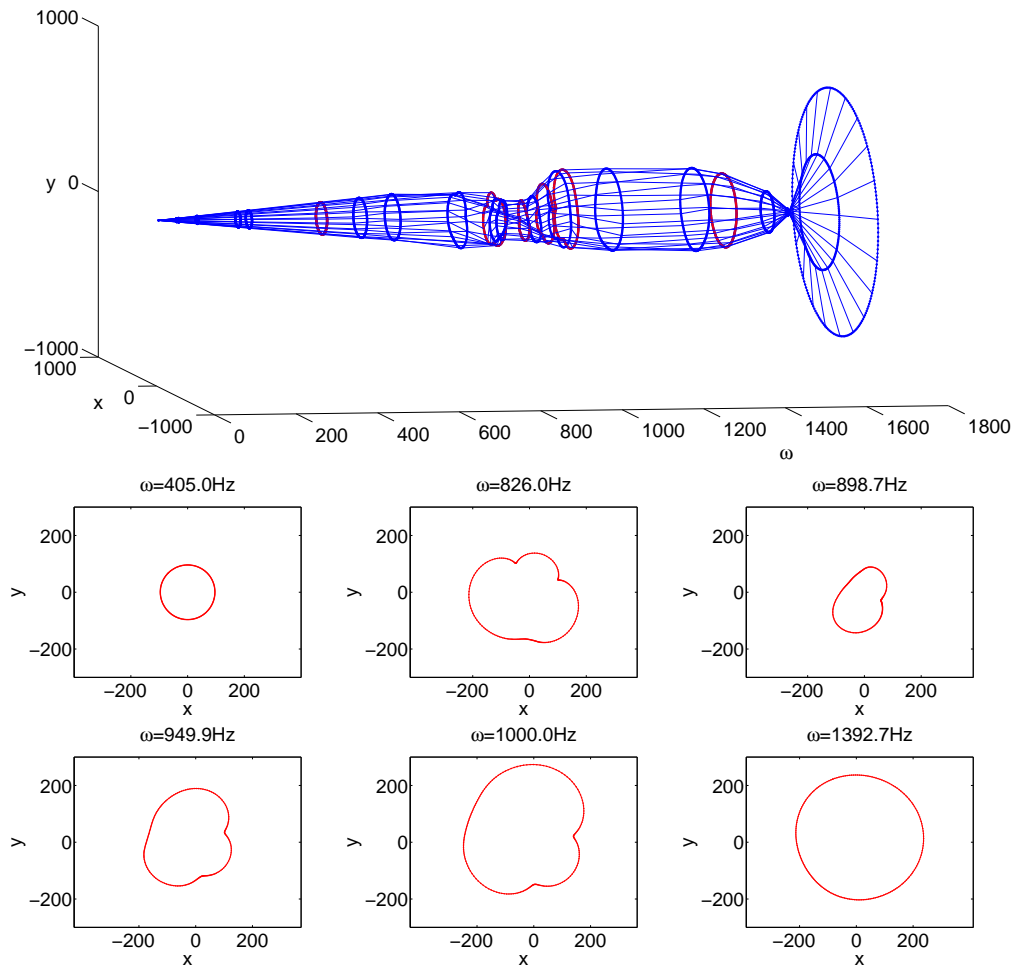
Figure 7.10: Continuation of periodic solutions of Eq. (7.22) in absence of constant load w.r.t. driving frequency; the bottom line shows the detailed orbits drawn in red in the top figure. The reduced amplitudes around driving frequencies of 1000 Hz are due to the entrainment phenomenon also observed in the simulations.

Figure 7.10 shows the results of this continuation of the stable periodic orbits of the system (7.22) in the co-rotating frame. These are equivalent to the quasiperiodic solutions of the system (7.7) in the fixed frame for which both, the subharmonic and the harmonic response are present. The orbits depicted in red in the upper diagram are shown again in the lower row for better visibility. The entrainment of the subharmonic in the region of resonance of the first bending mode can be observed nicely in this frame of reference. Between 700 Hz and 1000 Hz and again at about 1500 Hz, the amplitude of the subharmonic responce decreases significantly. This entrainment effect can also

be observed in the simulations and in the experiments in the vicinity of the resonance of the first bending mode.

For some parameter regions the entrainment becomes so strong that the subharmonic is completely suppressed. This is shown in the left diagram of Figure 7.11. It shows the locus of the Hopf bifurcation which is at the onset of the oil whirl in the frequency-bearing clearance $\omega - c_r$ domain. In the region above the blue line the periodic orbit
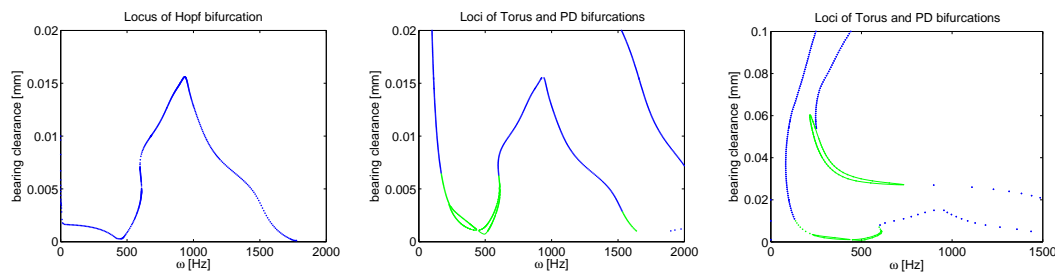
**Figure 7.11:** Left: Locus of the Hopf bifurcation that marks the onset of oil whirl in the $\omega - c_r$ domain for the system (7.22) in a co-rotating frame of coordinates; center and right: Corresponding Loci of torus and period doubling bifurcations of the system in fixed frame of coordinates. The right diagram shows a larger part of the parameter range and the locus of the second torus and period doubling bifurcation.

exists and is stable. Below it, there exits a stable fixed point which corresponds to a stable periodic orbit with rotational frequency omega in the fixed frame, i.e. an harmonic response. For small values of c_r the subharmonic response disappears in a region around 900 Hz.

In order to compare this result from the slightly simplified case of zero load in the co-rotating frame to the full problem in the fixed frame, we have computed the location of the onset and suppression of the oil whirl in the presence of an harmonic unbalance forcing and a static load in the fixed frame of coordinates (7.7). The center and the right diagram in Figure 7.11 show the results. For this, we proceed as in Section 7.5.2 to reach the small stable $\frac{2\pi}{\omega}$-periodic orbit present for small values of ω. Again the technique of sweeping the parameter domain with branches started from previously computed solutions allows to draw a locus curve of the secondary bifurcations.

The curve of Hopf bifurcations is replaced by the locus curve of torus bifurcations whose shape is allmost identical to the former. In some parameter regions the torus curve splits into two curves of period doubling bifurcations where a Floquet multiplier passes through -1 on each branch. The point of intersection of the torus curve two multipliers pass through -1. This situation is known as 1 : 2-resonance. The complicated bifurcation behavior in the vicinity of such a resonance is described in (Kuznetsov, 2004) and in the references given in that book, especially (Arnol'd, 1987; Gambuado, 1985). The diagram in the center shows the same part of the $\omega - c_r$ domain as the left diagram, while the right diagram shows a larger parameter region which
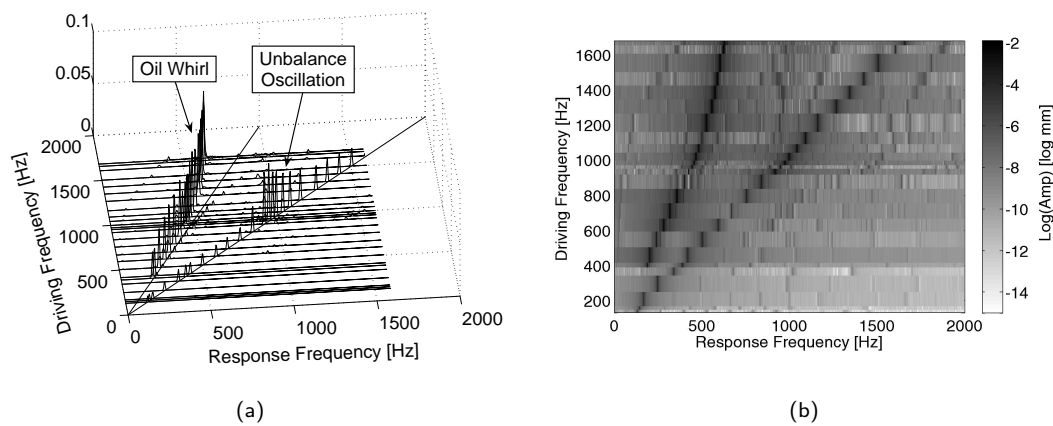
Figure 7.12: Power spectrum of vibrations measured in an experiment for ramping up the driving frequency of the rotor from 130 Hz to 1700 Hz; panel (a) shows a waterfall diagram and panel (b) a logarithmic intensity plot.

shows the curve of secondary torus bifurcations from the unstable periodic orbit, like they where observed in Figure 7.9 of Section 7.5.2.

This result shows that neglecting gravity and transformation to a co-rotating frame yields a significant simplification of the equation of motion, while the prediction of the onset of the oil whirl and entrainment remains unaffected.

7.7   Continuation of Quasiperiodic Oscillations

In this section the continuation method for invariant tori presented in (Schilder & Peckham, 2007) is applied to the 3 beam element model of the turbocharger with constant gravity load and unbalance forcing in a co-rotating frame of coordinates. Loci of invariant tori with fixed rotation number are computed and compared to periodic solutions of the system without gravity. Parts of the content of this section are joint work with Frank Schilder, Jens Starke, Mizuho Inagaki, Hinke Osinga, and Bernd Krauskopf, which has been published in (Schilder *et al.*, 2007).

7.7.1   Poincaré Section for Experimental Data

The experimental results presented in Section 6.3 of Chapter 6 showed the presence of two principal vibration modes which are due to unbalance and oil whirl. These vibration modes have been described in detail there. For convenience we show again a typical power spectrum from the experimental results in two different ways in Figure 7.12. One can clearly observe the two principal vibration modes as peaks in the waterfall diagram in panel (a) and as darker lines in the intensity plot in panel (b). The
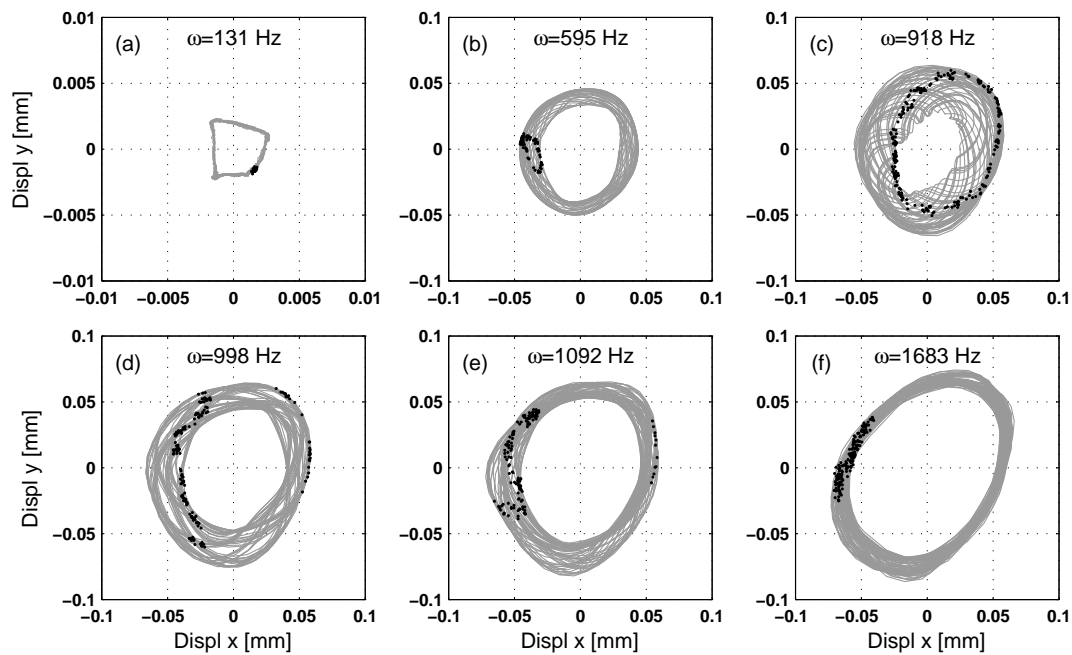
Figure 7.13: Orbits of turbine dynamics (gray) overlaid with their Poincaré sections (black) measured for different rotational speeds (note the different scale for ω = 131 Hz). Especially for driving frequencies of 595 Hz and 918 Hz the invariant circles on the tori are clearly visible, while for higher driving frequencies the invariant circles are broken up and show phase locking.

ratio of the frequency of the subharmonic to the driving frequency is approximately $\frac{1}{2}$ for low driving frequencies. For driving frequencies higher than 1000 Hz the ratio drops significantly below $\frac{1}{2}$.

Figure 7.13 shows the increasingly complex behavior of the orbits measured at the turbine end of the shaft. For small rotational speeds (250 Hz) the orbit is periodic with a small amplitude. As the driving frequency rises above 400 Hz a second frequency appears, which results in quasiperiodic dynamics on a torus. Such behavior is best analyzed by stroboscopic or Poincaré maps: We mark the position of the turbine every time the impeller crosses the x-axis from positive to negative values. The periodic orbit of the turbine end of the shaft that we observe for low rotational speeds corresponds to a fixed point of the stroboscopic map; see Figure 7.13 (a). For increasing rotational speeds the Poincaré map shows invariant circles indicating the existence of invariant tori; see Figures 7.13 (b) and (c). For even higher speeds the invariant circles show phase locking, i.e. the quasiperiodic solution is replaced by stable periodic orbits of possibly longer periods on the invariant torus; see Figures 7.13 (d)–(f).

7.7.2 Computation of Quasiperiodic Oscillations

A vibration with two or more (but finitely many) incommensurate frequencies is a quasiperiodic solution of an ODE. Such quasiperiodic solutions appear e.g. in coupled or forced oscillators. A quasiperiodic solution never repeats and densely covers an invariant torus in phase space. The experimental data shown in Figures 7.13 (b) and (c) provide an example for such a behavior. In (Schilder & Peckham, 2007) a method is presented for the computation of quasiperiodic solutions with two incommensurate frequencies; for further references see also (Ge & Leung, 1998; Schilder *et al.*, 2006; Schilder *et al.*, 2005). The basic idea of this method is to compute an invariant circle of the period-$2\pi/\omega_1$ stroboscopic map, which is the intersection of the torus with the plane $t = 0$. Here, in the case of a forced oscillator, $\omega_1 = \omega$ is the forcing frequency and time is interpreted as an angular variable modulo the forcing period. By construction, the invariant circle has rotation number $\varrho = \omega_2/\omega_1$, where ω_2 is the additional response frequency of the occurring vibration. The invariant circle with rotation number ϱ is a solution of the so-called invariance equation

$$u(\theta + 2\pi\varrho) = g(u(\theta)), \tag{7.44}$$

where u is a 2π-periodic function and g is the period-$2\pi/\omega_1$ stroboscopic map of (7.22). We approximate the invariant circle u with a Fourier polynomial of the form

$$u_N(\theta) = c_1 + \sum_{k=1}^{N} c_{2k} \sin k\theta + c_{2k+1} \cos k\theta \tag{7.45}$$

and compute the real coefficient vectors $c_1, \ldots, c_{2N+1}$ by collocation at the uniformly distributed points θ_k, $k = -N, \ldots, N$ on the circle S^1. The stroboscopic map g is computed with the second-order fully implicit midpoint rule as the solution of a two-point boundary value problem. For this, we demand for $k = -N, \ldots, N$, that $u_N(\theta_k)$ and $u_N(\theta_k + 2\pi\rho)$ are connected by the flow of the equation of motion, i.e.

$$\dot{x}_k = T_1 f(x_k), \tag{7.46}$$
$$x_k(0) = u_N(\theta_k), \tag{7.47}$$
$$x_k(1) = u_N(\theta_k + 2\pi\rho), \tag{7.48}$$
$$P_1(x) = 0, \tag{7.49}$$
$$P_2(U_N) = 0. \tag{7.50}$$

P_1 and P_2 are scalar phase conditions which fix an initial point of one solution from $\{x_{-N}, \ldots, x_N\}$ and $\{u_{-N}, \ldots, u_N\}$, since tori, like periodic solutions, are only unique up to phase shifts. For more details we refer to (Schilder & Peckham, 2007) where the method is introduced, and to Figure 7.14, where the functions x_k and u_N are depicted on the torus.

To start the continuation of the torus in the two continuation parameters driving frequency ω_1 and bearing clearance c_r, it is necessary to construct starting solutions.
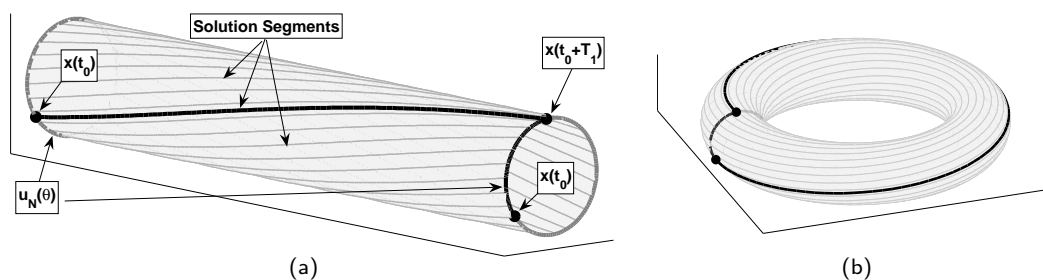
Figure 7.14: Illustration of the invariance equation (7.44). The solution curve starting at the point $x(t_0)$ crosses the invariant circle again in the point $x(t_0 + T_1)$ after one period (a). In angular coordinates on the invariant circle we have $x(t_0 + T_1) = u(\theta_0 + 2\pi\varrho)$. If we identify the circles at both ends of the tube, we obtain a torus (b).

These seed solutions for our subsequent continuations of tori are computed with the method of homotopy. To this end, we introduce an artificial parameter $\lambda \in [0, 1]$ as an amplitude of the gravitational forcing:

$$M\ddot{y} + (\omega G + C)\dot{y} + Ky = \widetilde{F}_\mathrm{b}(y, \dot{y}) + \lambda A(\omega t)^\mathrm{T} F_\mathrm{g} + \omega^2 F_\mathrm{unb}. \qquad (7.51)$$

In the following the case $\lambda = 0$ is referred to as the *zero-gravity system* and the case $\lambda = 1$ as the *Earth-gravity system*. The principle of homotopy is to compute a torus for $\lambda = 0$, where (7.51) is autonomous and a torus is easily constructed, and then to follow this torus as λ is slowly increased up to $\lambda = 1$. In the autonomous case, we can construct an invariant torus directly from a N-th order Fourier approximation of the form (7.45) of a $T_2 = 2\pi/\omega_2$-periodic solution of the zero-gravity system with frequency ω_2

$$x(t) = u_N(\omega_2 t) = u_N(\theta), \qquad (7.52)$$

where $\theta = \omega_2 t$. For the period-$2\pi/\omega_1$ stroboscopic map of this solution we have by definition

$$x(t + T_1) = g(x(t)) = g(u_N(\theta)), \qquad (7.53)$$

and we also have

$$x(t + T_1) = x\left(\frac{\theta}{\omega_2} + \frac{2\pi}{\omega_1}\right) = x\left(\frac{1}{\omega_2}\left[\theta + 2\pi\frac{\omega_2}{\omega_1}\right]\right) = u_N\left(\theta + 2\pi\varrho\right). \qquad (7.54)$$

So the Fourier approximation already fulfills the invariance equation. Finally, the solution segment of the seed solution which connects a starting point $x(t_0)$ with the endpoint $x(t_0 + T_1)$ is given by $x(t) = u_N(\theta)$, where $(\theta - t_0/\omega_2) \in [0, 2\pi\varrho]$ (cf. Figure 7.14).

For the system under consideration it turns out that the zero-gravity tori are such accurate approximations to the Earth-gravity tori that the latter can be computed in just one homotopy step. In panels (b) and (c) of Figure 7.15 a series of computed tori in the zero-gravity system and in the Earth-gravity system is depicted for varying radial bearing clearance c_r and driving frequency ω. The zero-gravity tori are almost identical

to the Earth-gravity tori. This is a first indication that neglecting gravity is a valid and powerful simplification of the model equation, since the computation of invariant tori (for $\lambda = 1$) is a much harder problem than the analysis of periodic solutions (for $\lambda = 0$). Hence, a reduction of this numerical complexity is desirable.

Furthermore, the behavior of periodic solutions with respect to parameter variations can be studied by changing the parameters independently and perform one-parameter continuation. For quasiperiodic tori this is not true, since quasiperiodic solutions are not structurally stable, i.e. a quasiperiodic vibration with two incommensurate frequencies can be changed into a phase-locked state by arbitrarily small changes in any parameter (Wiggins, 1990; Kuznetsov, 2004; Strogatz, 2000). Therefore, the continuation of quasiperiodic tori requires two free parameters to follow solutions with fixed frequency ratio (rotation number), and their loci are curves in a two-parameter plane. For example, note the slight shift in some of the positions of Earth-gravity tori in Figure 7.15 (a) with respect to the seed solutions. The union of the locus-curves of quasiperiodic tori covers a set of large measure (Glazier & Libchaber, 1988; Kuznetsov, 2004; Strogatz, 2000) in parameter space. In other words, there is a non-zero probability to observe quasiperiodic behavior in physical systems.

According to the above construction, the computation of periodic solutions for $\lambda = 0$ is equivalent to a computation of invariant tori for $\lambda = 0$. It shows that these tori are good approximations of the tori for $\lambda = 1$ for certain parameters. The computation of the invariant tori allows one to identify such parameter regions where neglecting gravity is a sound assumption, i.e. where the tori of the Earth-gravity system and the periodic solutions of the zero-gravity system do not differ significantly. In these regions one can obtain the response behavior of the turbocharger model much easier by studying the periodic solutions of the autonomous ODE (7.51) with $\lambda = 0$.

7.7.3   Computational Results

To test the validity of the zero-gravity assumption we sweep the two-parameter plane of radial bearing clearance c_r and forcing frequency ω with a large number of curves of Earth-gravity tori with fixed rotation number to obtain a picture as complete as possible. We then compare these results with the respective computations of periodic solutions for the zero-gravity approximation. All the computations were performed on Equation (7.51) in co-rotating coordinates. Note that, due to the shift in frequencies, the rotation numbers ϱ_f in the fixed frame and ϱ_r in the co-rotating frame systems are related via $\varrho_f = |\varrho_r - 1|$. In the results below we find $\varrho_r \leq 1$, thus $\varrho_f = 1 - \varrho_r$. This corresponds to the results in (7.30) where a similar transformation is obtained for the period length T_2 of the periodic solutions in the zero-gravity system.

The starting point for the whole computational process is a Fourier approximation of the periodic solution of the zero-gravity system for $\omega = 1000\,\text{Hz}$ and $c_r = 0.02\,\text{mm}$. It is
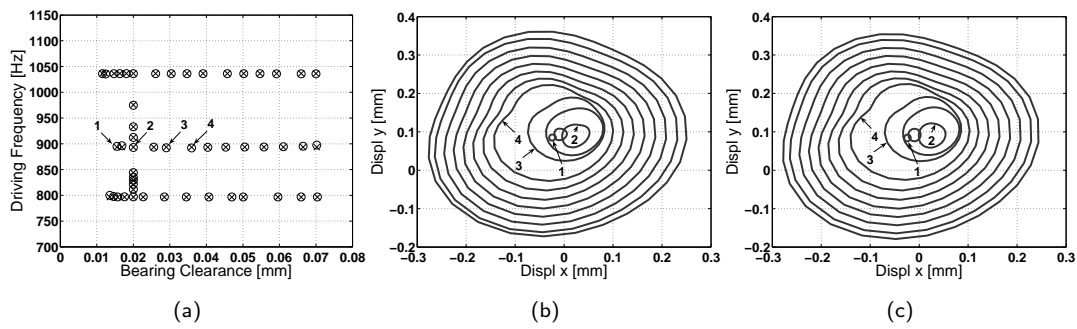
Figure 7.15: Positions of the seed solutions (label ×) and corresponding earth-gravity tori (label ○) in the (c_r, ω) plane (a). The invariant circles for Earth gravity (b) and the corresponding periodic solutions for zero gravity (c) for the starting positions along the row near $\omega \approx 894\,\text{Hz}$. The tori at the labeled positions are shown in Figure 7.16.

obtained by simulation and a subsequent Fourier transformation with $N = 15$ Fourier modes in (7.45). Then, by continuation of this periodic solution with respect to the forcing frequency or the bearing clearance, we cover the parameter space with a set of starting points for subsequent torus continuation. These starting solutions are shown in Figure 7.15 (a) as the columns and rows of crosses. The covered parameter range is $c_r \in [0.01\,\text{mm}, 0.08\,\text{mm}]$, which is the design margin of the used journal bearing, and $\omega \in [700\,\text{Hz}, 1200\,\text{Hz}]$, which is a principal range of operation for the turbocharger. Furthermore, the entrainment occurs in this frequency range in the experiment.

As explained in the previous section, initial approximations of tori in the Earth-gravity system can be constructed from these periodic solutions. These tori are computed with $N = 15$ Fourier modes and $M = 100$ Gauß collocation points and the mesh size is kept fixed for all subsequent computations. In the homotopy step we keep the radial bearing clearance c_r fixed and take the forcing frequency ω as a secondary free parameter. The obtained starting positions of tori are marked with circles in Figure 7.15 (a). Note that most of the starting positions coincide with the seed positions. The differences in the forcing frequencies mean that tori with a certain rotation number are observed for slightly different rotational speeds in the two systems. In other words, the response frequencies differ somewhat.

It shows that the distribution of starting solutions is dense enough to cover the (c_r, ω)-plane with loci of tori with fixed rotation numbers so that meaningful conclusions can be drawn. If the locus curves were to scarce in the parameter plane, more seed solutions with different rotation numbers would have to be computed.

In panels (b) and (c) of Figure 7.15 we compare the two types of solutions. Both graphs illustrate the change of the invariant circle in the stroboscopic map as the bearing clearance is increased and the forcing frequency is kept (approximately) constant $\omega \approx 900\,\text{Hz}$. The two sets of circles are clearly very similar. The full tori for the starting positions labeled 1 to 4 are shown in Figure 7.16 together with a plot of the
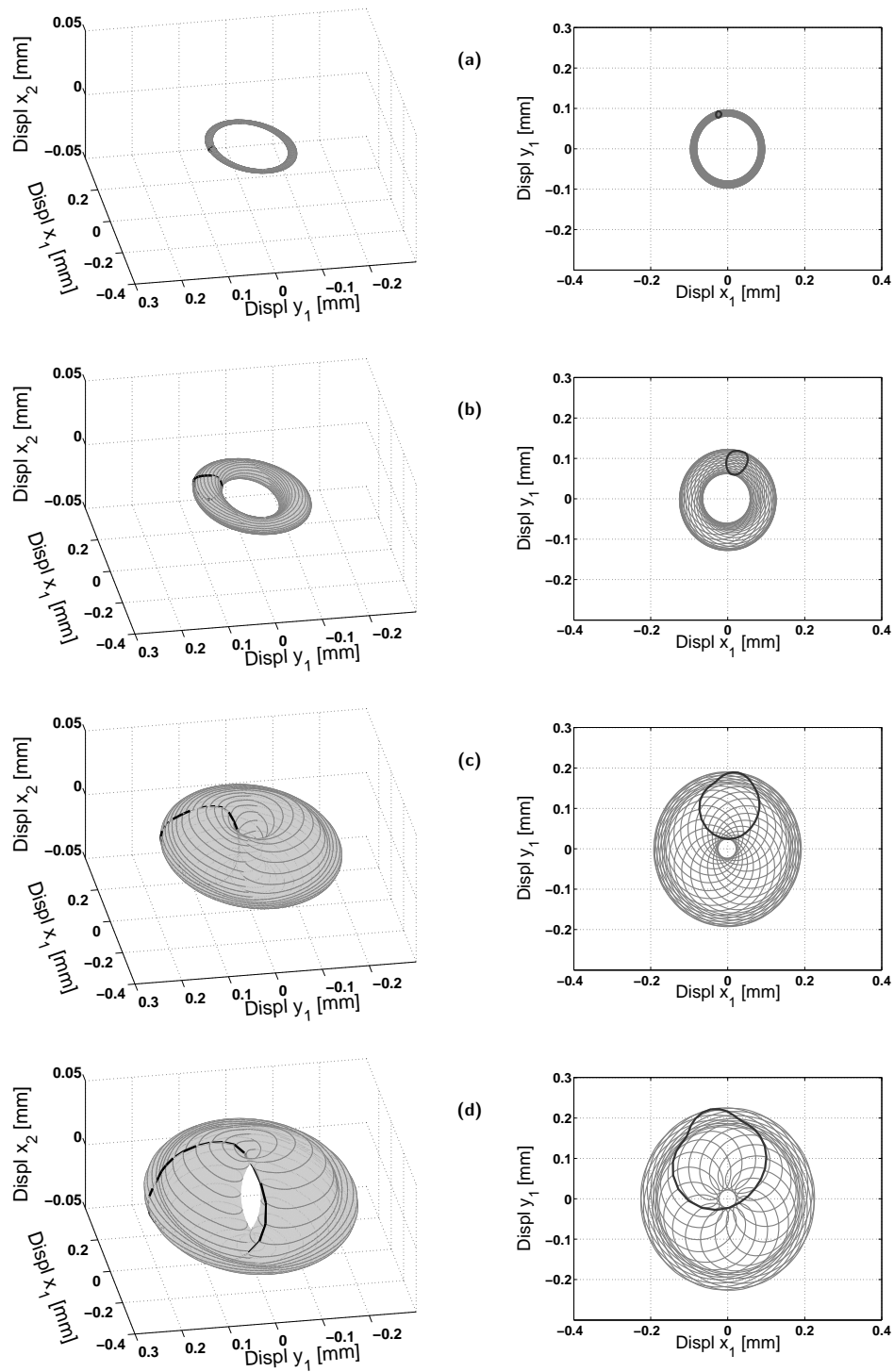
**Figure 7.16:** The left-hand column of (a)–(d) shows starting tori with labels 1, 2, 3 and 4, respectively, along the row $\omega = 894\,\text{Hz}$ in Figure 7.15 (a). The corresponding x- and y-displacements at the first FEM-node are shown in the right-hand column. The dark closed curve is the invariant circle of the period-$2\pi/\omega_1$ stroboscopic map.

x-y-displacements at node 1. A comparison of the results in Figure 7.16 (b) with the experimentally observed orbits and Poincaré sections depicted in Figure 7.13 (c) shows that, even though our finite beam-element model with oil-film forces is quite coarse, the numerical results are in good qualitative agreement with the experiment. Note that the Poincaré sections are defined differently in these figures.

A comparison of the two sets of resulting two-parameter curves is shown in Figure 7.17 with loci of tori with fixed rotation number in panel (a) and loci of periodic solutions with fixed frequency ratio in panel (b). The color bar indicates the rotation numbers that are associated with these curves. For easier interpretation they are shifted back to fixed-frame frequencies. The second response frequency ω_2 is the product of this shifted rotation number with the driving frequency shown on the vertical axis

$$\omega_2 = \rho_f \omega. \tag{7.55}$$

The curves match very well: Only in a band around 900 Hz there are some visible differences, which are small. At a first glance we observe that in the region covered the frequency ω_2 of the self-excited oscillation is approximately half the driving frequency, in accordance with the experimental data (cf. Figure 7.12). The line with constant $c_r = 0.02$ mm and varying driving frequency is of particular interest, since this is the value of the bearing clearance used in the current design of the turbocharger. Along this cross-section the rotation number decreases initially, stays almost constant for $\omega \in [830\,\text{Hz}, 970\,\text{Hz}]$ and then starts to increase again. This behavior occurs in the same region as the shift of the oil whirl response frequency away from the straight line $\omega_2 = 0.5\omega$ in Figure 7.12. However, in contrast to the experiment, it returns to $\rho_f = \frac{1}{2}$ for even higher frequencies.

Figure 7.17 also shows two dashed bifurcation curves, namely, a locus of Neimark-Sacker bifurcations (a) and the corresponding locus of Hopf bifurcations (b). These curves are parts of the curves shown in Figure 7.11 and match very well each other in this frequency range. For small bearing clearance, to the left of the Neimark-Sacker curve, the response is periodic and has the same frequency as the forcing. In the zero-gravity system this corresponds to an equilibrium solution. If this curve is crossed from left to right the quasiperiodic response is born and its amplitude grows rapidly as the bearing clearance is further increased. This can be seen from the invariant circle in Figure 7.15 (b) and the increasingly larger tori in Figure 7.16. Again the zero-gravity system exhibits very similar behavior, as is illustrated with panels (b) and (c) of Figure 7.15, where periodic solutions are compared with invariant circles of tori along the line $\omega = 894$ Hz. These results indicate that for the range of forcing frequencies considered here a reduction of the bearing clearance could dramatically reduce the amplitude of the quasiperiodic vibration or even suppress the second frequency completely.

Figure 7.17 (a) shows a total of 51 curves of tori and along each curve we computed 200 tori, which is the reason why some curves end in the middle of the figure. The
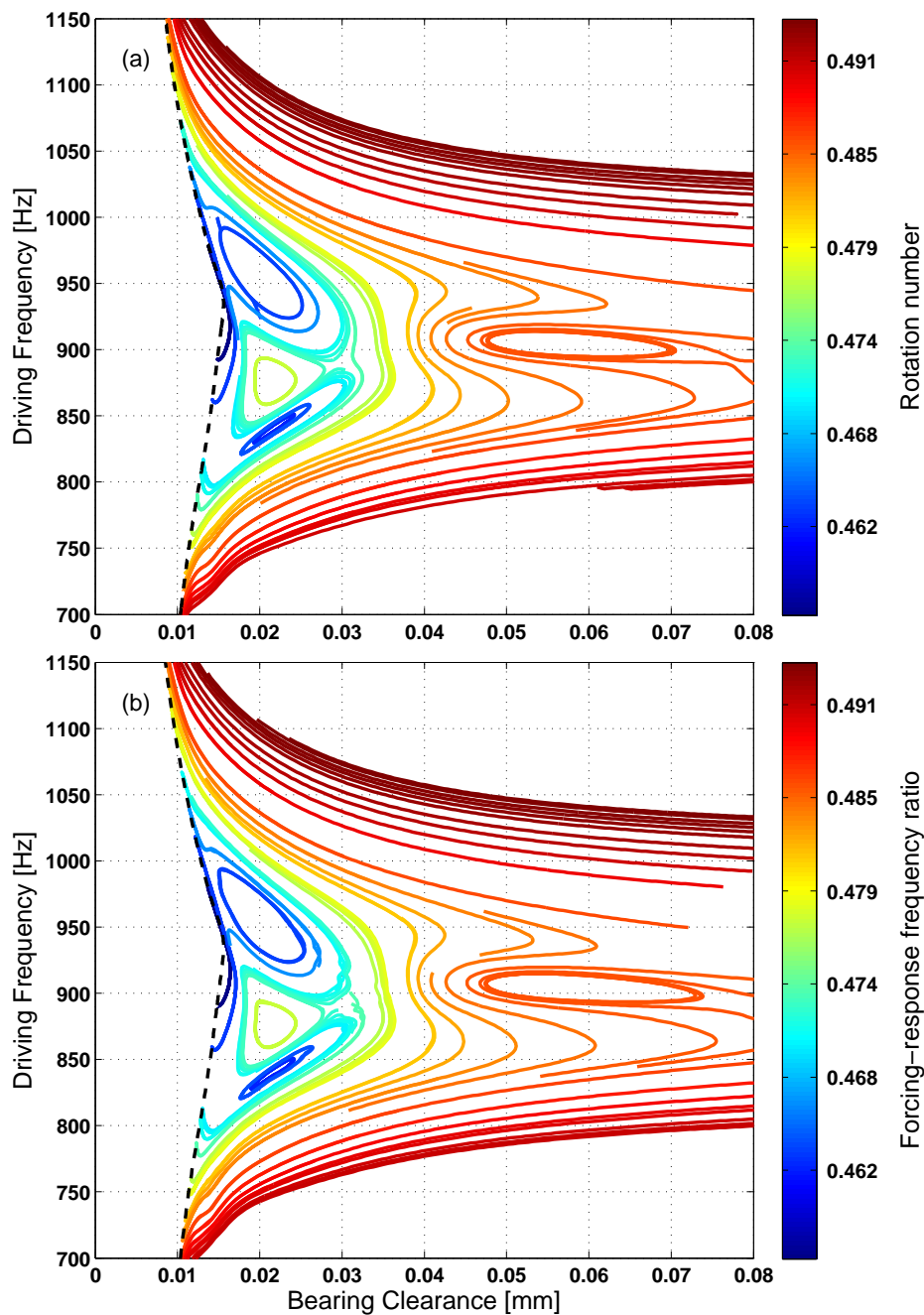
Figure 7.17: Curves of quasiperiodic tori with fixed rotation number of the Earth-gravity system (a) and curves of periodic solutions with fixed frequency ratio of the zero-gravity system (b). The diagram gives an overview of the second response frequency as a function of the bearing clearance and the forcing frequency. The color bar indicates the rotation number or frequency ratio associated with each curve, which was shifted back to fixed-frame frequencies for easier interpretation. The dashed curve in panel (a) is the locus of the Neimark-Sacker bifurcations, and the dashed curve in panel (b) is the locus of Hopf bifurcations (cf. Fig. 7.11). The second frequency is suppressed to the left of these curves, that is, there are no tori for bearing clearances smaller than ≈ 0.01 mm.

computation of the tori took approximately four weeks on an Intel Xeon CPU 2.66GHz, that is, the average time to compute one torus is about four minutes. The computation of the corresponding curves of periodic solutions in panel (b) with the same number of solutions along each curve was completed within 24 hours, that is, the computation of one periodic solution takes about nine seconds. Therefore, neglecting the gravity forcing in (7.51) yields a drastic gain in computation time, while the accuracy of the results is only slightly affected. As our computations show, the qualitative behavior of the two systems virtually coincides for the investigated parameters, and one might ask whether the introduced approximation error is at all significant. The results clearly suggest that one could perform an analysis of periodic solutions of the zero-gravity system and look at the Earth-gravity system only for reference and verification.

7.8   Influence of inertia terms

In the previous sections we have seen that continuation methods can be efficiently used to compute the frequency response of forced oscillating systems. In Section 7.7.3 it was demonstrated the transformation of the equation of motion into a co-rotating frame of reference and the subsequent neglecting of the gravity forcing provides a very useful and yet still accurate simplification in the parameter range of interest. We will now use this knowledge to examine the influence of the inertia correction to the short bearing solution of the pressure distribution in the journal bearing. The exact formula for this correction is given in Statement 5.2 in Chapter 5 and we will not repeat it here. The important difference to the previous sections is the implicit nature of the equation of motion, because the corrected pressure distribution depends on the nodal acceleration. In Section 7.2.1 it is shown how this can be overcome by an internal Newton method, so that we still can apply AUTO for the continuation of the periodic orbits. The correction parameter $\sigma \in [0, 1]$ is introduced to perform homotopies from the uncorrected pressure distribution $p = p^0$ to the inertia corrected pressure distribution $p = p^0 + \varepsilon p^1$ by $p(\sigma) = p^0 + \sigma \varepsilon p^1$. Hence, the bearing forces depend on σ and are equal to (5.159) and (5.160) for $\sigma = 0$ and to (5.168) and (5.170) for $\sigma = 1$.

7.8.1   Simple 4-D System

In order to illustrate the influence of the pressure correction and also its validity over a larger range of parameters, we examine the simple 4-D bearing model (6.16). Transformed to a co-rotating frame of coordinates the equations of motion are

$$\ddot{x} = \omega^2 x + 2\omega \dot{y} + \frac{1}{M}\left(-D(\dot{x} - \omega y) + \tilde{F}_{\text{bear}} + \omega^2 F_{\text{unb}}\right),$$

$$\ddot{y} = \omega^2 y - 2\omega \dot{x} + \frac{1}{M}\left(-D(\dot{y} + \omega x) + \tilde{F}_{\text{bear}}\right).$$

Note that here F_{unb} is transformed to a constant load. The gravity forcing has already been dropped.

To investigate the ratio of forcing frequency and response frequency directly, we additionally scale the time such that in the fixed frame the forcing has period 1

$$2\pi\tau = \omega t, \tag{7.56}$$

which results in

$$x'' = 4\pi\left(\pi x + y' + \frac{1}{M}\left(-\frac{D}{\omega}(x' - \pi y) + \frac{\pi\tilde{F}_{\mathrm{bear},1}(\sigma, W)}{\omega^2} + \pi F_{\mathrm{unb}}\right)\right), \tag{7.57}$$

$$y'' = 4\pi\left(\pi y - x' + \frac{1}{M}\left(-\frac{D}{\omega}(y' + \pi x) + \frac{\pi\tilde{F}_{\mathrm{bear},2}(\sigma, W)}{\omega^2}\right)\right), \tag{7.58}$$

where $'$ denotes the derivative with respect to τ. We identify 4 parameters in the system which we will use for continuation in the following: the driving frequency ω, the amplitude F_{unb} of the unbalance forcing, the correction factor σ which couples in the inertia correction, and the bearing width W, which we use to examine the range of validity of the inertia correction. All other parameters, especially the bearing radius and clearance, remain fixed at the usual values ($R = 3\,\mathrm{mm}$ and $c_r = 0.02\,\mathrm{mm}$, $D = 0.001\,\mathrm{g/s}$, $M = 1\,\mathrm{g}$).

The starting values for the parameters are $\omega = 16\pi$, $\sigma = 0$ and $W = 0.25\,\mathrm{mm}$. For $F_{\mathrm{unb}} = 0$ the system has a trivial fixed point for any value of ω, which is unstable for most values of ω. Continuation of the equilibrium with increasing F_{unb} as continuation parameters yields a non-trivial branch of equilibria. On this branch a Hopf bifurcation occurs after which the equilibria are stable. This happens for relatively large values of F_{unb}. The stable equilibria of the system in the co-rotating frame correspond to periodic orbits of the system in the fixed frame, which are phase-locked to the driving frequency in the case of strong forcing. In the next step we continue the stable periodic orbit that emerges at the Hopf bifurcation point backwards in F_{unb} and pick a solution with $F_{\mathrm{unb}} = 10^{-3}\,\mathrm{mm\,g}$. Now, we split the continuation process. First, a family A of periodic orbits is computed with respect to the driving frequency. Then, another family B of periodic orbits is computed after the inertia correction is switched on, i.e. the starting solution is continued until $\sigma = 1$, and then the driving frequency is increased. From each family we pick 20 solutions in steps of 100 Hz on the branches. All these are continued in the bearing width from $W = 0.25\,\mathrm{mm}$, a value for which the additional assumption (5.22) on the relation of width and radius is fulfilled, to $W = 2$.

In Figure 7.18 we show the results of these continuations. We plot the continuation branches in the driving frequency – bearing width plane ($\omega - W$). The period length of the corresponding periodic orbit is color encoded with shades of red indicating a period length T close to 2 and shades of blue indicating lower values of T. The graph on the left hand side shows the families of periodic solutions without inertia correction initiating at $W = 0.25$ from the previously computed branch A. The graph on the right
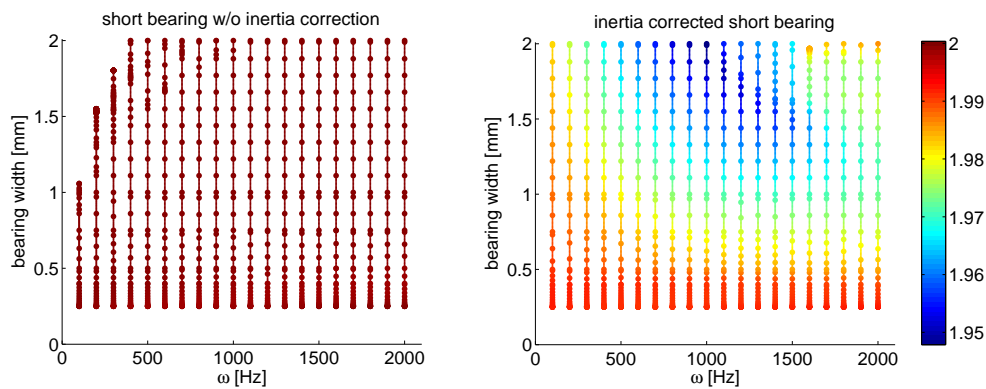
Figure 7.18: Branches of periodic solutions in the $\omega - W$ plane with the corresponding period length color encoded. The thicker points show the actually computed solutions. Left graph: Along the branches without inertia correction the period length varies very little and stays close to 2. Right graph: The solutions to the inertia corrected problem in the co-rotating frame coordinates show reduced period lengths, especially around $W = 1.5$ mm and $\omega = 1000$ Hz, which corresponds to increased period lengths the fixed frame, i.e. reduced response frequencies.

hand side shows the families of solutions initiating from the branch B computed before with the inertia correction switched on.

The period length of the uncorrected model show almost no dependence on ω and W along the branches and the period length remains 2 over the whole parameter range. This corresponds to a self-excited oscillation with frequency $\omega_2 = \frac{\omega}{2}$ which we have also observed in most of the simulations.

It can clearly be seen, that already for $W = 0.25$ the period length of the inertia corrected solutions is reduced. In the fixed frame of coordinates this corresponds to a reduction of the frequency of the self-excited oscillation, as we have shown in (7.30). For increasing W the frequency shift gets stronger until approximately $W = 1.5$. From this value on, the period length increases again on the branches with higher driving frequency ω and decreases further on those with lower ω. For small W the frequency shift between the branches on the left and those on the right is constant. This corresponds to a linear shift of the subharmonic response. For higher W however, the difference in period length between the branches first increases with omega until around $\omega = 1000$ Hz. This corresponds to the 'bending' away of the oil whirl peaks from the $\frac{\omega}{2}$-line in Figure 7.12. For $\omega > 1000$ Hz the difference in period length decreases again, a behavior not observed in experiment. Note that the value $W = 5.4$ mm used in the previous simulations cannot be reached along the read branches as the computations break down on the way, due to strongly increasing periods. This can be explained by the fact that especially the inertia correction for the short bearing (5.63) is no longer valid for larger values of W and gives erroneous results, while the uncorrected short bearing solution still yields quite reasonable results. In Section 5.6 the analysis of the asymptotic behavior of the bearing integrals showed similar results.

However, for small values of the bearing width for which both orders of the short bearing approximation are valid, the inertia correction leads to a significant reduction of the subharmonic response frequency over the whole frequency range. Allthough, there can be other explanations for the shift of the frequency ratio, the results in this section show that the influence of the inertia correction has to be considered as a possible explanation of the this experimentally observed behavior.

7.8.2   Inertia Correction for 3-Element Model

In the previous section we have seen, that the inertia correction has an effect on the frequency of the self-excited oscillation. We have noticed there, that in the case of the zeroth order approximation of the bearing pressure distribution the frequency ratio of self-excited oscillation and forcing do not depend on the bearing width, but they do in the case of first order approximation. For larger values of W the results tend to be erroneous as we have also seen in Section 5.6. However, values for W small enough for inertia correction to be valid do not suffice to contain a rotor with the given specifications.

However, to show the applicability of the method also to the 32-dimensional model of the turbocharger, we computed continuations of periodic orbits in the correction parameter σ for 2 different driving frequencies ($\omega = 20\,\text{Hz}, 1200\,\text{Hz}$) using a bearing width of $W = 5.4\,\text{mm}$ as it was also used in the experiments. The equation of motion is given by (7.22) and like in the previous section we introduce the inertia correction parameter σ with which we do a homotopy from bearing function given by the zeroth order short bearing approximation to the first order approximation.

The starting solutions are chosen from the family of periodic orbits which has been computed in Section 7.6 with the zeroth order short bearing approximation as bearing model (5.159),(5.160), and which is depicted in Figure 7.10. Along this family of periodic orbits, the ratio of the frequency of the self excited oscillation and the forcing is not constant. This figure corresponds to the cut along the line $c_r = 0.02$ in panel (b) of Figure 7.17 which is described in Section 7.7.3. We observe that the ratio drops significantly in the frequency range around $900\,\text{Hz}$ where we have a resonance of the first bending mode (cf. the linear stability analysis in Fig. 7.4). Note, that the frequencies of the solution seen in the co-rotating frame and in the fixed frame of coordinate transform into each other according to Equation (7.30). To facilitate the comparison with the experimental results, we show the frequency ratio calculated in the fixed frame.

From the starting solution we initiate the continuation by increasing the parameter σ. The continuation process is quite slow because of the internal Newton method. It is not possible to reach the value $\sigma = 1$, because the period length of the periodic orbit becomes very large and the computations stop due to convergence problems. In
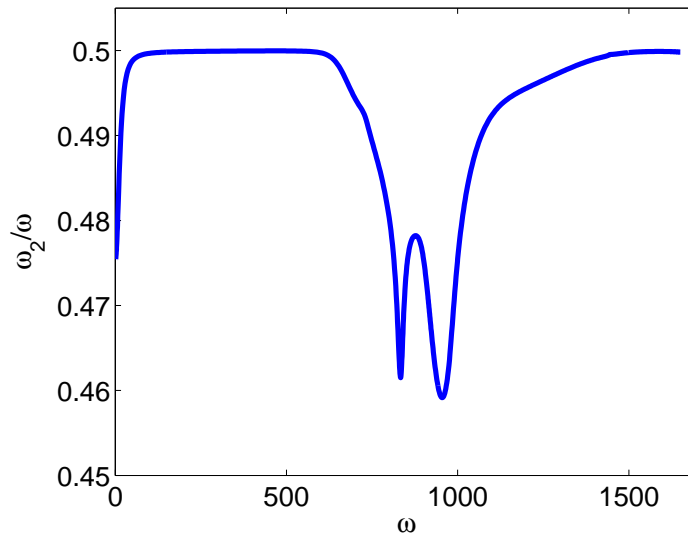
Figure 7.19: Ratio of the frequency of the self-excited oscillation and the forcing frequency for family of periodic orbits depicted in Figure 7.10. In contrast to the experimental result, the ratio increases to 0.5 again after the entrainment region around 1000Hz.
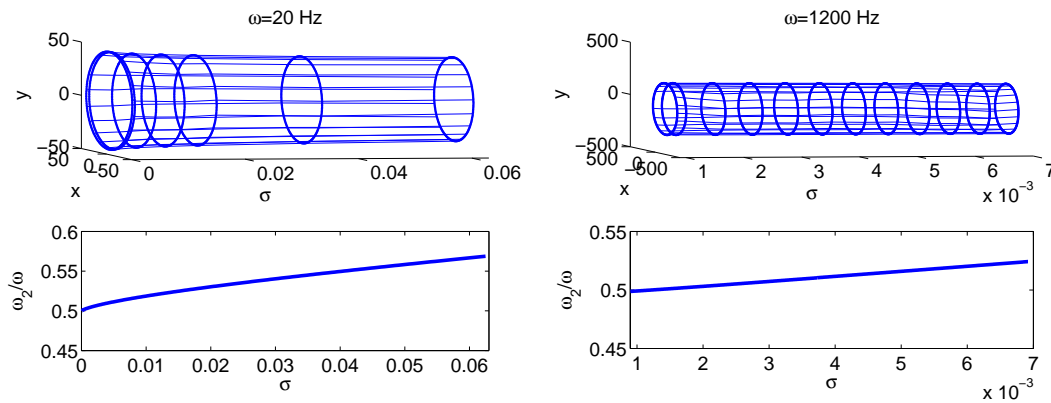
Figure 7.20: 2 families of periodic orbits with different driving frequency computed by continuation in the inertia correction factor σ; the lower graphs show the dependence of the frequency of the self-excited oscillation from σ. The shift of the frequencies goes to the opposite direction as the one observed in the experiments.

Figure 7.20 we depict the two families of periodic solutions in dependence of σ. While the orbit structure does not change very much in both cases, the ratio of the frequencies increases with σ. For the low forcing frequency the change of the ratio is smaller than for the large forcing frequency.

These results are in contrast to what we observe in the experiment. There, no shift away from the frequency ratio $\frac{1}{2}$ is observable for low driving frequencies, while for higher driving frequencies the ratio drops below $\frac{1}{2}$. So, the results show that for larger values of the bearing width the inertia correction of the short bearing pressure distribution

does not explain the frequency shift. However, this is not a surprising result, since it was already shown in Section 5.6 that the validity of the short bearing approximation, and especially of the first order correction p^1 5.63 is not given for $W = 5.4\,\mathrm{mm}$.

Nevertheless, these computations show that the continuation of periodic orbits is also possible if we apply the internal Newton method to solve the implicitly given equation of motion. The steps taken by the predictor of AUTO are small enough, such that the last value computed for $\dot{x}$ in the user supplied function is also good starting point for the internal Newton method, and convergence is achieved in very few iteration steps. It can hence be used in the evaluation of other bearing models even if these involve implicit terms, and can therefore assist in the future development of a lubrication model which describes the frequency shift of the subharmonic response better than the lubrication models used here.

7.9 Conclusions

In this chapter we analyzed the bifurcation behavior of several models for fast rotating bodies in journal bearings. Two models of a turbocharger were used as examples. A four dimensional prototypical model was also analyzed. We summarize our findings:

7.9.1 Torus Bifurcation at the onset of Oil Whirl

The continuation of the periodic orbits with respect to the driving frequency show that a torus bifurcation occurs at the onset of the oil whirl of the rotor of the turbocharger. The periodic orbit of the harmonic response becomes unstable at the critical frequency and a stable invariant torus bifurcates from it. This behavior is observed in both, the large 112-dimensional and the smaller 32-dimensional turbocharger model. In the case without unbalance forcing a Hopf bifurcation occurs at a frequency close to the critical frequency of the forced case.

7.9.2 Computation of Locus Curves and Suppression of Whirl

The locus curve of the Hopf bifurcation at the onset of instability can be computed directly with AUTO in the damping-driving frequency domain as well as in the bearing clearance-driving frequency domain. The locus curve of the torus bifurcation has to be detected by sweeping the parameter space with branches of periodic solutions. Comparison of the two curves shows no significant differences. The self-excited oscillation can be suppressed by large external damping or for small values of the bearing clearance. From a physical point of view, a large bearing clearance leads to the undamping of the conical mode via oil-film forces.

7.9.3 Computation of Quasiperiodic Tori Justifies Neglecting Static Loads

The continuation of quasiperiodic tori in the two parameters bearing clearance and the driving frequency verified that gravitational forces can be neglected for higher rotational speeds. This leads to a dramatic reduction of computational effort if the model is formulated in co-rotating coordinates, because invariant tori of the Earth-gravity system are well approximated by tori constructed from periodic solutions of the zero-gravity system. These periodic solutions can be computed much simpler and the available efficient methods like AUTO can be applied to substantially more detailed models of a turbocharger, or other machinery with fast rotating parts. For systems where the static loads cannot be considered to be small perturbations, the computation of invariant tori is necessary and the method proposed in (Schilder & Peckham, 2007) and applied above works well for moderately large systems. On the one hand it is more memory consuming than direct simulation. On the other hand it is faster and gives more information about the dynamics, since it allows to compute also unstable tori and hence the analysis of hysteresis effects.

7.9.4 Validity of Inertia Correction of Short Bearing Approximation

The effect and the validity of the inertia correction of the short bearing approximation of pressure distribution in the journal bearings can be studied efficiently by performing a homotopy between zeroth order and first order short bearing approximation. The internal Newton method is applied to solve the implicit equation of motion inside the user supplied function for AUTO and performs well. For the 4-D toy problem with small bearing width fulfilling (5.22), the inertia correction leads to a significant reduction of the ratio of the frequency of the self-excited oscillation and the driving frequency as observed in the experiments. This reduction persists under a change of the bearing width up to values of $W = 2\,\mathrm{mm}$. While the validity of the inertia correction of the short bearing approximation is not given for the 32-dimensional turbocharger model with bearing width $W = 5.4\,\mathrm{mm}$, the proposed procedure of using a co-rotating frame of reference, neglecting gravity, and applying the internal Newton method proves to be applicable for the continuation of such systems. It could be used in the future to study the behavior of other models for systems with fast rotating parts which include lubrication models leading to implicit equations of motion.

Chapter 8

Conclusions and Outlook

The following closing remarks summarize the most important results of the present thesis and show up some possible directions for future research.

The starting point for the thesis was the need for a more detailed and exact model for the prediction of the vibration of a passenger car turbocharger. Vibrations in rotating machinery are a common problem and the prediction of the frequencies and the amplitudes of the occurring oscillations and their dependence on physical parameters such as bearing geometry, lubricant viscosity or temperature, and rotational frequency is of utter importance for the development of more efficient and reliable designs. Therefore, a general model for rotating beams in oil-lubricated bearings has been developed in this work and has been successfully applied to predict the lateral vibrations of a turbocharger in simple journal bearings.

By applying Euler-Bernoulli beam theory and the Lagrange formalism we have derived a model for a continuous, isotropic rotor of varying diameter to which rigid disks modelling fly-wheels are attached. Special attention has been given to the effects of rotatory inertia and gyroscopic effects which become more and more influential on the rotors eigenfrequencies for rising rotational frequencies. The misalignment of the center of gravity of the cross-sections of the beam with axis of rotation leads to a periodic unbalance forcing. The bearing reaction forces are modeled as nonlinear point forces at two points along the axis of the rotor. For the numerical simulation of the model equations, the finite element discretization of the equations for the continuous beam has been realized by the approximation with piecewise cubic polynomials, leading to Rayleigh beam elements. The resulting ordinary differential equation describes the lateral motion in the finite element nodes. The modeling approach in this work is valid for small displacements and neglects shear deformation which is justified for slender beams. For non-slender beams with larger diameter-to-length ratio the inclusion of shear effects by using e.g. Timoshenko beam theory is necessary.

One of the main results of the work is the proof of existence of solutions for the equa-

tions of motion. It is given for the quite general class of locally Lipschitz-continuous support-functions by first applying Galerkin's method to the problem with linear spring and damper support, and then using a Banach fixed point argument to obtain existence also in the nonlinear case. A special difficulty is the confinement of the rotor into the bearings and the absence of a growth condition for the bearing functions for large eccentricities. Hence, the result for the nonlinear support only yields short time existence and no statement is made about possible collisions with the bearing casing. For simpler polynomial bearing functions it should be possible to prove the existence of solutions global in time which are bounded at the positions of the bearings such that no collisions occur, because global a priori estimates can be easily obtained. The more complicated bearing functions for hydrodynamic bearings do not show such a simple growth behavior for large eccentricities. They are however also restoring forces and therefore a proof of long time existence should also be possible with some more technical considerations.

Another main result of the thesis is the derivation of inertia corrections to the thin film equations used in the modeling of the bearings and the examination of their influence on the rotor self-excited oscillation. In previous models, the reaction forces of the oil-lubricated journal bearings were modeled by using Reynolds' equation for the pressure distribution in the thin lubricant film and subsequent integration over the journal surface. In the present work the short bearing approximation was applied in first simulations of the system. This simplification allows for an analytical expression of the forces and hence fast numerical evaluation. These simulations yield already qualitatively good results. The main oscillation phenomena observed in the experiments are captured in the model. The harmonic unbalance oscillation is present and a resonance of a bending mode occurs at the same driving frequency as in the experiment. The fluid-induced self-excited oscillation, the well known rotor instability called oil whirl, also appears in the model, and the onset frequency is close to the experimentally measured one.

The frequency of the self-excited subharmonic oscillation, however, is predicted too high. In the experiment the ratio of subharmonic frequency driving frequency is $\frac{1}{2}$ between the onset of the instability and the resonance of the bending mode, and it drops to approximately $\frac{2}{5}$ with increasing rotational frequencies above the resonance of the bending mode. In the simulations this ratio remained constant equal to $\frac{1}{2}$ for all rotational frequencies. This small difference between model and experiment resulted in a deeper investigation of the derivation of the lubrication model.

Considerations about the fluid average circumferential velocity lead to the introduction of a phenomenological correction term into the short bearing pressure solution, which allowed for a tuning of the subharmonic response frequency. There is a one-to-one correspondence between that velocity and the subharmonic response frequency. The success of the phenomenological model showed that the frequency of the self-excited

oscillation depends strongly on the lubrication model. In order to give also a modification of the old lubrication model based on first principles, we have derived new inertia correction terms for Reynolds' equation and also for the short bearing approximation based on an additional relation between bearing width and radius. The introduction of these correction terms into the equation of motion complicates its numerical solution, because it is changed from an explicit to an implicit ordinary differential equation, but it can still be solved by applying the appropriate implicit methods like e.g. `DASPK` (Brenan *et al.*, 1989). For bearing dimensions as in the experimental setup, the inertia corrections of Reynolds' equation showed no detectable effect on the frequency of the oil whirl. For very short bearings however an small decreasing effect could be observed in the simulations.

Numerical continuation methods for periodic orbits and quasiperiodic orbits have proved to be more efficient for performing extensive parameter studies of oscillating systems. Using the package `AUTO` (Doedel *et al.*, 2000) locus curves of the Hopf bifurcations and the torus bifurcations at the onset of the oil whirl were computed in the unforced and forced case, respectively, thereby allowing the direct determination of the regions of stability of the rotor. A transformation of the equations of motion to a co-rotating frame of coordinates together with neglecting the static load makes the system autonomous, a significant simplification. For the example of the turbocharger, neglecting the static load is justified for larger rotational velocities. This is shown by computing the quasiperiodic solutions of the non-autonomous system by applying a recently introduced Fourier method for the continuation of tori and comparing them with the periodic ones of the simplified autonomous system. By applying this simplification it was also possible to examine the validity of the inertia correction in the short bearing approximation over a larger range of parameters. All in all, the application of continuation methods together with the simplification of the system to co-rotating coordinates and the neglect of the static load is shown to be a powerful tool in the investigation of rotordynamic models and should be considered as an alternative to the time integration methods popular in current CAE methods.

The phenomenological correction of the bearing reaction forces seems to be a good alternative starting point for further research. Its influence on the frequency response is much stronger than the inertia corrections and changes in the response frequency similar to the experiment could be achieved. There are some possible further developments. First, an even more detailed analysis of the lubrication model taking into account thermic effects on the bearing geometry, the effect of the oil inlet, or non-Newtonian behavior of the lubricant (San Andrés & Kerth, 2004) could lead to a change in the average circumferential velocity. Also cavitation effects, turbulence or secondary flows, i.e. liquid flowing in the direction opposite the rotation of the shaft, have been neglected in this work, but could reduce that velocity and hence the frequency of the oil whirl.

Another interesting application for the phenomenological correction is its application in situations where fast evaluation of the bearing response is important and has to be done very often, like in an optimization setting. In (Strauß, 2005) the shape of the rotor has been optimized with respect to the unbalance response for a similar model but with linear spring and damper bearings. The nonlinear effects of the bearings, especially the fluid induced instability, were not considered there. To include them, the computation of periodic obits, e.g. by a boundary value method, is necessary which is computationally expensive. If the bearing geometry is not part of the optimization, the frequency response behavior for the oil whirl which depends mainly on that geometry could be prescribed by applying the phenomenologically corrected model during the optimization. After the optimization or at some intermediate stage a more detailed and computationally more expensive lubrication model could than be used for verification only.

The research presented in this thesis has contributed successfully to the developement of a model for rotating machinery and the examination of the parameter dependencies of the occuring oscillations. Parts of the results are also currently applied at the Toyota Central Research and Development Laboratories (TCRDL) to compute the response vibration of a turbocharger in floating ring bearings and are included in a pending patent application (Rübel *et al.*, 2006) in Japan.

Appendix A

Euler Angles

Figure A.1: Euler angles of a rotating disc

In Section 2.3 we use Euler angles to describe the position of a disk in space. The Euler angles used here and in (Nelson & McVaugh, 1976) differ slightly from those commonly used in textbooks like (Nolting, 1989; José & Saletan, 1998) and in parts of the engineering literature (Yamamoto & Ishida, 2001). We shall therefore give here the explicit derivation for the expression of the momentary angular velocity Ω in terms of the Euler angles.

The position of the cross-section relative to the origin is given by the Euler angles (γ, β, ϕ) shown in Figure A.1. The three angles describe three successive rotations of the disk whose principal axis of inertia (e_1, e_2, e_3) are assumed to be initially collinear with the space coordinate system (e_x, e_y, e_z). The first rotation leaves the y-axis fixed and rotates the disk by the angle γ about this axis. The second rotation leaves the image $e_{x'}$ of the vector e_x fix and rotates the disk by β. The third rotation which corresponds to the spin of the disk rotates the coordinate system about the image of e_z under the first two equations by the angle ϕ. The rotation matrices for the three rotations are

$$R_1 = \begin{pmatrix} \cos\gamma & 0 & -\sin\gamma \\ 0 & 1 & 0 \\ \sin\gamma & 0 & \cos\gamma \end{pmatrix}, \tag{A.1}$$

$$R_2 = \begin{pmatrix} 1 & 0 & 0 \\ 0 & \cos\beta & \sin\beta \\ 0 & -\sin\beta & \cos\beta \end{pmatrix}, \tag{A.2}$$

$$R_3 = \begin{pmatrix} \cos\varphi & \sin\varphi & \\ -\sin\varphi & \cos\varphi & \\ 0 & 0 & 1 \end{pmatrix}. \tag{A.3}$$

Successive application of the rotations yields the transformation matrix which allows the calculation of the angular velocity in the body system (e_1, e_2, e_3)

$$R = R_3 R_2 R_1 \tag{A.4}$$
$$= \begin{pmatrix} \cos\varphi\cos\gamma + \sin\varphi\sin\gamma\sin\beta & \sin\varphi\cos\beta & -\cos\varphi\sin\gamma + \sin\varphi\sin\beta\cos\gamma \\ -\sin\varphi\cos\gamma + \cos\varphi\sin\gamma\sin\beta & \cos\varphi\cos\beta & \sin\varphi\sin\gamma + \cos\varphi\sin\beta\cos\gamma \\ \cos\beta\sin\gamma & -\sin\beta & \cos\beta\cos\gamma \end{pmatrix}.$$

From Figure A.1 we see that the momentary angular velocity is given by

$$\Omega = \dot\gamma e_y + \dot\beta e_{x'} + \dot\phi e_3. \tag{A.5}$$

In this equation e_y is the unit vector in y-direction, e_3 is the normal vector to the plane (and also spans a principal axis of inertia), and $e_{x'}$ is the unit vector along the image of the x-axis after the first rotation. The coordinates of e_y in the rotating body coordinate system are $R \cdot e_y$, those of $e_{x'}$ are given by $RR_1^{-1} \cdot (1, 0, 0)^T$. Hence we can write

$$\Omega = \begin{pmatrix} \sin\varphi\cos\beta & \cos\varphi & 0 \\ \cos\varphi\cos\beta & -\sin\varphi & 0 \\ -\sin\beta & 0 & 1 \end{pmatrix} \begin{pmatrix} \dot\gamma \\ \dot\beta \\ \dot\varphi \end{pmatrix}. \tag{A.6}$$

In Section 2.3 the Euler angles and the kinetic energy of the rotating disk are expressed in terms of the shaft's prescribed spin velocity ω which is assumed to be constant and the tangential vector $t = (\partial_z u, \partial_z v, 1) = (u', v', 1)$ of the center curve $r_0(z, t)$. We give the detailed derivations here for completeness. To simplify the notation we denote the

derivative of a given quantity f with respect to z by f', and the derivative with respect to t by $\dot{f}$.

From Euler-Bernoulli theory we know that the tangential vector to the center-line is orthogonal to the disk and hence collinear to e_3. From this and Fig. A.1 we can derive that

$$\tan \gamma \;=\; u', \tag{A.7}$$

$$\tan \beta \;=\; \frac{-v'}{\sqrt{1 + u'^2}}. \tag{A.8}$$

The angle ϕ of the rotation about the axis spanned by e_3 equals the spin of the disk if there is no torsion. We shall assume this and we set

$$\phi = \omega t. \tag{A.9}$$

If the inclination of the shaft is small, so are γ and β and we have

$$\gamma = u' + O(u'^3), \tag{A.10}$$

$$\beta = -v' + O(v'^3, v'u'^2). \tag{A.11}$$

Furthermore from (A.7) and (A.8) we get the following for the angular velocities:

$$\dot{\gamma} \;=\; \frac{\dot{u}'}{1 + u'^2} = \dot{u}' + O(u'^2), \tag{A.12}$$

$$\dot{\beta} \;=\; -\frac{\dot{v}' + \dot{v}'u'^2 - u'v'\dot{u}'}{\sqrt{1 + u'^2}(1 + u'^2 + v'^2)} = -\dot{v}' + O(u'^2, u'v', v'^2), \tag{A.13}$$

$$\dot{\varphi} \;=\; \omega. \tag{A.14}$$

The rotational energy of a rigid body rotating about an axis through its center of gravity is given by

$$T_{rot} = \frac{1}{2}\left(I_1\Omega_1^2 + I_2\Omega_2^2 + I_3\Omega_3^2\right), \tag{A.15}$$

where Ω is the angular velocity in the coordinate system spanned by the principal axis of inertia. We want to express this energy in terms of u and v. First we plug in the expressions for Ω from Eq. (A.6).

$$
\begin{aligned}
2T_{rot} \;=\;& I_1(\dot{\gamma}\sin\varphi\cos\beta + \dot{\beta}\cos\varphi)^2 \\
& +I_2(\dot{\gamma}\cos\varphi\cos\beta - \dot{\beta}\sin\varphi)^2 \\
& +I_3\left(\dot{\varphi} - \dot{\gamma}\sin\beta\right)^2 \\
=\;& \frac{1}{2}(I_1 + I_2)\left(\dot{\gamma}^2\cos^2\beta + \dot{\beta}^2\right) \\
& +I_3\left(\dot{\varphi}^2 - 2\dot{\gamma}\dot{\varphi}\sin\beta + \dot{\gamma}^2\sin^2\beta\right) \\
& +\frac{1}{2}(I_1 - I_2)\left((\dot{\beta}^2 - \dot{\gamma}^2\cos^2\beta)\cos 2\varphi + 2\dot{\beta}\dot{\gamma}\cos\beta\sin 2\varphi\right). \tag{A.16}
\end{aligned}
$$

Then we insert the expressions for γ and β from above and neglect all terms of order u'^2, v'^2, $u'v'$, and higher,

$$
\begin{aligned}
2T_{rot} \quad \approx \quad & \frac{1}{2}(I_1 + I_2)\left(\dot{u}'^2 + \dot{v}'^2\right) \\
& + I_3\left(\omega^2 + 2\omega\dot{u}'v'\right) \\
& + \frac{1}{2}(I_1 - I_2)\left((\dot{v}'^2 - \dot{u}'^2)\cos 2\omega t - 2\dot{u}'\dot{v}'\sin 2\omega t\right).
\end{aligned} \tag{A.17}
$$

Appendix B

Tools from Functional Analysis

In (Jost, 1998) we find the following variant of Poincaré's inequality.

Lemma B.1 (Generalized Poincaré Inequality). *Let $\Omega \subset \mathbb{R}^d$ be convex, $u \in H^{1,p}(\Omega)$. Then for every measurable $B \subset \Omega$ with $|B| > 0$ we have*

$$\left(\int_\Omega |u - \bar{u}_B|^p \right)^{\frac{1}{p}} \leq \frac{C}{|B|} \left(\int_\Omega |Du|^p \right)^{\frac{1}{p}}, \tag{B.1}$$

where $\bar{u}_B = \frac{1}{B} \int_B u(x) dx$ is the average of u on B.

In (Evans, 1998) Gronwall's inequality is used for proving a priori estimates of solutions of PDEs. We cite the differential version here.

Lemma B.2 (Gronwall's Inequality). *Let $\eta : [0, T] \to \mathbb{R}^+$ be absolutely continuous and satisfy for almost all t the differential inequality*

$$\eta' \leq \phi(t)\eta(t) + \psi(t) \tag{B.2}$$

with nonnegative, summable functions $\phi : [0, T] \to \mathbb{R}^+$ and $\psi : [0, T] \to \mathbb{R}^+$. Then η satisfies

$$\eta(t) \leq e^{(\int_0^t \phi(s)ds)} \left[\eta(0) + \int_0^t \psi(s)ds \right]. \tag{B.3}$$

Lemma B.3. *The mass matrix appearing in the ODE of the Galerkin approximation (3.52) is nonsingular.*

Proof. M is defined by applying the scalar product $m(.,.)$ to the elements of the orthogonal basis $\{w^k\}_k \subset H^2(\Omega)$ which are chosen as approximation function,

$$M_{jk} = m(w^k, w^j) \quad \text{for} \quad 1 \leq j, k \leq n. \tag{B.4}$$

Suppose M is singular. Then the columns of M are linear dependent and there are $\lambda_1, \ldots, \lambda_n$, with at least one $\lambda_i \neq 0$, such that the columns can be combined to 0,

$$0 = \sum_{k=1}^{n} \lambda_k m(w^k, w^j) = m\left(\sum_{k=1}^{n} \lambda_k w^k, w^j\right) \quad \text{for} \quad 1 \leq j \leq n. \tag{B.5}$$

Now we form the scalar product of this vector with the vector $\bar{\lambda} = (\bar{\lambda}_1, \ldots, \bar{\lambda}_n)^T$ and obtain

$$0 = \sum_{j=1}^{n} \bar{\lambda}_j m\left(\sum_{k=1}^{n} \lambda_k w^k, w^j\right) = m\left(\sum_{k=1}^{n} \lambda_k w^k, \sum_{j=1}^{n} \lambda_j w^j\right) = \left\|\sum_{j=1}^{n} \lambda_j w^j\right\|_{H_m^1(\Omega)}^2,$$

since $m(.,.)$ is a scalar product. Hence

$$\sum_{j=1}^{n} \lambda_j w^j = 0,$$

which is a contradiction, because the $\{w^k\}_{k=1,\ldots,n}$ are elements of an orthogonal basis and hence linearly independent. Therefore, M is nonsingular. $\qquad\square$

Appendix C

Element Matrices

In Chapter 4 we derive the element matrices for a finite rotating Rayleigh beam element and for rigid disks by the use of Hermite polynomials as shape functions. The exact form of the functions and of the matrices is given in this appendix.

C.1 Shape Functions

The Hermite polynomials which are used for the interpolation of the displacement of a beam element with prescribed nodal displacements u_k, v_k, u_{k+1}, v_{k+1} and inclinations β_k, γ_k, β_{k+1}, and γ_{k+1} are given by

$$\Psi_1(z) = 1 - 3\left(\frac{z-z_k}{l_k}\right)^2 + 2\left(\frac{z-z_k}{l_k}\right)^3, \tag{C.1}$$

$$\Psi_2(z) = (z-z_k)\left(1 - 2\left(\frac{z-z_k}{l_k}\right) + \left(\frac{z-z_k}{l_k}\right)^2\right), \tag{C.2}$$

$$\Psi_3(z) = 3\left(\frac{z-z_k}{l_k}\right)^2 - 2\left(\frac{z-z_k}{l_k}\right)^3, \tag{C.3}$$

$$\Psi_4(z) = l_k\left(-\left(\frac{z-z_k}{l_k}\right)^2 + \left(\frac{z-z_k}{l_k}\right)^3\right), \tag{C.4}$$

and the displacement is given by

$$\begin{bmatrix} u \\ v \end{bmatrix} = \begin{bmatrix} \Psi_1 & 0 & 0 & \Psi_2 & \Psi_3 & 0 & 0 & \Psi_4(z) \\ 0 & \Psi_1 & -\Psi_2 & 0 & 0 & \Psi_3 & -\Psi_4(z) & 0 \end{bmatrix} q_k = W_k q_k, \tag{C.5}$$

where $q^T = (u_k, v_k, \beta_k, \gamma_k, u_{k+1}, v_{k+1}, \beta_{k+1}, \gamma_{k+1})$. The derivative in axial direction is given by

$$\begin{bmatrix} u' \\ v' \end{bmatrix} = \begin{bmatrix} \Psi_1' & 0 & 0 & \Psi_2' & \Psi_3' & 0 & 0 & \Psi_4'(z) \\ 0 & \Psi_1' & -\Psi_2' & 0 & 0 & \Psi_3' & -\Psi_4'(z) & 0 \end{bmatrix} q_k = W_k' q_k \tag{C.6}$$

with

$$\Psi'_1(z) = \frac{6}{l_k}\left(-\frac{z-z_k}{l_k} + \left(\frac{z-z_k}{l_k}\right)^2\right), \tag{C.7}$$

$$\Psi'_2(z) = 1 - 4\frac{z-z_k}{l_k} + 3\left(\frac{z-z_k}{l_k}\right)^2, \tag{C.8}$$

$$\Psi'_3(z) = \frac{6}{l_k}\left(\frac{z-z_k}{l_k} - \left(\frac{z-z_k}{l_k}\right)^2\right), \tag{C.9}$$

$$\Psi'_4(z) = -2\frac{z-z_k}{l_k} + 3\left(\frac{z-z_k}{l_k}\right)^2. \tag{C.10}$$

For the second derivatives we have

$$\begin{bmatrix} u'' \\ v'' \end{bmatrix} = \begin{bmatrix} \Psi''_1 & 0 & 0 & \Psi''_2 & \Psi''_3 & 0 & 0 & \Psi''_4(z) \\ 0 & \Psi''_1 & -\Psi''_2 & 0 & 0 & \Psi''_3 & -\Psi''_4(z) & 0 \end{bmatrix} q_k = W''_k q_k. \tag{C.11}$$

with

$$\Psi''_1(z) = \frac{6}{l_k^2}\left(-1 + 2\frac{z-z_k}{l_k}\right), \tag{C.12}$$

$$\Psi''_2(z) = \frac{4}{l_k} + 6\frac{z-z_k}{l_k^2}, \tag{C.13}$$

$$\Psi''_3(z) = \frac{6}{l_k^2}\left(1 - 2\frac{z-z_k}{l_k}\right), \tag{C.14}$$

$$\Psi''_4(z) = -\frac{2}{l_k} + 6\frac{z-z_k}{l_k^2}. \tag{C.15}$$

C.2 Element Matrices for Rigid Disks

The mass matrix M^d for the rigid disk elements is given by

$$M^d = \begin{pmatrix} m & 0 & 0 & 0 \\ 0 & m & 0 & 0 \\ 0 & 0 & I & 0 \\ 0 & 0 & 0 & I \end{pmatrix}, \tag{C.16}$$

the gyroscopic matrix G^d by

$$G^d = \omega\begin{pmatrix} 0 & 0 & 0 & 0 \\ 0 & 0 & 0 & 0 \\ 0 & 0 & 0 & I_p \\ 0 & 0 & -I_p & 0 \end{pmatrix}, \tag{C.17}$$

and the damping matrix by

$$
C^d = \begin{pmatrix}
c & 0 & 0 & 0 \\
0 & c & 0 & 0 \\
0 & 0 & 0 & 0 \\
0 & 0 & 0 & 0
\end{pmatrix},
\tag{C.18}
$$

where c is the damping coefficient for the external damping.

C.3   Rayleigh Beam Element Matrices

The mass matrix is split into two parts, the matrix M_t for the translational inertia

$$
M_t = \frac{\mu l}{420}
\begin{pmatrix}
156 & & & & & & & \\
0 & 156 & & & & \text{Sym.} & & \\
0 & -22l & 4l^2 & & & & & \\
22l & 0 & 0 & 4l^2 & & & & \\
54 & 0 & 0 & 13l & 156 & & & \\
0 & 54 & -13l & 0 & 0 & 156 & & \\
0 & 13l & -3l^2 & 0 & 0 & 22l & 4l^2 & \\
-13l & 0 & 0 & -3l^2 & -22l & 0 & 0 & 4l^2
\end{pmatrix},
\tag{C.19}
$$

and the matrix M_r for the rotatory inertia

$$
M_r = \frac{\mu r^2}{120l}
\begin{pmatrix}
36 & & & & & & & \\
0 & 36 & & & & \text{Sym.} & & \\
0 & -3l & 4l^2 & & & & & \\
3l & 0 & 0 & 4l^2 & & & & \\
-36 & 0 & 0 & -3l & 36 & & & \\
0 & -36 & 3l & 0 & 0 & 36 & & \\
0 & -3l & -l^2 & 0 & 0 & 3l & 4l^2 & \\
3l & 0 & 0 & -l^2 & -3l & 0 & 0 & 4l^2
\end{pmatrix}.
\tag{C.20}
$$

For our choice of damping, the damping matrix is a multiple of the translatory mass matrix

$$
C = \frac{cl}{420}
\begin{pmatrix}
156 & & & & & & & \\
0 & 156 & & & & \text{Sym.} & & \\
0 & -22l & 4l^2 & & & & & \\
22l & 0 & 0 & 4l^2 & & & & \\
54 & 0 & 0 & 13l & 156 & & & \\
0 & 54 & -13l & 0 & 0 & 156 & & \\
0 & 13l & -3l^2 & 0 & 0 & 22l & 4l^2 & \\
-13l & 0 & 0 & -3l^2 & -22l & 0 & 0 & 4l^2
\end{pmatrix}.
\tag{C.21}
$$

The skew symmetric gyroscopic matrix is

$$
G = \frac{\omega I_p}{30l}
\begin{pmatrix}
0 & & & & & & \\
-36 & 0 & & & \text{Skew–sym.} & & \\
3l & 0 & 0 & & & & \\
0 & 3l & -4l^2 & 0 & & & \\
0 & -36 & 3l & 0 & 0 & & \\
36 & 0 & 0 & 3l & -36 & 0 & \\
3l & 0 & 0 & -l^2 & -3l & 0 & 0 \\
0 & 3l & l^2 & 0 & 0 & -3l & 4l^2 & 0
\end{pmatrix},
\tag{C.22}
$$

and the stiffness matrix is

$$
K = \frac{EI_a}{l^3}
\begin{pmatrix}
12 & & & & & & \\
0 & 12 & & & \text{Sym.} & & \\
0 & -6l & 4l^2 & & & & \\
6l & 0 & 0 & 4l^2 & & & \\
-12 & 0 & 0 & -6l & 12 & & \\
0 & -12 & 6l & 0 & 0 & 12 & \\
0 & -6l & 2l^2 & 0 & 0 & 6l & 4l^2 & \\
6l & 0 & 0 & 2l^2 & -6l & 0 & 0 & 4l^2
\end{pmatrix}.
\tag{C.23}
$$

Appendix D

Specifications of Turbocharger Beam Models

D.1 13 Element Beam Model

In Chapters 4 and 6 we consider a beam model consisting of 13 Euler beam elements. Turbine and impeller are modeled with rigid disks attached in different nodes. A further refinement is the use of a two layer shaft model. Considering two layers of different material along the shaft allows for a more detailed description of the shaft. We consider now the following shaft with 13 elements that have the following parameters:
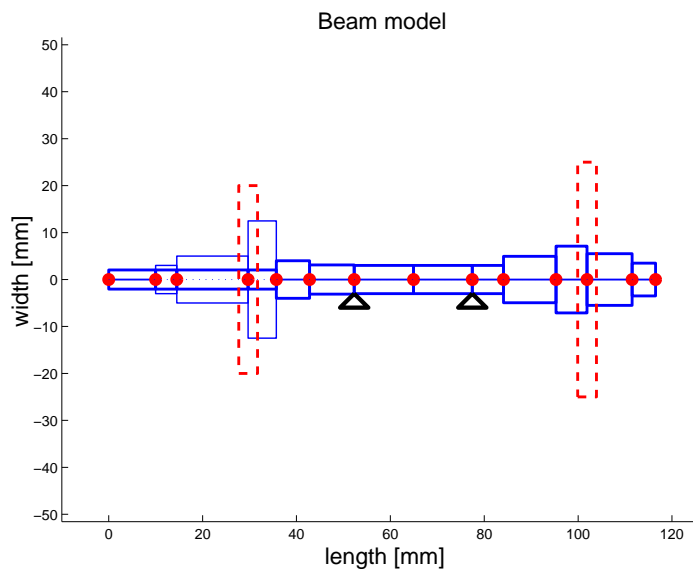

Figure D.1: Detailed beam model of turbocharger.

#	Length [mm]	Ø [mm]	Inner Shaft		Outer Shaft		
			Young's modulus [N/m²]	Density [kg/m³]	Ø [mm]	Young's modulus [N/m²]	Density [kg/m³]
1	10.0	4.1	7800	2.058e11			
2	4.5	4.1	7800	2.058e11	6.0	0	7.35e10
3	15.2	4.1	7800	2.058e11	10.0	0	7.35e10
4	6.0	4.1	7800	2.058e11	25.0	0	7.35e10
5	7.1	8.0	7800	2.058e11			
6	9.5	6.2	7800	2.058e11			
7	12.65	6.0	7800	2.058e11			
8	12.5	6.0	7800	2.058e11			
9	6.65	6.0	7800	2.058e11			
10	11.2	9.9	7800	2.058e11			
11	6.6	14.2	0	2.058e11			
12	9.6	11.0	0	2.058e11			
13	5.0	7.0	7800	2.058e11			

The parameters of the rigid disks are the following:

	Mass [kg]	Diametral inertia moment I_d [kgm²]	Polar inertia moment I_p [kgm²]
Impeller	1.3328e-2	1.2740e-6	2.1560e-6
Turbine	4.3414e-2	3.1360e-6	5.8800e-6

A picture of this model is shown in Figure D.1, showing the beam elements from left to right and also the positions of the bearings. The thinner lines represent the outer shaft elements and the red dashed lines symbolize the two rigid disks.

From this geometry data one can calculate the effective masses and moments of inertia of each element, which are needed for the setup of the system's matrices. They are given by the following formulas:

$$\mu = \pi l \left(r_i^2 \rho_i + (r_o^2 - r_i^2)\rho_o \right), \tag{D.1}$$

$$I_p = \frac{\pi}{2} \left(\rho_i r_i^4 + \rho_o(r_o^4 - r_i^4) \right), \tag{D.2}$$

$$I_a = \frac{\pi}{4} \left(\rho_i r_i^4 + \rho_o(r_o^4 - r_i^4) \right), \tag{D.3}$$

$$E_Y I_d = = \frac{\pi}{4} \left(E_{Y,i} \rho_i r_i^4 + E_{Y,o} \rho_o(r_o^4 - r_i^4) \right). \tag{D.4}$$

These effective parameters are used in the calculation of the system matrices and the equation of motion.

The unbalance parameters for the above beam model are

$$a_3 = 1.35 \times 10^{-7} kgm, \qquad\qquad \psi_3 = \pi, \qquad\qquad (D.5)$$
$$a_5 = 1.50 \times 10^{-7} kgm, \qquad\qquad \psi_5 = 0, \qquad\qquad (D.6)$$
$$a_{11} = 2.01 \times 10^{-7} kgm, \qquad\qquad \psi_{11} = 0, \qquad\qquad (D.7)$$
$$a_{13} = 2.07 \times 10^{-7} kgm, \qquad\qquad \psi_{13} = \pi \qquad\qquad (D.8)$$

where a_i is the unbalance amplitude, and ψ_i is the phase of the unbalance vector in node i.

D.2   3 Element Beam Model

In Chapters 6 and 7 we consider a simplified smaller 3 element beam model. This model (c.f. Figure D.2) has only one layer and it has the following specifications.

| #	Length [mm]	⌀ [mm]	Shaft Young's modulus [N/m^2]	Density [kg/m^3]
1	35	6	7800	2.058e11
2	25	6	7800	2.058e11
3	35	10	7800	2.058e11
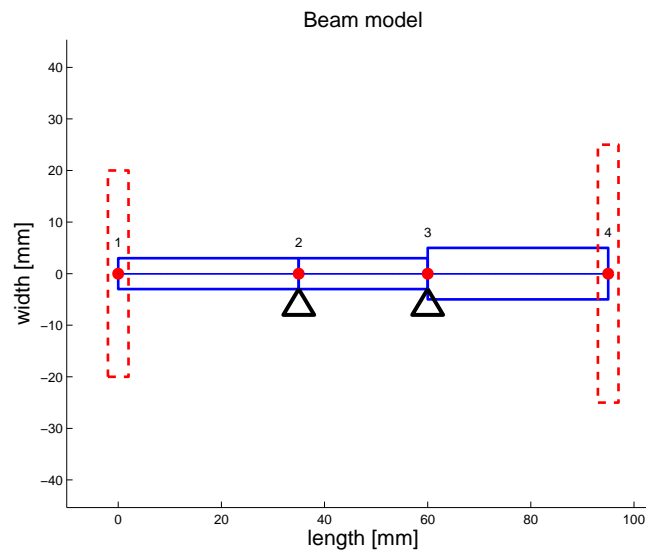
Figure D.2: 4 element beam model of turbocharger.

The parameters of the two rigid disks attached at both ends are

	Mass [kg]	Diametral inertia moment I_d [kgm^2]	Polar inertia moment I_p [kgm^2]
Impeller	2.0e-2	0.5e-6	2e-6
Turbine	3.0e-2	0.7e-6	3e-6

The unbalance parameters for the above beam model are

$$a_1 = 1.35 \times 10^{-7} kgm, \qquad\qquad \psi_3 = \pi, \qquad\qquad \text{(D.9)}$$
$$a_4 = 2.07 \times 10^{-7} kgm, \qquad\qquad \psi_{13} = \pi. \qquad\qquad \text{(D.10)}$$

Appendix E

Detailed Formulas for the Inertia Correction p^1

E.1 Short Bearing Approximation

The detailed solution for the pressure p^1 can be computed by solving the integrals in (5.60). Additionally to the expression on Equation (5.61) the solution can be written in a more convenient form in terms of p_0, h_i, and V_i ($i = 0, 1$)

$$p_1 = \frac{z(z-1)}{h_0^5}\left(z(z-1)G + \sum_{i=0}^{4} H_i\right). \tag{E.1}$$

Here the following abbreviations are used

$$\Psi(t,\varphi) := (\gamma' - \frac{1}{2})\kappa\sin\varphi + \kappa'\cos\varphi, \tag{E.2}$$

$$G(t,\varphi) := \frac{1}{K}(\frac{3}{2}(\partial_\varphi h_0)^2\Psi - \frac{3}{2}h_0\partial_\varphi\Psi\partial_\varphi h_0 + \frac{1}{2}h_0^2\partial_\varphi^2\Psi - \frac{3}{2}h_0\Psi\partial_\varphi^2 h_0), \tag{E.3}$$

$$H_4(t,\varphi) := -\frac{1}{40}\mathcal{R}\left(-3\partial_\varphi^2 h_0 + 24\partial_\tau\Psi - 10\partial_\tau\partial_\varphi h_0 + 2\partial_\varphi\Psi\right)h_0^4, \tag{E.4}$$

$$H_3(t,\varphi) := \left(\mathcal{R}\left(\frac{3}{10}\Psi\partial_\tau h_0 + \frac{1}{2}\partial_\tau h_0\partial_\varphi h_0 + \frac{3}{20}(\partial_\varphi h_0)^2 - \frac{81}{70}\Psi^2 + \frac{13}{20}\Psi\partial_\varphi h_0\right)\right.$$
$$\left. + 3\Psi - 4\partial_\varphi h_0 + 3\partial_\varphi V_\varphi^1\right)h_0^3, \tag{E.5}$$

$$H_2(t,\varphi) := \left(-3KV_\varphi^1\partial_\varphi h_0 - \frac{1}{2}\partial_\varphi^2\Psi - 3K\partial_\varphi h_1\right)\frac{h_0^2}{K}, \tag{E.6}$$

$$H_1(t,\varphi) := \left(18Kh_1\Psi + \frac{3}{2}\Psi\partial_\varphi^2 h_0 + \frac{3}{2}\partial_\varphi h_0\partial_\varphi\Psi\right)\frac{h_0}{K}, \tag{E.7}$$

$$H_0(t,\varphi) := -\frac{3}{2}(\partial_\varphi h_0)^2\frac{\Psi}{K}. \tag{E.8}$$

E.2   Correction to Solution of Reynolds' Equation

In Section 5.1.6 the equation for the correction term p^1 to the solution of Reynolds' equation is derived. The right hand side of this elliptical equation is given here.

$$\Psi(p^0, h^0, h^1, V_\varphi^0, V_\varphi^1) =$$

$$\mathcal{R}h_0^4((-\frac{9}{560}\partial_\varphi p^0 \partial_\varphi^3 p^0 - \frac{9}{560}(\partial_\varphi^2 p^0)^2)\delta^4$$

$$+ (-\frac{3}{140}(\partial_\varphi \partial_z p^0)^2 - \frac{9}{560}\partial_z p^0 \partial_\varphi^2 \partial_z p^0 - \frac{3}{280}\partial_\varphi^2 p^0 \partial_z^2 p^0 - \frac{9}{560}\partial_\varphi p^0 \partial_z^2 \partial_\varphi p^0)\delta^2$$

$$- \frac{9}{560}\partial_z p^0 \partial_z^3 p^0 - \frac{9}{560}(\partial_z^2 p^0)^2)$$

$$+\mathcal{R}h_0^{\,3}((-\frac{3}{80}(\partial_\varphi p^0)^2 \partial_\varphi^2 h - \frac{3}{16}\partial_\varphi p^0 \partial_\varphi^2 p^0 \partial_\varphi h_0)\delta^4$$

$$+ (-\frac{3}{40}\partial_\varphi p^0 \partial_\varphi h_0 \partial_z^2 p^0 - \frac{9}{80}\partial_\varphi h_0 \partial_z p^0 \partial_\varphi \partial_z p^0)\delta^2)$$

$$+\mathcal{R}h_0^2(-\frac{9}{40}\delta^4 \partial_\varphi p^{0\,2}(\partial_\varphi h_0)^2 + (\frac{1}{10}\partial_t \partial_z^2 p^0 + \frac{1}{120}\partial_\varphi^3 p^0 V_\varphi^0)\delta^2$$

$$+ \frac{1}{120}\partial_z^2 \partial_\varphi p^0 V_\varphi^0 + \frac{1}{10}\partial_t \partial_z^2 p^0)$$

$$+h_0(((\frac{1}{24}\partial_\varphi^2 p^0 V_\varphi^0 \partial_\varphi h_0 + \frac{1}{4}\partial_\varphi p^0 \partial_t \partial_\varphi h_0 + \frac{1}{4}\partial_\varphi^2 p^0 \partial_t h_0 + \frac{1}{2}\partial_t \partial_\varphi p^0 \partial_\varphi h_0)\delta^2$$

$$+ \frac{1}{4}\partial_t h_0 \partial_z^2 p^0 - \frac{1}{12}\partial_z^2 p^0 V_\varphi^0 \partial_\varphi h_0)\mathcal{R}$$

$$- \frac{3}{2}\delta^2 \partial_\varphi^2 p^0 - \frac{1}{2}\partial_z^2 p^0)$$

$$+ \quad (\delta^2 \partial_\varphi p^0 \partial_\varphi h_0 \partial_t h_0 \mathcal{R} - 5\delta^2 \partial_\varphi p^0 \partial_\varphi h_0)$$

$$+h_0^{-1}((\frac{3}{20}(V_\varphi^0)^2 \partial_\varphi^2 h_0 + \frac{1}{2}V_\varphi^0 \partial_t \partial_\varphi h_0)\mathcal{R}$$

$$+ (-3h_1 \partial_\varphi^2 p^0 - 3\partial_\varphi h_1 \partial_\varphi p^0)\delta^2 - 3h_1 \partial_z^2 p^0)$$

$$+h_0^{-2}((V_\varphi^0 \partial_t h_0 \partial_\varphi h_0 + \frac{3}{10}(V_\varphi^0)^2(\partial_\varphi h_0)^2)\mathcal{R}$$

$$+ 6\partial_\varphi V_\varphi^1 - 6h_1 \delta^2 \partial_\varphi p^0 \partial_\varphi h_0 - 8V_\varphi^0 \partial_\varphi h_0)$$

$$+h_0^{-3}(-6\partial_\varphi h_1 V_\varphi^0 - 6\partial_\varphi h_0 V_\varphi^1). \tag{E.9}$$

Appendix F

Integration of Bearing Integrals with Sommerfeld Variable Transformation

We want to solve the following integrals that appear in the calculation of the bearing forces

$$F_N = -\frac{W^3 R \rho \nu \omega}{c_r^2} \int_0^1 \int_0^{2\pi} (p^0)^+ \, d\varphi \, dz, \tag{F.1}$$

$$F_T = -\frac{W^3 R \rho \nu \omega}{c_r^2} \int_0^1 \int_0^{2\pi} (p^0)^+ \, d\varphi \, dz, \tag{F.2}$$

where

$$p^0 = -6z(z-1)\frac{\left((\gamma' - \frac{1}{2})\kappa \sin \varphi + \kappa' \cos \varphi\right)}{(1 - \kappa \cos \varphi)^3}. \tag{F.3}$$

We set

$$a = \kappa', \tag{F.4}$$

$$b = \kappa(\gamma' - \frac{1}{2}), \tag{F.5}$$

$$C = \frac{W^3 R \rho \nu \omega}{c_r^2}, \tag{F.6}$$

$$\psi = \arg(a - ib). \tag{F.7}$$

The pressure is positive for

$$\varphi \in [\varphi_1, \varphi_2] = [-\psi - \frac{\pi}{2}, -\psi + \frac{\pi}{2}]. \tag{F.8}$$

Hence, the integrals become

$$F_N = -C \int_0^1 \int_{\varphi_1}^{\varphi_2} -6z(z-1) \frac{b \sin \varphi \cos \varphi + a \cos^2 \varphi}{(1 - \kappa \cos \varphi)^3} \, d\varphi \, dz, \tag{F.9}$$

$$F_T = -C \int_0^1 \int_{\varphi_1}^{\varphi_2} -6z(z-1) \frac{b \sin^2 \varphi + a \cos \varphi \sin \varphi}{(1 - \kappa \cos \varphi)^3} \, d\varphi \, dz. \tag{F.10}$$

The integration with respect to z is readily done and yields

$$F_N = -C \int_{\varphi_1}^{\varphi_2} \frac{b \sin \varphi \cos \varphi + a \cos^2 \varphi}{(1 - \kappa \cos \varphi)^3} \, d\varphi, \tag{F.11}$$

$$F_T = -C \int_0^1 \int_{\varphi_1}^{\varphi_2} \frac{b \sin^2 \varphi + a \cos \varphi \sin \varphi}{(1 - \kappa \cos \varphi)^3} \, d\varphi. \tag{F.12}$$

To solve the integrals with respect to φ we introduce the variable transformation which is due to Sommerfeld

$$1 - \kappa \cos \varphi = \frac{1 - \kappa^2}{1 - \kappa \cos \theta}. \tag{F.13}$$

This yields

$$\cos \varphi = \frac{\kappa - \cos \theta}{1 - \kappa \cos \theta}, \tag{F.14}$$

$$\sin \varphi = \frac{-\sqrt{1 - \kappa^2} \sin \theta}{1 - \kappa \cos \theta}, \tag{F.15}$$

$$\varphi = \arctan(\frac{-\sqrt{1 - \kappa^2} \sin \theta}{\kappa - \cos \theta}), \tag{F.16}$$

$$\frac{d\varphi}{d\theta} = \frac{(\kappa - \cos \theta)(-\sqrt{1 - \kappa^2} \cos \theta) + \sqrt{1 - \kappa^2} \sin^2 \theta}{\left(1 + \frac{(1-\kappa^2) \sin^2 \theta}{(\kappa - \cos \theta)^2}\right)(\kappa - \cos \theta)^2} \tag{F.17}$$

$$= \frac{(\sqrt{1 - \kappa^2}(\sin^2 \theta + \cos^2 \theta - \kappa \cos \theta))}{(\kappa - \cos \theta)^2 + (1 - \kappa^2) \sin^2 \theta} \tag{F.18}$$

$$= \frac{-\sqrt{1 - \kappa^2} \kappa \cos \theta}{\kappa^2 - 2\kappa \cos \theta + \cos^2 \theta + \sin^2 \theta - \kappa^2 \sin^2 \theta} \tag{F.19}$$

$$= \frac{\sqrt{1 - \kappa^2}}{1 - \kappa \cos \theta}. \tag{F.20}$$

Using the transformation formula we obtain the new integral boundaries

$$\theta_1 = \arctan(\kappa - \cos \varphi_1, -\sqrt{1 - \kappa^2} \sin \varphi_1), \tag{F.21}$$

$$\theta_2 = \arctan(\kappa - \cos \varphi_2, -\sqrt{1 - \kappa^2} \sin \varphi_2). \tag{F.22}$$

The integrals transform to

$$
F_N = -C \int_{\varphi_1}^{\varphi_2} \frac{b \sin \varphi \cos \varphi + a \cos^2 \varphi}{(1 - \kappa \cos \varphi)^3} \, d\varphi
$$

$$
= -C \int_{\theta_1}^{\theta_2} \left(a \left(\frac{\kappa - \cos \theta}{1 - \kappa \cos \theta} \right)^2 - b \frac{\sqrt{1 - \kappa^2} \sin \theta (\kappa - \cos \theta)}{(1 - \kappa \cos \theta)^2} \right) \frac{\sqrt{1 - \kappa^2}(1 - \kappa \cos \theta)^3}{(1 - \kappa^2)^3 (1 - \kappa \cos \theta)} \, d\theta
$$

$$
= -C \int_{\theta_1}^{\theta_2} \left(a \frac{(\kappa - \cos \theta)^2}{(1 - \kappa^2)^{\frac{5}{2}}} - b \frac{\sin \theta (\kappa - \cos \theta)}{(1 - \kappa^2)^2} \right) d\theta, \tag{F.23}
$$

and analogously

$$
F_T = -C \int_{\varphi_1}^{\varphi_2} \frac{b \sin^2 \varphi \varphi + a \cos \varphi \sin \varphi}{(1 - \kappa \cos \varphi)^3} \, d\varphi
$$

$$
= -C \int_{\theta_1}^{\theta_2} \left(b \frac{\sin^2 \theta}{(1 - \kappa^2)^{\frac{3}{2}}} - a \frac{\sin \theta (\kappa - \cos \delta)}{(1 - \kappa^2)^2} \right) d\theta. \tag{F.24}
$$

The three resulting integrals are

$$
A_1 = \int_{\theta_1}^{\theta_2} \frac{(\kappa - \cos \theta)^2}{(1 - \kappa^2)^{\frac{5}{2}}} \, d\theta \tag{F.25}
$$

$$
= \frac{(\kappa^2 + \frac{1}{2})(\theta_2 - \theta_1) - 2\kappa(\sin \theta_2 - \sin \theta_1) + \frac{1}{4}(\sin 2\theta_2 - \sin 2\theta_1)}{(1 - \kappa^2)^{\frac{5}{2}}}, \tag{F.26}
$$

$$
A_2 = \int_{\theta_1}^{\theta_2} \frac{\sin \theta (\kappa - \cos \theta)}{(1 - \kappa^2)^2} \, d\theta = \frac{-\kappa(\cos \theta_2 - \cos \theta_1) + \frac{1}{4}(\cos 2\theta_2 - \cos 2\theta_1)}{(1 - \kappa^2)^2}, \tag{F.27}
$$

$$
A_3 = \int_{\theta_1}^{\theta_2} \frac{\sin^2 \theta}{(1 - \kappa^2)^{\frac{3}{2}}} \, d\theta = \frac{(2(\theta_2 - \theta_1) - \sin 2\theta_2 + \sin 2\theta_1)}{4(1 - \kappa^2)^{\frac{3}{2}}}, \tag{F.28}
$$

which finally gives the following formulation for the forces

$$
F_N = -C(a A_1 - b A_2), \tag{F.29}
$$

$$
F_T = -C(b A_3 - a A_2). \tag{F.30}
$$

References

ARNOL'D, V. I. 1987. *Geometrische Methoden in der Theorie der gewöhnlichen Differentialglei-chungen*. Birkhäuser.

ASSEMIEN, A., BAYADA, G., & CHAMBAT, M. 1994. Inertial effects in the asymptotic behavior on a thin film flow. *Aymptotic Analysis*, **9**, 177–208.

BANGERTH, W. 2002. posted in the mailing list of `deal.II`; `http://www.dealii.org`.

BANGERTH, W., HARTMANN, R., & KANSCHAT, G. 2007. deal.II — a general-purpose object-oriented finite element library. *ACM Trans. Math. Softw.*, **33**(4).

BANGERTH, W., HARTMANN, R., & KANSCHAT, G. 2008. `deal.II` *Differential Equations Analysis Library, Technical Reference*. `http://www.dealii.org`.

BAYADA, G., & CHAMBAT, M. 1986. The Transition between the Stokes Equations and the Reynolds Equation: A Mathematical Proof. *Applied Mathematics and Optimization*, **14**, 73–93.

BEYN, W.-J., CHAMPNEYS, A., , DOEDEL, E., GOVAERTS, W., KUZNETSOV, Y., & SANDSTEDE, B. 2002. *Handbook of Dynamical Systems*. Vol. 2. Elsevier. Chap. B.4: Numerical Continuation and Computation of Normal Forms, pages 149–219.

BOURGEAT, A., MIKELIĆ, A., & TAPIÉRO, R. 1993. Dérivation des équations moyennées décrivant un écoulement non newtonien dans un domaine der faible épaisseur. *Comptes rendus de l'Académie des Sciences de Paris*, **Série I, t. 316**, 965–970. in french.

BRAESS, D. 2007. *Finite elements. Theory, fast solvers and applications in solid mechanics. Translated from German by Larry L. Schumaker.* Cambridge University Press, Cambridge.

BRENAN, K. E., CAMPBELL, S. L., & PETZOLD, L. R. 1989. *Numerical solution of initial value problems in differential algebraic equations*. North-Holland.

BRENNER, S. C., & SCOTT, L. R. 1994. *The Mathematical Theory of the Finite Element Method*. Springer.

BREZIS, H. 1999. *Analyse fonctionnelle*. Dunod. in french.

CHILDS, D. 1993. *Turbomachinery Rotordynamics*. Wiley.

CHOW, S.-N., & HALE, J. K. 1982. *Methods of Bifurcation Theory*. Springer.

CIARLET, P. G. 1978. *The Finite Element Method for Elliptic Problems*. North Holland.

CLOUGH, R. W. 1960 (September). The finite element method in plane stress analysis. *In: Proceedings, 2nd Conference on Electronic Computation, Pittsburgh, Pennsylvania*. A.S.C.E. Structural Division.

CRANDALL, S. H. 1995. Rotordynamics. *Pages 3–44 of:* KLIEMANN, W., & S., NAMACHCHIVAYA. (eds), *Nonlinear Dynamics and Stochastic Mechanics. Dedicated to Prof. S. T. Ariaratnam on the occasion of his sixtieth birthday*. CRC Mathematical Modelling Series. CRC Press.

CRANDALL, S. H., & EL-SHAFEI, A. 1993. Momentum and Energy Approximations for Elementary Squeeze-Film Damper Flow. *Transactions of the ASME: Journal of Applied Mechanics*, **60**(September), 728–736.

CRANDALL, STEPHEN H. 1996. Oil whirl and oil whip, nonlinear limit-cycle phenomena. *Pages 51–64 of:* KLIEMANN, W. H., LANGFORD, W. F., & NAMACHCHIVAYA, N. S. (eds), *Nonlinear dynamics and stochastic mechanics. Proceedings of the international symposium, Waterloo, Canada, August 28-September 1, 1993.* Fields Inst. Commun., vol. 9. American Mathematical Society.

DAVIS, T. A. 2004. Algorithm 832: UMFPACK V4.3—an unsymmetric-pattern multi-frontal method. *ACM Trans. Math. Softw.*, **30**(2), 196–199.

DAVIS, T. A. 2007. *UMFPACK Version 5.2 User Guide*. Dept. of Computer and Information Science and Engineering, Univ. of Florida. http://www.cise.ufl.edu/research/sparse/umfpack.

DEUFLHARD, P., & BORNEMANN, F. 1994. *Numerische Mathematik, Bd.2*. de Gruyter.

DEUFLHARD, P., & HOHMANN, A. 1993. *Numerische Mathematik Bd. 1*. de Gruyter.

DHOOGE, A., GOVAERTS, W., KUZNETSOV, YU. A., MESTROM, W., & RIET, A. M. 2004 (July). *MATCONT - A Continuation Toolbox in Matlab*. URL: http://sourceforge.net/projects/matcont/.

DOEDEL, E., KELLER, H., & KERNEVEZ, J. 1991a. Numerical Analysis and Control of Bifurcation Problems - (I) Bifurcation in Finite Dimensions. *International Journal of Bifurcation and Chaos*, **1**(3), 493 – 520.

DOEDEL, E., KELLER, H., & KERNEVEZ, J. 1991b. Numerical Analysis and Control of Bifurcation Problems - (II) Bifurcation in Infinite Dimensions. *International Journal of Bifurcation and Chaos*, **1**(4).

DOEDEL, E.J., PFAFFENROTH, R.C., CHAMPNEYS, A.R., FAIRGRIEVE, T.F., KUZNETSOV, YU.A., OLDEMAN, B.E., SANDSTEDE, B., & WANG, X. 2000. *Auto2000: Continuation and bifurcation software for ordinary differential equations (with HomCont)*. Concordia University, http://cmvl.cs.concordia.ca/auto/.

DUVNJAK, A., & MARUŠIĆ-PALOKA, E. 2000. Derivation of the Reynolds Equation for Lubrication of a Rotating Shaft. *Archivum Mathematicum (BRNO)*, **36**, 239–253.

EATON, J. W. 2002. *GNU Octave Manual*. Network Theory Limited. `http://www.octave.org`.

EHRICH, F. F. (ed). 1999. *Handbook of Rotordynamics*. 3rd edn. Krieger Publishing.

EL-SHAFEI, A. 1995. Modeling Fluid Inertia Forces of short Journal Bearings for Rotordynamic Applications. *Transactions of the ASME: Journal of Sound and Vibration*, **117**(October), 462–469.

ELROD, H. G. 1981. A cavitation algorithm. *Transactions of the ASME, Journal of Lubrication Technology*, **103**, 350–354.

ESHLEMAN, R.L., & EUBANKS, R.A. 1969. On the critical speed of a continuous rotor. *Transactions of the ASME, Journal for Engineering in Industry*, **91**(4), 1180–1188.

EVANS, L. C. 1998. *Partial Differential Equations*. Graduate Studies in Mathematics, vol. 19. American Mathematical Society.

FENICHEL, N. 1971. Persistence and Smoothness of Invariant Manifolds for Flows. *Indiana Univ. Math. J.*, **21**, 192–226.

GAMBUADO, J. M. 1985. Perturbation of the Hopf Bifurcation by an External Time-Periodic Forcing. *Journal of Differential Equations*, **57**, 172–199.

GASCH, R., & PFÜTZNER, H. 1975. *Rotordynamik: Eine Einführung*. Springer.

GASCH, R., NORDMANN, R., & PFÜTZNER, H. 2002. *Rotordynamik*. 2nd edn. Springer.

GE, T., & LEUNG, A.Y.T. 1998. Construction of invariant torus using Toeplitz Jacobian matrices/fast Fourier transform approach. *Nonlinear Dynamics*.

GLAZIER, J.A., & LIBCHABER, A. 1988. Quasi-periodicity and dynamical systems: an experimentalist's view. *IEEE Trans. Circuits and Systems*, **35**(7), 790–809.

GUCKENHEIMER, J., & HOLMES, P. 1983. *Nonlinear Oscillations, Dynamical Systems, and Bifurcations of Vector Fields*. Springer.

HAIRER, E., & WANNER, G. 1996. *Solving ordinary differential equations. II: Stiff and differential-algebraic problems. 2nd rev. ed.* Springer Series in Computational Mathematics. 14. Berlin: Springer.

HAN, S. M., BENAROYA, H., & WEI, T. 1999. Dynamics of Transversely Vibrating Beams Using Four Engineering Theories. *Journal of Sound an Vibration*, **225**(5), 935–988.

HOLLIS, P., & TAYLOR, D. L. 1986. Hopf Bifurcations to Limit Cycles in Fluid Film Bearings. *Transactions of the ASME: Journal of Tribology*, **108**(April), 184–189.

HOLT, C., SAN ANDRÉS, L., SAHAY, S., TANG, P., LA RUE, G., & GJIKA, K. 2005. Test Response and Nonlinear Analysis of a Turbocharger Supported on Floating Ring Bearings. *Transactions of the ASME, Journal of Vibration and Accoustics*, **127**, 107–115.

IMAI, M., KITO, K., & OKA, T. 1985a. Measurement of Human Skull Vibration: Dynamic Response of a Skull in the Living Human. *Jap. Soc. ME & BE*, July. in japanese.

IMAI, M., KITO, K., & OKA, T. 1985b. Measurement of Human Skull Vibration: Vibration Mode of a Dry Skull with Holographic Interferometry. *Jap. Soc. ME & BE*, July. in japanese.

INAGAKI, M. 2002. personal communication. Toyota Central Research & Development Laboratories, Inc.

JOSÉ, J. V., & SALETAN, E. J. 1998. *Classical Dynamics, A Contemporary approach*. Cambridge University Press.

JOST, J. 1998. *Partielle Differentialgleichungen*. Springer. in german.

K., HALE. J. 1969. *Ordinary Differential Equations*. Wiley.

KELLER, H. B. 1977. Numerical solution of bifurcation and nonlinear eigenvalue problems. *Pages 359–384 of:* RABINOWITZ, P. H. (ed), *Applications of Bifurcation Theory*. Academic Press.

KIKUCHI, N. 1986. *Finite Element Methods in Mechanics*. Cambridge University Press.

KUZNETSOV, YU. A., & LEVITIN, V. V. 1997. *CONTENT: Integrated Environment fo Analysis of Dynamical Systems*. CWI, Amsterdam. URL: http://www.math.uu.nl/people/kuznet/CONTENT/.

KUZNETSOV, YU.A. 2004. *Elements of applied bifurcation theory*. 3rd edn. Applied Mathematical Sciences, vol. 112. Springer-Verlag, New York.

LANDAU, L. D., & LIFSCHITZ, E. M. 1983. *Lehrbuch der theoretischen Physik, Band 7, Elastizitätstheorie*. 5th edn. Akademie-Verlag, Berlin. in german.

LANG, O. R., & STEINHILPER, W. 1978. *Gleitlager*. Springer. Chap. 7: Radialgleitlager - Theoretische Grundlagen.

LUND, J. W. 1987. Review of the concept of dynamic coefficients for fluid film journal bearings. *Transactions of the ASME, Journal of Tribology*, **109**, 37–41.

MEIROVITCH, L. 1986. *Elements of Vibration Analysis*. second edn. Wiley.

MUSZYNSKA, A. 1986. Whirl and Whip – Rotor/Bearing Stability Problems. *Journal of Sound and Vibration*, **110**(3), 443–462.

MUSZYNSKA, A. 1987. Tracking the Mystery of Oil Whirl. *Sound and Vibration*, February, 8–11.

MUSZYNSKA, A. 1988. Stability of Whirl and Whip in Rotor/Bearing Systems. *Journal of Sound and Vibration*, **127**(1), 49–64.

NATARAJ, C., ASHRAFIUON, H., & ARAKERE, N. K. 1994. Effect of Fluid Inertia on Journal Bearing Parameters. *Tribology Transactions*, **37**(4), 784–792.

NAYFEH, A.H. 2000. *Nonlinear interactions*. Wiley Series in Nonlinear Science. Wiley-Interscience [John Wiley & Sons], New York.

NAYFEH, A.H., & BALACHANDRAN, B. 1995. *Applied nonlinear dynamics*. Wiley Series in Nonlinear Science. John Wiley & Sons Inc., New York.

NAZAROV, S. A. 1990. Asymptotic solution of the Navier-Stokes Problem on the flow of a thin layer of fluid. *Siberian Mathematical Journal*, **32**(2), 296–307.

NELSON, F. C. 2003. A Brief History of Rotordynamics. *S&V, Sound and Vibration*, **37**(6).

NELSON, H. D. 1980. A Finite Rotating Shaft Element Using Timoshenko Beam Theory. *Transactions of the ASME, Journal of Mechanical Design*, **102**(October), 793–803.

NELSON, H. D., & McVAUGH, J. M. 1976. The Dynamics of Rotor-Bearing Systems Using Finite Elements. *Transactions of the ASME, Journal of Engineering for Industry*, May, 593–600.

NEWKIRK, B. L., & TAYLOR, H. D. 1925. Shaft whirling due to oil action in journal bearings. *Gen. Electr. Rev.*, **28**(7), 559–568.

NOLTING, W. 1989. *Grundkurs: Theoretische Physik;1. Klassische Mechanik*. Verlag Zimmermann-Neufang, Ulmen.

OCKENDON, H., & OCKENDON, J. R. 1995. *Viscous Flow*. Cambridge University Press.

RANNACHER, R. 2000. *Vorlesungsskript Numerische Mathematik 2, Numerische Methoden für Partielle Differentialgleichungen, Universität Heidelberg*.

RANNACHER, R. 2001. *Vorlesungsskript Numerische Mathematik 3, Numerische Methoden für Probleme der Kontinuumsmechanik, Universität Heidelberg*.

RÜBEL, J., STARKE, J., INAGAKI, M., KAWAMOTO, A., & ABEKURA, T. 2006. *Vibration analysis method of rotor supported by floating bush bearing*. Application of Japanese Patent (App. No. 2006-312247) by the patent section of TOYOTA CRDL.

San Andrés, L. 2006. *Class Notes to Lubrication Theory, TAMU*. obtained from http://www1.mengr.tamu.edu/Tribology/.

San Andrés, L., & Kerth, J. 2004. Thermal effects on the performance of floating ring bearings for turbochargers. *Journal of Engineering Tribology, Special Issue on Thermal Effects on Fluid Film Lubrication, IMEchE Proceedings, Part J*, **218**(5), 437–450.

San Andrés, L., Childs, D., & Zhou, Y. 1995. Turbulent-Flow Hydrostatic Bearings: Analysis and Experimental Results. *Int. J. Mech. Sci.*, **37**, 815–829.

Schilder, F. 2004. *Torcont v1 (2003) User Manual, Applied Non-linear Mathematics Preprint 2004.18*. University of Bristol. http://www.dynamicalsystems.org/sw/sw/detail?item=44.

Schilder, F., & Peckham, B.B. 2007. Computing Arnol'd tongue scenarios. *Journal of Computational Physics*, **220**(2), 932–951.

Schilder, F., Osinga, H.M., & Vogt, W. 2005. Continuation of quasi-periodic invariant tori. *SIAM Journal on Applied Dynamical Systems*, **4**(3), 459–488.

Schilder, F., Vogt, W., Schreiber, S., & Osinga, H.M. 2006. Fourier methods for quasi-periodic oscillations. *Internat. J. Numer. Methods Engrg.*, **67**(5), 629–671.

Schilder, F., Rübel, J., Starke, J. amd Osinga, H. M., Krauskopf, B., & Inagaki, M. 2007. Efficient computation of quasiperiodic oscillations in nonlinear systems with fast rotating parts. *Nonlinear Dynamics*, **51**(4), 529–539.

Shampine, Lawrence F., & Reichelt, Mark W. 1997. The MATLAB ODE suite. *SIAM J. Sci. Comput.*, **18**(1), 1–22.

Shampine, L.F. 2002. Solving $0 = F(t, y(t), y'(t))$ in Matlab. *J. Numer. Math.*, **10**(4), 291–310.

Sommerfeld, A. 1964. *Mechanik der Deformierbaren Medien*. Vorlesungen über Theoretische Physik, vol. 2. Akademie Verlag.

Stoer, J., & Bulirsch, R. 2002. *Introduction to numerical analysis*. 3rd edn. Texts in Applied Mathematics. Springer, New York.

Strang, G., & Fix, G. J. 1973. *An analysis of the finite element method*. Prentice Hall.

Strauss, F. 2005. *Design optimization of rotating bodies*. Ph.D. thesis, University of Heidelberg.

Strauss, F., Inagaki, M., & Starke, J. 2007. Reduction of vibration level in rotordynamics by design optimization. *Journal of Structural and Multidisciplinary Optimization*, **34**(2).

STROGATZ, S.H. 2000. *Nonlinear dynamics and chaos: with applications to physics, biology, chemistry, and engineering*. Cambridge University Press, Perseus Publishing.

SZERI, A. Z. 1998. *Fluid Film Lubrication, Theory and Design*. Cambridge University Press.

TRABUCHO, L., & VIAÑO, J. M. 1995. *Mathematical modelling of rods*. Handbook of numerical analysis. Volume IV: Finite element methods (part 2), numerical methods for solids (part 2). North-Holland. Pages 487–974.

VANCE, J. M. 1988. *Rotordynamics of Turbomachinery*. Wiley.

WIGGINS, S. 1990. *Introduction to Applied Nonlinear Dynamical Systems and Chaos*. Berlin, Heidelberg, New York: Springer-Verlag.

YAMAMOTO, T., & ISHIDA, Y. 2001. *Linear and Nonlinear Rotordynamics*. Wiley.

ZEIDLER, E. 1990. *Nonlinear Functional Analysis and its Applications*. Vol. 2. Springer.